Fakultät für Elektrotechnik und Informationstechnik

Advanced Thermodynamic Measurements as Degradation Tracking Technique in Lithium-Ion Cells

Dipl.-Ing. Patrick J. Oßwald

Vollständiger Abdruck der von der Fakultät für Elektrotechnik und Informationstechnik der Technischen Universität München zur Erlangung des akademischen Grades eines

Doktor-Ingenieurs (Dr.-Ing.)

genehmigten Dissertation.

Vorsitzender: Prof. Dr. Sebastian Steinhorst

Prüfende der Dissertation:

1. Prof. Dr. Andreas Jossen
2. Prof. Dr. Harry Hoster

Die Dissertation wurde am 27.04.2017 bei der Technischen Universität München eingereicht und durch die Fakultät für Elektrotechnik und Informationstechnik am 07.07.2017 angenommen.

Abstract

An increased driving distance for electric vehicles requires improvements in the energy density of lithium-ion cells by either a higher packing density of existing active materials or by introducing new materials with higher specific capacity or higher voltages. With increasing energy content of the cell, accurate estimations of internal parameters become necessary, as the cell voltage, current, and surface temperature may not be enough to reflect the cell's current state of health. In order to maintain the high safety requirements and guarantee an optimised economical usage of the cell, methods to track the ongoing degradation of lithium-ion cells during storage and operation are required.

In this work, various electrochemical characterisation techniques are critically addressed and their applicability as degradation tracking technique is discussed. An ageing study with various commercial 18650 cells with different cathode materials is conducted and in order to determine the source of degradation, the performance of the cells is investigated. Since all cells have a graphite anode, the impact of different cathode materials on the measurements are analysed in detail. While differential voltage analysis, a well-established method in literature, is considered to be the reference, further insights into the cell's state of health are gained by means of electrochemical impedance spectroscopy and thermodynamic measurements.

A newly developed modification technique allows for measurements of local potentials during the operation of the cell. Using this approach for electrochemical impedance spectroscopy, the impact of cell design, cell temperature and excitation frequency on the current density distribution is investigated. It is shown that a variation in the evoked electrode area will have a significant impact on the measured impedance spectra. In this context, the interpretability of impedance measurements is discussed since a variation in the current density distribution caused by inhomogeneous degradation will superimpose the spectra variations caused by changes in the electrochemical performance of the cell.

Thermodynamic measurements require a long time, making it unsuitable for fast check-ups. Therefore, various approaches to reduce the measurement time are presented. The influence of the cell temperature and discharge current on state of charge inhomogeneities and the equalisation time is investigated. This leads to an optimised discharge procedure, minimising gradients within the active material and along the electrodes. Finally, a mathematical approach is presented, compensating the voltage relaxation after a discharge step. In comparison to available literature, the measurement time was reduced by a factor of ten. As a result, advanced thermodynamic measurements can be performed within 24 h.

The accuracy of the measurement is quantified by comparing the results of the degradation study to results obtained by differential voltage analysis. For the compared cells, the results of both methods are very similar. To reconfirm the accuracy and applicability of advanced thermodynamic measurements as possible degradation tracking technique, half-cell measurements as part of the subsequent post-mortem study are used.

Zusammenfassung

Eine größere Reichweite für elektrifizierte Fahrzeuge erfordert eine Erhöhung der Energiedichte in Lithium-Ionen-Zellen, welche mit Hilfe einer höheren Packungsdichte bekannter Materialien oder durch den Einsatz neuer Materialien mit größerer spezifischer Kapazität oder höherer Spannung realisiert werden kann. Mit steigendem Energieinhalt der Zelle wird eine akkurate Zustandsbestimmung von internen Parametern notwendig, da Zellspannung, Strom und Oberflächentemperatur gegebenenfalls nicht mehr ausreichen, um den Zustand einer Zelle präzise wiederzugeben.

In dieser Arbeiten werden verschiedene elektrochemische Charakterisierungsmethoden kritisch betrachtet und die Möglichkeit, damit die fortschreitende Alterung einer Zelle zu bestimmen, wird diskutiert. Eine Alterungsstudie mit unterschiedlichen kommerziellen Zellen im 18650-Format mit verschiedenen Kathodenmaterialien wird durchgeführt und die Leistungsfähigkeit der Zelle charakterisiert, um die Ursachen der Alterung zu bestimmen. Da alle Zellen Graphit als Anodenmaterial beinhalten, wird der Einfluss der verschiedenen Kathodenmaterialien im Detail betrachtet. Die differentielle Spannungsanalyse, eine in der Literatur etablierte Methode, wird als Referenz definiert und weitere Einblicke in die Zelle werden mit Hilfe von elektrochemischer Impedanzspektroskopie und thermodynamischen Messungen gewonnen.

Eine neuentwickelte Modifizierungstechnik erlaubt lokale Potentialmessungen während des Betriebes der Zelle. Mit Hilfe dieses Ansatzes wird der Einfluss von Zelldesign, Temperatur und Anregungsfrequenz auf die Stromdichteverteilung während einer Impedanzmessung untersucht. Es wird gezeigt, dass eine Veränderung der angeregten Elektrodenfläche einen maßgeblichen Einfluss auf das gemessene Spektrum hat. In diesem Zusammenhang wird die Interpretierbarkeit der Impendazspektroskopie diskutiert, da eine Veränderung der Stromdichteverteilung, hervorgerufen durch eine inhomogene Alterung innerhalb der Zelle, die Effekte, die durch die Alterung der Zelle entstehen, überlagert.

Thermodynamische Messungen hingegen benötigen viel Zeit und sind daher für die Anwendung als schnelle Charakterisierungsmethode während einer Alterungsstudie ungeeignet. Um dieses Problem zu beheben, werden verschiedene Lösungsansätze präsentiert. Der Einfluss der Zelltemperatur und des Entladestroms auf lokale Lithiierungsinhomogenitäten und deren Ausgleichsvorgänge wird untersucht. Dies ermöglicht eine optimale Entladestrategie während der Messung, bei der Inhomogenitäten innerhalb der Schicht sowie entlang der Elektrode minimiert werden. Zum Abschluss wird ein mathematischer Ansatz präsentiert, der die Spannungsrelaxation nach einem Entladeschritt kompensiert. Dies reduziert die Messzeit im Vergleich zu vorhandener Literatur um den Faktor zehn, was eine vollständige Messung innerhalb von 24 Stunden ermöglicht.

Die Genauigkeit der Methodik wird quantifiziert, indem die Ergebnisse der Alterungsstudie mit den Ergebnissen der differenziellen Spannungsanalyse verglichen werden. Für die verglichenen Zellen erzielen beide Methoden sehr ähnliche Ergebnisse. Um die Genauigkeit der Methode und ihre Anwendbarkeit als Alterungsbestimmung nochmals zu bestätigen, werden die Ergebnisse mit Halbzellenmessungen aus der abschließenden Post-mortem-Studie verglichen.

Acknowledgements

When setting foot on Singaporean ground for the first time, I could not have imaged, what great journey would lie ahead of me.

I would like to thank Prof. Dr. Andreas Jossen and Prof. Dr. Harry Hoster for their support throughout the years and giving me the opportunity to be a part of the TUM CREATE project. Furthermore, I would like to express my gratitude to the Singaporean National Research Foundation, who initiated and funded TUM CREATE as part of the CREATE programme in the first place.

I am very thankful to my parents, who supported, guided and inspired me along this long way and who put a lot of effort into dropping by in Singapore whenever possible, making 10.000 kilometres feel like a stone's throw.

I want to thank my colleagues at TUM CREATE in Singapore as well as my colleagues at the Institute for Electrical Energy Storage Technology at TUM in Germany who contributed to this work by discussions, suggestions, corrections, and a good laugh at the coffee machine: Namely Jan Geder, Nicolas Bucher, Jochen Friedl, Steffen Schlüter, Arun Nagasubramanian, Ali Rinaldi, John Romero, John Carmack, Jürgen Garche, Frank Kindermann, Ralph Karl, and Peter Keil. Thank you, David Ciechanowicz, for financial support (100 $) and competition at the table soccer. Thank you, Thomas Kindler, for your help by making our relocation to Germany incredibly easy.

Very special thanks go to the members of 3015, Simon Erhard, Bernhard Rieger, and Alexander Rheinfeld for the great and productive time.

And of course, to the one special person, Annette Trippe. Thank you for your help, your patience and your never-ending support. This journey would have been nothing without you.

Contents

List of Figures

List of Tables

Chapter 1

Introduction

Motivation

Lithium-ion cells are the most common power source for mobile applications and due to progressing research and further enhancements regarding energy density and cycle life in recent years, they became the energy storage system of choice for electrified transport systems as hybrid electric vehicles (HEVs) and electric vehicles (EVs). From their commercialisation by Sony in 1991 onwards, lithium-ion batteries replaced nickel-metal hydride and nickel–cadmium batteries within a few years in most applications. From all available electrochemical power sources, lead-acid batteries still have the largest share in terms of stored energy and market volume. With increasing number of stationary applications and electric vehicles using lithium-ion cells, it seems to be only a matter of time when lithium-ion cells take the lead.

The reduction of average fleet emission down to $95\,g_{CO_2}\,km^{-1}$ as legislated by the European Union [67] forces automotive original equipment manufacturers (OEMs) to significantly extend their product portfolio regarding new and affordable models of HEVs and EVs. The battery is the most expensive single component within the manufacturing process of an EV and an important factor in the value added chain, with prices currently ranging between 250 and $400\,\$\,kWh^{-1}$ [23, 148]. Despite the forecast price drop below $200\,\$\,kWh^{-1}$ by 2020 [148], the occurring costs of 12 000 \$ for a 60 kWh battery pack, necessary to achieve an estimated driving range of 400 km, will remain an important criteria whether people can be convinced to buy EVs. Therefore, it is obvious that an economically responsible usage of the cell by extending not only its size and energy density but also its operating lifetime is a crucial requirement to increase the acceptance of EVs as an alternative to internal combustion engine vehicles (ICEs).

A high energy density, low production costs and environmental compatibility are just a few of the many important topics, companies and research institutes all around the world have to address to allow battery cells to become cheaper and more reliable. In this progress, the number of possible materials under consideration to be used as anode, cathode or electrolyte has increased significantly. With changing anode and cathode materials, the question arises if information gained from the materials' specific open circuit voltages (OCVs) is sufficient to allow for a detailed estimation of the cells

state of health (SoH). In combination with the increasing energy density and larger battery pack size of currently up to 100 kWh for Tesla's Model S P100D battery pack [202], the importance of an accurate and reliable tracking of degradation mechanisms is obvious. Under the progressive circumstances and the sophisticated demands in the automotive industry with respect to redundant safety systems, precise and easily applicable characterisation techniques need to be available.

The high susceptibility of lithium-ion cells regarding high temperatures and unsuitable voltage ranges further highlight the requirement of accurate tracking of the cell's electrochemical properties during its operation as well as along the cell's cycle life. While many techniques are well established methods in electrochemistry to characterise cells on a lab scale to fulfil scientific curiosity, progress regarding the applicability in automotive applications needs to be made.

This work critically addresses common electrochemical characterisation methods such as electrochemical impedance spectroscopy, differential voltage analysis and cyclic voltammetry. Their applicability as degradation tracking techniques is reviewed by means of local potential measurements, a newly developed modification method, allowing to obtain a fundamental understanding of the current density distribution, local state of charge inhomogeneities and their equalisation in cylindrical cells.

Thermodynamic measurements are added to this list of characterisation methods by improving the measurement in terms of speed and accuracy. Advanced thermodynamic measurements are compared to the established methods to investigate if the method is a possible candidate to successfully track and identify degradation mechanisms in lithium-ion cells. The comparison is performed during a degradation study using commercially available cells with the various cathode materials. The ageing study is designed to separate the degradation effects occurring during the life-time of battery cells under various operating conditions or during storage.

Outline

The aim of this work is the investigation of degradation of lithium-ions cells using various electrochemical characterisation techniques and their verification by means of post-mortem studies and modification procedures. The focus was set on the application and critical validation of well-established methods as well as the development and improvement of promising non-destructive methods, which allow for a fast and accurate determination of the state of health of a battery during its lifetime. Chapter 2 comprises the **Fundamentals of Lithium-Ion Batteries**. A short introduction into thermodynamics and the electrochemical basics of lithium-ion cells is given. The different components of a cell are introduced and the recent developments of cathode materials used in lithium-ion cells are presented in detail. The various degradation mechanisms during storage and operation of these materials are discussed based on available literature. This is followed by Chapter 3, in which an overview of the various **Characterisation and Modification** methods and techniques applied in this work is given. The introduction and the experimental description of in-operando methods, commonly used to track changes occurring with ongoing degradation of the respective cell, is followed by the presentation of various techniques to modify cells which allow for the measurement of additional parameters of the cell. Using a newly developed approach for in-operando current density distribution measurements, the impact of cell design, temperature and excitation frequency on **Electrochemical Impedance Spectroscopy** is investigated in detail in Chapter 4. Based on these findings, the applicability of the method as degradation tracking technique is discussed. In Chapter 5, the framework of meaningful thermodynamic measurements is discussed and based on the requirements for quasi-electrochemical and thermal equilibrium, **Advanced Thermodynamic Measurements** are developed. The acceleration of the measurement principle allowed the technique to be included into the ageing study and the findings obtained during the **Tracking of Cell Degradation** mechanisms are presented in Chapter 6. The method is discussed in the context with results from other well-established methods as electrochemical impedance spectroscopy and differential voltage analysis. The thesis is concluded by a short summary of the presented results and an outlook to possible fields of interest is given.

Chapter 2

Fundamentals of Lithium-Ion Cells

This chapter aims to give an understanding about the working principles of lithium-ion cells. The working principles are derived from thermodynamic fundamentals and a detailed introduction to entropy in lithium-ion cells is given. The design of lithium-ion cells is introduced by discussing the individual cell components in detail with a special focus on degradation mechanisms referring to recent literature. If not specifically highlighted, the fundamentals in thermodynamics and electrochemistry in this chapter are based on the Encyclopaedia of Electrochemistry Vol. 1 - Thermodynamics and Electrified Interfaces [16] and Atkins' physical chemistry [11]. The variations in terms of notation within available literature caused the need to adjust the original form in some cases to allow for a coherent description in this work.

2.1 Introduction into the thermodynamics of lithium-ion cells

The state of a closed system is defined by its internal energy U, the total kinetic and potential energy of the molecules within the system. The change of the system's inner state can be expressed by

$$\Delta U = U_f - U_i \tag{2.1}$$

representing the internal energy difference between the initial system U_i and the final system U_f. To decrease the system's internal energy, interaction with the surrounding is required.

In an adiabatic system, only work is performed with

$$\Delta U = w_{adiabatic} \tag{2.2}$$

If the system is non-adiabatically connected to a second system with a different temperature, the change in the internal energy can be expressed by the amount of transferred heat

$$\Delta U = q_V \tag{2.3}$$

presuming a constant volume, indicated by the index V. The combination of Eq. 2.1 - 2.3 leads to the first law of thermodynamics. One of the first statements is attributed to Rudolf Clausius' publication in 1850 about the cyclic thermodynamic processes

> *[..] dass in allen Fällen, wo durch Wärme Arbeit entstehe, eine der erzeugten Arbeit proportionale Wärememenge verbraucht werde, und dass umgekehrt durch Verbrauch einer ebenso grossen Arbeit dieselbe Wärmemenge erzeugt werden könne.* [45]

> *In all cases in which work is produced by the agency of heat, a quantity of heat is consumed which is proportional to the work done; and conversely, by the expenditure of an equal quantity of work an equal quantity of heat is produced.* [209]

This statement is expressed by

$$\Delta U = q + w \tag{2.4}$$

whereas the change in a closed system's internal energy ΔU is the sum of the transferred energy in form of heat q and its performed work w, independent of the performed path. With the expression for the reversible expansion work

$$w = -\int_{V_1}^{V_2} p dV \tag{2.5}$$

an infinitesimal quantity change of transferred heat dQ is defined by

$$dQ_p = d(U + pV) \tag{2.6}$$

whereas the index p indicates constant pressure. The integration of this differential expression leads to the introduction of the state function Enthalpy H, a measure of the energy content of the system, defined by the sum of the system's internal energy U and the product of its pressure p and volume V

$$H = U + pV \tag{2.7}$$

In 1851, Clausius published a statement regarding the spontaneity of a reaction, establishing the basis for the second law of thermodynamics.

> *[...] es kann nie Wärme aus einem kälteren in einen wärmeren Körper übergehen, wenn nicht gleichzeitig eine andere damit zusammenhängende Aenderung eintritt* [46]

Heat can never pass from a colder to a warmer body without some other change, connected therewith, occurring at the same time. [47]

In his 1865 published work, he implemented his statement mathematically by introducing the new thermodynamic property Entropy S, from the Greek word $\tau\rho o\pi\acute{\eta}$, (Transformation) [48].

$$dS = \frac{dq_{rev}}{T} \tag{2.8}$$

The index *rev* indicates the reversibility of the heat transfer. Similar to U and H, it is not possible to quantitatively measure an absolute value of S and therefore only a change ΔS can be calculated or measured according to

$$\Delta S = S_2 - S_1 = \int_1^2 dS = \int_1^2 \frac{dq_{rev}}{T} \tag{2.9}$$

S expresses the part of a system's energy, which cannot be converted into mechanical work. Entropy is therefore commonly considered as a measure of disorder within a macroscopic thermodynamic system.

The second law of thermodynamics

$$\Delta S_{tot} \geq 0 \tag{2.10}$$

expresses the system's tendency to maximise its entropy, whereas the equal sign is related to reversible processes and the inequality sign describes irreversible processes. The reduction of entropy in a system is only possible, when another system's entropy is increased by at least the same amount. The combination of Eq. 2.6, Eq. 2.8 and Eq. 2.10 leads to

$$dS \geq \frac{dU + pdV}{T} \tag{2.11}$$

Assuming an environment with constant pressure and constant temperature, Eq. 2.11 leads to the introduction of the state function Gibbs' Free Energy G, which is expressed by

$$G = U + pV - TS = H - TS \tag{2.12}$$

The Gibbs' Free Energy is the maximum useful work a system can perform. For $\Delta G = 0$, the system is in an equilibrated state. A change in the Gibbs' Free Energy $\Delta G < 0$ indicates a spontaneous reaction at which the system releases energy, whereas $\Delta G > 0$ is an externally forced increase by the specific amount of energy. Generalising the approach to a system with multiple components, the mole number n of each component

i needs to be considered as independent variables. The change in the system's Gibbs' Free Energy is expressed with the total differential by

$$dG = \left(\frac{\partial G}{\partial T}\right)_{p,n_i} dT + \left(\frac{\partial G}{\partial p}\right)_{T,n_i} dp + \sum \left(\frac{\partial G}{\partial n_i}\right)_{T,p,n_j;i\neq j} dn_i \tag{2.13}$$

Due to the law of mass action, adding or changing the amount of component i will have an effect on the other components $j \neq i$ and a chemical reaction will occur until the system's state is again equilibrated ($\Delta G = 0$).

Thus it appears that a different ratio of the components will lead to a change in the Gibbs' Free Energy of the system, while the enthalpy H of the system remains constant. The partial derivative of G with respect to the component n_i as stated in Eq. 2.13 leads to

$$\left(\frac{\partial G}{\partial n_i}\right)_{T,p,n_j,i\neq j} dn_i = \mu_i \tag{2.14}$$

The chemical potential μ of a species i can be understood as the additional amount of energy a system gains / loses, if 1 mol of component i is added to / removed from the system. With

$$\left(\frac{\partial G}{\partial T}\right)_{p,n_i} dT = -SdT \tag{2.15}$$

and

$$\left(\frac{\partial G}{\partial p}\right)_{T,n_i} dp = Vdp \tag{2.16}$$

the change in the Gibbs' Free Energy as stated in Eq. 2.13 is simplified to

$$dG = -SdT + Vdp + \sum \mu_i dn_i \tag{2.17}$$

The interaction between ions of the same species is discarded in ideal solutions, as no interference between the ions occurs. But with increasing concentration c of solved ions in the compound, a measurable, repulsive interaction due to the positive charge of the ions is observable. This leads to the requirement of a certain amount of activation energy to start the favoured reaction and reduces the ion's activity a, which is expressed by the activity coefficient f_i and the mole fraction of the substance in the mixture x_i

$$a_i = x_i f_i \tag{2.18}$$

Consequently, for non-ideal solution the definition of the chemical potential has to be specified and the concentration of the respective species i in the substance has to be considered. The chemical potential is extended to

$$\mu_i = \mu_i^0 + RT \ln a_i \tag{2.19}$$

with the temperature T and the ideal gas constant R. μ_i^0 is the chemical potential of the pure substance defined at standard temperature $T = 298.15\,\mathrm{K}$ and standard pressure $p = 101.325\,\mathrm{kPa}$.

At a phase boundary of two materials with different chemical potentials $\mu_i(\mathrm{I})$ and $\mu_i(\mathrm{II})$, an equalisation process will occur until the system is equilibrated. Due to the ion exchange between the two phases, an electrolytic double layer with an electrical surface charge is developed and the equilibrated state can be expressed by

$$\mu_i(\mathrm{I}) + z_i F \varphi(\mathrm{I}) = \mu_i(\mathrm{II}) + z_i F \varphi(\mathrm{II}) \tag{2.20}$$

with the number of transferred electrons z_i, the Faraday constant F and the electrical potential φ. The term $z_i F \varphi$ describes the additional electrical energy a species has to obtain to overcome this electrostatic field. This expression leads to the definition of the electrochemical potential μ^*, where the energy of a species with a defined concentration is increased from its standard state to a higher potential

$$\mu_i^* = \mu_i + z_i F \varphi \tag{2.21}$$

In electrochemistry, an electrode is defined as a system built up by two or more contacting phases, including at least one ionic and one electronic conducting phase. In context of lithium-ion cells, phase (I) is a metal or metal ion intercalating electrode and phase (II) is the electrolyte, containing dissolved ions of the respective metal. The electrochemical potential at the boundary of an electrode and the electrolyte is given by

$$\mu_{e^-,L}^* = \mu_{e^-,Me}^* \tag{2.22}$$

and inserting Eq. 2.19 and 2.21 leads to

$$\mu_{e^-,L}^0 + RT \ln a_{e^-,L} + zF\varphi_L = \mu_{e^-,Me}^0 + RT \ln a_{e^-,Me} + zF\varphi_{Me} \tag{2.23}$$

The electrochemical potential difference $\Delta\varphi_0$ between the phases (I) and (II), whereas equilibrium conditions are implied by the index 0, is calculated by

$$\Delta\varphi_0 = \varphi_{e^-,Me} - \varphi_{e^-,L} = \frac{\mu_{e^-,L}^0 - \mu_{e^-,Me}^0}{zF} + \frac{RT}{zF} \ln \frac{a_{e^-,L}}{a_{e^-,Me}} \tag{2.24}$$

In its general form, this equation is known as the Nernst equation and describes the activity dependency of the electrode potential of a Red-Ox couple

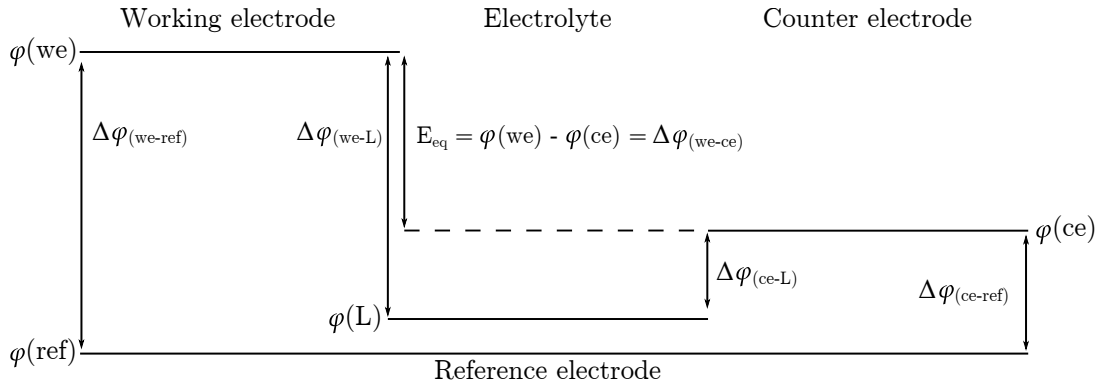

Figure 2.1 – Electrochemical potentials inside a lithium-ion cell

$$E_{eq} = E^0 + \frac{RT}{zF} + \ln \frac{a_{Ox}}{a_{Red}} \tag{2.25}$$

In literature, the term electromotive force E_{EMF} is still commonly used when referring to the cell voltage under equilibrium conditions. The wording *force* might be misleading in this context as no force in the meaning of classical mechanics is present and the term E_{EMF} is replaced by the more general statement of the cell's equilibrium potential E_{eq}.

The electrochemical potential difference between the solid and the liquid phase $\Delta\varphi_{(I)-(II)}$ is not measurable. Consequently, another electrode serves as measurement reference, whereas an additional interface between different electrochemical potentials is developed. Fig. 2.1 illustrates the electrochemical potentials within a lithium-ion cell with a working electrode, a counter electrode and an additional reference electrode. Consequently, the cell's equilibrium potential can be calculated by

$$E_{eq} = \varphi(we) - \varphi(ce) = \Delta\varphi_{(we-ce)} \tag{2.26}$$

With Eq. 2.13, Eq. 2.26 leads to the correlation between the cell voltage E_{eq} and the Gibbs' Free Energy G in a lithium-ion cell under consideration that the electrochemical potential of the intercalation electrodes varies with changing degree of lithiation x

$$E_{eq}(x) = -\frac{\Delta_r G(x)}{nF} \tag{2.27}$$

The index r indicates the changes of the Gibbs" Free energy during the completion of the chemical reaction and Eq. 2.12 can be rewritten as

$$\Delta_r G(x) = \Delta_r H(x) - T\Delta_r S(x) \tag{2.28}$$

To apply the fundamentals onto a lithium-ion cell, a short introduction of the set-up and reaction mechanisms is given. The cell consists of two electrodes which are

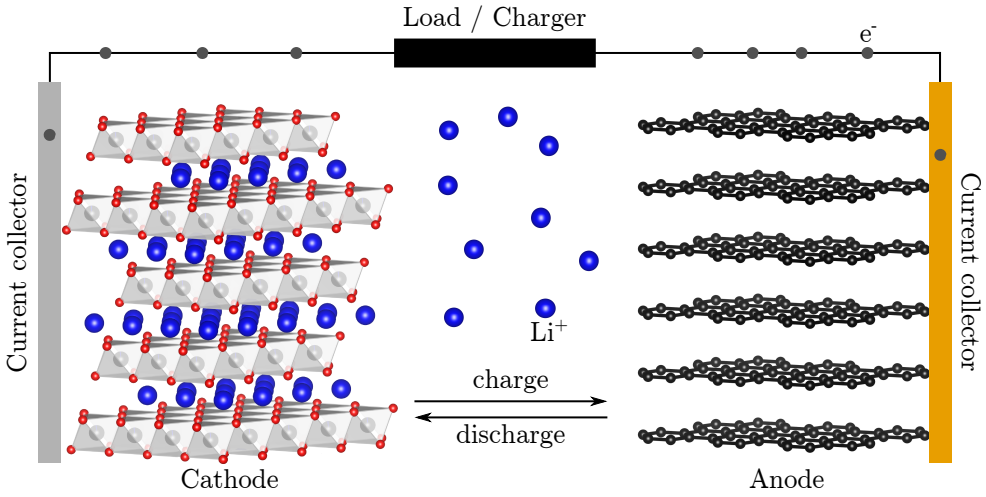

Figure 2.2 – Schematic drawing of the working principle of a lithium-ion cell

ionically connected by an electrolyte and electronically separated by a separator. Fig. 2.2 exemplifies the operation mode of a lithium-ion cell during charge or discharge.

The half-cell reaction of the positive electrode, in this case a metal oxide cathode with M = Mn, Co, Ni, Al representing transition metals, is expressed by

$$\mathrm{Li_{x-ffi}MO_2} + \mathrm{ffiLi^+} + \mathrm{ffie^-} \longleftrightarrow \mathrm{Li}_x\mathrm{MO_2} \tag{2.29}$$

and the half-cell reaction of the negative electrode, in this case graphite is expressed by

$$\mathrm{Li_{y+ffi}\,C_6} \longleftrightarrow \mathrm{Li}_y\mathrm{C_6} + \mathrm{ffiLi^+} + \mathrm{ffie^-} \tag{2.30}$$

The symbol $\longleftrightarrow$ indicates the reaction's reversibility and x, y is the advancement of reaction in this context, representing the degree of lithiation of the respective intercalation material. The overall cell reaction is generally described by

$$\mathrm{Li}_y\mathrm{C_6} + \mathrm{Li}_x\mathrm{MO_2} \longleftrightarrow \mathrm{Li_{y+ffi}C_6} + \mathrm{Li_{x-ffi}MO_2} \tag{2.31}$$

In case of a discharge of the full-cell, an oxidation takes places at the anode, while the respective reduction occurs at the cathode side. From electrochemical principles, the anode is defined as the reaction partner, where the oxidation occurs and electrons are delivered. Rechargeable lithium-ion cells (also denoted as secondary lithium-ion cells) are a reversible electrochemical system. Hence, the oxidation process is reversed during charge and the oxidation occurs at the metal oxide electrode. As commonly accepted in literature for the avoidance of confusion, the definition for the discharge state is used when referring to anode and cathode, meaning that the term anode (negative electrode)

always refers to the graphite electrode and cathode (positive electrode) always refers to the metal oxide electrode.

The active material is coated on a current collecting metal foil, usually thin metal films of copper or aluminium. While metal ions (Li^+) are free to move through the electrolyte, the accompanying electrons are forced through an external current path (e^-).

Derived from Eq. 2.26, the cell's equilibrium potential E_{eq} is expressed as the difference of the cathode and anode half-cell potentials versus lithium, which serves in lithium-ion half-cells as reference and counter electrode as illustrated in Fig. 2.1

$$E_{eq} = E_{cathode} - E_{anode} \tag{2.32}$$

Without any dynamic load conditions, E_{eq} is approximately equal to the cell's open circuit voltage U_{OCV}, measurable at the cell's terminal. In this work, the term potential E relates to a defined, calculable value, defined by the electrochemical properties of the involved species whereas the term voltage U refers to the respective measurable value between two electrodes. Under dynamic load conditions, when a charge or discharge current I is applied, the cell voltage U_{cell} deviates from E_{eq} by the overpotential η due to the various impedances inside the cell and the relation is given by

$$U_{cell} = E_{eq} \pm \eta \tag{2.33}$$

whereas $\pm$ indicates that the sign of the overpotential depends if the cell is charged (+) or discharged (-). η can be expressed by

$$\eta_{total} = \eta_{charge\,transfer} + \eta_{s,ohmic} + \eta_{s,conc} + \eta_l \tag{2.34}$$

with the overpotential caused by charge transfer resistance $\eta_{charge\,transfer}$, the ohmic resistance of the active material $\eta_{s,ohmic}$, the concentration resistance $\eta_{s,conc}$, which includes both, contribution from anode and cathode side and the resistance of the electrolyte η_l [22].

A dynamic load violates the thermal and particularly the electrochemical equilibrium on a long time scale [107]. Equalisation processes due to lithium-ion concentration gradients throughout the cell lead to a continuously changing U_{OCV} and the time dependent term $\delta(x, t_i)$ is used to describe the difference between E_{eq} and U_{OCV}

$$U_{OCV}(x, t_i) = E_{eq}(x, t_0) + \delta(x, t_i) \tag{2.35}$$

in dependence of the degree of lithiation of the respective electrode for any point time t_i. The possible shape of the function $\delta(x, t_i)$ is discussed in more detail in Sec. 5.3.

2.2 Entropy in lithium-ion cells

The correlation of the Gibbs' Free Energy G and the cell voltage E_{eq} as described in Eq. 2.27

$$E_{eq}(x) = -\frac{\Delta_r G(x)}{nF} \tag{2.27}$$

leads in combination with Eq. 2.12 to the dependency of E_{eq} on the enthalpy H and entropy S

$$E_{eq}(x) = \frac{\Delta_r H(x) - T\Delta_r S(x)}{nF} \tag{2.36}$$

The derivative of Eq. 2.36 with respect to the temperature leads to

$$\left.\frac{\partial E_{eq}(x)}{\partial T}\right|_{p,x} = -\left.\frac{1}{nF}\Delta_r S(x)\right|_{p,x} \tag{2.37}$$

indicating that the temperature dependency of the cells equilibrium potential only depends on the system's entropy. Sources for the various contributions to the entropy of an electrochemical system were analysed in detail by Fultz [69, 71] and Richardson [168]. The contributions are divided into two sources of origin. The first one is the entropy contribution by the material which is intercalated into the host structure, in this case lithium-ions. The second group is based on the electronic properties of the materials, which is either driven by the material properties itself or due to the changes occurring during intercalation. The focus is set on the contribution of the configurational ionic and electronic entropy as well as the vibrational entropy, as they were identified to be the main source within lithium-ion cells [164, 166, 167].

2.2.1 Ionic entropy contributions

Configurational ionic entropy

The number of distinguishable states of the system W is defined by the possible configurations in an ideal solution with ideally distributed lithium. The total number of available sites $\hat{n} = nN_A$ and the number of occupied sites $\hat{n}_{Li} = n_{Li}N_A$ with the Avogadro constant N_A and the number of moles n leads to the definition of the filling factor x

$$x = \frac{\hat{n}_{Li}}{\hat{n}} \tag{2.38}$$

The number of available states is calculated by [11]

$$W(\hat{n}_{Li}) = \frac{\hat{n}!}{\hat{n}_{Li}(\hat{n} - \hat{n}_{Li})!} \tag{2.39}$$

The Stirling's approximation $\ln a! \approx a \ln a - a$ and Eq. 2.38 lead to the expression of

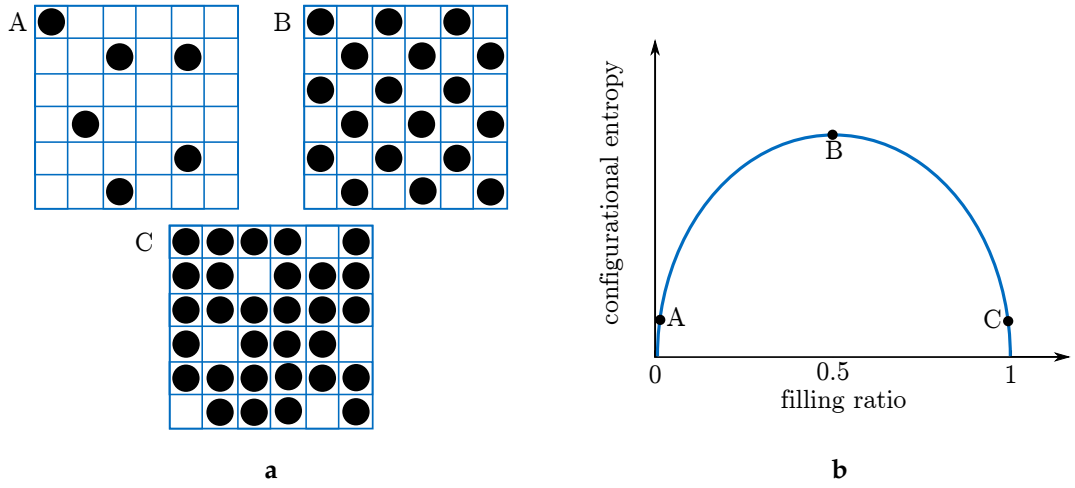

Figure 2.3 – Schematic illustration of the change in configurational entropy with changing filling ratio

$$\ln \frac{\hat{n}!}{\hat{n}_{Li}(\hat{n}-\hat{n}_{Li})!} \approx -[x \ln x + (1-x)\ln(1-x)] \tag{2.40}$$

With the Boltzmann's equation $S = k_B \ln W$, the difference in the configurational entropy of an lithiated compared to the empty host structure can be calculated with

$$\Delta S_{conf} \approx -k_B[x \ln x + (1-x)\ln(1-x)] \tag{2.41}$$

and changes in the configurational entropy by adding or removing 1 mol of lithium leads to the expression

$$\frac{\partial \Delta S_{conf}(x)}{\partial x} = -k_B N_A \ln\left(\frac{1-x}{x}\right) \tag{2.42}$$

In Fig. 2.3a, three characteristic scenarios of possible lithium-ion (black circles) arrangements in a fixed host structure are illustrated. Scenario A and C are almost empty and almost full. The resulting number of possible arrangements are the same in this example, defined either by six lithium-ions or six vacancies. For scenario B where 50 % of the sites are occupied, the number of possible arrangements is the largest, even though the one shown is the energetically most favourable. In an ideal scenario, this leads to a change in the configurational entropy as shown in Fig. 2.3b, where the course of the configurational entropy is schematically displayed. Up to a filling ratio of 50 %, the increasing number of possible arrangements leads to a higher configurational entropy and, since the lithium-ions are non-distinguishable, above 50 % to a decrease.

As discussed in Sec. 2.3, continuous lithium-ion intercalation will lead to structural changes as first and second order phase transitions in anode and cathode materials

used for lithium-ion cells. Consequently, a change in configurational entropy due to the rearrangement of the intercalated lithium in the host structure is observed.

Vibrational entropy

The vibrational entropy S_{vib} is defined by the stiffness of different bounds between the atoms of the intercalation compound. During intercalation, the stiffness changes and phase transformations can lead to a rearrangement of the bonds. The vibrational entropy can be calculated using the vibrational density of states (DoS) $g(\epsilon)$ and the phonon occupancy factor $n(\epsilon)$

$$S_{vib}(T) = -3k_{\mathrm{B}} \int_0^{\infty} g(\epsilon)[(n(\epsilon)+1)\ln(n(\epsilon)+1) - n(\epsilon)\ln(\epsilon)]d\epsilon \quad [69] \tag{2.43}$$

whereas ϵ defines the respective energy state of the phonon [69]. Compared to the configurational entropy S_{conf}, the vibrational entropy S_{vib} exhibits a temperature dependency. Consequently, a measurement of the vibrational entropy at low temperatures using the heat capacity of the compound is preferable, as no ion rearrangements occur, but in the field of lithium-ion batteries this is not applicable. A second approach to determine the vibrational entropy is the usage of Debye-temperatures θ_{D}, an approximation of the phonon energy spectrum. Using values from literature, Reynier and co-workers calculated the contribution of vibrational entropy in graphite by

$$\Delta S_{vib} = k_{\mathrm{B}} \left(\ln\left(\frac{\theta_{\mathrm{D0}}}{\theta_{\mathrm{D}\perp}}\right) + 2\ln\left(\frac{\theta_{\mathrm{D0}}}{\theta_{\mathrm{D}\parallel}}\right)\right) \tag{2.44}$$

in which $\theta_{\mathrm{D}\parallel}$ defines the motion of lithium-ion along the plane of the graphite layer and $\theta_{\mathrm{D}\perp}$ defines lithium-ion motions normal to the graphene layer [166].

2.2.2 Electronic entropy contributions

Configurational electronic entropy

While the contribution of the configurational ionic entropy S_{conf} in electrochemical systems was investigated in detail and the results are widely accepted, the impact of the configurational electronic entropy S^e_{conf} to the overall entropy is still under discussion. While the entropy of motion of electrons S^e_{mot} is calculated to contribute only a small percentage, various phase ordering mechanisms cannot be fully explained by ionic behaviour. A second type of electronic entropy is suggested, resulting from the characteristics of electron-hole pairs [37].

In lithium-ion cells mixed-valence transition metal oxides, where the chemical compound obtains metal with different oxidations states, are commonly used as cathode materials. Ceder et al. reported on difficulties to determine the contribution of configurational ionic entropy due to the creation of Jahn–Teller Mn^{3+} and non-Jahn–Teller Mn^{4+}-ions during the delithiation of $LiMnO_2$ [38]. In analogy to Eq. 2.41, the contribution of the electrons towards the overall entropy of the system can be calculated by

$$\Delta S^{e}_{conf} \approx -k_{\mathrm{B}}[x_e \ln x_e + (1 - x_e)\ln(1 - x_e)] \tag{2.45}$$

whereas x_e denotes the filling factor of the respective charge carrier within the structure. Zhou and co-workers investigated the phase separation in Li_xFePO_4 (LFP) where a miscibility gap between triphylite ($LiFePO_4$) and heterosite ($FePO_4$) occurs [251]. They concluded that the additional entropy contribution from the electrons enhances the separation into a two-phase system instead of the formation of an ordered compound. Furthermore, the occurrence of a solid solution at higher temperatures as shown in Fig. 2.6 is mainly driven by the disorder caused by electron-hole pairs instead of ions.

Motion entropy

A second electronic contribution towards the overall entropy is the electronic motion entropy S^{e}_{mot}. For every system above 0 K, the electronic thermal energy U_{el} can be approximated by

$$U_{el} = n_e \frac{T}{T_f} k_{\mathrm{B}} T \tag{2.46}$$

whereas n_e is the number of electrons and T/T_f defines the ratio of excited electrons at the temperature T_f. The derivative with respect to the temperature leads to the heat capacity C_{el} of the electrons, given by

$$C_{el} = \frac{\partial U_{el}(T)}{\partial T} = \frac{1}{3}\pi^2 \rho(\epsilon_{\mathrm{F}}) k_{\mathrm{B}}^2 T \quad [70,\ 109] \tag{2.47}$$

with the electronic density of states at the Fermi level $\rho(\epsilon_{\mathrm{F}})$. Due to the integration from absolute zero to T_f, the expression for S^{e}_{mot} is the same as the heat capacity

$$S^{e}_{mot} = \int_0^{T_f} \frac{\partial C_{el}(T)}{\partial T} dT' = \frac{1}{3}\pi^2 \rho(\epsilon_{\mathrm{F}}) k_{\mathrm{B}}^2 T_f \quad [70,\ 109] \tag{2.48}$$

Reynier and co-workers calculated the motion entropy in Li_xCoO_2 (LCO) [164] for the lithiation range, when the material exhibits metallic properties. The contribution when the material features insulating properties are suggested to become zero. They concluded that the impact of contribution of electronic entropy towards the system's overall entropy is negligibly small.

2.3 Cell components

2.3.1 Cathode

The cathode is a host structure, where lithium-ions can be reversibly inserted and removed. Beside a high specific capacity, a high and stable voltage versus lithium metal

Table 2.1 – Properties of different commercially available cathode materials [98, 237, 248]

Material	Structure	Voltage vs. Li/Li^+ / V	Capacity / $mAh\,g^{-1}$
$LiCoO_2$	layered	3.9	140 - 200
$LiNi_{0.8}Co_{0.15}Al_{0.05}O_2$	layered	3.8	180 - 200
$LiNi_{0.33}Mn_{0.33}Co_{0.33}O_2$	layered	3.8	160 - 200
$LiFePO_4$	olivine	3.4	150 - 170
$LiMn_2O_4$	spinel	4.1	100 - 120

is desirable to allow for a high energy density of the cell. Further important aspects are a good cycle performance and the usage of non-toxic, low-cost materials.

Cathode materials can be categorised in three different groups, based on their crystal structure, namely layered oxide, olivine and spinel. The following sections will give a short overview of the recent developments of cathode materials regarding new materials and performance improvements. A general overview of different, most common commercially available cathode materials is given in Tbl. 2.1.

Layered structures

The most common materials are layered transitions metal oxides, whereas Li_xCoO_2 (LCO), first presented by Goodenough and co-workers in 1980 [139], was the first one to be commercialised by Sony in 1991. LCO has a hexagonal crystal structure known as O3(II) for a wide range of lithiation. For $0.46 < x < 0.533$, a reversible crystal structure transition to monoclinic occurs [39, 163]. Further delithiation below 0.46 leads to a strong degradation of the material and a significant capacity fade is observed [163]. Cobalt in the host structure is oxidised from to Co^{3+} to Co^{4+}, known to be an unstable oxidation state. It is believed that a high concentration of Co^{4+} destroys the crystallinity, lowering the theoretical specific capacity of $274\,mAh\,g^{-1}$ to a usable capacity of $140\,mAh\,g^{-1}$ in applications due to the limited lithiation range of the material. Research efforts were made to understand the responsible mechanisms [2, 122, 189, 191] and to stabilise the material for a wider lithiation range, e.g. by coating the LCO particles [42, 43].

Certain drawbacks remain, mainly the high cost and toxicity of cobalt as well as the thermal instability of the material [52]. Charging the cathode above 4.6 V can cause oxygen to be released from the material with a high risk of exothermal reactions with the electrolyte. As a consequence, cobalt is replaced by nickel and Li_xNiO_2 (LNO) was introduced as a more environmental friendly and cheaper alternative. However, the lower price for nickel could not compensate the disadvantages of a complicated synthesizing process in which cation mixing often results in an occupation of the Li^+ site by Ni^{2+}, with the consequence of a blocked Li^+ diffusion path [60]. The main factor for the power loss in LNO based cells was identified by Amine et al. to be the increasing impedance, originating from increasing charge transfer resistance at the cathode/electrolyte interface [9].

The severe problem of thermal instability at a high state of charge (SoC) was solved by only partially replacing cobalt with nickel and mixed compounds of $Li_xNi_yCo_{1-y}$

(LNCO) with aluminium doping [4] impeded the usage of pure LNO as commercial cathode material. For cathode materials with a stoichiometry of $LiNi_{0.8}Co_{0.2-y}Al_yO_2$ with $0 < y < 0.1$ a significant stabilisation in the cell impedance was observed. An Al content above 10 % leads to a significant increase in the degradation due to the increasing occurrence of Al defects in the lattice structure [85]. For an aluminium content below 5 % no decrease in specific capacity was measured [40], making $Li_xNi_{0.8}Co_{0.15}Al_{0.05}O_2$ (NCA) the most common stoichiometry with a specific capacity of $180\,mAh\,g^{-1}$. While cobalt helps to order the crystal structure in the $Li_xNi_{0.8}Co_{0.15}Al_{0.05}O_2$ (NCA) compound, the well distributed aluminium in the material prevents the full delithiation. A significant reduction in cation mixing and no second order phase changes in the material are reported by Croguennec and co-workers [49] and Trease et al. [207].

Vesta 3, a 3D visualization program for crystal morphologies [140] was used to draw the crystal structure of NCA illustrated in Fig. 2.4a using the crystallographic information file (CIF) published by Guilmard et al. [79] as input. The stoichiometry of the material in the investigated cell in this work varies slightly compared to the input file ($LiNi_{0.75}Co_{0.2}Al_{0.05}O_2$) but no significant differences in the structure are expected. The refinement of the X-ray diffraction (XRD) suggested the coexistence of two phases, as shown in the phase diagram in Fig. 2.4b. Similar results were obtained by Yoon and co-workers, who observed the existence of two hexagonal phases for a large lithiation range and the occurrence of a third towards higher SoCs. The good thermal stability of NCA compared to LCO or LNO is explained by the suppression of the third, unstable phase [236]. In contrast, Albrecht et al. [4] and Madhavi et al. [123] reported a well-defined layer structure, represented by single phase, independent from the degree of lithiation. The lithium diffusion is characterised by a two-dimensional path throughout the structure with a SoC dependent diffusion coefficient. A V-shaped course is reported by Amin et al. [8], where the coefficient decreases from $D = 7 \cdot 10^{-10}\,cm^2\,s^{-1}$ for the fully lithiated material towards $D = 5 \cdot 10^{-11}\,cm^2\,s^{-1}$ for $x = 0.5$ and then increases again for the fully delithiated material.

Despite the advancements in cycle life and thermal stability, multiple problems during ageing are reported for NCA in literature and are controversially discussed [40, 112, 180, 250]. Chen et al. reported on the effect of the powder morphology and suggested that a high particle density helps stabilising the cell impedance during the ageing of the cell [40].

Zheng and co-workers reported on increasing grain boundary layer thickness during the first cycle that led to the formation of micro cracks at the grain boundaries [250]. The ordered α-$NaFeO_2$-type structure of the material changes to a partially ordered structure and then further to a disorder rock-salt structure [250].

Kojima et al. found an irreversible NiO-like structure on the surface of NCA particles, consisting of inactive divalent (Ni^{2+}) or trivalent (Ni^{3+}) species, suggesting a direct correlation between the capacity fade of the material and the evolution of the NiO-like phase [112]. The combination of NCA cathodes with dimethyl carbonate (DMC) based electrolytes were investigated by Saito et al. and the group reported on the reaction on the surface of the particles [180].

A continuous formation of the surface film and the consumption of lithium in the

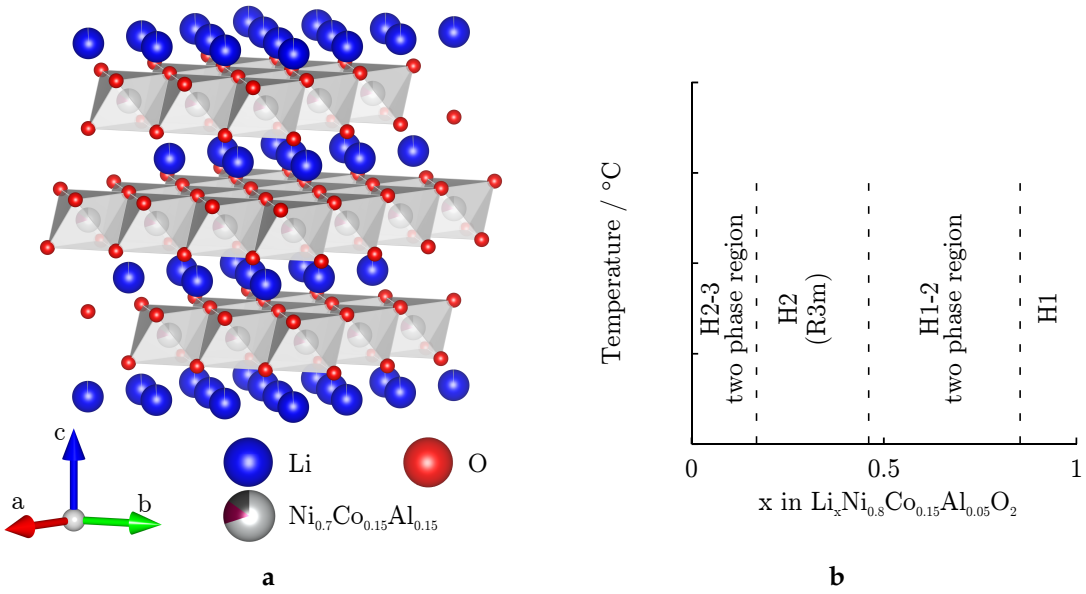

a **b**

Figure 2.4 – Crystal structure based on [79] a and phase diagram of NCA based on [236] b

reaction to form lithium carbonate were investigated [180] and led to the formation of a lithium poor NCA cubic phase on the surface of the particles, consequently leading to a decrease in power capability and capacity, according to:

$$LiNi_{0.8}Co_{0.15}Al_{0.05}O_{2(\text{hexagonal})} + x\,CH_3OCO_2CH_3 \longrightarrow Li_{1-2x}Ni_{0.8}Co_{0.15}Al_{0.05}O_{2(\text{cubic})} + x\,Li_2CO_3 + 2\,x\,CH_3{}^+$$

Watanabe and co-workers further investigated the micro crack generation in NCA after cycling the cathodes at elevated temperatures and cycling the cell for different depths of discharge (DoDs). The group was not able to confirm the emergence of a solid electrolyte interphase (SEI) on the surface nor structural changes in the NCA crystals, using XRD and X-ray photoelectron spectroscopy (XPS) analysis [222], but reported on the infiltration of electrolyte into the NCA secondary particles [221].

To further improve the cycle stability of the material, Cho et al. suggested a dry coating of SiO_2 nanoparticles on the NCA [44]. The distribution of Si on the surface lead to a significant increase in capacity retention after cycling the cell at elevated temperatures as the amount of Ni^{2+} species on the surface was reduced.

Another commercially available compound is known as $Li_xNi_{1/3}Mn_{1/3}Co_{1/3}O_2$ (NMC), a solid solution of $Li_xNi_{0.5}Mn_{0.5}O_2$ and Li_xCoO_2 [36]. A wide range of possible stoichiometries can be found in literature with $Li_xNi_{0.33}Mn_{0.33}Co_{0.33}O_2$ as the most common one due to its high theoretical specific capacity of up to 274 mAh g^{-1} [150]. During charge, Ni^{2+} is oxidised to Ni^{3+} ($1 > x > 0.66$) and with further delithiation from Ni^{3+} to Ni^{4+} for $0.66 > x > 0.33$. For higher voltages, Co^{3+} is oxidised to Co^{4+} ($0.33 > x > 0$) causing a strong voltage increase [88]. The advantage of the material is a lower concentration of Co^{4+} as well as a suppressed interchange from lithium with one of the transition metals. Advantageous is the absence of Ni^{3+} and Mn^{3+} in fully lithiated $Li_xNi_{0.33}Mn_{0.33}Co_{0.33}O_2$ resulting in no local Jahn-Teller distortion [130]. In contrast to LNO, partially delithiated

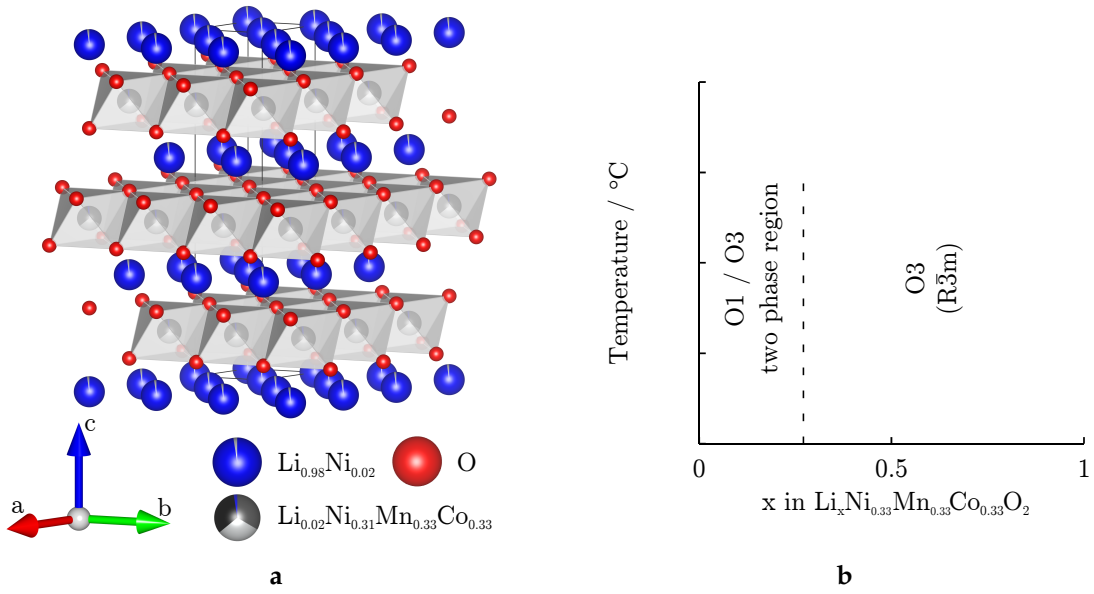

a **b**

Figure 2.5 – Crystal structure based on [230, 235] a and phase diagram of NMC based on [114] b

NMC has a negative Jahn-Teller distortion, resulting in a small negative volume effect, which was found to be a possible reason for the improved cycle life of the material [130]. Manganese (Mn^{4+}) is not oxidised during lithiation and therefore does not increase the specific capacity of the material. Nevertheless, it was found to further stabilise the crystal structure, resulting in a prolonged cycle life compared to LCO.

Fig. 2.5 exemplifies the crystal structure of $Li_xNi_{0.33}Mn_{0.33}Co_{0.33}O_2$ a as well as the phase diagram depending on the degree of lithiation b. The CIF published by Yin et al. [235] was used to reproduce the crystal structure. The 1:1:1 ratio is indicated by the multiple colours of the representing transition metal atoms. The described cation mixing, where Ni^{2+} occupies the Li^+ site is likewise considered. The intercalation of the lithium-ion into layered compounds is facilitated by a two-dimensional diffusion pathway similar to NCA. The values for the diffusion coefficient in NMC reported in literature range, depending on the applied characterisation technique and temperature between $5.5 \cdot 10^{-8}\,cm^2\,s^{-1}$ for electrochemical impedance spectroscopy (EIS) at 60 °C and $4.6 \cdot 10^{-10}\,cm^2\,s^{-1}$ for GITT measurements at 25 °C with only small variation over the SoC [7].

As illustrated in Fig. 2.5b, NMC exhibits a rhombohedral R$\bar{3}$m space group (*O3*) for a lithiation range of $1 < x < 0.3$ with a small volume change of 1 % [230, 235]. Further de-intercalation leads to the appearance of a trigonal P$\bar{3}$m1 space group (*O1*) [235]. Both, a two-phase region and a hybrid phase (*H1-3*) as present in LCO [42] are suggested but not investigated in detail. For $Li_{0.04}Ni_{0.33}Mn_{0.33}Co_{0.33}O_2$ a nearly single (*O1*) phase is reported [235]. The phase diagram and the occurrence of the additional phase illustrated in Fig. 2.5b. A specific information of a temperature range was omitted as no details of the temperature dependency of the crystal structure are available. Due to the irreversible re-intercalation of lithium into the O1 phase, a full delithiation in commercial cells is

prevented by limiting the charging cut-off voltage.

During cycling, the formation of a NiO-like structure is found on the surface of the particles, similar to the structure found on NCA materials. Kang et al. found the source for the first cycle capacity loss not to be a parasitic side reaction on the surface but rather due to an extreme slow lithium diffusion if x in $Li_xNi_{0.33}Mn_{0.33}Co_{0.33}O_2$ reaches 1 [100]. These finding were later confirmed by Buchberger et al. [32].

Shikano and co-workers used X-ray absorption near-edge structure analysis to gain a detailed insight on the morphology of the NMC particles' surface' [190]. The formation of a lithium poor cubic structure results in an increasing charge transfer resistance at the cathode/electrolyte interface and reduces the power capability of the cell. Especially during cycling at elevated temperatures, transition metal dissolution is found to be a significant source for capacity fade due to loss of active material (LAM) in the cathode. It is also found to lower the power capability of the cell, as traces of dissolved transitions metals can be found on the negative electrode, where a continuous growth of the SEI layer is triggered [32]. This effect is even further enhanced, if the charge cut-off voltage U_{cco} is increased to voltages above 4.5 V [249].

Phospho-olivine structures

The second group of cathode materials includes phospho-olivine structures, with Li_xFePO_4 (LFP) as the most common material, presented by Goodenough and co-workers in 1997 [155]. Several advantages with regards to safety, environmental compatibility, costs and long-term cycle life are obtained but discrepancies with regard to energy density need to be accepted. A high cycle stability and power capability is achieved, enabling LFP based cells to be used in power tool applications. The low electronic conductivity of LFP ($10 \cdot 10^{-9}\,\mathrm{cm\,s^{-1}}$) has to be overcome by carbon coating or by substituting various cations with other transition metals [127, 220, 246].

LFP exhibits an orthorhombic crystal structure with a Pmnb space group, displayed in Fig. 2.6a. The CIF data published by Roberts et al. [176] were used to visualise the structure. A drawback of the material is the low diffusion coefficient of lithium into the host structure due to the one-dimensional diffusion paths in the crystal structure [141]. Depending on the SoC, a diffusion coefficient from $2.9 \cdot 10^{-11}$ to $1.1 \cdot 10^{-12}\,\mathrm{cm^2\,s^{-1}}$ is reported [143].

Fig. 2.6b shows the phase diagram of LFP. It has to be noted that the phase diagram highly depends on the particle size [137, 216] and the continuous improvement in LFP synthesis lead to a shrinking in particles size from micro- to nanometre. Delacourt et al. [55] and Dodd et al. [58] investigated experimentally the phase transition in LFP depending on temperature and degree of lithiation. During lithiation, the amount of $FePO_4$ denoted as heterosite (H) phase decreases, while $LiFePO_4$ denoted as triphylite (T) phase increases, resulting in a stable voltage plateau at 3.45 V versus lithium metal [134]. Above a certain threshold temperature, according to literature approximately 140 °C, a mixed phase of a solid solution (SS) and the H or T phase can be observed, whereas the phase fully disappears with increasing temperature. A more precise investigation on the stoichiometry of the two-phase region was done by Yamada and co-workers [232], where a small deviation of the two separated reaction products during lithiation and

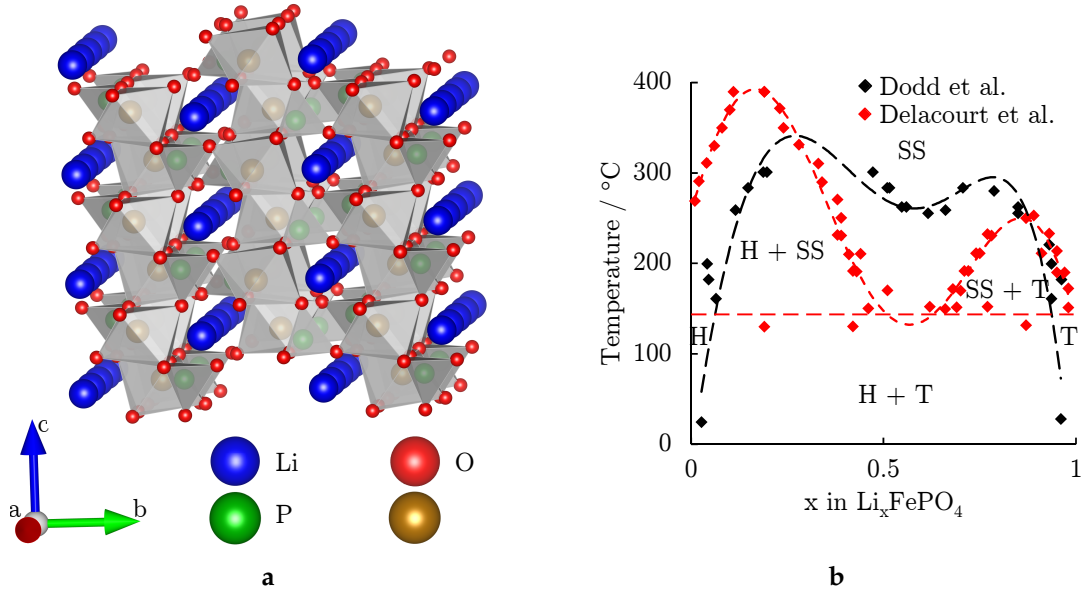

a **b**

Figure 2.6 – Crystal structure based on [176] a and phase diagram of phospho-olivine compounds based on [55] and [58] b

delithiation is found. Instead of pure $LiFePO_4$ and $FePO_4$, the coexistence of $Li_\alpha FePO_4$ with $0 < \alpha < 0.032$ and $Li_{1-\beta}FePO_4$ with $0 < \beta < 0.038$ is shown for a large lithiation range.

The major degradation mechanism was identified in early studies to be iron dissolution at elevated temperatures [10]. Beside the resulting loss of active material (LAM) in the positive electrode, a major problem was identified to be the catalysing effect of Fe^{2+} on the negative electrode to enhance the SEI formation process [63].

Amine et al. [10] reported a significant metal dissolution of 535 ppm after one week at 55 °C, but were able to suppress it to a certain amount when using an electrolyte with lithium bis(oxalato)borate (LiBOB) instead of lithium hexafluorophosphate ($LiPF_6$) as conducting salt. Zaghib et al. suggested a synthesis method, leading to a stable carbon-coated and impurity free LFP. It is assumed to prevent the metal dissolution, as they found no evidence of iron on the separator/anode interface for various anode materials [239].

A detailed study on the morphology and conductivity of LFP was published by Scipioni and co-workers and new and cycled states were compared. The particle size distribution indicated particle cracking during the cycling of the cell, leading to smaller particles and a significant degradation of the carbon coating. Consequently, iron dissolution and the formation of a SEI-like layer on the particles is reported [186]. In combination with $LiPF_6$, LFP was found to be very stable at room temperature. For elevated temperatures up to 60 °C, an increase in the cathode degradation was observed, with iron dissolution and the development of an unspecified surface layer as the main reasons [113].

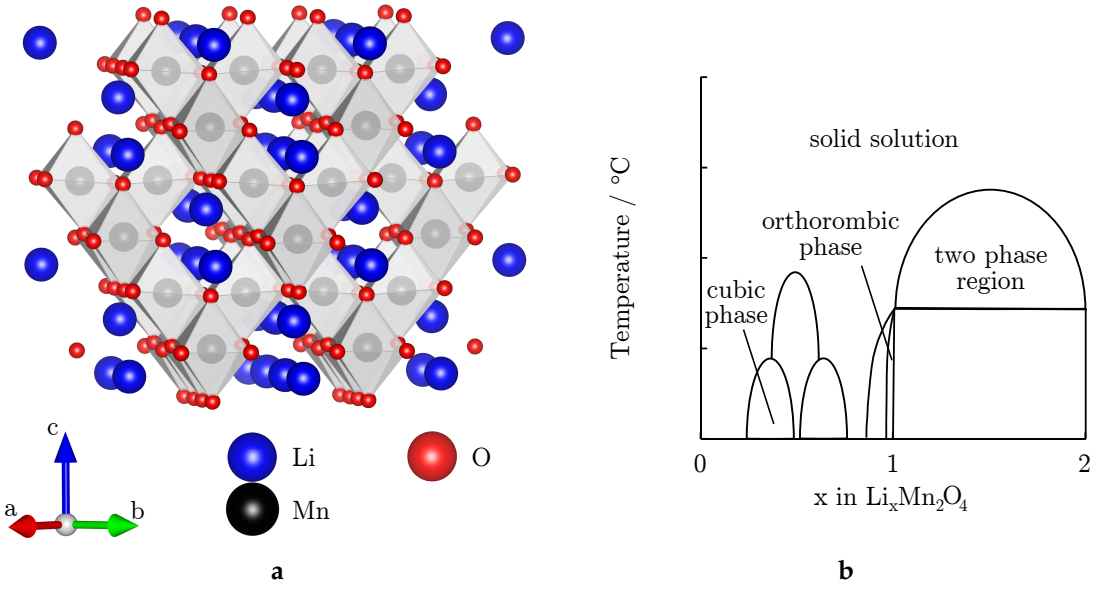

Figure 2.7 – Crystal structure based on [20] a and phase diagram of LMO spinel compounds b

Spinel structures

The third group consists of three-dimensional spinel materials. $Li_xMn_2O_4$ (LMO) is the most established material, combining the advantages of low price, non-toxicity and environmental friendliness. Two major voltage plateaus are observed when the material is fully lithiated, one for $0 < x < 1$ at 4 V and one for $1 < x < 2$ at 2.8 V giving the material a theoretical capacity of 285 mAh g^{-1}. The crystal structure in Fig. 2.7a was drawn based on the CIF data published by Berg et al. [20]. A complete phase diagram of the structure for the whole lithiation range is not available in literature, as the results vary based on e.g. analysis methods and synthesising processes. To give an approximate overview, the phase diagram shown in Fig. 2.7b is based on Monte Carlo simulations of lithium-ion ordering in the compound considering Jahn-Teller distortions [211]. Similar results were found by a detailed XRD analysis, performed by Ohzuku and co-workers [149]. They found the existence of two cubic phases with different lattice parameters ($a_1 = 8.045$ Å, $a_2 = 8.142$ Å) for a lithium range of $0.27 < x < 0.6$, one cubic phase for $0.6 < x < 1$ and two cubic and one additional orthorhombic phase for $1 < x < 2$.

The phase transition from cubic spinel to orthorhombic structure for $x = 1$ causes a significant increase in volume of up to 16 % [211]. To avoid particle disintegration and loss of connection, the lithiation range in applications is limited which reduces the usable specific energy to 120 mAh g^{-1} [72, 203] and results in a reversible change in volume of 2.3 percent during cycling. The lattice constants of the material vary non-linearly with the degree of lithiation due to the different available phases and their changing ratio [97, 149]. Further spinel materials as $LiM_{0.5}Mn_{1.5}O_4$ (with M = Ni, Fe, Co), in which manganese is partially replaced, are found to be promising candidates as high voltage cathode materials. So far, the upper limit of the electrochemical stability window of the available electrolytes is at around 4.5 V prohibits a safe long-term use of these materials in commercial applications [105, 106]. Guyomard et. al. found a mixture of

Table 2.2 – Summary of degradation effects for various cathode materials

NCA	NMC	LMO	LFP
phase transition	phase transition	phase transition	metal dissolution
infiltration of electrolyte	cation mixing	metal dissolution	particle cracking
surface reaction	surface reaction	micro cracks	surface reactions
micro cracks			

EC:DMC (2:1) with $LiPF_6$ to be the most suitable electrolyte due to its stability up to 4.9 V at room temperature and 4.8 V at elevated temperatures [81]. If the temperature is increased to 70 °C, a strong surface layer formation occurs [72, 135]. Further studies on the $Li_xMn_2O_4$ (LMO) / graphite cell system were performed by Amatucci and co-workers [5, 6]. They found the main degradation mechanisms to be the Jahn-Teller distortion when the cathode material is discharged to 3 V and below versus lithium metal. At this potential, the manganese in the structure is trivalent (Mn^{3+}) and further lithiation leads to a split in the oxidation state to Mn^{2+} and Mn^{4+}. The Mn^{2+}-ions dissolve into the electrolyte and lead, similar to the Fe dissolution in LFP, to a continuous growth of the SEI layer on the anode after deposing on the surface. The reaction products serve as a catalyst for further electrolyte decomposition and cause the second major degradation effect in LMO / graphite cells [5]. Snydacker et al. improved the cycle stability of LMO by reducing the metal transition of the spinel by coating the particles with Li_3PO_4. While other coatings were either unstable under lithiated or delithiated conditions, Li_3PO_4 was shown to be stable over the full lithiation range [193].

Tab. 2.2 summarises the main degradation effects of the investigated cathode materials. In addition to the very specific degradation effects for each material, all positive electrodes suffer under the high voltage versus lithium metal, leading to corrosion of the binder and current collector material. With this wide range of possible cathode materials, tailor made blended electrodes are used in lithium-ion cells to combine the advantages of different materials to achieve advanced performance in the large range of applications as stationary devices, mobile consumer electronics and electric vehicles. For this purpose, synthesized powders are mixed before coating. Combining the advantages of blended cathodes by mixing spinel and hexagonal structured materials was discussed by Numata et al. for LNCO/LMO and by Tran et al. [206] for NCA/LMO. Both observed that a combination of the materials reduced the Mn dissolution from the spinel significantly, enhancing the cycle life and improving the poor electrochemical performance of the spinel material, especially at elevated temperatures. In contrast, Dubarry and co-workers investigated a combination of NMC and LMO cathode blends and found over-lithiation in the LMO material due to the poor rate capability of the NMC material [62], leading to additional capacity fade in the cells.

2.3.2 Electrolyte

The electrolyte is a non-aqueous ion-conductor, allowing the transfer of lithium-ions from one electrode to the other. In lithium-ion cells, the electrolyte consists of organic solvents and a conducting salt. The solution consists of one or a mixture of different

carbonate esters as ethylene carbonate (EC), polycarbonate (PC), diethyl carbonate (DEC) and dimethyl carbonate (DMC). The conducting salt used in most cells is $LiPF_6$, due to its comparable low toxicity, high solubility and high stability with both, anode and cathode materials for a large temperature range [184]. The temperature and concentration dependency of the lithium-ion diffusion in a PC/EC/DMC mixture was extensively investigated by Valøen et al., whereas the transport properties for different concentrations and varying temperatures were experimentally determined [210]. To minimise the risk of forming toxic hydrofluoric acid, alternative conducting salts as lithium perchlorate ($LiClO_4$) or LiTFSI are investigated [51].

Large efforts are put into research and development to reduce the disadvantages of current electrolytes. The lower boundary of the theoretical electrochemical stability window of the organic solvents varies between 73 mV to 232 mV but decreases significantly in real life applications [228], depending on the composition and ratio of the different solvents used. Additives as vinylene carbonate (VC) [117] help to increase the performance of the cell by improving the formation process of the SEI [243]. The high flammability can be reduced by adding ionic liquid but with drawbacks regarding the high current performance due to the lower ion diffusion coefficients of ionic liquids [78].

2.3.3 Anode

From an energetic perspective, metallic lithium is the ideal anode material for lithium-ion cells due to its flat and low voltage as well as the high specific capacity of 3860 $\mathrm{mAh\,g^{-1}}$. However, the formation of dendrites during cycling, penetrating the separating layer between anode and cathode, can cause short circuits and will lead in a worst case scenario to a thermal runaway of the cell. Research effort is made to find possibilities to suppress the dendrite formation e.g. with $CsPF_6$ as electrolyte additive [227]. Due to these still existing severe safety concerns, lithium metal is not used as anode material in secondary cells. Alternatives in the market are different carbon-based materials as graphite, hard and soft carbon as well as $Li_4Ti_5O_{12}$ (LTO). Due its low cost, comparably high energy density of 372 $\mathrm{mAh\,g^{-1}}$ and low potential between 80 mV and 600 mV versus lithium metal, graphite is currently the most common material [187] and for all commercial cells investigated in this work the anode material of choice. Fig. 2.8a illustrates the structure of LiC_6, where lithium is fully intercalated in the graphene layers.

The fully lithiated material is written as LiC_6 and the phase is stage 1, as six carbon atoms are required to host one lithium-ion. The possible range of lithiation is given by $0 < x < 1$, whereas a full lithiation of $x = 1$ is usually not achieved in commercial cells, as the anode is over-dimensioned to prevent lithium plating. As shown schematically in Fig. 2.8b, graphite undergoes a number of phase changes during the intercalation of lithium [53]. At room temperature, LiC_6 and LiC_{12} coexist as a two-phase system for a lithiation range between $0.5 < x < 1$. At $x = 0.5$, a phase transition occurs, where the LiC_6 is eliminated. For further de-intercalation ($0.25 < x < 0.5$) and at temperatures below 10 °C, a coexistence of LiC_{12} and LiC_{24} known as stage 2 and stage 3 are present. If the temperature is increased, stage 3 merges into a diluted stage 2. With decreasing amounts of lithium in the host structure, stage 3 and the diluted stage 2L become present

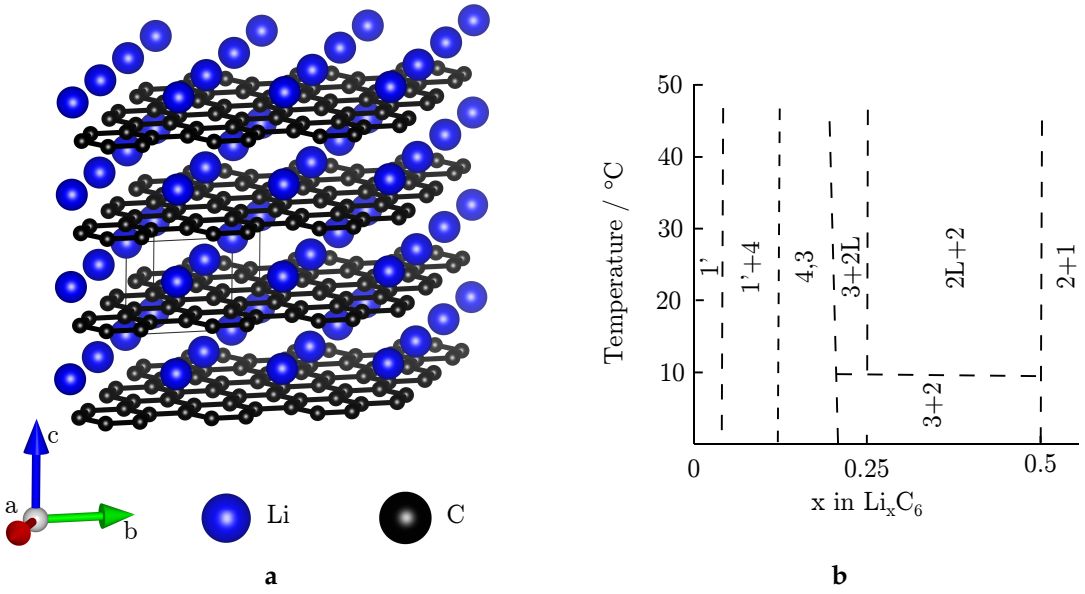

Figure 2.8 – Crystal structure a and phase diagram of graphite based on [53] b

for $x < 0.25$. The last two phase changes occur when host materials form the stage 3/stage 4 mixture and when this merges with decreasing degree of lithiation into a diluted stage 1 with coexisting stage 4 [53].

While intercalating lithium into the host structure, the anode operates below the electrochemical stability window of the electrolyte, causing the formation of the SEI on the electrode surface by electrochemically reducing the electrolyte. This complex structure consists of reaction products of the used solvents and conducting salt and has unique properties [14, 25]. The reaction continues until the complete surface is covered and causes an initial capacity fade of up to 10 %, depending on the formation process and the electrode surface area [121]. While lithium-ions can still migrate through the layer, it is nearly impermeable for other electrolyte components. Different strategies to control the SEI formation process with the aid of additives are investigated to improve the long-cycle life of the cell. In an ideal scenario, the stable surface layer allows the operation of the cell without further reduction of the electrolyte and prevents the co-intercalation of solvent molecules into the structure, which would lead to significant capacity losses due to the ex-foliation of the graphite [224].

Under operation, a volume change in the host structure of up to 5 % is observed, when lithium is intercalated and de-intercalated during a charge-discharge cycle [172]. These mechanical changes in the material lead to a continuous change of the surface layer and allow further side reactions, leading to a constant growth of the SEI. During storage, continuous side reactions on the anode are observed with an increasing reaction rate at elevated temperatures. These undesired reactions continuously consume lithium, leading to a capacity fade, denoted as loss of lithium inventory (LLI). The change in volume and possible intercalation of molecules from the electrolyte can cause cracking and delamination of the particles from the rest of the coating. If parts of the active material lose electrical contact to the current collector, the particles become electrochemically

Table 2.3 – Summary of degradation effects in graphite

Degradation mechanism	Caused by	Effect on cell level
Graphite ex-foliation	High anode potential	Loss of active material (LAM)
SEI growth	Low anode potential, high temperatures	Impedance rise, loss of lithium inventory (LLI)
Gasing	infraction of electrolyte's stability window	Swelling of cell, loss of electrolyte
Particle cracking	low / high SoCs, mechanical stress	LAM, LLI due to new SEI formation
SEI dissolution	high temperatures, high SoCs	Swelling of cell
Lithium plating	low temperatures, high charge currents, high SoCs	LLI, risk of short circuit
Loss of particle/particle and particle/current collector contact	mechanical stress	LAM

inactive and lithium intercalation and de-intercalation is stopped. Depending on the degree of lithiation when the particle loses contact, a combination of LAM and LLI occurs. Furthermore, with increasing passivation layer thickness, the impedance of the cell increases. The additional over-potential reduces the power capability and the efficiency of the cell. A special concern regarding the cell's safety is the hindered lithium diffusion through the SEI. Especially at lower temperatures and high charge currents the risk of lithium plating increases [24]. As a consequence, further electrolyte decomposition and gas evolution occurs and the dendrites can lead to local short circuits or in a worst case scenario to a thermal runaway of the cell. In Tab. 2.3, the major degradation mechanisms of graphite-based anodes are summarised.

A number of anode materials with a significantly higher energy density than graphite are investigated, but suffer from major drawbacks as extensive volume changes during cycling (LiSn [245]) or low Coulombic efficiency at the initial cycle (Si [101]).

2.3.4 Separator

Beside the main task of physically separating anode and cathode from each other, an ideal separator has to fulfil a long list of requirements. It is characterised by a high electrochemical resistance to sustain the degradation by the electrolyte. Stable mechanical properties and a low thickness allow for an easy handling process without adding dead volume or weight to the cell. A high porosity and a homogeneous pore-size distribution lead to a low ionic resistance. With regard to safety, easy wetting of the separator is important as dry areas can lead to inhomogeneities in the cell. In case of a thermal runaway, a shut-down mechanism is preferable. Most separators consist of a single polymer as polyethylene (PE) and polypropylene (PP) or a polymer trilayer (PP-PE-PP) [50]. Depending on the manufacturing process, different physical properties can be achieved [212, 244]. For lab scale experiments, where energy and power density

are not a crucial factor, glass fibre separators allow for an easy handling due to their high mechanical stability. Beside the previously mentioned active materials, non-active components of the cell also undergo degradation mechanisms. The separator undergoes continuous mechanical deformation, affecting the porosity of the layer. An increase in tortuosity extends the diffusion path of the lithium-ions and may reduce the transport capabilities in the electrolyte [151], resulting in a higher cell impedance.

2.3.5 Current collector

Due to the low price, good conductivity and lightweight, aluminium is the material of choice for the positive current collector in commercial cells. For the anode, the choice depends on the coated active material. Due to the graphite's low potential versus lithium metal, aluminium forms a lithium-aluminium alloy, requiring copper to be used. The lower electric conductivity of aluminium ($3.55 \cdot 10^7\,\mathrm{S\,m^{-1}}$ [160]) compared to copper ($5.88 \cdot 10^7\,\mathrm{S\,m^{-1}}$ [160]) is compensated by a bigger foil thickness. Recent improvements in energy density in commercial 18650 cells can be mainly attributed to an increase in fabrication improvements as reducing the current collector thickness [187]. Aluminium, used as the material for the current collector of the positive electrode is subjected to local corrosion. The building of surface layers and mounds is observed due to the high oxidation potential during the charge process of the cell. The usage of $LiPF_6$ based electrolyte aggravates the corrosion process but does not suppress the oxidation of the surface layer [242]. Copper on the other hand, used as current collector material for negative, carbon based electrodes, is electrochemically more stable but partially cracking at very low potentials versus lithium metal was reported by Braithwaite et al. [31].

2.3.6 Binder

The binder (e.g. polyvinylidene fluoride (PVdF), carboxymethyl cellulose (CMC)) is responsible for the stability of the coating and the physical connection of the particles as the coating undergoes mechanical stress [171, 173, 174] and side reaction with the electrolyte during cycling. To prevent LAM, a high chemical stability of the binder is a crucial factor of the electrochemical long-term performance of the cell. Demirocak et al. investigated the impact of different ageing scenarios as high-current cycling and elevated temperatures on PVdF [56]. A decreasing modulus of elasticity especially at high currents leads to a loss of coating stability and particle loss was more likely to occur.

Conductive carbon, used as coating additives, enhances the electron transport within the electrode. Its participation in electrochemical reactions lowers the electronic connection between particles or clusters, leading to an increase in over-potential and causes additional LAM.

2.4 Cell types

The major cell types for lithium-ion cells are cylindrical, pouch and prismatic cells. Cylindrical cells are categorised and named by their dimension, whereas the 18650 format (18 mm diameter, 65 mm length) is the most common one, used in most mobile

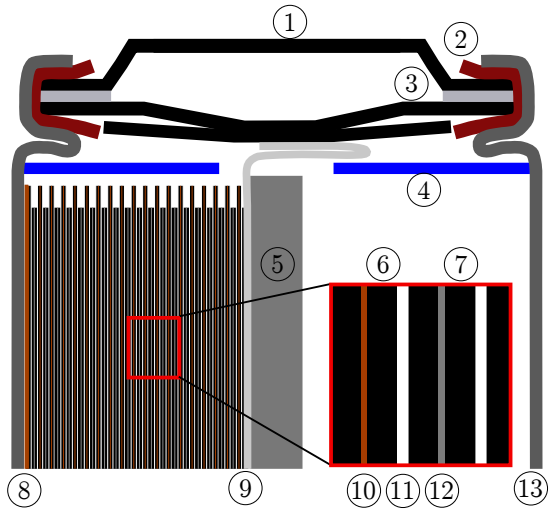

1 Positive cell terminal
2 Sealing
3 PTC device
4 Polymer spacer
5 Centre steel rod
6 Anode active material
7 Cathode active material
8 Negative current tab
9 Positive current tab
10 Negative current collector
11 Separator
12 Positive current collector
13 Cell housing (negative cell terminal)

Figure 2.9 – Schematic drawing of a typical commercial 18650 cell

devices as laptops [159]. This cell type is used for most experiments in this work and Fig. 2.9 illustrates the set-up of this cell type. The second cell type used is a slightly larger cylindrical cell with a 26650 format (26 mm diameter, 65 mm length).

The double coated positive and negative electrodes are rolled up with a separator in between, denoted as jelly roll. After contacting the jelly roll (negative electrode: cell housing, positive electrode: cell cap), electrolyte is added and the cell is closed. A PTC (positive temperature coefficient) device within the current path is commonly used as safety device in many cells. In case of a severe temperature increase of the cell, e.g. caused by an external short circuit of the cell, the resistance of the PTC increases, limiting the current of the cell. The second design possibility are pouch cells, which commonly comprise a stack of electrodes, alternating anode and cathode. The advantages of pouch cells are their flexible design and increase in gravimetric energy density, as the steel container used for cylindrical cells is replaced by an aluminium coated polymer casing. On the other hand, additional support to stabilise the cell and an increase in production complexity facilitate only a slow transition towards pouch cells as the major cell type [159]. A compromise between the cylindrical hard case and the soft pouch cell are prismatic cells. This cell format combines the safety advantages of a stable cell housing of a cylindrical cell with efficient cooling capabilities of a pouch cell. The increase in market share is especially driven by the increasing application in electric vehicles such as BMW's i-Series [170] and e.g. the Audi hybrid models [12].

Based on the intended use, cells are specially designed to either deliver high discharge currents (high power design) or store as much energy as possible (high energy design). The high power capability requires thinner electrode coatings to maximise the electrode area and to reduce the lithium-ion diffusion path, therefore the ratio between active material and current collector changes. Tbl. 2.4 gives an overview of the quantity and the respective weight ratio, based on data reported by the Center for Transportation Research

Table 2.4 – Exemplary material composition of commercial high energy and power cells [73]

Material	High energy cell 10 Ah		High power cell 1 Ah	
	Quantity / g	wt. %	Quantity / g	wt. %
Anode (dry)	78.5	23	5.6	17
Cathode (dry)	161.0	47	9.3	30
Active material	140.8	41	7.4	23
Electrolyte	61.8	18	4.4	13
Separators	6.0	2	1.6	5
Package	35.8	10	11.5	35

Table 2.5 – Cost estimation of cell components [147]

Material	Unit	Estimated value
Li_xCoO_2	\$ kg^{-1}	59
$Li_xNi_{1/3}Mn_{1/3}Co_{1/3}O_2$	\$ kg^{-1}	38
$Li_xNi_{0.8}Co_{0.15}Al_{0.05}O_2$	\$ kg^{-1}	37
Li_xFePO_4	\$ kg^{-1}	20
$Li_xMn_2O_4$	\$ kg^{-1}	10
Graphite	\$ kg^{-1}	10
$Li_4Ti_5O_{12}$	\$ kg^{-1}	12
Electrolyte (1.2 M $LiPF_6$ EC:DMC)	\$ kg^{-1}	18
Separator (PP / PE / PP trilayer)	\$ m^{-2}	2
Current collector foil (Al)	\$ m^{-2}	0.8
Current collector foil (Cu)	\$ m^{-2}	1.8

group of the Argonne National Laboratory [73]. Ongoing research, the improvement of manufacturing processes, variations in the raw material prices as well as the introduction of new materials leads to continuously changing values.

Based on market prices of 2012, estimations of the manufacturing costs of a cell are made based on the used components [147] and presented in Tbl. 2.5. The cathode has the largest share in weight and quantity and, depending on the used material, the highest specific price (\$ kg^{-1}) of all components. With a factor of six in costs between LMO and LCO, it is obvious that, beside the previously mentioned criteria such as power and energy density, safety and cycle stability, the large price difference is a significant factor defining the intended usage of the material for different applications as power tools, electric vehicles or stationary applications.

Chapter 3

Characterisation and Modification

This chapter describes the experimental cells investigated in this work and gives an overview of the most common electrochemical characterisation methods for lithium-ion cells. Beside the basic fundamentals of the techniques, the applicability regarding degradation investigation is discussed. The description of non-destructive methods which allow for an in operando observation of the decreasing performance is followed by a presentation of destructive methods, which are used to either verify predictions made with in situ methods, to improve the respective measurement technique or to give a more detailed insight into internal cell parameters.

3.1 Investigated cells

All cells investigated in this work are commercially available 18650 cells, designed for high power applications. The anode material of all cells is graphite, the most common anode material. To investigate variations in the cell's electrochemical performance, different cathode materials were chosen. The first cell, denoted as cell A, has a nominal capacity C_n of 1.5 Ah and the cathode is a blend of $Li_xNi_{0.8}Co_{0.15}Al_{0.05}O_2$ - $Li_xMn_2O_4$ [181] with a ratio of 3:1 determined by XRD, XPS and inductive coupled plasma (ICP) measurements. The second cell investigated (Cell B) has a nominal capacity C_n of 2.25 Ah with a $Li_xNi_{1/3}Mn_{1/3}Co_{1/3}O_2$ cathode [195]. The third cell (Cell C) has a Li_xFePO_4 cathode with C_n = 1.1 Ah [1]. In Tbl. 3.1, relevant parameters such as cut-off voltages and geometric dimensions of the cells are listed.

The position of the current tab(s) of the respective electrode are given in Tbl. 3.1. The beginning of the jelly roll is defined as the start of the rolling process and is therefore located in the cell centre. Analogously, the end of the jell roll is defined. In Fig. 3.1, the voltages of the different cells during a 0.05C charge and discharge are displayed as a function of the cell capacity a as well as of the cell's SoC b. Due to the blended cathode material, cell A features numerous small voltage plateaus during the discharge process, while the voltage of cell B decreases linearly. Cell C with a LFP cathode reveals a nearly flat and constant voltage, revealing the influence of different voltage plateaus of the graphite anode.

Scanning electrode microscope (SEM) pictures of harvested electrodes of the inves-

Table 3.1 – Properties of investigated cells

Name	Cell A	Cell B	Cell C	Cell D
Cathode material	NCA-LMO	NMC	LFP	LFP
Anode material	Graphite	Graphite	Graphite	Graphite
Nominal voltage U_n / V	3.60	3.70	3.25	3.25
Charge cut-off voltage U_{cco} / V	4.20	4.20	3.60	3.60
Discharge cut-off voltage U_{dco} / V	2.75	2.50	2.00	2.00
Max. charge current / A	1.5	2.25	4	10
Max. discharge current / A	10	10	30	70
Nominal capacity C_n / Ah	1.50	2.25	1.10	2.5
Capacity C_{n,cm^2} / mAh cm^{-2}	2.11	3.31	1.36	2.67
Electrode Area A / cm^2	708	675	809	1876
Thickness coating cathode / µm	71	78	72	63
Thickness coating anode / µm	48	73	34	35
Thickness curr. coll. cathode / µm	18	15	20	20
Thickness curr. coll. anode / µm	13	11	10	13
Weight / g	48	43	39	76
Number of curr. tabs per electrode	1	1	1	4

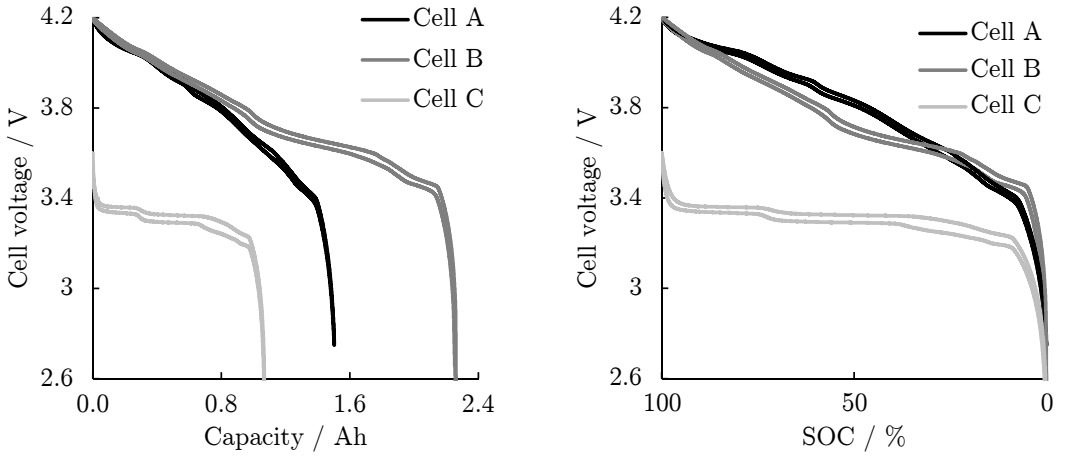

a 0.05C charge and discharge voltage as a function of cell capacity

b 0.05C charge and discharge voltage as a function of the SoC

Figure 3.1 – Charge and discharge behaviour of the investigated cells

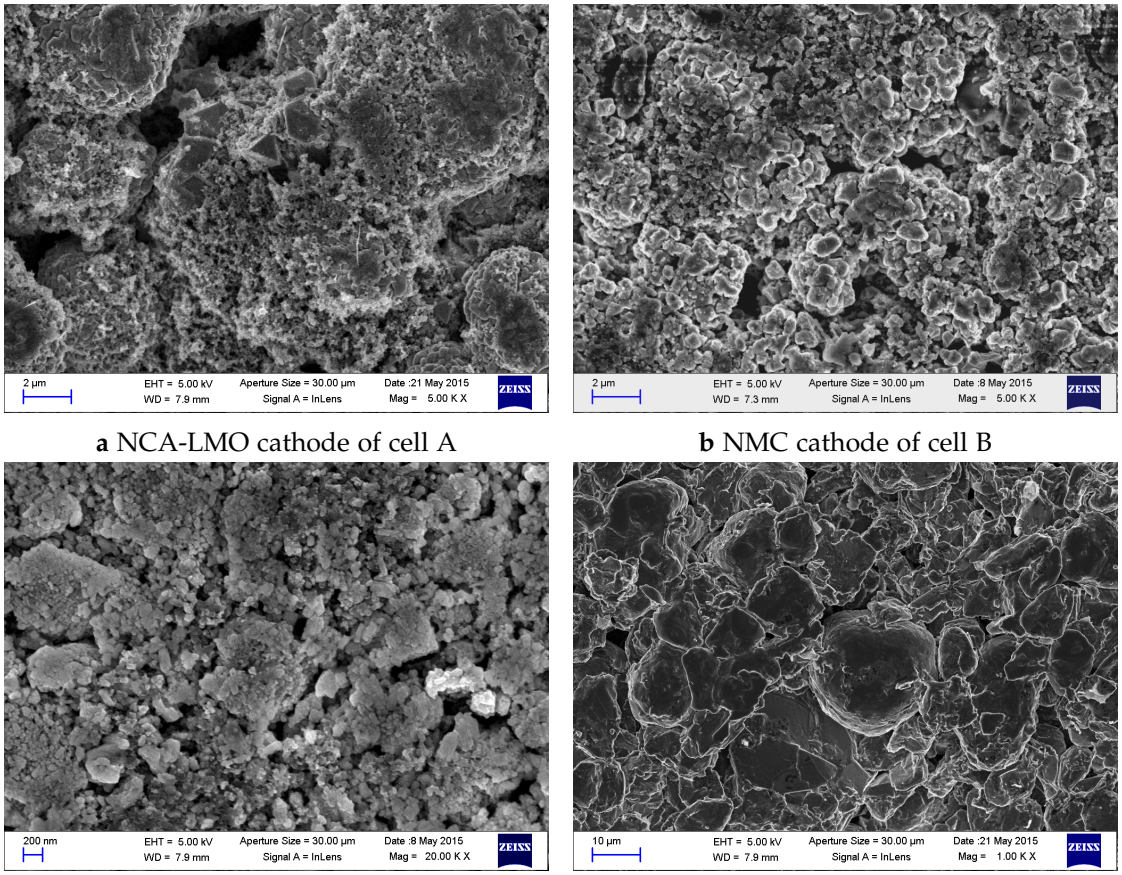

a NCA-LMO cathode of cell A

b NMC cathode of cell B

c LFP cathode of cell C

d Graphite anode of cell A

Figure 3.2 – SEM Pictures of cathodes a - c and one anode d, harvested from investigated 18650 cells

tigated cells are displayed in Fig. 3.2. All pictures were taken using a Zeiss Supra 55VP Field Emission Scanning Electron Microscope (FESEM) with an acceleration voltage $U_{acc} = 5\,\text{kV}$ and an aperture size of 30 µm. In Fig. 3.2a, the different materials in the NCA-LMO blend cathode can be distinguished. The small NCA particles are agglomerated in clusters with a large variation in size and the LMO particles are distributed throughout the NCA clusters. They are clearly identifiable due to their larger, cubic-shaped structure, characterised by a symmetrical shape and even surfaces.

The NMC material, shown in Fig. 3.2b features a similar structure except that the clustered particles are larger in size. To allow for a clear identification of LFP nano particles, a four times larger magnification of $2 \cdot 10^4$ is applied in Fig. 3.2c. The anode displayed in d was harvested from cell A. The chosen magnification was 10^3 due to large variation in particle size between 6 µm and 30 µm. Even though the cell is considered as new from a lifetime perspective, the formation process already took place and a thin SEI layer was formed on the surface. Nevertheless, the structure of the graphite particles is clearly visible. Due to the similarity of all three anodes, only one SEM picture is shown.

Beside the three main cells, additional experiments were made on commercially available 26650 cylindrical cells with a LFP cathode and graphite anode, referred as cell

D in this work. The cells have a nominal capacity C_n of 2.5 Ah. The larger cell size and geometric design allowed modification processes to gain further insight into the current density distribution of the cell. The modification process will be presented in detail in Sec. 3.6 while obtained results with focus on equalisation processes of SoC inhomogeneity and current density distribution are discussed in Sec. 5.1 and Sec. 4.

3.2 Electrochemical impedance spectroscopy

EIS is an alternating current (AC) characterisation, by which the response of the electrochemical system to an excitation with a defined frequency range at various SoCs is interpreted. Two different principles can be applied. For the galvanostatic mode, an excitation current with a constant amplitude is applied and the voltage response is measured. In the potentiostatic mode, the cell is excited by an AC voltage signal within a defined frequency range and the current response is measured. As the slope of cell voltage varies and can be very small for some cells, the resulting current amplitude can vary significantly. Both techniques rely on the frequency dependency of different electrochemical processes within the cell [89, 90, 185]. Using a sinusoidal excitation current

$$I(t) = I_0 sin(\omega t) \tag{3.1}$$

the complex impedance $Z(\omega)$ with $\omega = 2\pi \cdot f$ of a cell is defined by

$$Z(\omega) = \frac{U(\omega)}{I(\omega)} \cdot e^{j\phi(\omega)} \tag{3.2}$$

with the voltage U, current I and the phase angle ϕ between the two signals. $Z(\omega)$ can be divided in the real part $Z'(\omega)$ and imaginary part $Z''(\omega)$

$$Z(\omega) = Z'(\omega) + j \cdot Z''(\omega) \tag{3.3}$$

The applied frequency f can be as high as multiple MHz and low as a few µHz [96]. To analyse the electrochemical processes in lithium-ion cells, a frequency range between 100 kHz and 10 mHz is sufficient [96]. The signal excitation frequency and the respective electrochemical processes dominating the spectrum is illustrated in Fig. 3.3.

Fig. 3.4 illustrates the two most common ways to plot impedance data. In the Nyquist diagram in Fig. 3.4a, -$Z''(\omega)$ is plotted against $Z'(\omega)$. The Bode plot b shows the magnitude $|Z|$ as well as the phase angle ϕ against the frequency of the applied excitation signal. Characteristic frequency ranges attributed to inductive behaviour, transfer through SEI, charge transfer and solid state and liquid phase diffusion are highlighted [89, 185].

EIS is an established method to characterise cells under various conditions and the impact of variables as SoC [13, 215], temperature [169, 177], temperature gradients [208] and short-term history of the cell [107] is widely discussed in literature. This

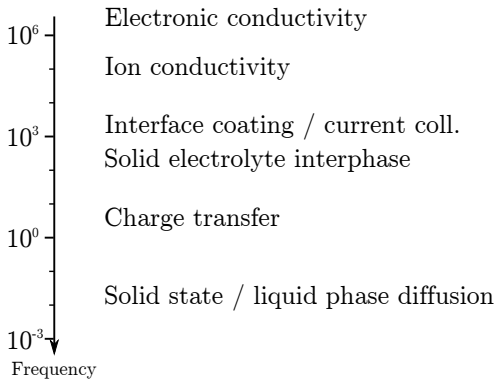

Figure 3.3 – Estimated ranges of effects in dependence on the excitation signal frequency

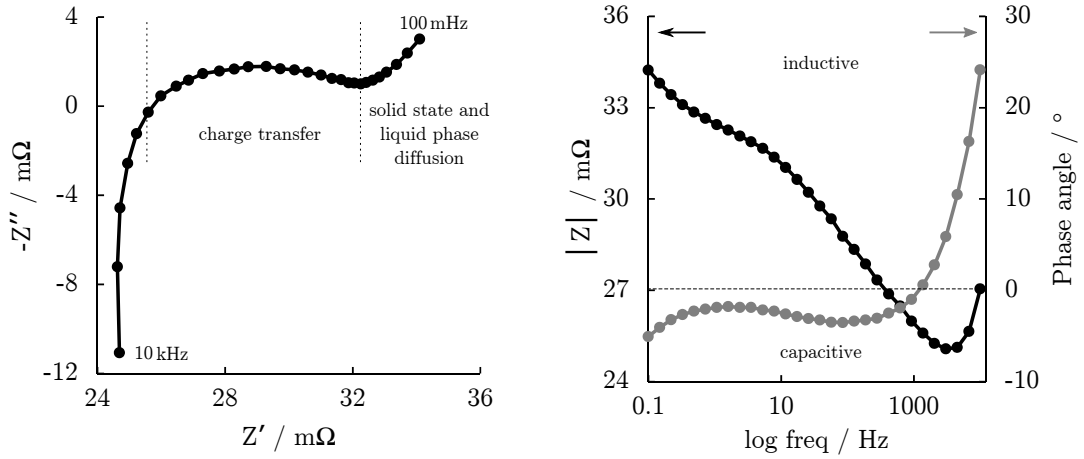

a Nyquist plot **b** Bode diagram

Figure 3.4 – Exemplary Nyquist plot and Bode diagram of an impedance measurement on cell C (LFP/C) at 25 °C with an excitation current of 50 mA at 50 % SoC

qualifies EIS measurements as a promising candidate to track degradation mechanisms in cells, assuming that the reason for the performance decrease is clearly identifiable and attributable to a certain frequency range. Parameters as ohmic resistance, charge transfer resistance and diffusive behaviour are extracted from EIS measurements during the ongoing ageing studies, the state at begin of life (BoL) and end of life (EoL) is compared and conclusions regarding electrochemical origins of the changes are made. Beside the correlation of the increase in ohmic resistance and the growth of surface layers on anode and cathode, a detailed explanation of further changes is missing [77, 138, 234]. Furthermore, little is known about the influence of cell design on the impedance spectra. Especially in the context of inhomogeneous ageing within the cell, the impact of the alternating current density distribution along the electrodes needs to be analysed.

Consequently, measurements of local potentials during the AC operation of a modified commercial cell were investigated and conclusions regarding the current density distribution are discussed in Sec. 4. Based on the tab position, temperature and the

frequency of the applied excitation current varying contributions of the cell components towards the spectra were observed. By varying the cell temperature, the decay of the potential distribution along the electrode and thereby evoked electrode area was controlled. A final statement regarding the applicability of EIS measurements as a reliable and useful degradation tracking tool for various cell systems is presented in Sec. 4

3.3 Differentiating techniques

Differentiating techniques are based on direct current (DC) measurements, sweeping the full SoC range in either charge or discharge direction. A constant current (CC) is applied to the cell and the correlation between cell voltage and capacity is analysed. The most common differentiating techniques in literature to separate the electrode information are the incremental capacity analysis (ICA)

$$ICA = \frac{dQ}{dV} \tag{3.4}$$

and the differential voltage analysis (DVA)

$$DVA = \frac{dV}{dQ} \tag{3.5}$$

The main difference between the two methods is illustrated in Fig. 3.5, using cell C with LFP as cathode and graphite as anode active material. The peaks in the dV/dQ curve represent phase transitions, whereas the peaks in the dQ/dV curve represent phase equilibria [28]. Materials with two phase equilibrium regions (e.g. LFP, LTO or graphite for specific lithiation ranges) depict voltage plateaus during cycling, which result in a $\Delta V = 0$ and therefore a division by zero for the dQ/dV data. A further disadvantage of incremental capacity analysis (ICA) is the requirement for a very precise voltage resolution to lower the signal to noise ratio, which exceeds the specification of most commercially available test systems.

Similar to the cell voltage, dQ/dV and dV/dQ data can be expressed as a sum of the single electrodes by

$$\left(\frac{dQ}{dV}\right)_{cell} = \frac{1}{(dV/dQ)_{cathode} - (dV/dQ)_{anode}} \tag{3.6}$$

$$\left(\frac{dV}{dQ}\right)_{cell} = \left(\frac{dV}{dQ}\right)_{cathode} - \left(\frac{dV}{dQ}\right)_{anode} \tag{3.7}$$

to compare cells with different capacities as 18650 and coin cells, the data of differential voltage analysis (DVA) are normalised by the cell capacity Q_0, the actual measured capacity of the cell.

$$\frac{dV}{dQ_{norm}} = \frac{dV}{d(Q/Q_0)} = Q_0 \frac{dV}{dQ} \tag{3.8}$$

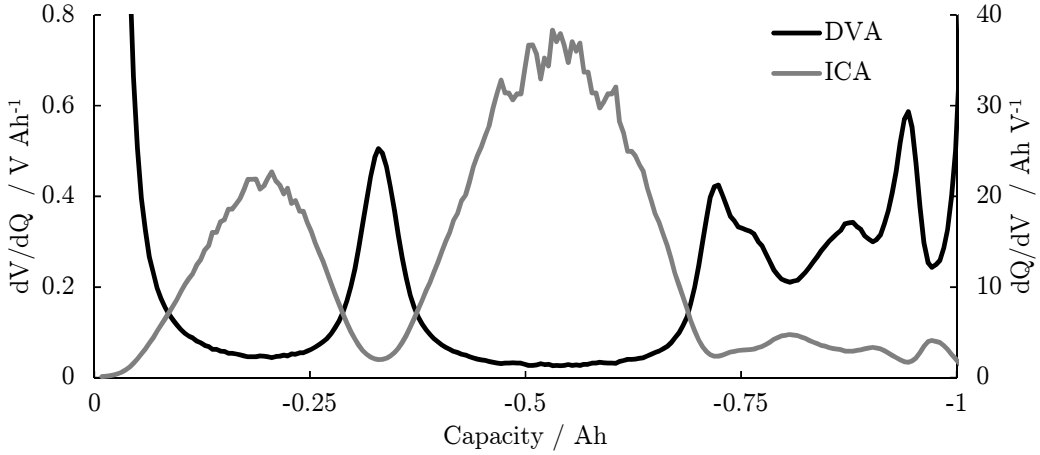

Figure 3.5 – Comparison of a 0.05 discharge curve of cell C, analysed by DVA and ICA

Due to the simplicity of the approach, DVA and ICA are used intensively for the characterisation and observation of lithium-ion cells during the degradation process [26, 27, 28, 29, 61, 64, 103, 178]. During the slow charge-discharge procedure, measurements require only a climate chamber to minimize temperature fluctuations and a defined starting point, as the measurement is sensitive of the starting SoC. For ICA measurements, a high precision for the voltage measurement is advantageous.

Bloom et al. used DVA for full-cells to track and analyse ageing mechanisms in graphite anodes [26, 27] and cathode materials such as NCA [28] and NMC [29]. The local maxima in the curves are allocated to the respective electrode and based on the shift along the x-axis as well as the relative shift between the peaks of the same electrode. Conclusions are drawn regarding the initial and final cell balancing and the respective possible sources of cell degradation which were mainly accredited to LAM and LLI. Similar results were obtained by Dubarry and co-workers during the extensive analysis on NMC-LMO cells for plug-in HEVs [61, 64].

Delacourt and co-workers used the method to analyse degradation mechanisms in commercial LFP / graphite cells under various ageing conditions [103, 178]. The main ageing mechanism was concluded to be LLI, whereas a degradation of the cathode material as source for the performance loss could be eliminated. Based on available literature, ICA and DVA are the most promising electrochemical methods to investigate the continuous degradation for the single electrodes.

A drawback of the measurements is the analysis' need of a full, slow charge and / or discharge cycle starting at a defined reference point to obtain the necessary results. Furthermore, a crucial requirement is a clear assignment of the respective maxima to the correct electrode, which presupposes either half-cell measurements or reliable and available reference in literature of the same or similar material. Due to the convenience of the measurement, DVA measurements are defined as the reference method to investigate the degradation of investigated cells during ongoing ageing progress. Detailed results will be presented and discussed in Sec. 6.2.2.

3.4 Cyclic voltammetry

Cyclic voltammetry (CV) is a common potentiodynamic measurement technique in the field of electrochemistry. In the conducted experiment, the cell voltage U_{cell} is controlled as a linear function of time and ramped with a constant slope ν between the charge cut-off voltage U_{cco} and discharge cut-off voltage U_{dco} according to

$$U(t) = U \pm \nu t \tag{3.9}$$

A positive slope implies charging whereas a negative slope implies discharging the cell. The resulting current is recorded and plotted versus the cell voltage [83]. If the scan rate ν is sufficiently small ($<$1 mV min^{-1}), an approximation of the solid state diffusion coefficient based on the peak current i_p can be made

$$i_p = 0.4463 \cdot \left(\frac{n^3F^3}{RT}\right)^{0.5} AD_0^{0.5}C^B\nu^{0.5} \quad [229] \tag{3.10}$$

with electrode surface area A, diffusion coefficient D_0 of the reactive species in the material and the respective bulk concentration c. The occurring maximum (peak current i_p) in the voltammogram indicates the balance potential where the most suitable reaction potential is counteracted by the depletion of the reacting species and the therefore occurring thickness increase in the diffusion layer. For lithium-ion batteries they correlate with the specific intercalation potentials of anode and cathode.

Fig. 3.6a highlights the impact of temperature on mass transport at a constant scan rate of 0.6 mV min^{-1}. The enhanced transport mechanisms lower the cell's overpotential with increasing temperature and the potential gap between the associated maxima in charge and minima in discharge direction becomes smaller.

In Fig. 3.6b, the influence of the scan rate on the voltammogram of cell A with a NCA-LMO cathode and graphite anode is illustrated. The peak current i_p (in mA) is divided by the scan rate (in mV min^{-1}), and the capacitance of each intercalation potential can be calculated by integrating the respective voltage range. Similar to the differentiating techniques described in the previous section, half-cell measurements are necessary to allow for a clear identification of the respective contributor. For a scan rate of $\nu = 0.6$ mV min^{-1} the intercalation potentials are clearly distinguishable for charge and discharge direction. For $\nu = 4$ mV min^{-1} the feature at 3.9 V vanishes for the discharge curve completely and an increasing overlap between the different intercalation potentials is observable due to the limited diffusion processes in the active material.

Even though CV is a common characterisation technique in the field of electrochemistry, the available literature for detailed degradation tracking studies in commercial lithium-ion cells is limited. Similar to the differentiating techniques as described in Sec. 3.3, the position and height of the peaks allow assumptions regarding the cell balancing and the condition of the respective electrode. Assuming the clear distinction of the specific intercalation potentials, estimations concerning the remaining specific capacity of each component in blended electrode materials can be made.

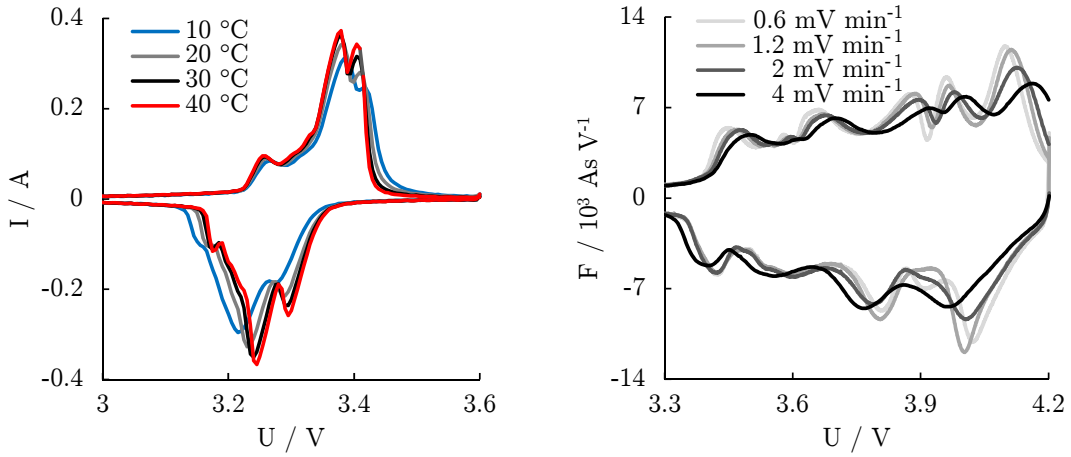

a CV of Cell C at different temperatures with a scan rate of 0.6 mV min^{-1}

b Integrated CV of Cell A for different scan rates at 20 °C

Figure 3.6 – Temperature a and rate b dependency of cyclic voltammetry measurements

Markevich [131] combined CV measurements with EIS and CC techniques to analyse self-discharge mechanisms of graphite anodes during cycle ageing. The separation of i_p peaks from each other and their decrease in height was explained by the variations in lithium-ion diffusion and LAM. Yu reported the dependency of the current peak on electrode thickness, temperature, sweep rate and electrolyte [238] for LFP and calculated the diffusion coefficient of lithium-ions in the active material. Sasaki characterised LNO-based cells after cycling the cell at high temperatures [182]. The decrease of i_p in the constant voltage (CV) diagram was analysed and attributed to LAM and increasing cell impedance.

Stiaszny et al. investigated cells with LMO-NMC cathode during cycling [196] and calendar ageing [197]. The CVs of anode and cathode materials were analysed and the changes in i_p were attributed to the loss of active material, as the discharge capacity, calculated by the integration of the various intercalation potentials, decreased. To obtain the detailed results, a scan rate of $\nu = 0.3\,\mathrm{mV\,min^{-1}}$ was applied. For a voltage range of $\Delta V = 1\,\mathrm{V}$, the measurement needed approximately 110 h for a full cycle.

Based on the various interpretations of the change in i_p discussed in literature, CV data gained during ageing characterisation tests need to be verified by additional measurements. Due to the similar information which can also be obtained in DVA measurements, a further significant drawback of CV techniques is the comparable long time for the check-up procedure. As a consequence, no detailed interpretation will be presented for CV measurements in chapter 4.

3.5 Thermodynamic measurements

A cell's entropy S depends on the configurational and vibrational contribution from ionic and electronic components of the system as presented in Sec. 2.2. These contributions

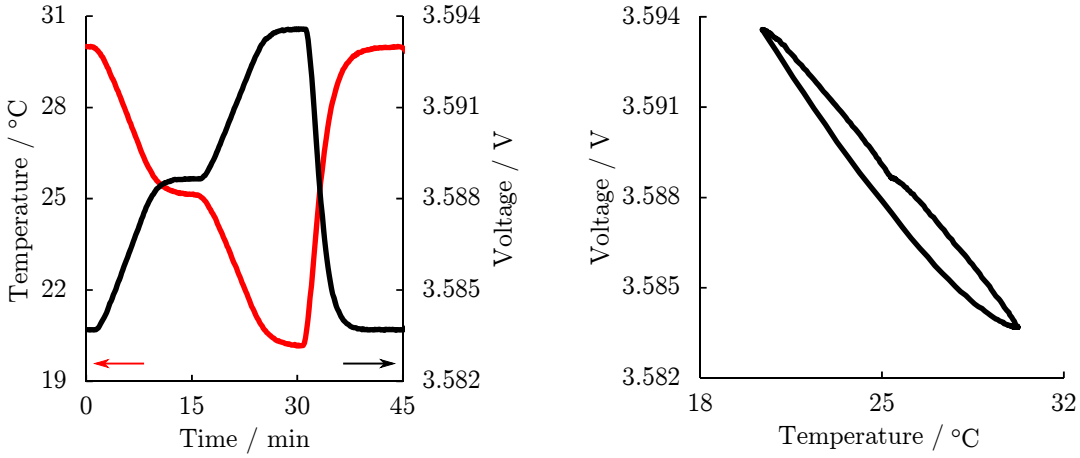

a Cell's voltage response to a change in temperature

b Linear correlation between cell voltage and temperature

Figure 3.7 – Voltage and temperature measurement a and the resulting V-T curve b of cell A for 30 % SoC

vary with the degree of lithiation in the host structure and the change in reaction entropy $\Delta_r S$ can be directly measured by thermodynamic measurements (TM) as a temperature dependency of the cell's equilibrium potential E_{eq}.

$$\left(\frac{\partial E_{eq}(x)}{\partial T}\right)_{p,x} = -\frac{1}{nF}\left(\frac{\partial}{\partial x}S(x)\right)_{p,x} = -\frac{1}{nF}\Delta_r S(x) \tag{2.37}$$

The response of the cell voltage on a decreasing cell temperature is exemplified shown in Fig. 3.7a. The change in the cell's OCV can be either negative or positive, if the cell temperature is decreased, resulting in a positive or negative sign for the entropy value. Fig. 3.7b illustrates the nearly linear coherence when the voltage is plotted versus the cell temperature. Deviations from this linear behaviour originate from the thermal gradient through the cell, when the radial heat transfer is slower than the temperature alteration rate. With the operation range from –20 °C to 60 °C for lithium-ion cells, the linearity is assumed to be valid [18, 199].

The potentials of anode and cathode versus lithium reveal a non-linear temperature coefficient dependency of the degree of lithiation. During discharge, the cathode is reduced, while the anode is oxidised and the cell's overall reaction entropy can be expressed by the sum of each component.

$$\Delta_r S_{cell} = \Delta_r S_{cathode} + \Delta_r S_{anode} \tag{3.11}$$

In the case of a discharge of the cell, it is represented by

$$\Delta_r S_{cell,discharge} = \Delta_r S_{cathode,reduction} + \Delta_r S_{anode,oxidation} \tag{3.12}$$

For graphite half-cell measurements, the reduction entropy is measured. The delithiated state is used as the preferred reference start point since nearly all lithium is deintercalated from the material when a voltage of 1 V with a sufficiently long CV phase is applied. Setting the fully lithiated state as a reference point bears the risk that lithium deposition takes places due to the low potential versus lithium metal. When combining two half-cell measurements, Eq. 3.12 is rewritten as

$$\Delta_r S_{cell,discharge} = \Delta_r S_{cathode,reduction} - \Delta_r S_{anode,reduction} \tag{3.13}$$

For the first time used by Thompson in 1981 to study the phase transformation in Li_xTiS_2 [204], the method became a common tool to either investigate the thermodynamic properties of electrode materials such as LCO [164], LMO [15, 203], LTO [94] or graphite [166] or to characterise commercial full-cells such as LCO / graphite [183, 199] or LFP / graphite systems [92]. Some studies investigating the impact of different ageing procedures as cycling [87, 125], high temperatures [126] or high voltage treatment [124] can be found in literature. Unfortunately, some of the made assumptions seem to be based on insufficient pre-processed data, leading to doubtful interpretation [124, 125, 126] and lacking reproducibility.

Due to the contribution of both anode and cathode, thermodynamic measurements qualify as a promising candidate to characterise commercial lithium-ion cells by analysing the temperature dependency of the OCV. Information similar to DVA can be obtained with the advantage that the measurement can be conducted at selected SoCs, either during charge or discharge. With frequent measurements during the e.g. charge process of EVs, detailed information can be gained. In contrast to that, long relaxation times until the cell reaches an electrochemical equilibrium prevent the measurement to be used successfully as a check-up technique. A small number of data points may lead to uncertainties in the determination of the position of the local extrema. Consequently, a compromise needs to be made between a larger number of data points, resulting in a higher accuracy and the measurement time, based on the intend usage of the technique, e.g. reoccurring check-ups or a detailed analysis at the EoL of a cell. To investigate the usability of thermodynamic measurements as a degradation tracking procedure, a significant increase in the measurement speed is desirable.

3.6 Cell modification

The cell's surface temperature at various positions, the applied current and the resulting voltage, measured at the cell's terminal are external parameters that can be easily determined during operation. Unfortunately, this information is not sufficient to fully describe the electrochemical performance of the cell, to guarantee an optimal operation mode at any time nor to predict the safety and reliability of the system. To gain more information, the modification of commercial cells is a powerful tool to access internal parameters. It can be distinguished into two different modification processes. The first one includes the investigation of the performance and a detailed electrochemical analysis of electrodes by means of half-cell measurements. As the cell needs to be dismantled and

rebuilt, it is a destructive method. Consequently, to avoid major changes in the cell, non-destructive methods are favourable. In this work, non-destructive modification processes are presented that allowed the insertion of lithium reference electrodes into commercial 18650 cells using a newly developed sealing system. Furthermore, a method to measure local potentials at different positions of the electrodes was introduced and successfully applied to investigate variations in the current density distribution of cylindrical cells [66, 153]

3.6.1 Half-cells

Half-cell measurements are useful to investigate single electrodes of dissembled full-cells. The harvested electrode material is rebuilt in a coin cell or pouch bag with fresh electrolyte and a new separator, using lithium metal as the counter electrode [104, 196, 213]. Caution in interpreting is necessary, as the rebuilding process can influence the electrochemical behaviour by changing various parameters. As the original electrolyte composition is usually unknown, adding new electrolyte can affect the SEI or general surface layers on the active material. If necessary, remaining electrolyte can be washed away by soaking the electrodes for 30 min in DMC and drying them afterwards for 120 min in the antechamber of the glove-box at ambient temperature. Zhang et al. reported partial removal of the graphite's SEI and changes in respect to calorimetric measurement results but no effect on cycling or thermodynamic measurements were observed during experiments [247]. Half-cells built with cathode material from the commercial cell following the same notation as full-cells, whereas discharging means that lithium in intercalated into the host structure and the cell voltage decreases. The harvested graphite electrodes, which are used as anode material in the commercial full-cells, become the cathode in a half-cell with lithium metal. To allow for a clear distinction and to avoid any confusion with the cathode materials in this work, half-cells with graphite are denoted as anode half-cells. Charging the graphite up to 1 V leads to full de-intercalation of lithium and allows for the definition of a well-defined reference point for following measurements.

Half-cell assembly

Fig. 3.8 illustrates the schematic assembly of coin cells as used for measurements in this work. The investigated full-cell was discharged at 0.2C until U_{dco} was reached and afterwards opened inside an MBraun glove-box with argon atmosphere. The jelly roll was taken out of the cell and the positive and negative electrode were carefully separated. 16 mm diameter samples were punched out at different locations of the electrode. The harvested electrode sample was placed in a 2016 cell housing bottom part (steel), covered with a glass-fibre separator (19 mm diameter, 500 µm thickness). Whatman™ glass-fibre separators from GE Healthcare Life Sciences were used instead of polymer-based separators due to their higher mechanical stability and easier handling. To allow for a homogeneous distribution of the electrolyte and to avoid any negative impact on the cell's performance, an excess amount of electrolyte of 120 µL (EC:DMC 1:1 (by volume) $LiPF_6$, Sigma-Aldrich) was added on the separator before placing the lithium metal foil (16 mm diameter, 400 µm thickness). Two steel spacers (400 µm thickness,

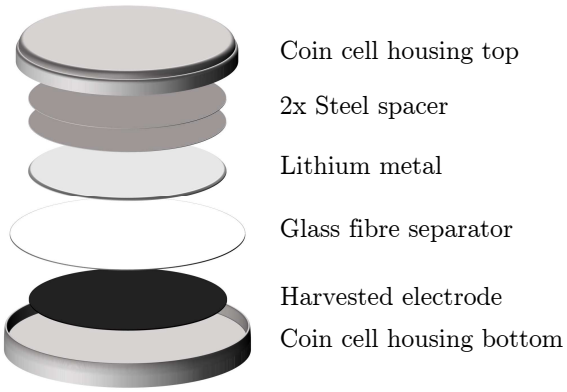

Figure 3.8 – Schematic assembly set-up of half-cells with retrieved electrode samples cycled vs. Li/Li^+ in a coin cell

16 mm diameter) guaranteed a homogeneous pressure in the cell for a good electrical contact. The cell was closed with a crimping tool (Hohsen Corp.) and either contacted via spot welded nickel tabs (4 cm length, 80 µm thickness, 0.5 cm width) or mounted into self-made cell holders.

The coated graphite and the metal oxide based active material of the investigated cells easily flake off from the current collector while the LFP coating needed heated N-Methyl-2-Pyrrolidone (NMP) and strong mechanical pressure for removal. Hence, it was refrained to remove the active material from the lithium averted side to avoid any negative impact on the samples. To exclude the possibility that the double-sided coating affects the electrochemical performance, half-cells with different active material backside loadings were tested by cycling the cells at 0.2C between the estimated cut-off voltages. Fig. 3.9a depicts the average discharge capacity of the first two cycles of the half-cells, where approximately 0 %, 50 % and 100 % of the coating remained on the backside of the sample. The samples with approximately 50 % loading were punched out from electrodes areas, where the coating remained on the current collector and partially flaked off as depicted in Fig. 3.9b. Each population consists of four coin cell samples. The error bars show the sample variance s^2 of each population. The data suggest that the measured capacity of the cell is not affected by the amount of active material on the backside of the current collector and only the lithium-facing active material participates in cycling. Moreover, a variation of approximately ± 2 % among all cells is measured and it is assumed that the cutting process leads to a certain loss of active material on the cutting edges. Due to the limitation of mechanical cutting possibilities, the uncertainty cannot be prevented and needs to be taken into account for further measurements.

Measurements

Fig. 3.10 illustrates the voltage profiles of the cathode materials, harvested from the commercial cells investigated in this work. The voltage boundaries of the half-cells need to be chosen carefully and an increase in cell capacity can be observed after the first cycle. With

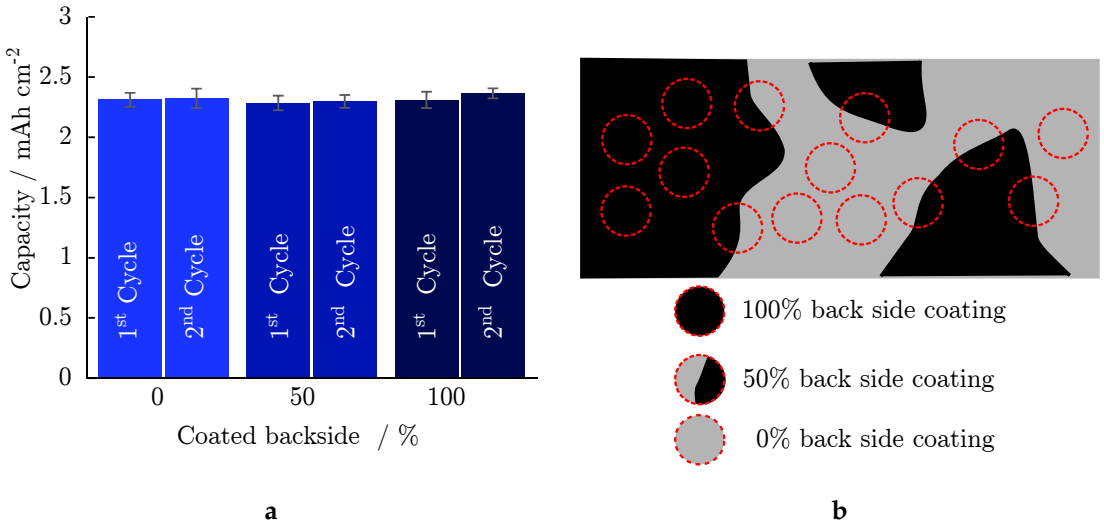

Figure 3.9 – 0.2C discharge capacities of assembled half-cells vs. Li/Li^+ using cell A's cathode with different amounts of active material on the lithium averted side of the counter electrode a and schematic drawing of coating flake off from the current collector b

$$E_{eq} = E_{eq,\,cathode} - E_{eq,\,anode} \tag{3.14}$$

the cut-off voltages U_{cco} and U_{dco} are calculated from the full-cell voltages, assuming that the anode potential does not fall below a certain voltage versus lithium in the fully charged state in a commercial cell.

Graphite exhibits a voltage plateau at approximately 80 mV during the progress of the stage 1 / stage 2 transition in the lithiation range of $0.5 < x < 1$ [53, 82]. Due to the overbalancing of the anode to avoid lithium plating, it is assumed that the graphite incorporated in the investigated full-cells does not show a voltage below this level when operated under low current operation. Including a possible overpotential of 30 mV during the charging process of the full-cell, leads to a minimum anode voltage of 50 mV versus Li/Li^+. This value was used to calculate the upper voltage limits for the cathodes which were set to 4.35 V for the metal-oxide based cells A and B and to 3.65 V for the phosphate based cathode material from cell C.

Due to the steep voltage increase for graphite at low degrees of lithiation and the steep voltage decrease for cathode materials at high degrees of lithiation, the cathode's discharge cut-off voltage U_{dco} and the anode's charge cut-off voltage U_{cco} can only be estimated. Based on the cell balancing, a maximum anode voltage of 600 mV is assumed, but to include uncertainties, the voltage limits for U_{dco} were set to 3 V for cell A and B and to 2.4 V for cell C. As a result, the cathode half-cells deliver a higher specific capacity C_{n,cm^2} (in mAh cm^{-2}) than calculated for the full-cell as indicated in Tbl. 3.2. The voltage profile of cell A shows a number of distinguishable turning points with a linear decrease. The slope of the discharge profile of cell B changes at 3.8 V and becomes smaller until the voltage drops at 3.55 V. The LFP cathode of cell C delivers a constant voltage of 3.4 V until a SoC of 20 %.

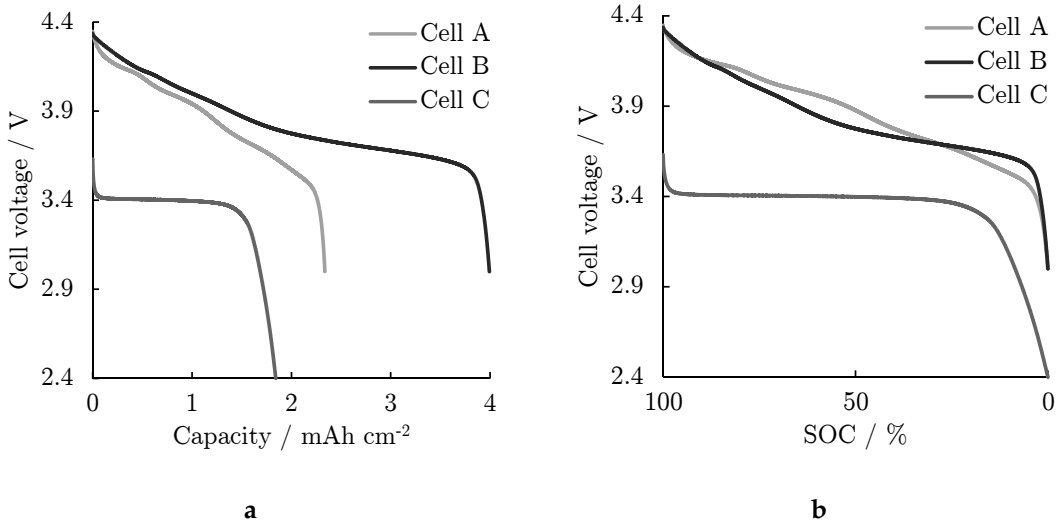

Figure 3.10 – Half-cell voltages of the cathode materials of the investigated cells, plotted versus capacity a and SOC b

Table 3.2 – Specific capacities of cells and respective electrodes during a C/20 discharge for the calculated charge and discharge cut-off voltages

Type	Cell / mAh cm^{-2}	Cathode / mAh cm^{-2}	Anode / mAh cm^{-2}
Cell A	2.11	2.35	2.46
Cell B	3.31	3.99	4.14
Cell C	1.36	1.86	1.73

Fig. 3.11a and b illustrate the graphite voltage profiles of the different cells. Due to the voltage plateau at a high degree of lithiation, the final degree of lithiation of the anode material is often unknown in a fully charged full-cell. As a consequence, the discharge cut-off voltage U_{dco} for the anode half-cells is set to 2 mV to allow for a full utilisation of the material but also to avoid any lithium deposition, despite the overpotential in coin cells due to their comparably high internal contact resistances. For the charge cut-off voltage U_{cco}, various limits between 0.5 V [35] and 1.5 V [165] are suggested in literature. As a compromise and to allow for the previously mentioned determination of a reliable and reproducible reference point, a voltage of 1 V was applied with a maximum CV phase of 60 min to fully remove the lithium.

Tbl. 3.2 presents the specific capacities of the investigated cells, calculated by the electrode area and the capacity of the full-cell during a C/20 discharge. It is observed that the electrodes measured as half-cells deliver a higher capacity. As lithium metal is used as the counter electrode, an infinite reservoir of lithium compared to the small capacity of the active material is available and the larger voltage range used during cycling leads to a bigger utilisation of the material.

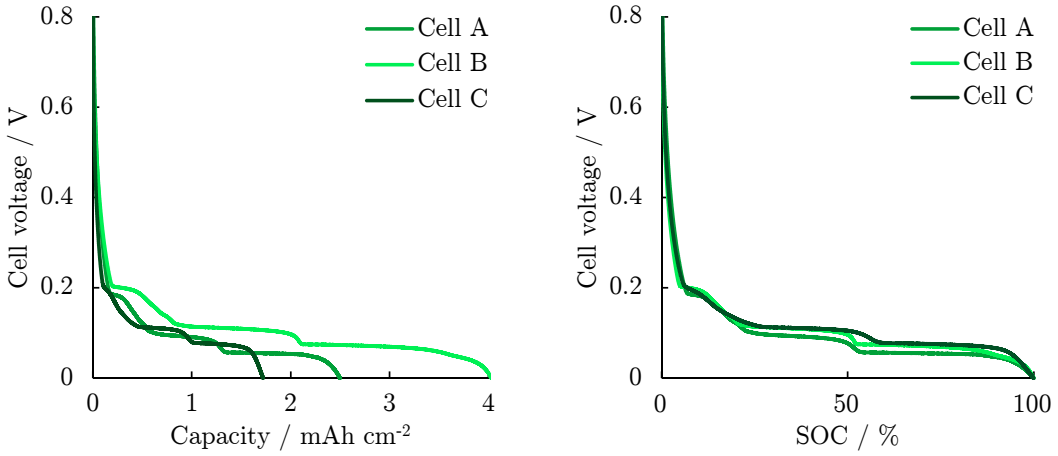

a Anode half-cell voltages over cell capacity **b** Anode half-cell voltages over SOC

Figure 3.11 – Half-cell voltages of the different anodes of the investigated cells plotted versus capacity a and SOC b

3.6.2 Reference electrode measurements

Reference electrodes are a valuable tool to investigate the cell balancing and the degradation process of the respective electrodes in full-cells. Since both electrode's electrochemical potentials change with the amount of stored lithium, both contribute to the measured change in cell voltage and as described in Sec. 2.1, the cell voltage can be expressed as the difference of both electrode potentials versus a defined reference value. To access the information of each electrode separately, instead of a conventional two-electrode measurement, a third electrode is inserted which allows for the observation of each potential. This requires a high reversibility and a stable potential relative to the solution phase without interfering with the electrochemical system.

In literature, different materials are discussed for application in lithium-ion cells. Beside the most common one, lithium metal, the application of other metals as silver [59], gold [194] or metal alloys as $LiSn_{4.4}$ [3, 9, 95] and Li_2Bi [75] is discussed but found either not to be suitable due to the strong polarisation effects of the electrode or only partially suitable for specific applications due to an unstable potential with changing alloying stoichiometry.

Active materials used in lithium-ion cells with a flat potential profile over a large SoC range as LTO with 1.567 V and LFP with 3.428 V vs. Li / Li^+ are suggested and successfully used for impedance measurements [59, 115]. But due to the high availability, using lithium metal is the preferred approach used in literature. The formation of a solid electrolyte interphase on the metal surface is reported to be self-limiting and stable over time [30]. A special focus is set on the position of the reference electrode, as it highly affects the reliability of the measurements [188, 205] by disturbing the ionic pathway.

a Designed hardware

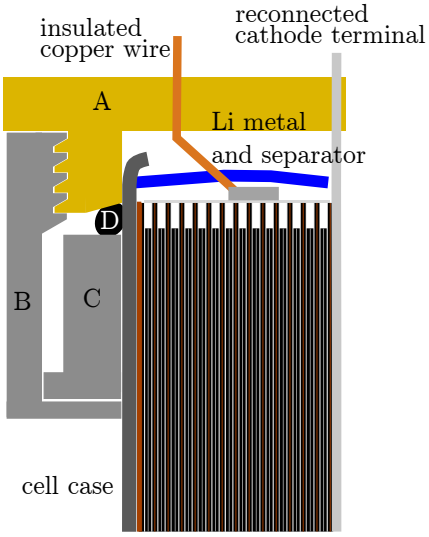

b Schematic drawing of the reference electrode insertion

Figure 3.12 – Picture a and schematic drawing b of the designed lock system to access and operate 18650 cells after opening

Modification procedure and reliability

When including lithium metal reference electrodes in commercials cells, special focus needs to be set on the integrity of the electrochemical system. To allow for a stable long-term behaviour of the cell, the reference electrode needs to be inserted directly during manufacturing [146] or a proper sealing after modification is crucial [136]. Due to the limited space and access possibilities, the size of the reference electrode should be as small as possible to avoid any interaction with the electric fields and the diffusion path in the cell. The introduction into commercial 18650 cells via the bottom of the cell requires additional effort and allows to operate the cell only under argon atmosphere [19].

Inserting a reference electrode in the middle of the cell was performed by Wu and co-workers [225] but is not possible for commercial cells with a steel rod in the cell centre as the ionic pathway is interrupted due to the lack of electrolyte. The free space in 18650 cells is limited and the small gap between the jelly roll and top part of the cell is the most promising place to fit one or two reference electrodes into a cell [145]. To properly seal the cell after modification, a new lock system was manufactured by the affiliated workshop of TUM CREATE Ltd. The system consists of four parts as shown in Fig. 3.12a.

The top part (A) is manufactured of Nylon, a non-conductive and electrochemically stable polymer. It has an inner diameter of 18 mm and will finally operate as a new cap of the 18650 cell. Three feedthroughs allow to access the positive current collector, a reference electrode and if desirable a second reference electrode or a thermocouple. The two steel pieces of the bottom part (B, C) are counter screwed against the top part. A Kalrez O-ring (DuPont / USA) (D) is pinched between cell, top and bottom part and seals the inserted cell as schematically illustrated in Fig. 3.12b.

For modification purposes, the top part of the cell is removed in an argon filled

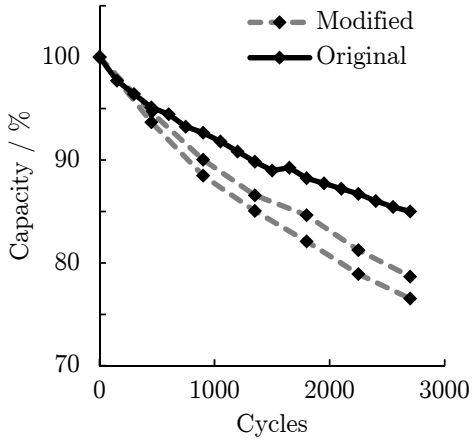

Figure 3.13 – 1C cycling performance comparison between original cells and cells after replacing the cap with a lock system at 25 °C

glove-box and the positive terminal is cut-off. The plastic spacer is lifted and a copper wire with an attached piece of lithium metal (2x 1 mm^2) is inserted. To prevent any risk of short-circuits, an additional layer of a 25 µm thick Celgard separator is placed between the jelly roll and the lithium metal. The disconnected cathode terminal is spot-welded to a new nickel tab and fed through the top part of the lock system. The feedthroughs are finally sealed with a two-component epoxy glue.

The advantages of the system are the mechanical stability, flexibility and re-usability. Due to the usage of chemically inert materials, the impact on the performance of the cell is reduced. To compare the long-term performance of the modified test cells using the lock system with unmodified cells, additional 1C cycle test as described in Sec. 6.1.1 with two cells were performed at 25 °C. Fig. 3.13 illustrates the comparison of the capacity fade for 2700 cycles. After 500 cycles, the capacity fade of the modified cells increases compared to the unmodified cells and follows are more linear decay. The additional capacity fade is 2 % after 1000 cycles and 4.5 % after 2000 cycles with a remaining capacity of 78.7 and 76.5 % after 2700 cycles.

Possible sources of the accelerated fading are the connection of the cathode tab, which does not meet industrial standards as it is spot-welded with a modified welding machine inside the glove-box. As a consequence, an increasing voltage drop due to the higher contact resistance and a local increase in temperature is expected. Despite the measured increase in degradation, the system demonstrated to be electrochemically stable and impermeable for water and oxygen.

Due to variations in the diameter of the commercial cells, three different types of lock-systems with a diameter of 18, 18.2 and 18.4 mm were manufactured. The ductility of the O-ring allowed the usage of the same size for all systems.

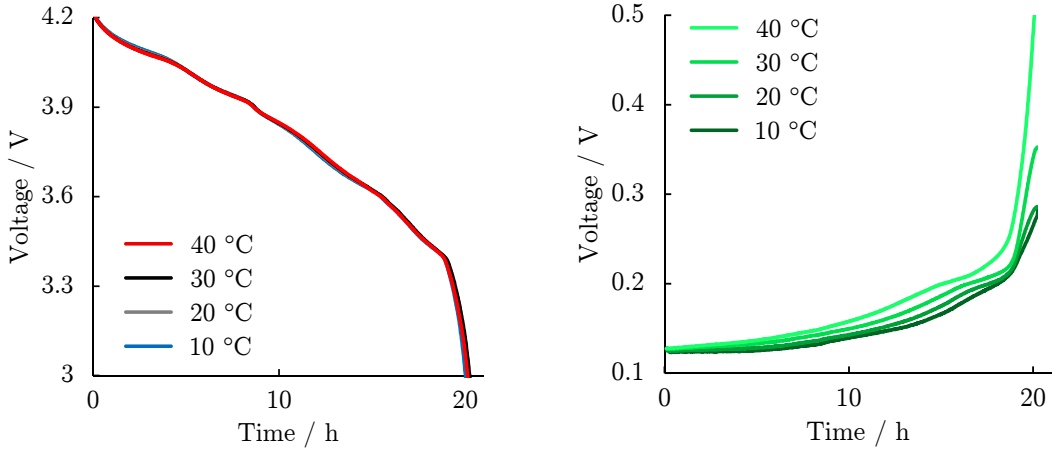

a Cell voltage **b** Anode half-cell voltage

Figure 3.14 – Full-cell a and anode b voltage of cell A during 0.05C discharge at different temperatures

Temperature dependency

For testing the temperature stability of the system, the cell was fully charged at 25 °C with a CC-CV protocol and a current of 0.1C to set a reproducible reference point. Subsequently, the cell was heated or cooled to the desired temperature and discharged and charged with a current of C/20. Fig. 3.14 illustrates the voltage profile for cell A a and the respective graphite anode versus Li/Li^+ b during the discharging process for 10, 20, 30 and 40 °C.

The full-cell shows a lower overpotential during the discharge process due to enhanced lithium-ion transport in the electrolyte and solid state diffusion in the active material with increasing temperature [156, 210]. The low current rate of 0.05C resulted in a similar capacity for all tests, whereas the capacity at 40 °C is only 0.7 % higher as for the charge at 10 °C. With the same degree of lithiation for both electrodes at the beginning of the charging process, the same values for the anode potential are expected, but not observed. The anode voltage reaches as high as 530 mV for 40 °C and only 232 mV for 10 °C. Possible reasons for the difference are: I) A temperature dependency of concentration gradients close to the reference electrode. With a capacity of 2 mAh and a size of only 1 mm^2, the present reference electrode causes a change in the concentration gradient within the electrolyte [54] II) Formation of an additional surface layer on the lithium metal, triggered by the enhanced reaction mechanisms at higher temperature, leading to a falsification of the observed potential III) Changes in the current density distribution in the cell due to the increasing current collector resistance for higher temperatures and a local measurement of the anode potential IV) Entropic contributions during the low state of charge as discussed in Sec. 3.5.

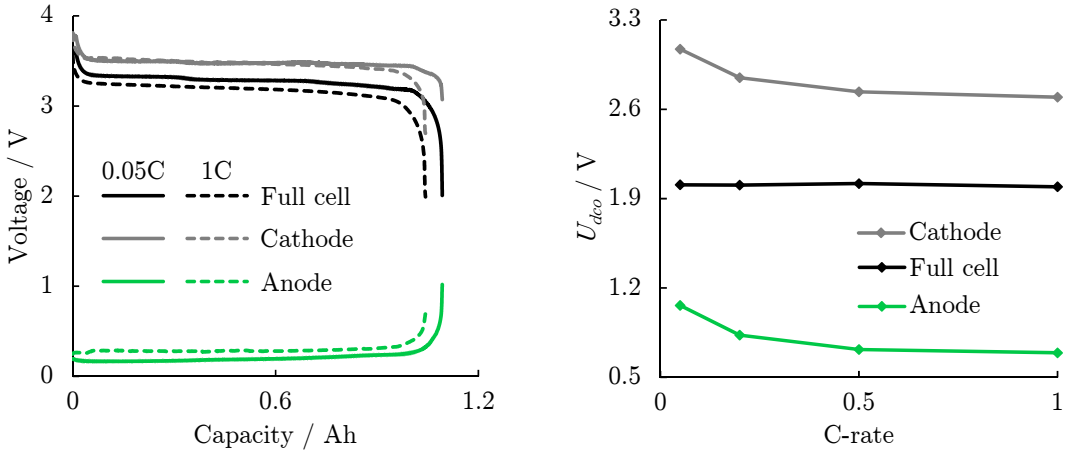

a Voltage profiles for 0.05 and 1C

b U_{dco} for different C-rates

Figure 3.15 – Reference electrode measurements a and cut-off voltages U_{dco} b of cell C at 25 °C for various discharge current rate

Current dependency

To verify the stability of the reference electrode and the system, the different cells were cycled under various conditions. Beside temperature variations, the impact of different discharge currents was tested and varied between 0.05C (55 mA) and 1C (1.1 A). Cell C was charged with a CC-CV protocol (0.2C, 15 min CV) subsequently to the discharge to allow for a comparable reference point and rested for 60 min between each cycle. The cell was discharged until the cut-off voltage U_{dco} of 2 V is reached. Fig. 3.15a shows the voltage profiles of the full-cell as well as the anode and cathode versus the lithium reference electrode during the discharge.

During the 1C discharge, the overpotential of the cell increased and it is observed that it is dominated by the overpotential on the anode side. For the 0.05C discharge, both anode and cathode contribute equally to achieving the discharge cut-off voltage. The final capacity achieved at 1C is 4.7 % lower compared to the 0.05C discharge. Based on the measurements, speculations regarding the originating effects can be made. One possible explanation could be that the LFP cathode is the limiting electrode with a steep voltage decrease towards the end of the discharge, indicating a full lithiation of the particles at the electrode/separator interface. The diffusion coefficient for lithium-ions in LFP for high degrees of lithiation is reported to be $3.91 \cdot 10^{-15}$ cm^2 s^{-1} [178, 179] while the diffusion coefficient in graphite was identified to range between 10^{-9} and 10^{-10} cm^2 s^{-1} for the expected SoC [119]. The anode is fully delithiated as indicated by the steep increase towards 1 V at the end of the discharge. For low currents as 0.05C, the lithium-ion diffusion in the material is sufficient and the cathode is capable of distributing the lithium-ions within the given time. Fig. 3.15b states the final voltage values of anode and cathode versus the reference electrode for different C-rates once the full-cell achieved the discharge cut-off voltage U_{dco} of 2 V. The increase of anode potentials with decreasing C-rates is observed for all measurements and the made assumptions regarding the

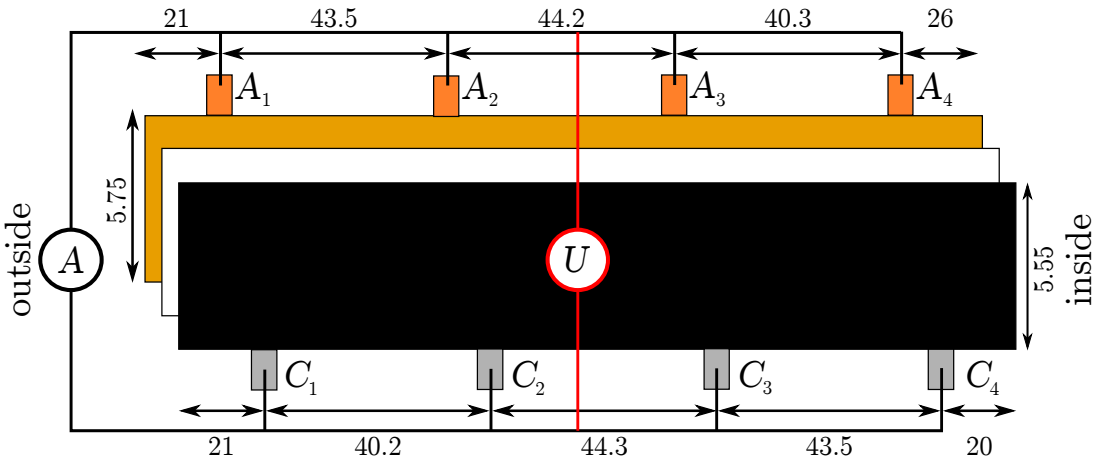

Figure 3.16 – Schematic drawing of experimental cell prior modification with the respective dimensions in cm, highlighting the four equidistant current tabs on each electrode

half-cell cut-off voltages described in Sec. 3.6.1 are confirmed.

3.6.3 Current density distribution measurements

The current density distribution in lithium-ion cells was investigated by Zhang and co-workers and large variations along the electrodes were observed, driven by the flat OCV of LFP and the different plateaus in the OCV of the graphite anode [240, 241]. The investigations were performed on a custom-made experimental pouch cell with a segmented cathode and a continuous anode, whereas the discharge current of each segment was measured by the voltage drop at a high precision shunt at each cathode segment. To gain results of cylindrical cells with their unique geometric properties, a simplified and cheaper approach was applied by modifying suitable cylindrical 26650 cells. The published approach [153] inspired other groups to apply the modification process for further studies [217].

Modification procedure

Commercially available 26650 LFP / graphite cells with a nominal capacity of 2.5 Ah and an average discharge voltage of 3.3 V were modified. The anode has a length of 175 cm and the cathode 169 cm as illustrated in Fig. 3.16. Each electrode has four almost equidistant current collecting tabs, which are spot-welded to the current collector foil. The operation mode of the original, unmodified cell is shown in Fig. 3.16. The cell is operated via the normal cell terminal, whereas the applied current is equally distributed along the four current tabs on each electrode. The measured cell voltage is the average cell voltage at the four different positions.

Opening the cell revealed the four current tabs on each electrode. In Fig. 3.17, pictures of the opened cell with the current tabs at the anode a and cathode side b are shown. The cells were opened in a discharged state in a MBraun glove-box under argon environment. The four current tabs on each electrode were separated and the caps removed. The separated tabs were extended by additional spot-welded nickel tabs (3 cm length, 4 mm

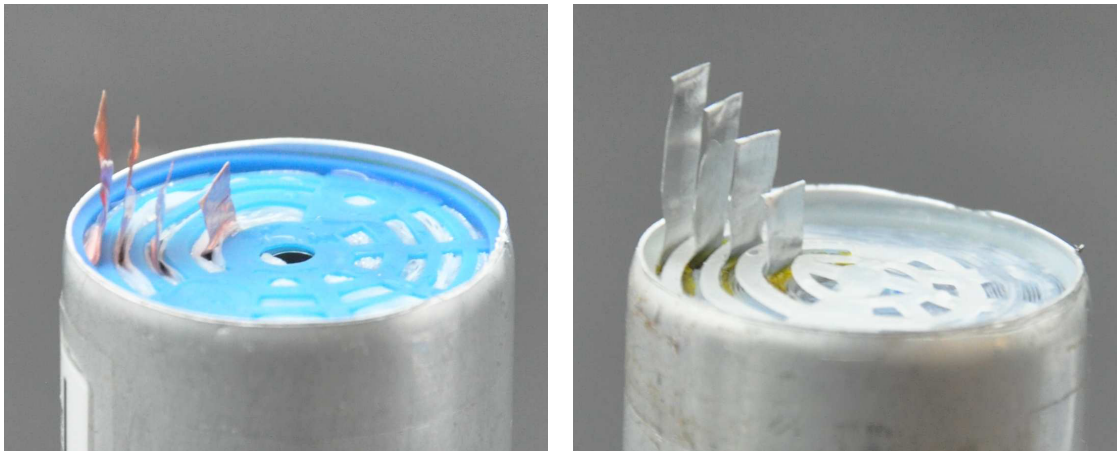

a Anode with four current tabs **b** Cathode with four current tabs

Figure 3.17 – Opened anode and cathode side during the modification process of commercial 26650 cylindrical cells

width, 80 µm thickness) using a modified MSK-310 compact AC pulse spot welder from MTI Corporation. Subsequently, the cells were resealed with custom-made polymer caps, made out of 6 mm Poly(methyl methacrylate) (PMMA). A schematic drawing is shown in Fig. 3.18a. The nickel tabs are fed through the polymer cap and fixed with epoxy glue. The modification leads to the possibility to operate the cell at various conditions, applying the current at a combination of current tabs at different positions along the electrode. The terminal T_{mn} is defined by the used anode A_{m} and cathode tab C_{n} with m, n $\in \{1;4\}$. The resulting terminal voltage and impedance is denoted as U_{Tmn} and Z_{Tmn}, respectively. Terminal T_{11} is the outermost, T_{44} the innermost tab configuration in the cylindrical cell.

Stability and reproducibility

The stability of the system was tested by performing 1C charge-discharge tests using all four connected current tabs on each side. The gained data were compared with ageing tests performed on cells without any modification. A 60 min charging scheme was applied, whereas the U_{cco} was set to be 3.6 V. If the CC charging was finalised before the time limit was reached, the charging continued as a CV charging scheme for the rest of the time. To discharge the cell, a 1C current was applied until $U_{dco} = 2$ V was reached. The testing of the modified cell was performed until 1000 cycles were completed. The resulting data are illustrated in Fig. 3.18b. As the tests with the unmodified cells were only considered as a reference, the tests were only performed as long as necessary, until significant differences were observable. During the first 200 cycles, the difference in capacity fade showed to be 0.23 %. After 480 cycles, the difference increased to 1.86 % (modified cell: 3.52 %, unmodified cells: 1.66 %). The overall capacity fade at the end of the test procedure was 10.62 %. All tests in this work were performed within the first 20 cycles of a cell's lifetime. Even though the degradation of the modified cell was comparably faster, an excellent long-term performance was achieved. Similar to the test

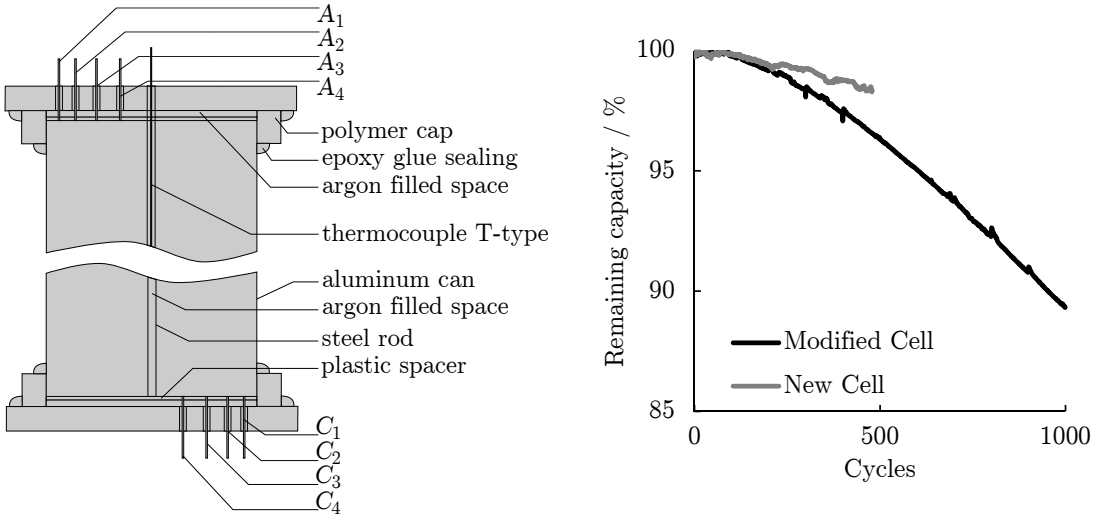

a Set-up of modified cell

b Comparison of capacity fade of modified and unmodified cell

Figure 3.18 – Schematic drawing of the experimental cell after modification and the capacity fade during 1C - 1C full cycles at 25 °C

cells in Sec. 3.6.2, an inhomogeneous current distribution due to the variation in the contact resistance and small amounts of side reactions due to the ingress of moisture and oxygen might be the explanation for the faster capacity decay.

Additionally, each cell was tested before and after the modification process at an ambient temperature of 22 °C by discharging the cell at 0.5C, 1C, and 2C. Between each discharge step, the cell was given a 2 h relaxation period and was charged with a CC-CV charging protocol (0.2C CC, 3.6 V CV, 0.01C current cut-off). All cycling experiments were conducted with a BaSyTec CTS to cycle the cells and an Agilent 39720 with a 20 channel multiplexer for supplementary voltage and temperature measurements. The cells were contacted with a spring loaded kelvin probe holder prior modification and 2 mm banana plugs, soldered on the nickel tabs after modification. Tbl. 3.3 summarises the resulting discharge capacities C_{mod} and C_{unmod} and the respective average discharge voltages $\bar{U}_{\text{mod}}$ and $\bar{U}_{\text{unmod}}$ for the three different discharge rates.

The cell is designed for high power applications and is able to carry constant discharge currents of up to 70 A and maximum current pulses of 120 A. The discharge capacities remain nearly constant with a small decrease by 0.6 % from 0.5C to 2C and the average discharge voltage decreases from 3.13 V to 2.95 V. After the modification, terminal T_{11} is used for the characterisation, hence the current flowing over this single current tab is multiplied by four. As a result, the average discharge voltage drops to 3.08 V for 0.5 and 2.76 V for 2C. The increase in the overpotential can be attributed to the additional contact resistances from the welding and soldering points, the connection via 2 mm banana plugs and the unsymmetrical utilisation of the current collector by applying the current at the outermost terminal only. The difference in the voltage curves for 0.5C and 2C is displayed in Fig. 3.19a. Towards the end of the discharge, the unsymmetrical utilisation becomes more dominant, causing a further increase in overpotential. Despite

Table 3.3 – Performance of an experimental cell before and after modification

C-rate	0.5C	1C	2C
C_{unmod} / Ah	2.6174	2.6101	2.6021
C_{mod} / Ah	2.6321	2.6120	2.5949
ΔC / % $_{C_{\text{unmod}} = 100\%}$	0.56	0.07	-0.28
$\bar{U}_{\text{unmod}}$ / V	3.1335	3.0504	2.9523
$\bar{U}_{\text{mod}}$ / V	3.0815	2.9498	2.7599
$\Delta\bar{U}$ / mV	52.0	100.6	192.4

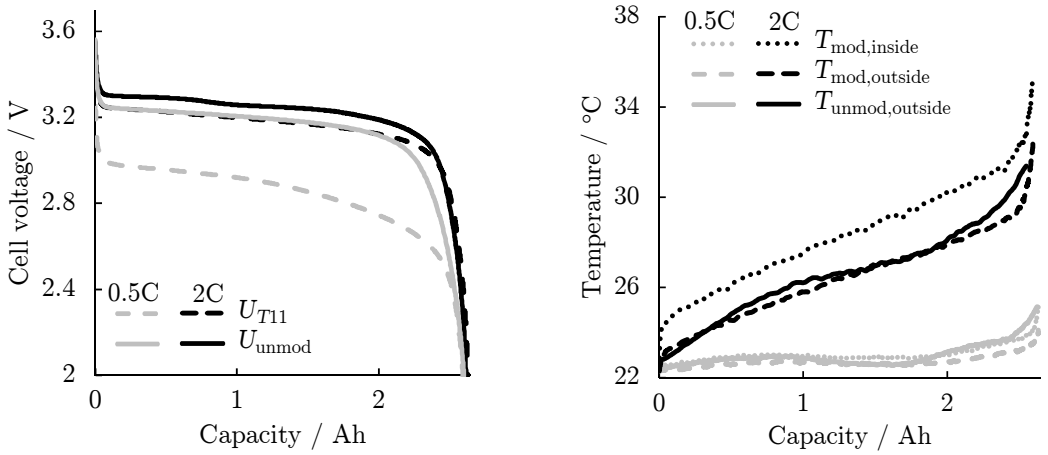

a Voltage

b Temperature

Figure 3.19 – Cell voltage and temperature before and after modification for different discharge rates at 25 °C

the increase in overpotential, the extractable capacity of the cell remains constant, whereas the differences at higher currents become smaller due to either a slight increase of the ambient temperature during or a longer relaxation time before testing

Beside the electrical parameters, the thermal properties of the cell were investigated, as a change in the temperature distribution in the cell will have a significant effect on the electrochemical properties. The possible access during the modification process allowed for the insertion of a thermocouple into the steel rod at the cell's centre as shown in Fig. 3.18a. In Fig. 3.19b the temperature of the cell surface for the modified and unmodified cell are displayed.

For a discharge of 0.5C, only small variations in the thermal properties are measurable and the self-cooling effect due to entropic effects in the graphite anode [167] in the range between 1 Ah and 2 Ah occurs at both measurements. An increase in discharge current to 2C leads to a surface temperature increase of up to 32 °C at the end of the discharge for the modified cell and up to 31 °C for the unmodified cell. While the temperature of the unmodified cell still features the entropic effect, it is vanished for the modified cell. It is assumed that the separation of the current tabs and the removal of the metal cap on both sides of the cell reduced the thermal conductivity, leading to a reduction of heat transport from the inside of the cell towards the cell surface. Furthermore, the polymer

caps added thermal capacity to the cell.

This modification procedure is used in this work to investigate variations in the current density distribution and the resulting SoC inhomogeneities. The obtained data are used to analyse equalisation processes of lithium-ion concentration along the electrodes which could lead to a reduced accuracy during thermodynamic measurements (Sec. 5.1.1) as well as understanding the impact of cell geometry on the AC current distribution during impedance measurements and the resulting spectra (Sec. 4.2).

Chapter 4

Electrochemical Impedance Spectroscopy

In literature, electrochemical impedance spectroscopy (EIS) is one of the most common characterisation techniques to investigate the electrochemical performance of lithium-ion cells. It is further used as a diagnostic tool to track the impact of degradation on the performance and to validate the cell's inner resistance [133]. Still, the direct correlation between the interpretation of measured data and their physical origins are controversially discussed in literature.

When used to track changes in dynamic processes during the cell's degradation [77, 93, 138, 196, 197, 198], an important prerequisite is the assumption that the degradation inside the cell is a constant process, occurring homogeneously along the electrodes. But as presented in various studies, degradation is highly influenced by the mode of operation and the resulting variations in current density distribution. The accompanying inhomogeneous temperature distribution leads to non-uniform passivation due to variations in the SEI thickness [33, 110, 157] and areas where lithium plating occurs [31, 214, 253].

Due to the importance of EIS measurements to investigate electrochemical systems, the method was applied during the degradation study and the measurements are discussed in Sec. 6.2. The focus of this chapter is to validate the applicability of the method and to scrutinise the interpretability of the results. As the current developments yield to cells with larger size and increasing energy content, the current density distribution within a cell becomes more important. The sensitivity of EIS spectra on various external parameters in complex systems as cylindrical cells is investigated. The cell design, cell temperature and excitation frequency are varied to gain a comprehensive understanding of the evoked electrode area and the resulting current density distribution is analysed by means of local potential measurements. Findings of the following section were partially published in [65], [66], [151] and [153].

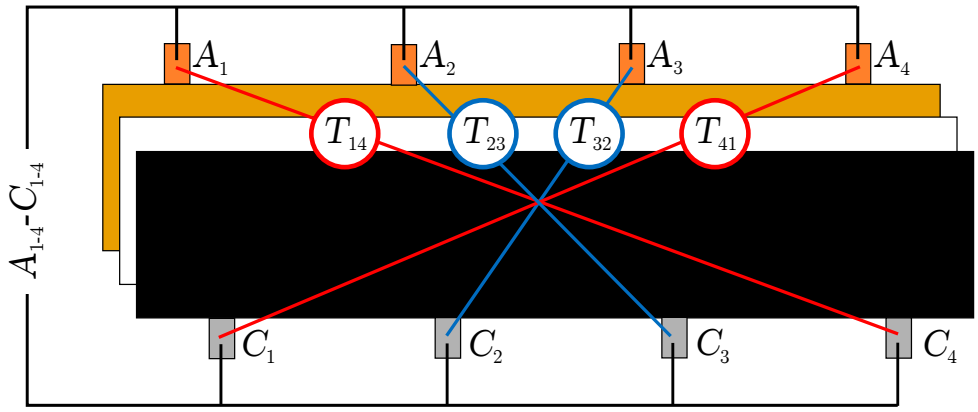

Figure 4.1 – Schematic drawing of the cell and the tab alignment used for the measurements shown in Fig. 4.2

4.1 Influences on electrochemical impedance spectroscopy

The impedance measurements in this part of the study were conducted on a Bio-Logic SAS VMP-3 with excitation currents between 30 mA and 200 mA. The applied frequencies ranged from 100 mHz to 10 kHz. For a homogeneous temperature distribution, the cell was placed 2 h prior the measurement into an ESPEC climate chamber. Between each change of operating tab pattern, a rest period of 10 min was maintained to eliminate possible temperature variations. With the modification process, significant changes on the cell housing and the possibilities to connect the cells were made. The exposure of an electrochemical system to the environment of the argon filled glove-box always bears the risk of contamination or electrolyte evaporation, affecting the performance of the cell. To guarantee reproducible measurements which allow for a meaningful interpretation of the data, preliminary tests were performed. Beside the long-term cycling test as shown in Sec. 3.6.3, the impact of the modification process on impedance measurements was tested. Fig. 4.1 gives a schematic overview of the cell and illustrates the tab alignment used for the measurements as presented in Fig. 4.2.

In Fig. 4.2a, the Nyquist plots of a modified and unmodified cell are compared. The minor differences in the data suggest that no significant impact on the electrochemical performance of the cell was provoked by the modification process. The additional contact resistances at the solder and welding points and the change in connecting the cell to the measurement system cause an increase in $Z'(\omega)$, resulting in a shift in the Nyquist diagram along the x-axis and the small differences between the contact resistances will lead to a small variation in the current density [151].

Fig. 4.2b and c illustrate the Nyquist diagram of two different operation modes. In both cases, one anode and one cathode current tab were used to apply the excitation current. To evaluate the current path dependency and the impact of the two different current collectors, the measurements were performed in two arrangements, whereas the respective operation mode was mirrored (e.g. $A_1 - C_4$ to $A_4 - C_1$). Despite small variation in the contact resistance, measurements show no impact of the current collector.

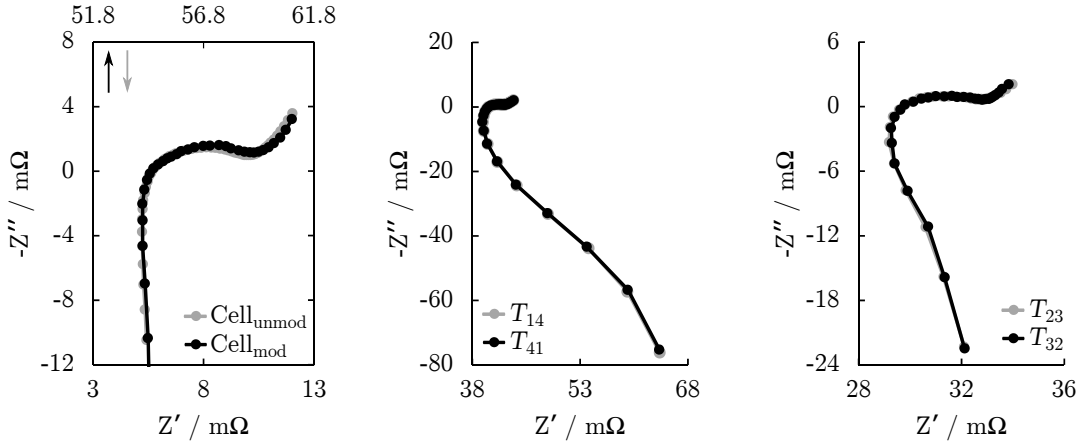

a Nyquist plot for modified and unmodified cell **b** Nyquist plot for T_{14} and T_{41} **c** Nyquist plot for T_{23} and T_{32}

Figure 4.2 – Nyquist plots of symmetrical impedance measurements

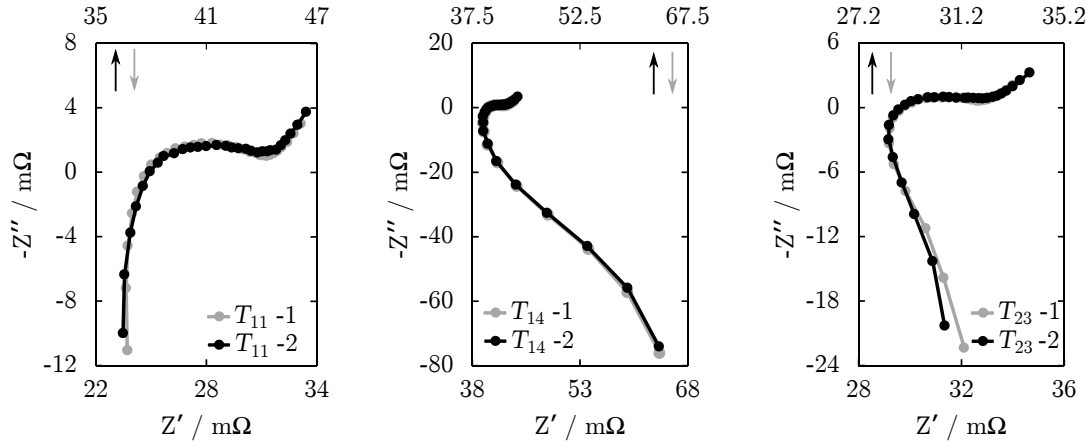

a Nyquist plot for T_{11} **b** Nyquist plot for T_{14} **c** Nyquist plot for T_{23}

Figure 4.3 – Comparison of impedance data of two modified cells for different operation modes

This is confirmed by measuring the thickness of the current collectors (CC_{Anode}: 13 µm, $CC_{Cathode}$: 20 µm) where the ratio in the thickness equalises the difference in the specific resistance of the material ($\rho_{Cu} = 1.72 \cdot 10^{-2}\,\Omega\text{mm}^2\,\text{m}^{-2}$, $\rho_{Al} = 2.65 \cdot 10^{-2}\,\Omega\text{mm}^2\,\text{m}^{-2}$). Even though all possible tab patterns were tested, due to the identical behaviour only selected data are shown.

Fig. 4.3a - c illustrate the difference between two modified cells, measured under various tab arrangements. While the values for $Z''(\omega)$ are identical, a constant shift in $Z'(\omega)$ is measured, indicating a variation in the previously mentioned contact resistances at the current taps.

4.2 Cell design

Three groups with three or four different tab pattern each are discussed. For the first group (Group I, Fig. 4.4) the current was applied at each anode and the respective opposite cathode tab, denoted as terminal T_{xx}. As a result, the distance between each current tab was as short as possible and remained nearly constant but the point of access moves from the outermost terminal T_{11} ($A_1 - C_1$) to the innermost terminal T_{44} ($A_4 - C_4$). For measurements of the second group (Group II, Fig. 4.5), a cathode tab and the next anode tab were used throughout the cell. Therefore, the distance between the current tabs is hold constant at approximately 42 cm, but the number of windings included in the current path increase and the area closer to the cell centre is utilised. The third set (Fig. Group III, 4.6) uses the same anode tab (A_1) but the cathode tab is varied from C_1 to C_4, changing the current path throughout the cell significantly by prolonging the current path as well as increasing the number of winding in between.

4.2.1 Group I

In Fig. 4.4a the operation modes of the measurements are schematically shown. In the Nyquist plot in Fig. 4.4b the similarity of the spectra of all four measurements for the high frequency region above 1000 Hz can be observed. For lower frequencies, Z' increases significantly when the outermost (T_{11}) and innermost (T_{44}) tabs are used.

The usage of terminals at the ends of the electrode results in an asymmetrical current density distribution, observable in a higher potential drop and higher impedance respectively. Therefore, due to their geometric similarity, measurements for T_{22} and T_{33} on one hand as well as measurements on T_{11} and T_{44} on the other hand exhibit similar spectra. Additionally, a further increase for the current terminal closer to cell centre (T_{33} and T_{44} respectively) is observed. The dominating effects in the frequency range between 10 Hz and 0.1 Hz are the charge transfer and the diffusive behaviour of the lithium-ions in the bulk material as schematically shown in Fig. 3.4a. The cell is assumed to be in an equilibrated state, where no temperature gradient and no local SoC inhomogeneities are present. It is concluded that the kinetic properties of the electrolyte and the bulk material depend on the position of the cell. As a first approach, the change in coating thickness is considered, when the electrodes are rolled. With a coating thickness $d_{electrode+} = 63\,\mu m$, an outer radius $r_o = 12.5\,mm$, inner radius $r_i = 2\,mm$ a change in thickness can be calculated to be a 1.5 % increase for the inner and 1.3 % decrease for the outer layer of the electrode coating. As the variation is larger than this small change, additional sources for the difference in kinetic and transport properties need to be found. Simulations [144] and measurements [219] suggest a pressure increase towards the cell centre, which would lead to a reduced amount of electrolyte towards the cell centre. Changes in the kinetic bulk properties as well as higher separator tortuosity due to increasing pressure were reported by Venugopal et al.[212] and Cannarella et al.[34], resulting in a higher lithium-ion diffusion path and a higher impedance. The findings of Gnanaraj et al. [74] and Barai et al. [17] indicate an impedance increase with higher pressure and match well with the measured data.

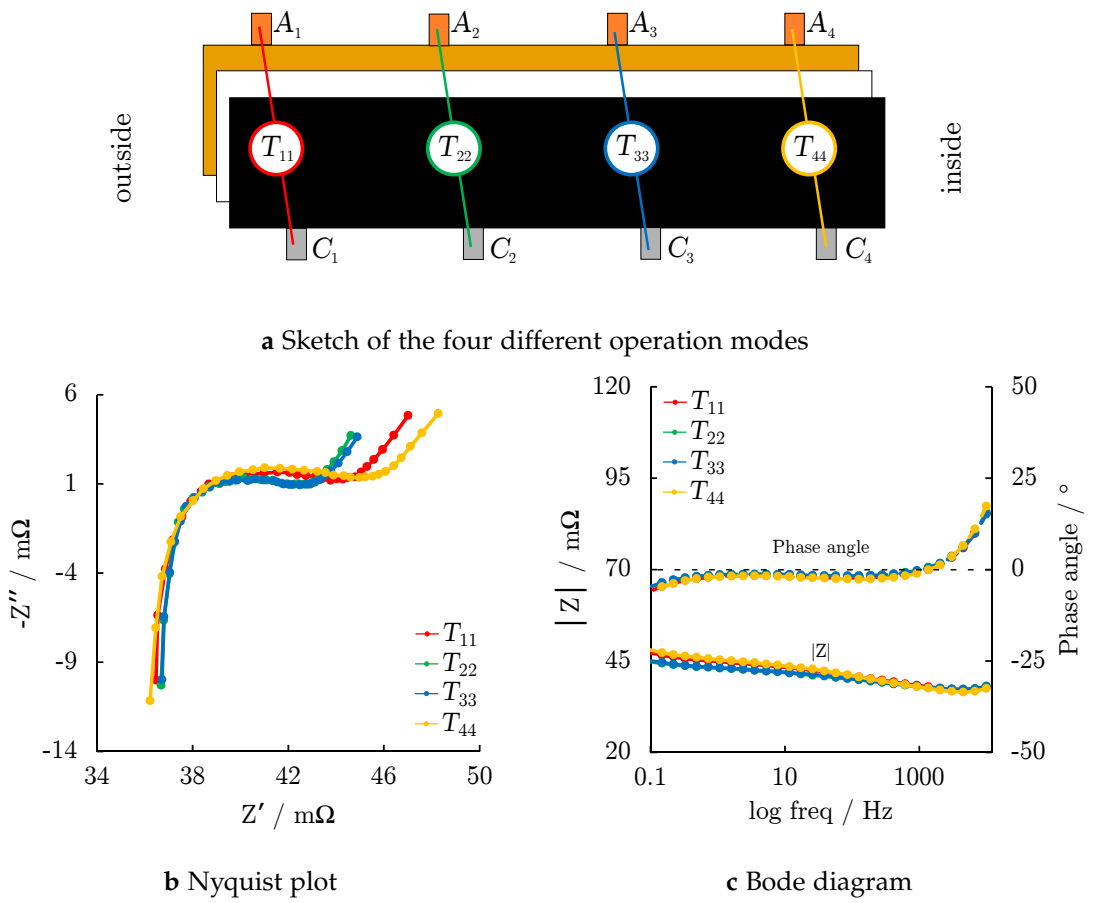

a Sketch of the four different operation modes

b Nyquist plot

c Bode diagram

Figure 4.4 – Impedance data for measurements at $T_{xx}(A_x - C_x)$

All four measurements show the same capacitive or inductive behaviour as indicated in by the Bode diagram, shown in Fig. 4.4c. The phase angle is independent from the used terminal position and the cell changes at approximately 1350 Hz from inductive to capacitive behaviour. The magnitudes $|Z_{T11}|$ and $|Z_{T44}|$ increase towards lower frequencies due to the higher values of Z'_{T11} and Z'_{T44}.

4.2.2 Group II

The second group consists of three different measurements, whereas one cathode tab and the next inner anode tab were used to apply the current. The general form is described as $T_{(x+1)x}$ (e.g. $A_2 - C_1$). Fig. 4.5 illustrates schematically the operation mode a and the Nyquist plot b and the Bode diagram c are shown. The distance between the current tabs was kept constant with approximately 42 cm for all three measurements, but the number of windings within the current path increases, as the used tab configuration gets closer to the cell centre.

The increase in $Z'(\omega)$ due to a pressure increase towards the cell centre as suggested in the previous section matches well with the data as shown. In the frequency range above 1500 Hz, the values for Z'' increases while Z' decreases as displayed in the Nyquist plot

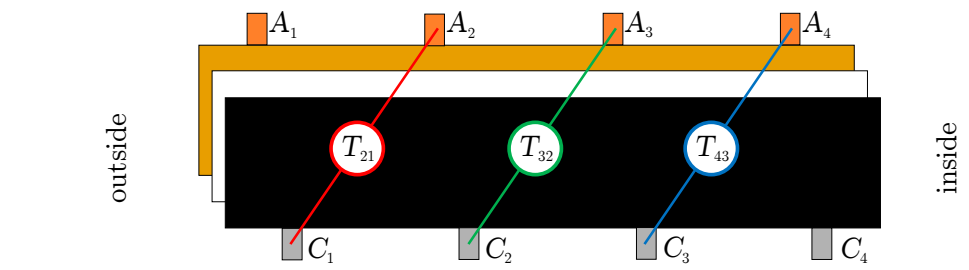

a Sketch of the three different operation modes

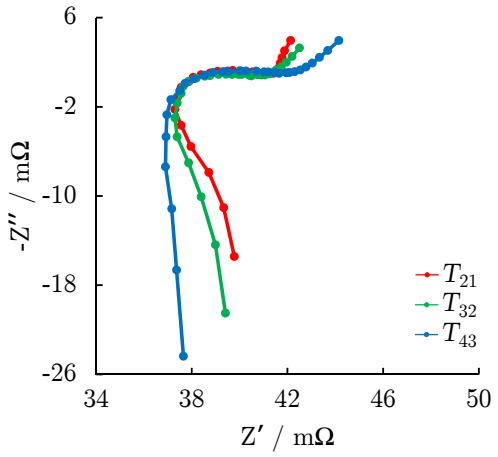

b Nyquist plot

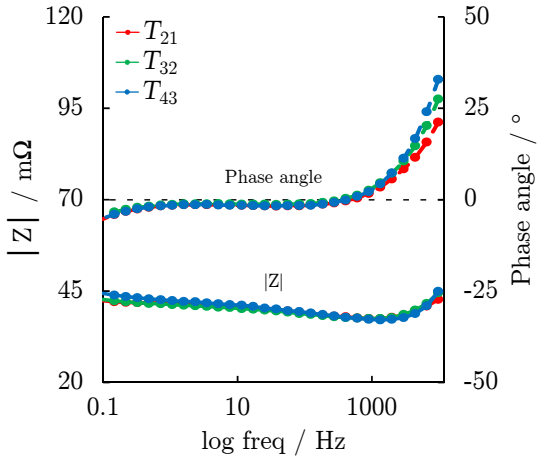

c Bode diagram

Figure 4.5 – Impedance data for measurements at $T_{x+1x}(A_{x+1} - C_x)$

b. In the same frequency range, a variation in the phase angle ϕ between the different measurements is observed but merges for lower frequencies. The work by Reimers [161, 162] describes the correlation of the geometric design of a cell and the effect on the inductive behaviour of the cell. With the adapted equation for the Archimedes' Spiral for cylindrical cells [80, 223], the number of windings can be calculated by

$$\Theta(\xi) \approx \frac{-r_0 + \sqrt{r_0^2 + \frac{D\xi}{\pi}}}{\frac{D\xi}{2\pi}} \tag{4.1}$$

where the radius of the cell's centre pin is given by $r_0 = 1.5\,\text{mm}$. ξ is the longitudinal distance between cell centre and the used current tab as displayed in Fig. 3.16. The electrode stack thickness $D = 0.279\,\text{mm}$ consists of thickness of the electrode coatings ($d_{electrode+}, d_{electrode-}$), current collectors ($d_{cc+} + d_{cc-}$) and separator ($d_{separator}$).

The number of electrode windings between the respective tabs was calculated to be 6.5 windings between C_1 and A_2, 8.5 between C_2 and A_3 and 12.5 between C_3 to A_4. The half winding originates from the cell design as displayed in Fig. 3.17, where the current tabs of the anode are shifted by a half a winding compared to the current tabs of the

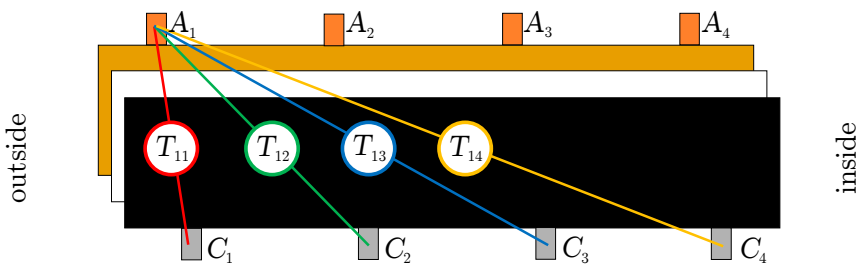

a Sketch of the four different operation modes

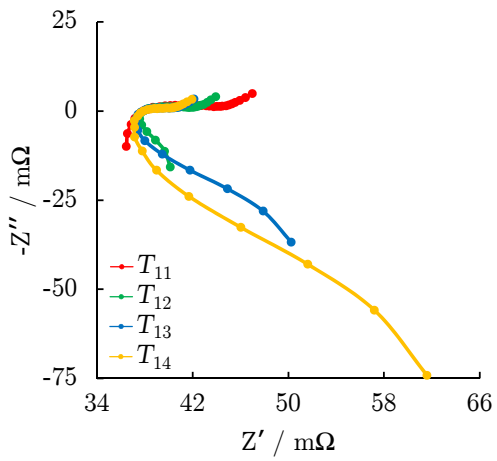

b Nyquist plot

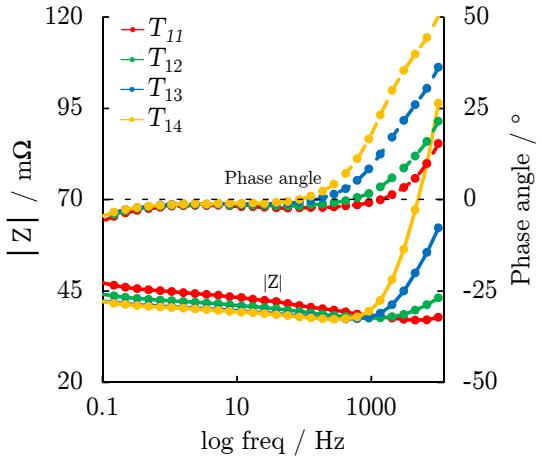

c Bode diagram

Figure 4.6 – Impedance data for measurements at $T_{1x}(A_1 - C_x)$

cathode. This suggests an inductive contribution of the current collector, depending on the average radius of the cell segment and therefore the number of traversed windings. To allow for a clearer observation of the effect, a third set of measurements is performed, maximising the difference in windings the current path.

4.2.3 Group III

For the measurements in the third group, only anode current tab A_1 was used, while the cathode current tab was varied from C_1 to C_4, as schematically displayed in Fig. 4.6a.

The Nyquist plot in Fig. 4.6b underlines the strong dependence of the spectra on the geometric design of the cell, with strong variation of $Z''(\omega)$ and $Z'(\omega)$. For the highest measured frequency of 10 kHz, Z'_{11} is only 60 % of Z'_{14} and Z''_{11} only 14 % of Z''_{14}. The threshold frequency, when the cell transits from inductive to capacitive behaviour increases with decreasing tab distance as observed in the Bode diagram in Fig. 4.6c and stated in Tbl. 4.1. The differences in the phase angle as well as $Z''(\omega)$ become smaller for frequencies below 100 Hz. In contrast, $Z'(\omega)$ increases in this frequency range for decreasing tab distance, attributed to the dominating effects of the asymmetrical current density distribution [151]. The opposite scenario with a constant current tab and varying

Table 4.1 – Position of cathode tab x with respective number of windings N_w, the distance between cathode and anode tab and the transition frequency with $\phi = 0$

C_x	N_w	Tab distance / cm	$f(\phi = 0)$ / Hz	$Z''(f = 10\,\text{kHz})$ / mΩ
1	0.5	3.6	1400	-7.3
2	6.5	43.8	500	-16.7
3	14.5	88.1	160	-36.8
4	26.5	131.6	80	-74.2

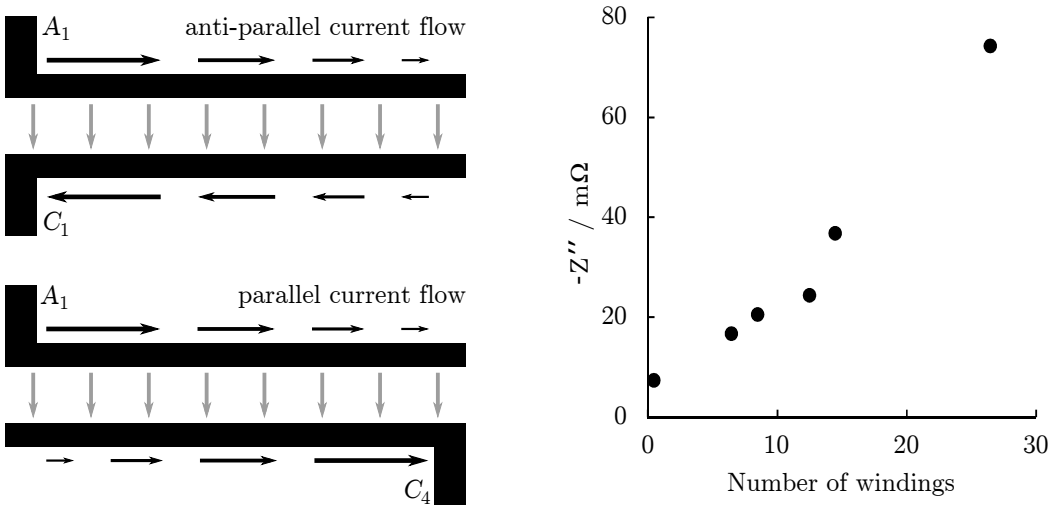

a Possible current flows

b $Z''(f = 10\,\text{kHz})$ in dependence of winding number in current path

Figure 4.7 – Effect of tap position on current flow in a spiral wound current collector

anode tab resulted in the same spectra as shown in Fig. 4.2b and will therefore not be discussed. The calculated number of windings, the distance between the tabs as well as the transition frequency is listed in Tab. 4.1.

Detailed investigations on the effect of cell geometry on the cell impedance was presented by Laman et. al, who used a spirally wound Li/MoS_2 experimental cell [116] to calculate the inductance of the electrode windings. Reimers presented a mathematical approach to calculate the potential and current distribution in cylindrical cells [161] and extend the approach with a coupled multi-physics cell model [162] focussing on the heat generation. Both predicted an increase of the cell inductance for higher excitation frequencies. Fig. 4.7 illustrates schematically the electronic current flow in the positive and negative current collector of the cylindrical cell for the tab arrangement using terminal T_{11} and terminal T_{14}.

For the first tab arrangement, both current carrying tabs are directly located next to each other, and the current path is similar to a cell in pouch cell format. For every electron participating in a charge transfer at any position of the cell, the electron is forced to flow from the outermost current tab towards the cell centre and back. As a result, the current flow is almost completely anti-parallel due to the small distance (πr_{tab})

between the two current tabs. With the usage of the cathode tabs closer to the cell centre, the tab-to-tab distance increases together with the number of winding included in the current path and the ratio of parallel and anti-parallel current flow is shifted, until only parallel current flow occurs in the tab configuration T_{14}. The number of windings within the current path and $Z''(f = 10\,\text{kHz})$ is shown in Fig. 4.7b, indicating a nearly linear correlation.

4.3 Temperature

Higher temperatures enhance the cell's kinetics and transport properties such as lower electrolyte resistance, higher diffusion coefficients in the electrolyte and active material, a lower charge transfer resistance and a lower ion transfer resistance through the solid electrolyte interphase [95, 238]. In contrast, the resistance of the current collector increases with increasing temperature due to the positive temperature coefficients of resistance for aluminium ($\alpha_{Al} = 4 \cdot 10^{-3}\,\text{K}^{-1}$) and copper ($\alpha_{Cu} = 3.93 \cdot 10^{-3}\,\text{K}^{-1}$). To investigate the superposition of these effects and to identify the effect of different temperatures on the current density distribution, an alternating current was applied at terminal T_{11} and the voltages at the terminals T_{22}, T_{33} and T_{44} were recorded. Exemplarily, the voltage responses to a 50 mA sinusoidal excitation current with 240 mHz and 167 mHz is displayed in Fig. 4.8 for 10 °C a and 40 °C b. For a clearer distinction, the voltage of each terminal was separated by 3 mV for purposes of illustration. The entropic coefficient of the cell at this SoC leads to an increase in cell voltage with increasing cell temperature. Furthermore, a reduction in the voltage amplitude is observed at higher temperatures for all local measurements.

Using these data, the amplitude of the voltage response is calculated for the last frequency applied (167 mHz) and displayed in c versus the distance to the current carrying tab. A higher cell temperature leads to a reduction in the absolute voltage amplitude. The amplitude of terminal voltage U_{T11} reduces from 2.33 mV at 10 °C to 1.54 mV at 40 °C. Normalising the voltage amplitude to $\hat{U}/\hat{U}_{max}$ as shown in Fig. 4.8d, reveals the strong non-linear temperature dependency of the current density distribution. The current collector resistance increases for both, the aluminium and copper, by approximately 12 % for a temperature increase of $\Delta T = 30\,°\text{C}$. As a consequence, the potential drop along the current collector is magnified, resulting in a fast decay of the measured voltage responses. This effect is further exaggerated by the enhanced kinetic and transport properties of the cell. As reported in literature, the ionic conductivity in the electrolyte is doubled [22] whereas the lithium-ion diffusion coefficient in LFP will increase by the factor of 20 for this temperature range [252].

4.4 Frequency

The response of a lithium-ion cell on an AC excitation current depends on the time constant distribution of the different electrochemical processes inside the cell [96, 120, 185, 213]. As discussed in the previous section, measurement equipment, geometric properties of the cell as well the tab position highly influence the response for high

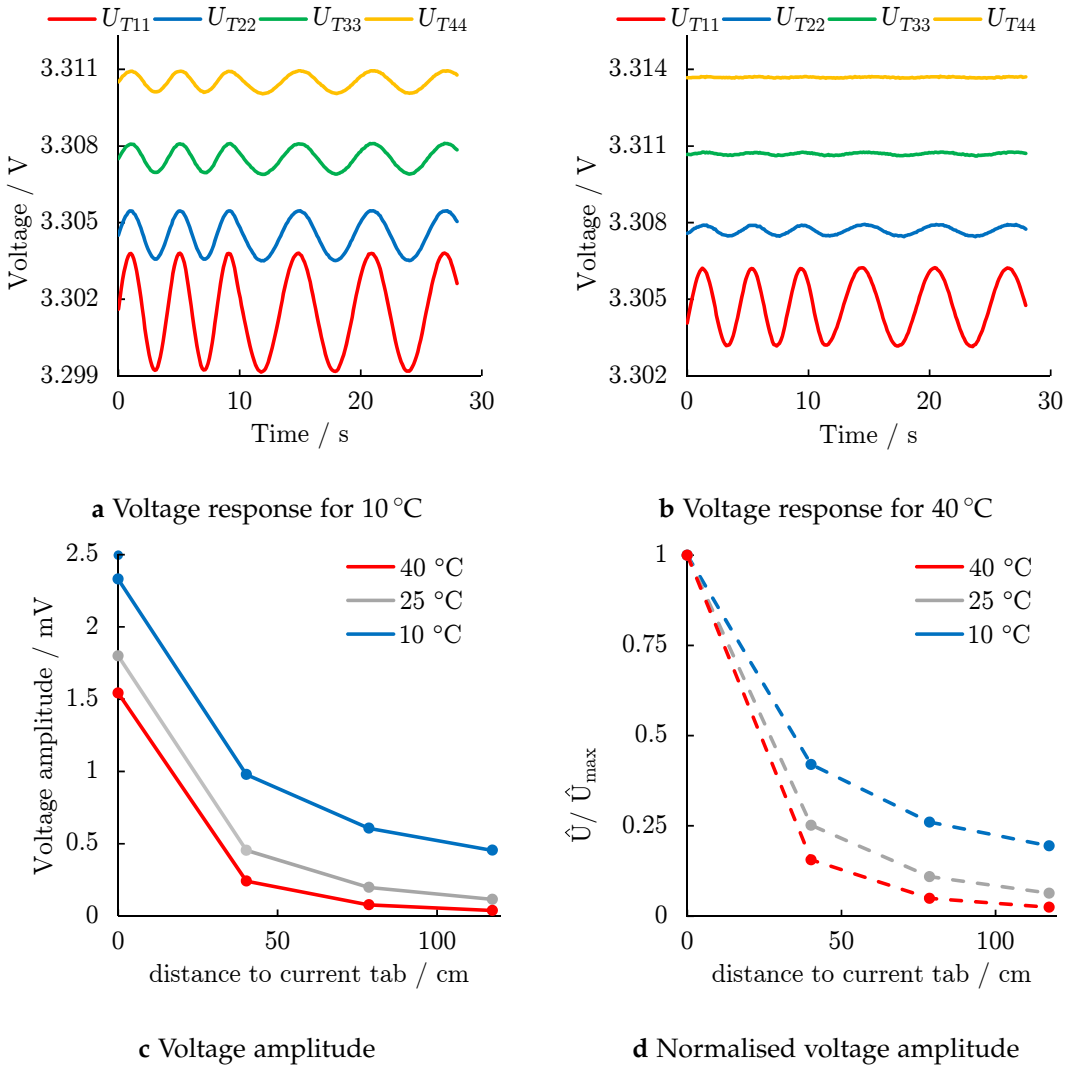

a Voltage response for 10 °C

b Voltage response for 40 °C

c Voltage amplitude

d Normalised voltage amplitude

Figure 4.8 – Voltage response to a 50 mA excitation current at different location of the electrode for 10 °C a and 40 °C b, separated by 3 mV for a clearer distinction. Resulting amplitudes $\hat{U}$ c and normalised amplitudes $\hat{U}/\hat{U}_{max}$ at $f = 167$ mHz d

frequency measurements above 1000 Hz. An additional high frequency contribution is caused by the contact resistance between the active material coating and the current collector and the accompanying polarization losses. In the mid-range frequency region between 1000 Hz and 10 Hz, the charge transfer resistance at the anode-electrolyte surface as indicated in Fig. 3.4a in Sec. 3.2 dominate the cell's response. Below these frequencies, the solid state and liquid phase diffusion of lithium-ions in the host structure of the cathode, e.g. LFP [90] and within the electrolyte are responsible for the system's response.

To investigate the frequency dependency of the current density distribution by means of local potential measurements, an excitation current of 50 mA was applied at terminal T_{11}. The voltage response was simultaneously measured at the terminals T_{11}, T_{22}, T_{33} and T_{44}, using the same Biologic VMP-3, which allows for a theoretical sampling rate of 5000 Hz with voltage precision of $\pm 5\,\mu$V. The amplitude of the measured voltage

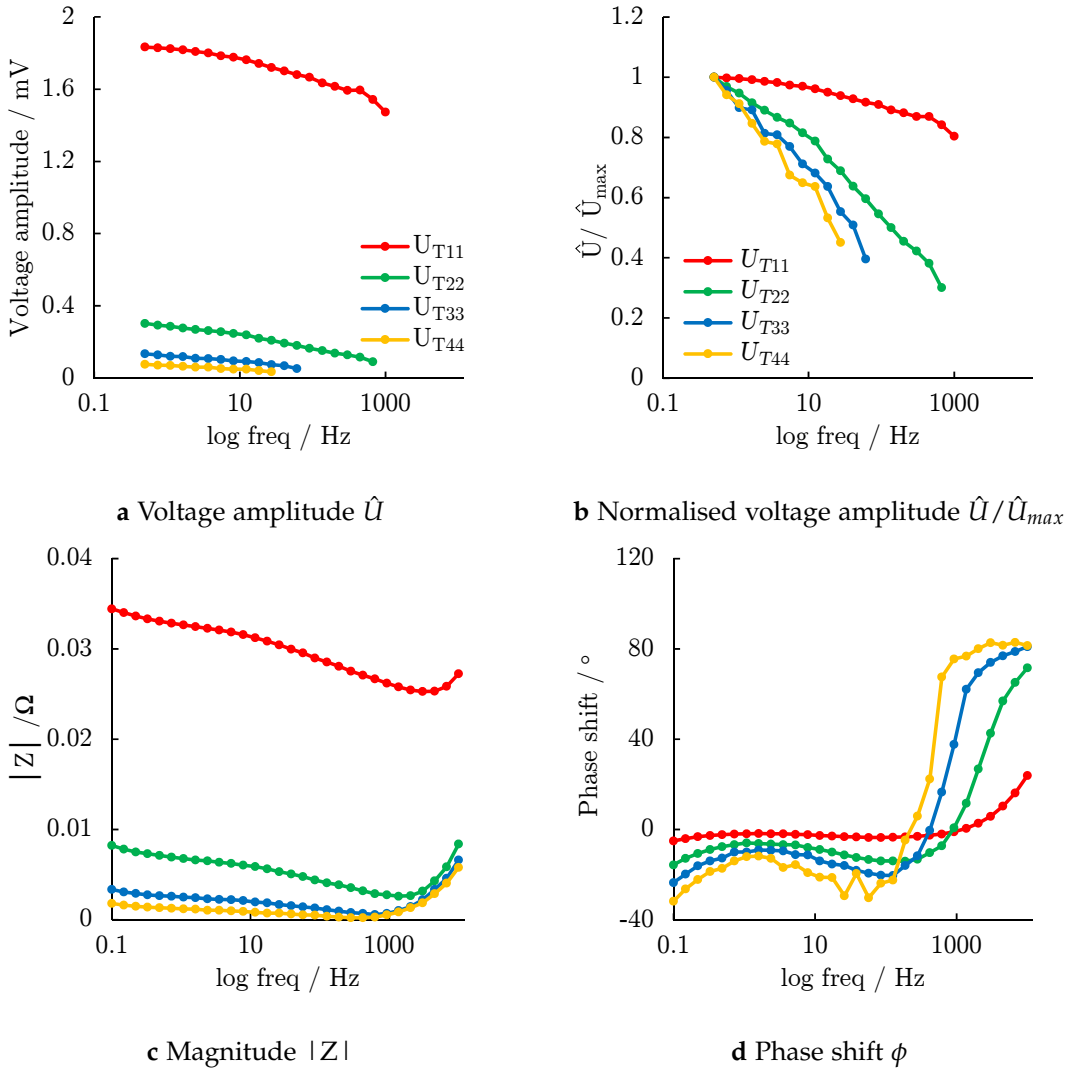

a Voltage amplitude $\hat{U}$

b Normalised voltage amplitude $\hat{U}/\hat{U}_{max}$

c Magnitude |Z|

d Phase shift ϕ

Figure 4.9 – Resulting voltage amplitude $\hat{U}$ a, normalised voltage amplitude $\hat{U}/\hat{U}_{max}$ b, magnitude |Z| c and phase shift ϕ d for an 50 mA excitation current within a frequency range between 10 kHz and 100 mHz at 25 °C

response was determined by using the curve fitting toolbox of MATLAB 2015b and the results are displayed in Fig. 4.9a.

Due to the limitations in sampling rate and accuracy in the measured amplitude, the highest reproducible frequency that allows for a reliable curve fitting is 1000 Hz at terminal T_{11} and 27 Hz at T_{44}. It is observed that the cell's local potential response clearly changes with frequency, as the amplitude decreases towards higher frequencies. Normalising the voltage amplitude as displayed in Fig. 4.9b, reveals that the amplitude does not only depend on the frequency of the excitation current but also clearly reveals non-linear attenuation along the current collector. This leads to the assumption that the area of utilised electrode material is in addition to its temperature dependency, as previously described in Sec. 4.3, also frequency dependent.

To determine the amplitude |Z| and the phase shift ϕ, a second set of measurements

was performed. Instead of measuring the cell's voltage response in the time domain with a high frequent sampling rate, the set-up's possibility of a four-terminal sensing by separating current and voltage sensing was used. Four measurements were performed at which an excitation current of 50 mA was applied at terminal T_{11} and the voltage sensing was done at T_{11}, T_{22}, T_{33} and T_{44} respectively. The amplitude $|Z|$ is calculated using the voltage response at the respective sensing terminal as illustrated in Fig. 4.9c and shows for all four terminals the same trend as the voltage amplitude measured within the time domain due to the damping of the voltage signal along the electrodes. The calculated phase shift, displayed in Fig. 4.9d shows a high similarity with the data shown in Fig. 4.6c, where the increasing number of windings in the current path lead to continuous shift of the threshold frequency and the cell's behaviour becomes inductive for a large frequency range. But in contrast to the previous set-up, the number of windings and therefore the ratio of parallel and anti-parallel current remains constant in the second measurement set-up, only the distance and number of windings to the sensing position increases. This leads to the assumption that the measurement, where the excitation current is applied at a different position than where the voltage response is measured, a sensitivity on the potential amplitude attenuation along the current collector as well as the geometric properties is observed.

4.5 Conclusion

The results shown in Sec. 4.3 indicate that a change in the cell temperature does not only change the electrochemical properties of the cell, but also changes the area of the utilised electrode when an AC current is applied. In combination with the results presented in Sec. 4.2, indicating that a change in the cell's geometric design and dimensions leads to significant changes in the resulting impedance spectra throughout the full frequency range, the importance of an accurate temperature control is emphasised and that both effects are superimposed for impedance measurements at different temperatures.

Transferring this statement towards the inhomogeneity during the ageing process of a cell, the question arises in how far the impedance spectra is superimposed by local inhomogeneities. Local variations in the cell's kinetic properties can cause the same variation in the current density distribution as a variation in the cell design. As a consequence, certain limitations to the interpretability and comparability of resulting impedance spectra of commercial cells might apply and need further investigations.

Chapter 5

Advanced Thermodynamic Measurements

This chapter addresses the various drawbacks of thermodynamic measurements (TM) and suggests possible solutions and improvements. Uncertainties affecting the electrochemical and thermal equilibrium such as local SoC and temperature inhomogeneities are investigated. To minimise the time demand of a characterisation step, the experimental set-up and test procedure were optimised to fulfil the requirements in a best possible way covering the full SoC range of a lithium-ion cell. To integrate advanced thermodynamic measurements (ATM) as a useful characterisation tool for frequent check-ups during ageing studies while maintaining a high number of data points, an approach to compensate long relaxation times is presented.

5.1 Requirement of equilibrium conditions

To achieve reliable thermodynamic measurements of lithium-ion cells, the cell needs to be in an equilibrated state, where no temperature variations or concentration gradients are present and no electrochemical side reactions occur. Due to the impossibility to achieve all requirements in a reasonable time, minimising parasitic side effects is desirable and therefore the focus is set on avoiding large lithium-ion concentration gradients within the cell.

5.1.1 State of charge

A homogeneous degree of lithiation along both electrodes is a crucial requirement for meaningful thermodynamic measurement. As highlighted in Eq. 2.36 in Sec. 3.5, the temperature dependency of the cell voltage changes non-linearly with the amount of lithium stored in the host structure and SoC inhomogeneities in the cell during measurements will lead to a falsification of the results. To avoid these uncertainties, mechanisms leading to a SoC distribution were investigated with modified cylindrical LFP/Graphite 26650 cells. A detailed overview of the cell's modification process is described in Sec. 4.2 and in *"Simulation and Measurement of Local Potentials of Modified Commercial Cylindrical Cells"* [153]. Results of this section were partially published in

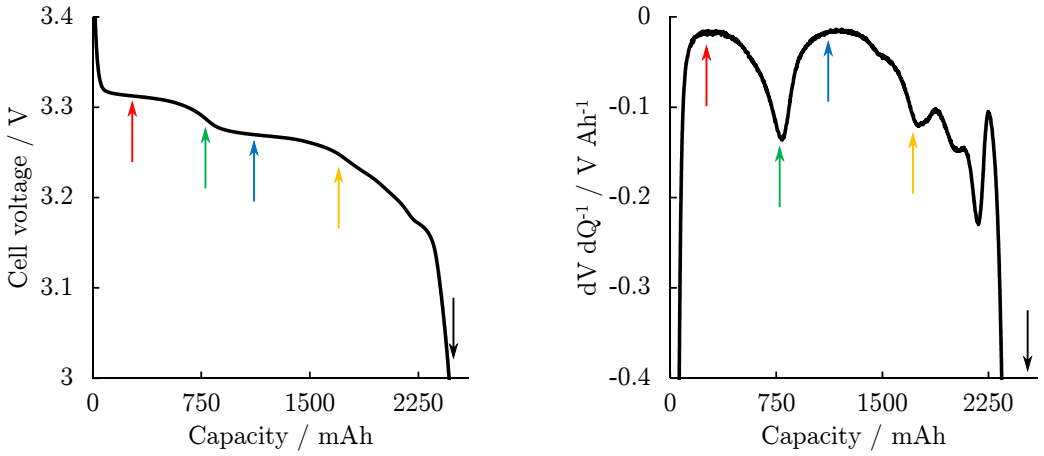

a Cell voltage **b** Differential voltage

Figure 5.1 – Cell voltage a and differential voltage b for cell D with discharge current of 250 mA (0.1C) at 30 °C

"Temperature dependency of state of charge inhomogeneities and their equalization in cylindrical lithium-ion cells" [152]

In Fig. 5.1, the voltage during the 0.1C discharge is displayed a and the differential voltage b is calculated. Five specific SoCs are chosen to investigate the equalisation processes. A flat voltage as seen for the SoCs highlighted by the red and blue pointer in the discharge curve indicates the existence of a two-phase behaviour in both electrodes without any phase transitions. Voltage steps in the discharge profile and the respective local minima in the voltage differentiation are attributed to the phase transition of the graphite anode from LiC_6 to LiC_{12} (75 % SoC) and LiC_{12} to LiC_{24} (35 % SoC). The last SoC investigated is the final state, once the battery is fully discharged.

The cells were stepwise discharged by 5 % with a current of 2.5 A (1C) for 3 min, followed by a relaxation step under open circuit conditions for 117 min. The discharge current is applied at terminal T_{11} and the voltage response along the electrode at terminal T_{22}, T_{33} and T_{44} is measured. Due to the strong asymmetric tab pattern, the worst case scenario regarding SoC inhomogeneity in the cell is provoked. The inhomogeneity in current density distribution in the current collectors reaches its maximum at the outermost current tabs for both electrodes, resulting in the highest potential difference possible between terminal T_{11} and T_{44}. A schematic drawing of the operation mode of the modified commercial cell is shown in Fig. 5.2a.

Fig. 5.2b shows the voltage difference $\Delta U_{T11-T44}$ between the two terminals T_{11} and T_{44} during the relaxation process for the five SoCs as highlighted in Fig. 5.1. For 0 % SoC, the voltage difference between the two terminals is equalised in 2 min. As indicated by the steep gradient of the cell voltage, a small variation in the SoC results in a high potential difference, which acts as a strong driving force for fast equalisation process along the electrode.

Following this argumentation, the SoC equalisation along the electrodes is expected to need more time in regions of voltage plateaus as 90 % and 60 % SoC compared

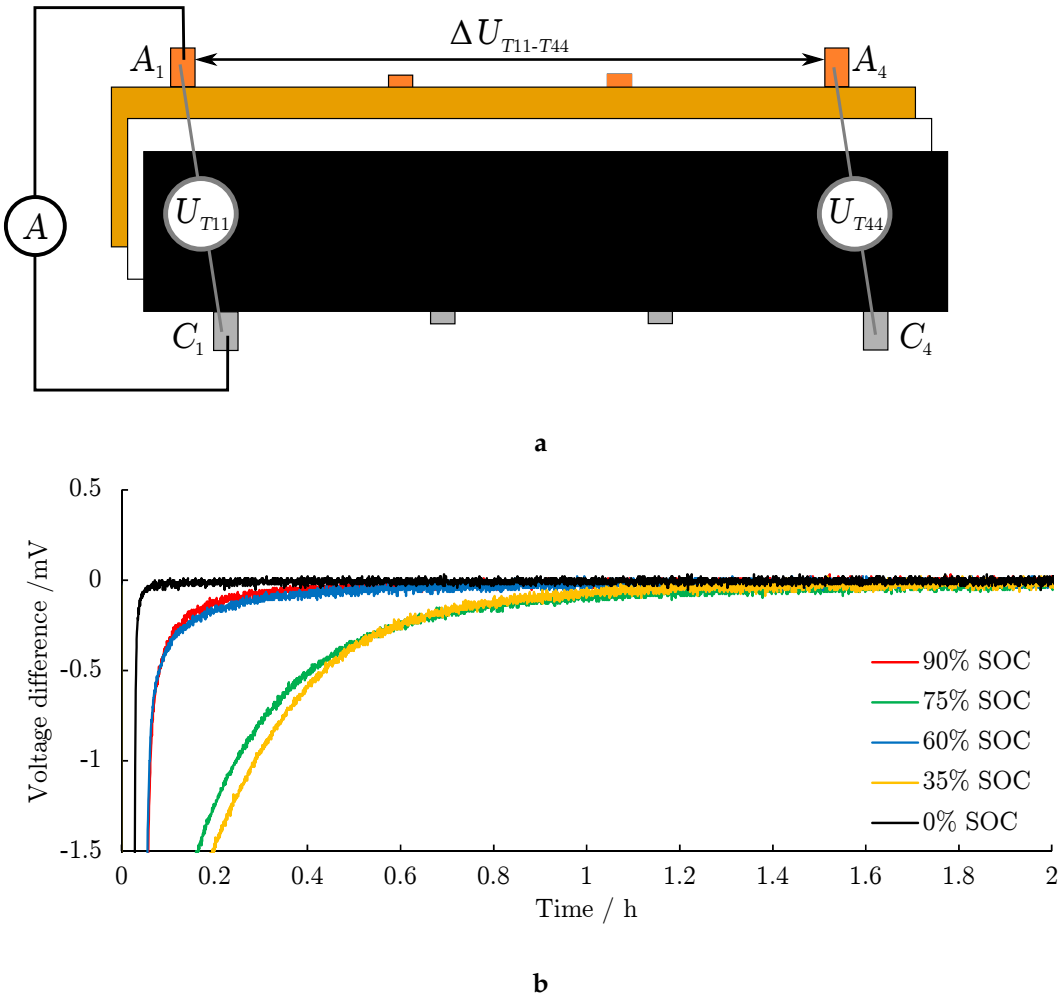

Figure 5.2 – Schematic drawing of the operating mode of the modified commercial cell D as presented in Sec. 3.6.3 a and equalisation process of the potential difference $\Delta U_{T11-T44}$ at specific SoCs b

to regions where a voltage step or gradient is present. With an equalisation time of 30 min for the mentioned SoCs compared to 75 min for 75 % and 35 % the opposite is observed. It is concluded that only minor equalisation processes take place. Due to the flat voltage profile for anode and cathode at these specific degrees of lithiation, the SoC inhomogeneity is too small to provoke a significant potential difference along the electrodes and therefore, the necessary driving force for the equalisation process is missing. As a consequence, a SoC inhomogeneity along the electrode is provoked and will increase until a discharge step results in a local potential difference.

With respect to thermodynamic measurements, SoC variations lower the accuracy of the measurement. The investigation was done on a test cell which allowed for a worst case scenario with a strong asymmetric position of the current terminal at one end of the electrode with a length of 160 cm and the active materials used exhibit large SoC ranges with a very flat potential curve versus Li/Li^+ (LFP / graphite). The investigated

cells A and B with a layered metal oxide as cathode material exhibit a more favourable cell design with the current tabs located at the opposite ends of the current collector foil and a stronger SoC dependency of the cell potential on the degree of lithiation as shown in Sec. 3.1. Consequently, a driving force to equalise the lithium-ion concentrations along the electrodes is always present. The current tab design of cell C favours the inhomogeneity in a similar way as the experimental cell, but the distance between current tabs and electrode end is only one third of the length of the experimental cell, leading in significantly smaller inhomogeneities. Though, measurements indicate that a homogeneous lithiation of the electrodes cannot be guaranteed and a low discharge current to adjust the SoC is necessary to minimise the potential decay along the current collector and therefore minimise the inaccuracy of the measurement. The detailed test scenario is discussed in Sec. 5.2

5.1.2 Temperature

After the violation of the electrochemical equilibrium in a lithium-ion cell, the equalisation of concentration gradients requires time and the cell voltage changes continuously during this time, driven by difference in the lithium-ion concentration in active material. The relaxation behaviour of the cell highly changes with temperature, as transport mechanisms in electrolyte and solid state diffusion in the active materials are highly temperature dependent [156, 210]. To improve the measurement speed, fast relaxation processes are desired, but the negative impact of degradation due to accelerated side reactions needs to be considered. Figure 5.3 illustrates the voltage relaxation after a 1C discharge step for 5 min with a subsequent 2.5 h rest period for different temperatures between 10 °C and 40 °C for the same system and the experimental set-up as used in 5.1.1.

For all temperatures, the cell was fully charged using a CC-CV charging protocol at room temperature to allow for a reproducible reference point with a similar degree of lithiation in both electrodes. The depicted SoCs are located in the first voltage plateau (90 %) as well as in the first voltage step in the discharge profile of the cell (75 %). Fig. 5.3a and b illustrates the discharge step and the voltage relaxation of the cell. It is observed that the cell voltage nearly reaches its equilibrated state at 40 °C within the measurement time, while lower temperatures down to 10 °C prevent a full equilibration. It therefore seems favourable to use higher temperatures as a start temperature for the thermodynamic measurement to reduce the time necessary for relaxation and therefore the duration of the characterisation. In Fig. 5.3c and d the voltage difference between terminal T_{11} and T_{44} is illustrated. The equalisation process at higher temperatures requires more time than for lower temperatures as the SoC inhomogeneity increases with increasing temperature as discussed in Sec. 4.2. Based on these findings, the most promising start temperature for thermodynamic measurement was defined to be 30 °C, compromising voltage relaxation time, SoC inhomogeneity equalisation time and minimising accelerating ageing mechanisms.

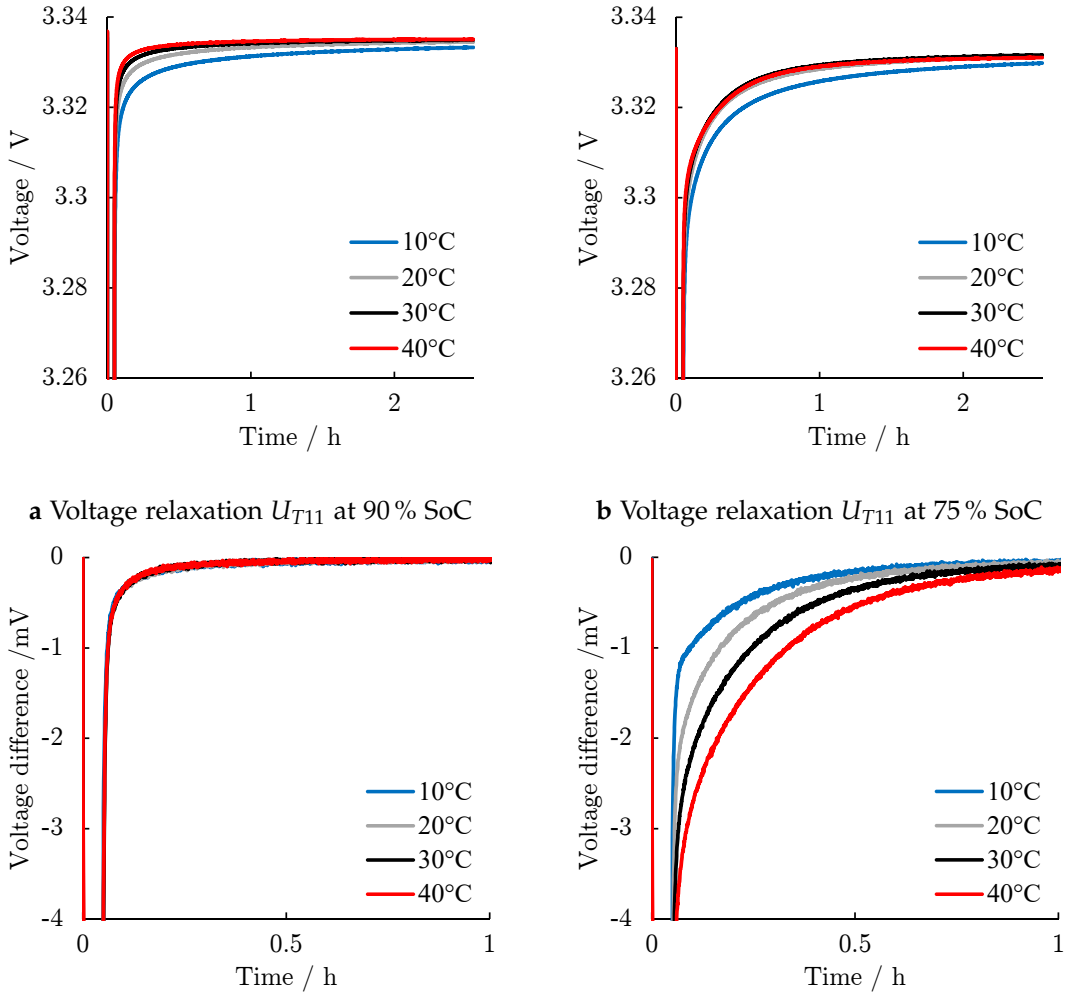

a Voltage relaxation U_{T11} at 90 % SoC

b Voltage relaxation U_{T11} at 75 % SoC

c Voltage difference $\Delta U_{T11-T44}$ at 90 % SoC

d Voltage difference $\Delta U_{T11-T44}$ at 75 % SoC

Figure 5.3 – Voltage relaxation U_{T11} a, b and voltage difference $\Delta U_{T11-T44}$ c, d of cell D after a 5 % discharge step with 2.5 A for different temperatures

5.2 Set-up and measurement procedure

Cells were charged and discharged with a BaSyTec CTS battery cycler. The battery cycler operating software BaSyTest allows additional input values via a programmable software interface, thus the voltage and temperature measurement accuracy was improved by connecting an Agilent 39720A with two 34901A 20 channel armature multiplexer. The Agilent 39720A was used as an 18-bit (5.5 digits) multimeter with a maximum absolute voltage error of 0.0020 % in the used 10 V range. The drift error is specified by the manufacturer as 0.0005 % for the measured value over a time period of 90 days at room temperature.

The temperature dependency of the voltage for the investigated cells was less than 600 µVK^{-1} for all and less than 100 µVK^{-1} for most SoC. The conducted temperature protocol considered the need for a large temperature range ΔT due to the small tem-

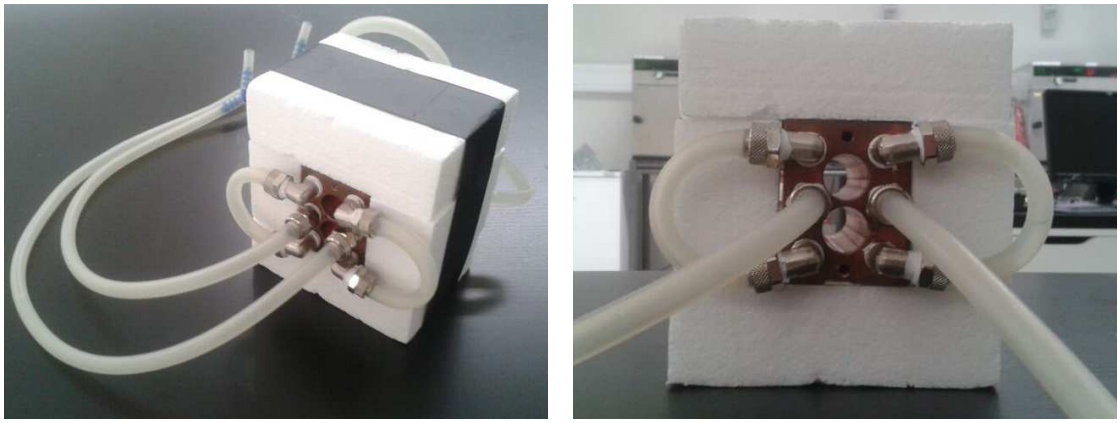

a Top view **b** Front view

Figure 5.4 – Copper block used for ATM with two holes for cylindrical cells with 18.2 mm diameter

perature induced voltage changes dU/dT, the time period, the temperature control unit needed to adjust the temperature accordingly and the necessity to avoid any negative impact of inadequate high or low temperatures on the cell. High temperatures above 40 °C foster accelerated ageing due to side reactions as e.g. electrolyte decomposition as well as self-discharge of the cell, while low temperatures reduce the lithium-ion diffusion within the cell, delaying the voltage relaxation process.

Two different temperature profiles were used for the thermodynamic measurements, depending on the used set-up. Recurring check-ups were conducted in a Memmert IPP 200 climate chamber where the cell temperature was controlled by forced convection. The large volume of the climate chamber slowed the heating and cooling process down, increasing the overall measurement time. As an advantage, the larger volume allowed a larger number of parallel measurements. Thus, the characterisation check-ups during the ageing period were carried out in the temperature chamber. To compensate for the limited cooling capability of the climate chamber and to reduce measurement time, a starting temperature of 26 °C instead of 30 °C was used, followed by two temperature steps of 4 K each, down to 18 °C. The cells were fully charged and, based on the previous results, stepwise discharged with a current of 0.08C for 30 min, resulting in 25 discharge steps with 4 % capacity each.

Detailed measurements with a high number of SoCs at BoL and EoL were carried out inside a custom-made copper block with cylindrical holes, illustrated in Fig.5.4. The copper block was coupled to a Julabo F12-MA Refrigerated/Heating Circulator with heating and cooling capacities of 2 kW and 0.16 kW respectively. The cells were connected to the battery cycler with spring loaded Kelvin probes by mounting two front panels on the copper block. Due to the differences in cell dimension between different manufactures, two copper blocks with 18.2 mm and 18.4 mm holes were manufactured to compensate diameter variations. For BoL and EoL testing, the number of measurement points was increased and the cells were step-wise discharged with 0.1C for 6 min, resulting in 100 SoC steps based on the cell's nominal capacity C_n.

For half-cell measurements, coin cells were placed with thermally conductive pads

on a liquid cooled plate (aluminium plate, copper tubing) and insulated. The small stack height of the coin cell ensures a uniform temperature in z-direction.

To minimise measurement time without violating the equilibrium conditions, the heat conductivity through the cell needs to be known. Due to the different number of windings, varying coating thickness and the unknown heat transfer rate between the different layers, a simulation of the values might be unreliable. Therefore, the heat transfer rate was determined experimentally by equipping cells of type A and C with thermocouples. All temperature measurements, inside as well as outside, were conducted with T-type thermocouples (class A) with an accuracy of $\pm 0.5\,\mathrm{K}$ from Labfacility Ltd. The conductor thickness was 200 µm for surface temperature measurements and 76 µm for in-cell measurements. One was mounted at the surface of the cell, one in the cell core. To achieve this, the thermocouple was introduced through a hole in the bottom after drilling a 1 mm diameter hole into the cell in an argon filled glove-box. To avoid electrical contact and to minimise any chemical contamination of the cell, the exposed metal junction of the thermocouple was insulated using Apiezon© wax. The feed through hole was sealed with a two-component epoxy glue. The modified cells were fully charged and then discharged to 60 % SoC. Resting for 60 hours allowed the cells to achieve quasi-equilibrium conditions with a negligibly small voltage relaxation. After inserting the cells into the copper block, the heating circulator conducted the desired temperature profile.

Fig. 5.5a shows the temperature of the circulator's water bath, the surface temperature of cell A as well as the respective core temperature. Starting at 30 °C, the circulator cooled the system to the pre-set temperature of 25 °C within approximately 9 min. This is the minimum time achievable, as it is limited by the cooling capability of 0.16 kW of the used circulator. Fig. 5.5b demonstrates the temperature difference between the water bath and the cell surface as well as the difference between cell surface and cell core. Due to the high thermal conductivity of copper, only minor differences between the water bath and the cell surface temperature are measurable. However, the lower thermal conductivity of the electrode layers inside the cells results in a temperature difference of up to 4 °C. A time delay of 5 min until the core temperature of the cell equalises is observed. Including a tolerance, the necessary homogeneous temperature distribution after a temperature step of $\Delta T = 5\,^{\circ}\mathrm{C}$ is achievable in an overall time of 15 min. Due to the higher heating capability of 2 kW, the temperature of 30 °C is achieved within 10 min, starting from 20 °C. Based on these findings, measuring the temperature of the cell surface is sufficient as long as the cell is given enough time to equalise. For the following data processing, the initial 14 min after a temperature change need to be discarded.

The last 5 % of the data of a temperature step are considered for the calculation, as a uniform temperature distribution throughout the cell is assumed. Fig. 5.6 illustrates the procedure where the four resulting data points are used as input for a linear regression approximation.

The linear regression model is calculated by

$$y = \beta_0 + \beta_1 x_i + \epsilon \quad [76] \tag{5.1}$$

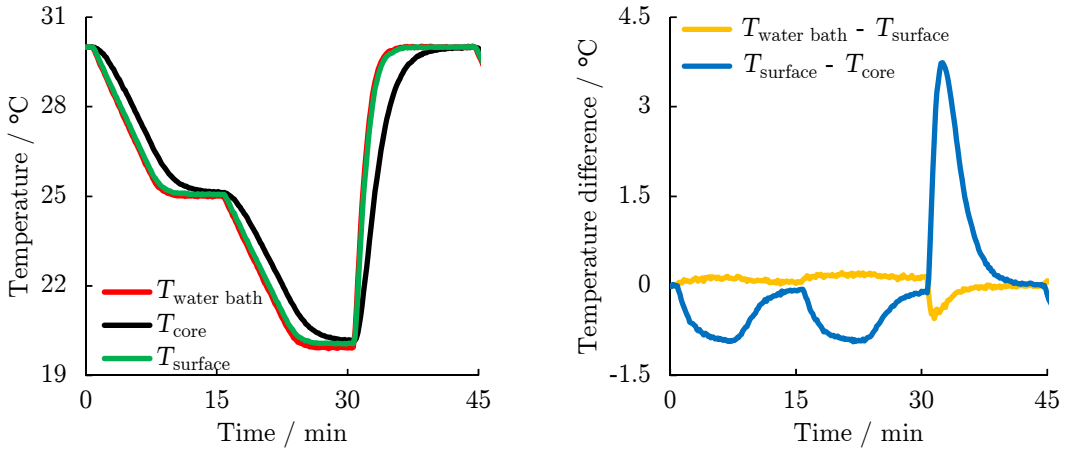

a Temperature of the Julabo water bath, cell surface and cell core

b Temperature difference

Figure 5.5 – Applied temperature profile a and measured time delay between water bath and different positions of cell A b

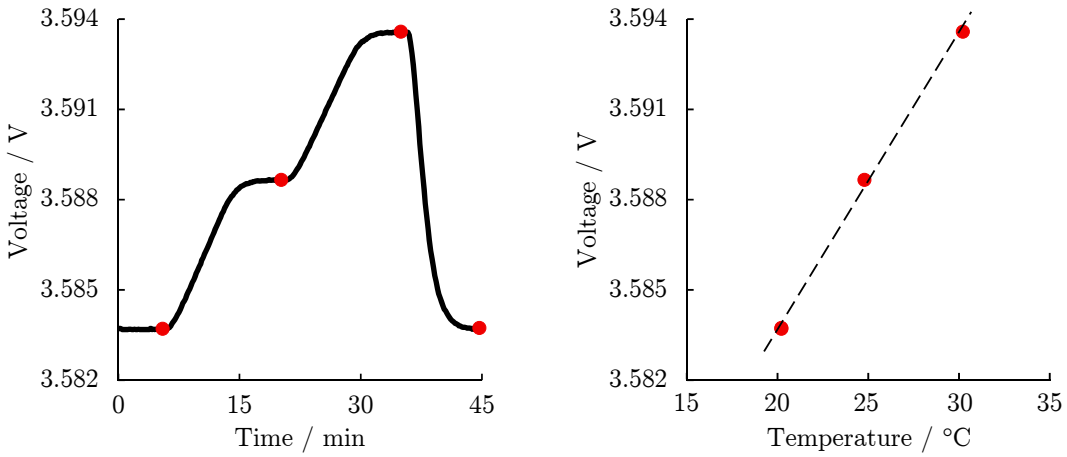

a Cell voltage

b Calculated regression line

Figure 5.6 – Temperature induced voltage change of cell A at an arbitrary SoC a and calculated regression line using voltage data at equilibrated conditions b

with the dependent variable y, the y-intercept β_0, the slope β_1, the independent variable x_i and the random error ϵ. Eq. 5.1 is minimised by the least square approach according to

$$(b_0, b_1) = \arg\min_{\beta_0,\beta_1} \sum_{i=1}^{n} [y_i - (\beta_0 + \beta_1 x_i)]^2 \quad [76] \tag{5.2}$$

For a more detailed description on the calculation of the linear regression, the reader is referred to statistics literature [233]. The calculated error is given in the data by error bars. The observational error ϑ due to measurement uncertainties can be calculated by

$$\vartheta\left(\frac{\partial E_{eq}(x)}{\partial T}\right) = \left(6\left(\frac{1}{2\Delta T}\vartheta E_{eq}(x)\right)^2 + \left(\frac{\Delta E}{2(\Delta T)^2}\vartheta T\right)^2\right)^{1/2} \quad [86] \tag{5.3}$$

The high voltage resolution of the Agilent 39720A and the precise temperature control leads to an error in the range of 10^{-6}, approximately 1 % of $\Delta_r S$.

5.3 Relaxation compensation

As described in Sec. 3.5, long relaxation times of the cell voltage and therefore a long measurement duration prevent thermodynamic measurements to be used as a common characterisation technique of lithium-ion cells. Dynamic load profiles provoke gradients in the lithium-ion concentration in the different components of the cell and inter-particle and intra-particle equalisation processes take place. The section has been partially published in [154].

It is desirable, to conduct the temperature change of the cell as soon as possible after the discharge current was applied. As voltage relaxation processes especially at low SoCs require a long time, the change of the cell voltage due to its entropic coefficient is superimposed or compensated by the voltage relaxation. Eq. 2.35, describing the voltage relaxation behaviour

$$U_{OCV}(x, t_i) = E_{eq}(x, t_0) + \delta(x, t_i) \tag{2.35}$$

needs therefore to be generalised by an entropic coefficient term. The cell voltage in dependence of the lithiation state x during a TM can therefore be expressed at any point in time t_i by

$$U_{OCV}(x, t_i, T_j) = E_{eq}(x, t_0, T_0) + \delta(x, t_i) + C(x)(T_j - T_0) \tag{5.4}$$

with the start temperature T_0 at the start time t_0, the temperature change $\Delta T = T_j - T_0$, the SoC and time dependent function $\delta(x, t_i)$ and the SoC dependent coefficient $C(x)$ with

$$C(x) = -\frac{1}{nF}\Delta_r S(x) \tag{5.5}$$

The entropic coefficient $C(x)$ correlates to β_1 in Eq. 5.1. By means of equivalent circuit modelling, the relaxation behaviour of the cell voltage $\delta(x, t_i)$ is mathematically expressed by

$$U_{OCV}(t) = E_{eq}(t = 0) + \sum_{1}^{i} a_i \exp^{\frac{t}{\tau_i}} \tag{5.6}$$

whereas the parameter τ_i is related to the time scales of the lithium-ion diffusion in the respective cell component. The number of necessary exponential terms i is discussed in literature and depends on the desirable accuracy over the data range [84, 91]. Due to the short time and the low amplitude of the applied current, no significant concentration gradient is expected to occur. The relaxation of the voltage originating from the solid state diffusion of the lithium-ions in the active material of the electrodes requires significantly more time than the equilibration of the concentration gradient within the electrolyte which is assumed to equilibrate within minutes [21, 22]. When short term equilibration processes are neglected, two exponential functions are sufficient to describe the relaxation behaviour. While Pei and co-workers suggested a linearly with time changing variable as time constant to fit the voltage behaviour and to predict the OCV [158], the approach in this work uses only constant values and the required accuracy was sufficiently high.

Despite the results in Sec. 5.1.2, it is hypothesised that the temperature change does not affect the relaxation process or is at least negligibly small. This leads to

$$\left(\frac{\partial \delta(x, t_i)}{\partial T}\right)_{p,x} \approxeq 0 \tag{5.7}$$

To verify this assumption, a number of experiments was conducted, where the relaxation time was shortened, the number of temperature steps and the temperature range was varied to determine the optimal test conditions.

The cell voltage after a discharge step was measured and the temperature was changed after 105 min while the relaxation process was still ongoing (sequence #A). Fig. 5.7 depicts the voltage relaxation for 70 % and 5 % SoC for a time period of 135 min. The changes in temperature are indicated by the highlighted area and the temperature effect on the cell voltage is clearly observable but is superimposed by the voltage relaxation. Using the raw data set would lead to a falsification of the entropic value, which would be underestimated in case a and overestimated in case b. The data range used as input for the background fitting is highlighted in red. By neglecting the first 20 % of the relaxation data, the number of necessary exponentials terms was reduced and the accuracy of the fitting was significantly improved. For shorter relaxation times, the neglected number of data points was increased, and either the relaxation time or the slope of the voltage relaxation $dVdt$ was used as a criterion. The resulting fit is displayed by the grey dashed lines. The fit is performed using MATLAB 2015b with the curve fitting toolbox. As input, Eq. 5.6 with $i = 1$, $i = 2$ and a third equation, namely the Michaelis-Menten equation, expressed by

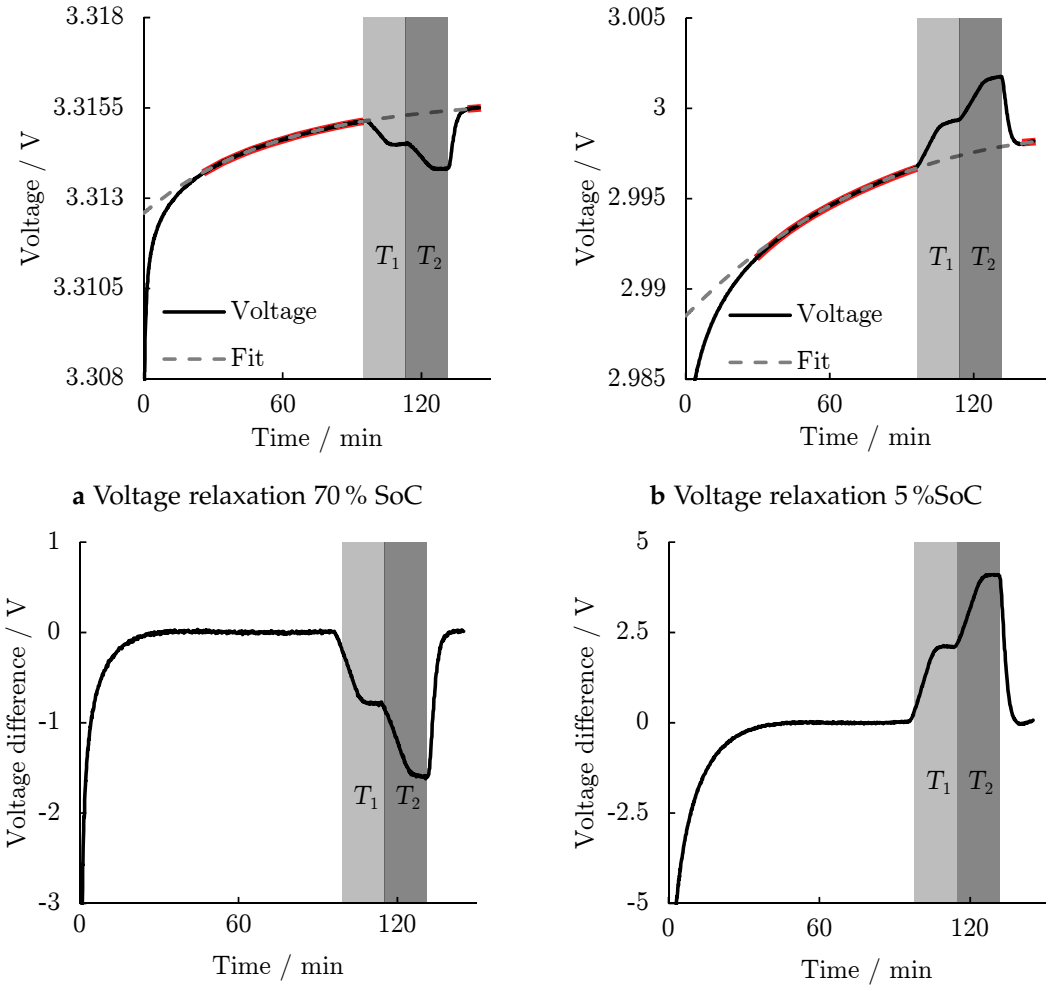

a Voltage relaxation 70 % SoC

b Voltage relaxation 5 %SoC

c Calculated voltage difference

d Calculated voltage difference

Figure 5.7 – Voltage relaxation after discharge step with curve fit, excluding the data measured during the temperature change a,b and resulting difference for two arbitrary SoCs c,d

$$\delta(x, t_i) = \frac{kt}{l + t} + m \tag{5.8}$$

with the fitting parameters k, l and m is used. Even though this equation is commonly used in enzyme kinetics [41] and has, adapted to lithium-ion batteries, no physical meaning, it was suitable to fit the voltage relaxation mathematically. Other fitting equations were evaluated during the approach but were found to be not suitable to fit the voltage relaxation behaviour sufficiently. Based on the fitting error calculated by least square approach, the most accurate function was chosen. Subtracting the fit from the raw data lead to Fig. 5.7c and d. The subtracted data were used to determine the entropic coefficient $C(x)$.

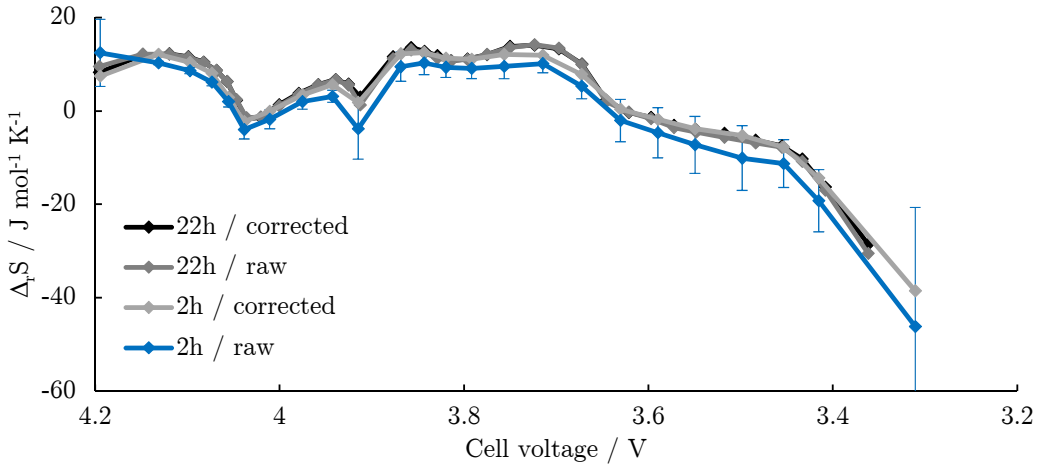

Figure 5.8 – Comparison of corrected and raw entropy data of cell type A with 60 min and 1320 min relaxation time per step versus cell voltage at 30 °C

In comparison, the same cell was tested a second time (sequence #B) whereas the relaxation time after the discharge step was adjusted to 1320 min (22 h). This long time period is assumed to allow all concentration gradients in the cell to fully equilibrate either along the electrode or throughout the layer of active material [108, 201]. Fig. 5.8 compares the different scenarios by illustrating the thermodynamic profile versus the cell voltage at 60 °C. For scenario #B, no differences between the original data and the corrected data are observed as expected, as the voltage relaxation did not superimpose the temperature dependency of the cell voltage. The corrected data from sequence #A also agree well with the long term data, leading to the conclusion that the previously made assumption expressed in Eq. 5.7 is reasonable.

The resulting entropy profile without any background correction deviates from the other measurements and the values are mostly below the correct data, underestimating the entropic coefficient at most SoCs. The error bars for this data set already indicate the large deviations, when the values are calculated with Eq. 5.2.

Even though the non-corrected data follow the original trends and the deviations are not significant, the importance of a background subtraction becomes crucial, when the relaxation time is prolonged. This can be either caused by larger inhomogeneities and therefore larger concentration gradients along the electrode, low SoCs with an increased diffusion path through a particle of the active material or if the kinetic properties of the cell become deteriorate e.g. because of an increasing SEI layer on the electrodes.

The entropy profile is depicted in Fig. 5.9 for the same cell after it was cycled for 2550 cycles with a 1C-1C charge-discharge scenario as described in Sec. 6. Due to the operation of the cell, the cell's relaxation behaviour is significantly changed. In the beginning of the discharge, the deviation between the measured and the calculated entropy values is rather small. However, below a cell voltage of 3.9 V the difference increases continuously towards lower SoCs, with discrepancies above 100 % to the relaxation corrected values. Thus it needs to be highlighted that a fit of the voltage relaxation and a subsequent background subtraction is mandatory to gain reliable and comparable results.

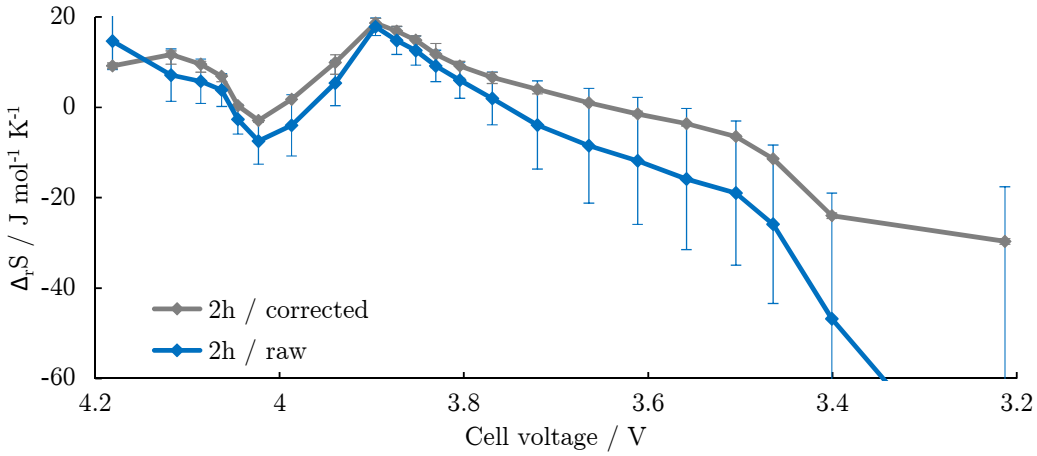

Figure 5.9 – Comparison of corrected and raw entropy data of cell type A with 60 min relaxation time and 120 min overall per step after 2550 1C charge/discharge cycles versus the cell voltage at 30 °C

Table 5.1 – Matrix of measurement parameters as shown in Fig. 5.10

Sequence	Step 1	Step 2	Step 3	Step 4	overall
#A	120 min 30 °C	30 min 20 °C	30 min 10 °C	30 min 30 °C	210 min
#B	1320 min 30 °C	30 min 25 °C	30 min 20 °C	30 min 30 °C	1410 min
#C	60 min 30 °C	15 min 20 °C	15 min 10 °C	15 min 30 °C	105 min
#D	27 min 30 °C	11 min 25 °C	11 min 20 °C	15 min 30 °C	64 min
#E	18 min 30 °C	11 min 25 °C	11 min 20 °C	5 min 30 °C	45 min
#F	18 min 30 °C	11 min 22 °C	5 min 30 °C		34 min

To investigate the possibility of further reducing the relaxation time, the cell was tested under various conditions in its new state denoted as sequence #C - #F. The parameters as initial temperature, temperature step, relaxation time prior to the temperature change and the duration of the single temperature step are shown in Tbl. 5.1

Fig. 5.10 displays the resulting entropy curves after the background subtraction was performed. Sequence #C shows the same features as the long term measurement used as reference curve before. If the relaxation time is shortened below 60 min, deviations around medium SoCs occur and the measurement becomes partially inaccurate. If the system does not have enough time to return to thermal equilibrium as provoked in sequence #E with only 5 min, the deviation increases furthermore. Using only one temperature step as performed within the measurement in sequence #F leads to an unreliable result of the linear regression to calculate the slope of $\partial U_{OCV}/\partial T$, as only two

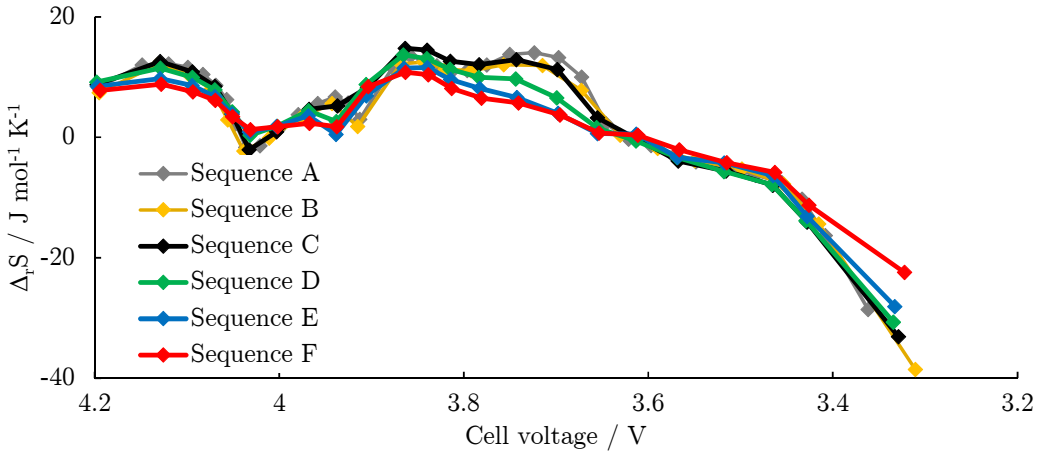

Figure 5.10 – Impact of different relaxation times and temperatures on the thermodynamic measurements as displayed in Tab. 5.1

data points are available. In combination with the short relaxation period, this sequence delivers the largest deviation compared to the reference curve.

5.4 Conclusion

The major drawback of thermodynamic measurements is the long relaxation time until the cell reached its electrochemical and thermal equilibrium after a current step, making the test method only interesting for basic characterisation of new materials. Compensating the voltage relaxation behaviour led to a significant increase in measurement speed without sacrificing the measurement's accuracy. By improving the experimental set-up and focusing on SoC ranges where the entropy profile of the cell exhibits defined characteristic, thermodynamic measurements can be accomplished within 24 h and achieve the testing time of established measurement methods as DVA. While the necessary high voltage resolution remains a challenge, gaining a measurement point at any SoC (e.g. during a stepwise charge) makes advanced thermodynamic measurements (ATM) a promising candidate to supplement or even substitute other techniques. The accuracy and interpretability of the data will be compared to other characterisation methods and discussed in Sec. 6.

Chapter 6

Tracking of Cell Degradation

In Sec 3.3, DVA was identified as one of the most promising techniques to characterise the performance of lithium-ion cells and to track the degradation during operation of the cell. The improvements in measurement speed and accuracy of the thermodynamic characterisation technique, presented in Sec. 5, indicate that similar results can be achieved and that it is qualified as an alternative test method. To compare the applicability of both characterisation techniques, a test matrix was specified in which the influence of calendar and cycle ageing on various cathode materials, namely NMC, NCA-LMO blend and LFP, was studied in detail. Fig. 6.1 illustrates the operation diagram of the ageing study.

The accuracies of DVA and advanced thermodynamic measurements (ATM) as characterisation tools are investigated by analysing the degradation of cell B and comparing the calculated results with half-cell measurements. Subsequently, the applicability of ATM on the blended cathode of cell A and the two-phase cathode material of cell C is discussed.

6.1 Accelerated battery ageing

The cells received an initial characterisation to quantify the quality of the cells and to eliminate cells from the test batch which differ significantly in their performance. In the next step, eight cells of each type (24 cells overall) were selected and characterised with DVA and thermodynamic measurements, whereas the state is defined as BoL. To investigate the influence of ageing on the electrochemical properties in the respective test cells, two different ageing scenarios have been performed. As discussed in section 2.3, cycling and storing leads to ageing of the cells but the dominating ageing mechanisms can differ. The first one focused on the degradation during operation and the cells were cycled with a current of 1C at 25 °C. The second batch was stored at elevated temperature of 60 °C at 100 % SoC. Every 14 days and, depending on the cell chemistry, every 150 or 300 cycles, the remaining capacity of the cells was determined. Additionally, four cells were characterised by thermodynamic measurements and four cells by DVA, whereas cells of each scenario were taken. The final criteria to stop the ageing procedure was, as often defined in literature, when the cell capacity dropped below 80 % of the nominal

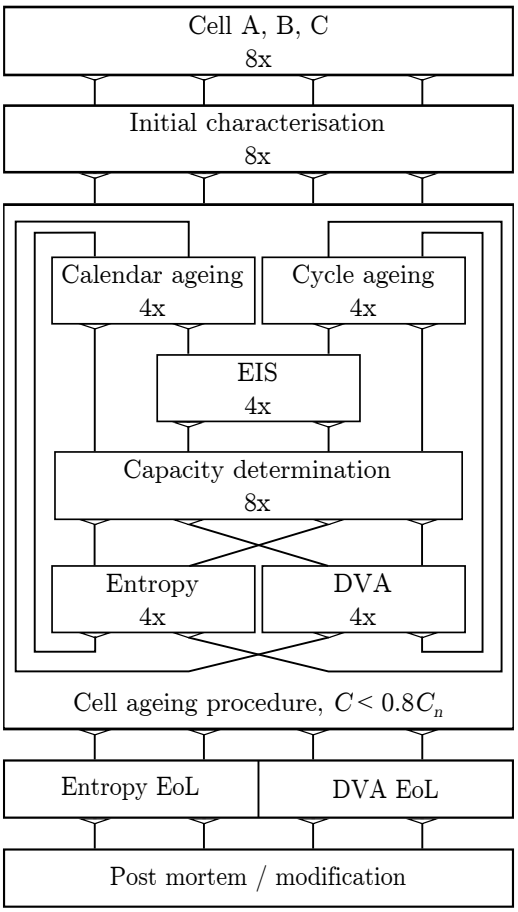

Figure 6.1 – Flow diagram of the performed ageing study

capacity C_n. Due to the good stability of cell A during calendar ageing and the long cycle life of cell C, the criteria was not achieved in this two cases and the testing ended due to time limitation. At EoL, a final characterisation was performed and a last DVA and thermodynamic measurement was conducted. Afterwards, cells were used for post mortem studies to confirm the assumptions regarding the degradation state of the cell. The post mortem studies included among other the analysis of the electrodes using half-cells, SEM pictures as well as modification to fit a reference electrode into the cell. As calendar ageing cannot be avoided while cycling the cells, attention needs to be paid to reduce the overlap by minimizing the temperature increase during cycling and to compensate for occurring long-term effects. The ageing behaviour of the tested cells are shortly discussed for both procedures.

6.1.1 Cycle ageing

Cells were cycled using a CC - CV charging and CC discharging procedure. The cells were cycled with 1 C between the recommended cut-off voltages with a limited CV phase during charge of 15 min. To minimise the temperature increase of the cells, all testing was performed in a Memmert IPP 200 incubator at 25 °C. To increase the heat dissipation,

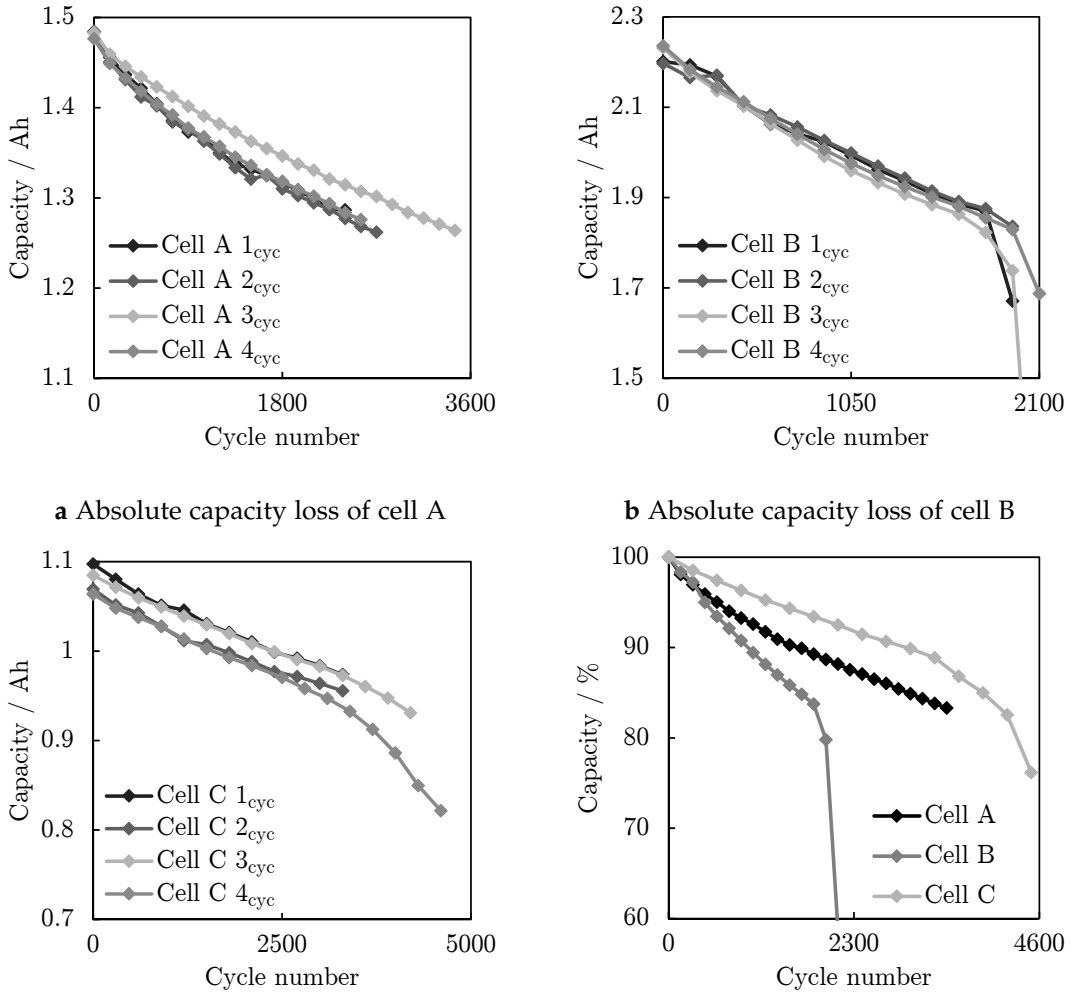

a Absolute capacity loss of cell A

b Absolute capacity loss of cell B

c Absolute capacity loss of cell C

d Average capacity loss

Figure 6.2 – Capacity decrease of cells cycled with 1C at 25 °C

additional fans were added at different locations inside the incubator for a homogeneous temperature distribution. After 150 cycles for the NCA and NMC cells and 300 cycles for the LFP cells respectively, a capacity check was performed to determine the remaining capacity C_{cycle}. Figure 6.2 illustrates the capacity decay for the different cells used.

The absolute capacity loss between each characterisation step decreases during the degradation of cell A a. A possible reason is the time limitation of the CV phase to 15 min during charge. Due to the increasing overpotential, the duration of the CC phase decreases and therefore the charge throughput is reduced with increasing cycle number. As a consequence, the amount of side reactions and volume expansion at very high SoCs is limited, prolonging the cell's life. The capacity fade is similar for three test cells, while the capacity loss of cell A 3_{cyc} is lower and is therefore tested for 3450 cycles.

Even though the testing procedure of Cell A and B is the same, the capacity loss of cell B reveals a linear behaviour until the remaining capacity reaches 85 % after approximately 2100 cycles b. At this point, the capacity drops significantly and the cells partially fail to

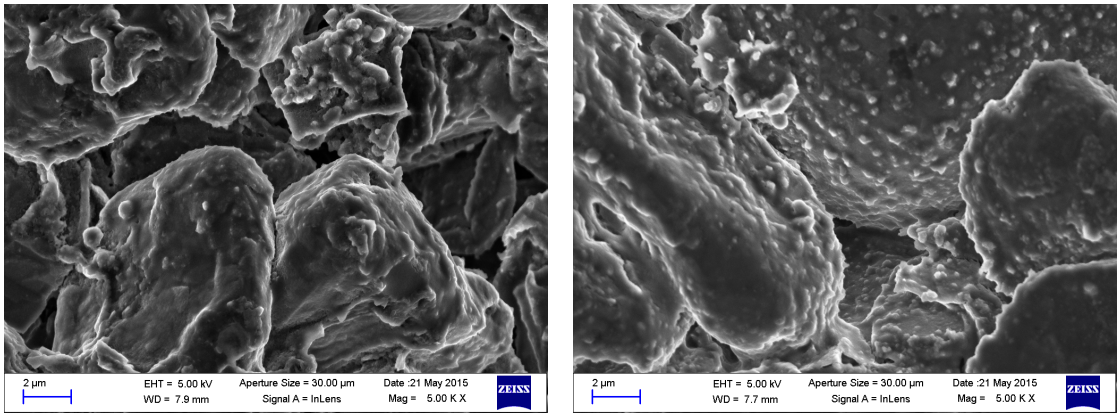

a Graphite electrode at new state **b** Graphite electrode after 2700 1C cycles

Figure 6.3 – SEM picture of the anode material of cell A before a and after cycling b

operate. To allow post mortem analysis and reliable half-cells, not all cells were cycled beyond this point. It is further observed that the remaining capacities of test cells B 3_{cyc} and B 4_{cyc} are constantly 2-3 % higher than the other two test cells.

LFP, the cathode material of cell C is well known for its good cycle stability. As a consequence, the number of cycles between each characterisation interval was increased to 300 cycles to minimise the overall testing time. The initial cell capacity C_n is stated by the manufacturer to be 1050 - 1100 Ah and varies more than the initial capacity of the other two cell types. The remaining capacity during cycling follows a linear decrease until 3300 cycles a. The capacity fading of cell C 4_{cyc} increased, when the remaining capacity dropped below 85 % and was cycled for 4800 cycles.

Fig. 6.2d compares the averaged relative capacity loss of the different cell types and reveals significant differences in the characteristic decay of the capacity and the long-term stability. While the LFP based cell shows the best cycle stability, the NMC based cells achieved only 50 % of the number of cycles before failure. Two SEM images of the graphite anode of cell A are displayed in Fig. 6.3. "New state" a in this context means "as delivered" and the formation of the cell was already performed by the manufacturer. A thin SEI layer covers the particles of the active material. After cycling b, the SEI grew significantly, covering the initial structure of the graphite surface. In addition, the particles are covered with dots, indicating a variation of nucleation centres on the surface, where side reactions as lithium deposition favourably occur [14, 132].

6.1.2 Calendar ageing

To accelerate the calendar ageing process, cells were fully charged to 100% SoC using a CC - CV charging procedure at 25 °C. A charging current of 0.2 C was applied until the charging cut-off voltage U_{cco} according to the data sheets was reached. The CV ended, as soon as the charging current I_c dropped below $C_n/100\,\mathrm{h}$, resulting in an increase in CV time during the ageing process but was necessary to adjust the correct SoC. All cells are specified for temperatures up to 60 °C and were therefore stored in a Memmert IPP200 incubator for 14 days at this temperature. After this time period, cells were cooled down

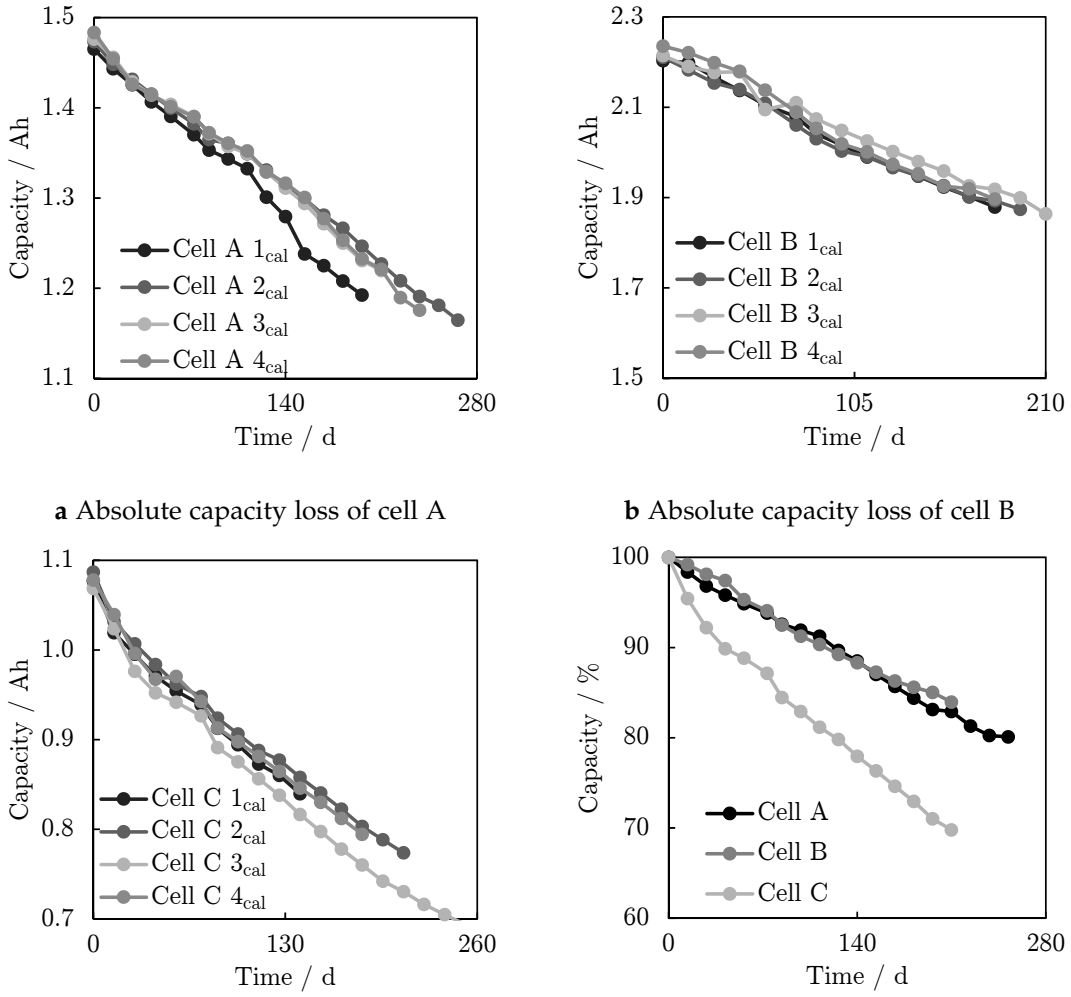

a Absolute capacity loss of cell A

b Absolute capacity loss of cell B

c Absolute capacity loss of cell C

d Average capacity loss

Figure 6.4 – Capacity decrease of cells stored at 60 °C and 100 % SoC

to 25 °C and fully discharged with 0.2 C until the discharge cut-off voltage U_{dco} of the cell was reached. The first discharge capacity was used to monitor the self-discharge of the cell during the ageing process. Afterwards, the cells were fully charged with the described CC - CV procedure and again discharged to determine the remaining discharge capacity C_{age}. The progress of C_{age} of the tested cells is displayed in Fig. 6.4.

The remaining capacities of cell A follow a linear decrease during the storage at 60 °C for up to 266 days a. In the beginning, the capacity decrease is similar for all four tested cells but starts to diverge after 166 days, whereas Cell A 1_{cal} exhibits the largest capacity loss with 18.6 % and a remaining capacity of 1.192 Ah after 196 days.

The degradation of cell B exhibits a linear slope with a high similarity between all tested cells b. The average capacity loss after 196 days is 15.1 %.

For cell C, the observable capacity losses during storage are significantly higher as for the two previously described cell types and the average remaining capacity after 126 days is 79.8 %. Cell C 3_{cal}, the cell with the largest capacity fade was stored for 252 days

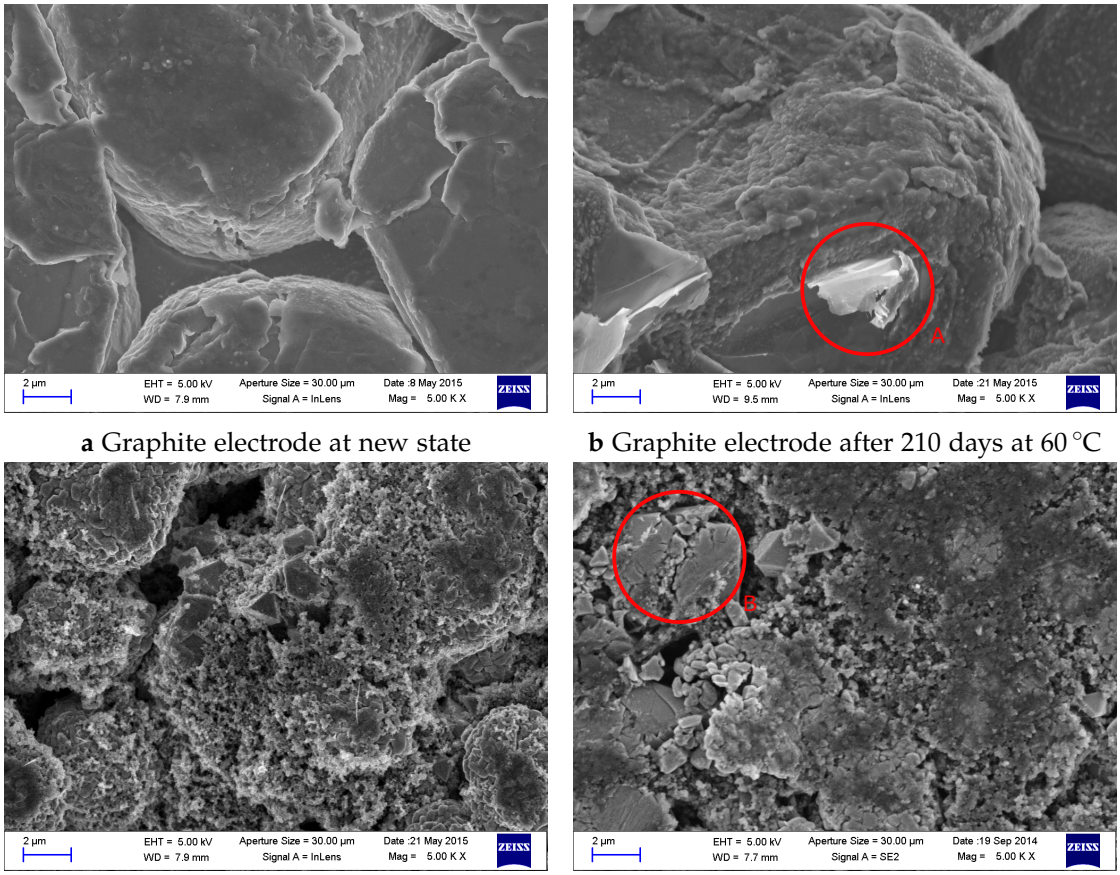

a Graphite electrode at new state

b Graphite electrode after 210 days at 60 °C

c NCA-LMO electrode at new state

d NCA-LMO electrode after 238 days at 60 °C

Figure 6.5 – SEM picture of the anode material of cell B and cathode material of cell A before (a, c) and after storage (b, d)

at the elevated temperature, exhibiting a remaining capacity of 0.649 Ah (64.9 %).

Fig. 6.4d compares the degradation process of the different cell types. Cell C, which had the best cycle stability shows a large sensitivity towards high temperatures and the remaining capacity drops below 80 % after 140 days. Cell A and B show very similar relative capacity loss during storage and the capacity remains for 256 days above 80 %.

The impact of 210 days of storage at 60 °C on the anode material of cell B 3_{cal} can be seen Fig. 6.5, where the aged state b is compared with a cell, which was opened shortly after the delivery a. A significant growth of the SEI layer on the graphite particles is observed. Beside reaction products from electrolyte solvent and conductive salt [218], high amounts of transition metals from the cathode are often found on the anode, if the cell is stored at high temperatures and at high SoCs [197]. The thermal instability of the SEI has a catalytic effect and causes a recurring formation process and therefore accelerates the degradation process [197]. Furthermore, structural deteriorations of the graphite flakes at different positions, highlighted as A, suggest partial LAM.

The SEM pictures of the NCA-LMO cathode shown in Fig. 6.5c and d compare a new cell with cell A 4_{cal} after 238 days of storage at 60 °C and 100 % SoC. The surface structure of the cathode changed observably. The cluster of single NCA particles, which are clearly

distinguishable in the new state, coalesce into a large, rough surface, whereas the single particles vanished. The structure of the LMO particles, identifiable by their symmetrical and well defined shape with a smooth surface exhibit large cracks, as highlighted in d.

6.2 Application of characterisation methods

The distinct features of the anode and cathode contributing to the full-cell profile are analysed using half-cell measurements of the electrodes, harvested from new cells. The half-cell and full-cell data are displayed in Fig. 6.6 and the anode and cathode profiles are shifted to match the full-cell features due to their higher utilisation range, when assembled in coin cells and cycled versus lithium metal.

To evaluate the ongoing degradation of the cell and to identify the sources of capacity fade, the changes and shift of the two electrodes are analysed. Three possible sources are identified to cause the capacity fade: I) Loss of active material (LAM) on the anode, e.g. delamination of active material as seen in Fig. 6.5b due to mechanical stress. II) LAM on the cathode, e.g. due to metal dissolution and cation mixing. III) Loss of lithium inventory (LLI) due to continuous side reactions, increasing the thickness of the SEI. A combination of LAM and LLI can be observed, if a fully lithiated particle loses electrical contact with the current collector and therefore its possibility to de-intercalate the lithium-ions.

The voltage of the cathode increases for low degrees of lithiation, causing the full-cell to reach the respective U_{cco}. Further lithium de-intercalation is either not possible or results in a significant harm of the material and is therefore prohibited. The anode remains at the stable voltage plateau at 80 mV for the stage 1 - stage 2 transition due to the higher capacity. Hence, the full-cell is limited by the upper voltage limit of the cathode, indicated as C_{limit} in Fig. 6.6. During discharge, the anode is fully delithiated and a steep voltage increase is observed towards full delithiation, equivalent to a full discharge of the full-cell. The limiting properties of the anode on the full-cell are indicated by the label A_{limit}.

The various degradation mechanisms as LAM and LLI continuously decrease the cell's performance by lowering the storable capacity and increasing the cell's internal impedance. Fig. 6.6 gives a schematic overview of the effect of various degradation mechanisms occurring during the calendar ageing study, when the cell is stored at elevated temperatures at 100 % SoC.

In a, the loss of 20 % of lithium inventory (LLI) is shown. As a result, the maximum degree of lithiation in the anode is reduced, e.g. from $Li_{0.9}C_6$ to $Li_{0.7}C_6$ and a shrinkage in the stage 1 - stage 2 voltage plateau is observed in the full-cell profile. The anode cut-off voltage during lithiation is constant, as long as the amount of lithium is sufficient to fill the anode to 50 %, at which point the phase transition occurs. For the discharge of the full-cell, the anode voltage during delithiation dominates the cell's cut-off voltage, remaining constant at 1 V, when the anode is fully delithiated. The utilisation of the cathode is limited in the same manner as the anode and the degree of full lithiation is reduced by 20 %, e.g. from $Li_1Ni_{1/3}Mn_{1/3}Co_{1/3}O_2$ to $Li_{0.86}Ni_{1/3}Mn_{1/3}Co_{1/3}O_2$ (assuming a BoL utilisation of $0.3 < x < 1$).

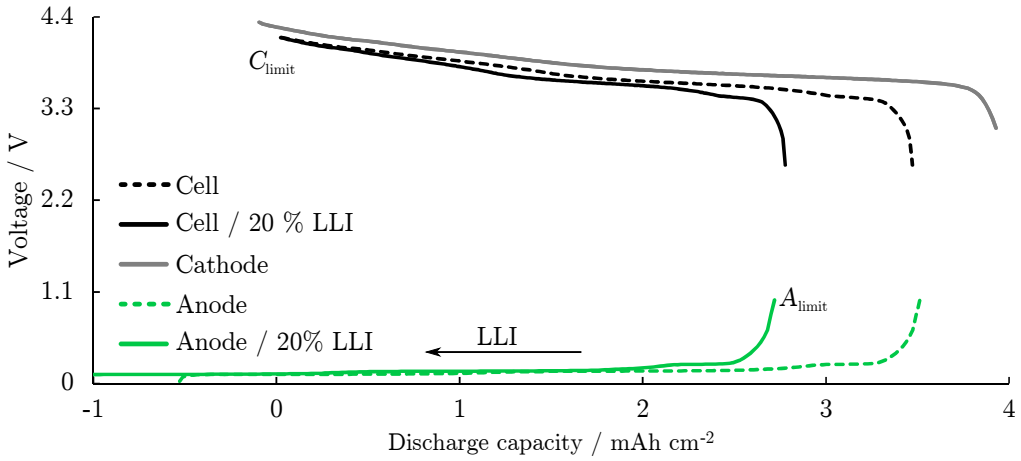

a Change in electrode utilisation due to 20 % LLI

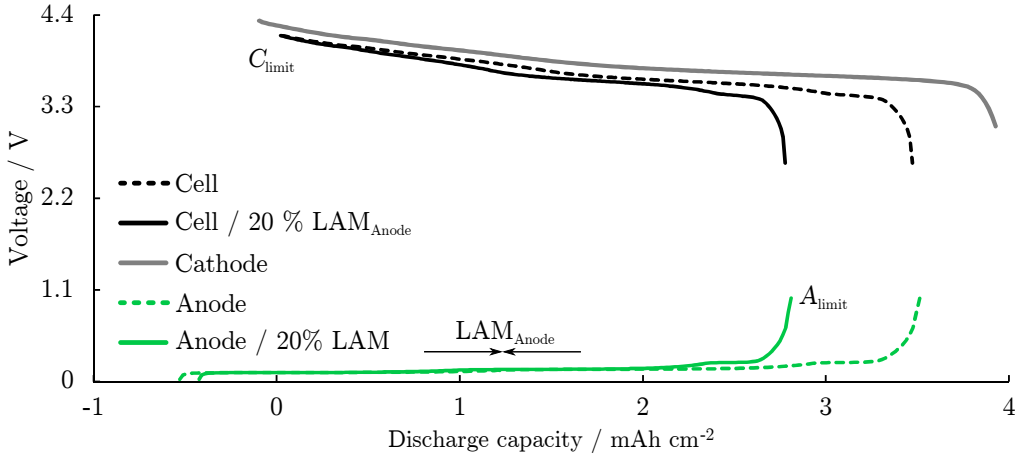

b Change in electrode utilisation due to 20 % LAM of the lithiated anode

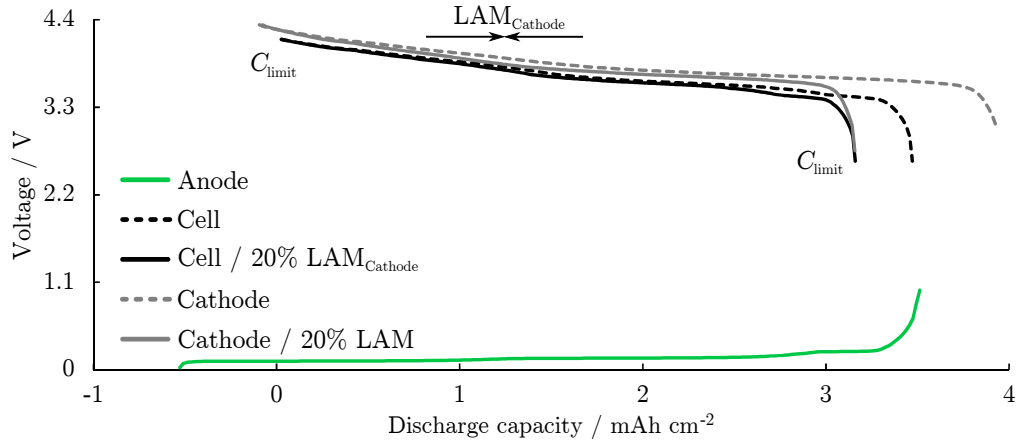

c Change in electrode utilisation due to 20 % LAM of the delithiated cathode

Figure 6.6 – Exemplified effect of LLI, anode LAM and cathode LAM on the discharge performance of cell B

In b, a loss of 20 % lithiated anode material is depicted. A loss of the material on the anode side could partially be compensated due to the overbalancing of the anode, but as it is fully lithiated in this example, the resulting capacity fade is also 20 %. The utilisation range of the cathode is limited and the highest degree of lithiation decreased.

A loss of 20 % cathode material during the storage time is exemplified in Fig. 6.6c. The material is considered to be delithiated in this state, therefore, no lithium is lost. This leads to a significant overbalancing of the anode. Due to the high degree of lithiation towards the end of the discharge, the voltage of the cathode decreases significantly. In contrast to the initial state, where the anode is the limiting electrode during the full-cell discharge, a limitation by the cathode is observed.

Due to the complexity of the electrochemical system, the separation of the different degradation is expected to be more difficult. Additional degradation such as loss of delithiated anode and lithiated cathode material, when the cell is fully discharged during the characterisation can occur. To track the impact of ageing mechanisms on full-cell level as well for the different cathode and anode materials, numerous characterisation methods are available as discussed in Sec. 3.6. Differential voltage analysis (DVA) and advanced thermodynamic measurements (ATM) were identified to be promising methods to reveal not only the remaining capacity of the cell but rather give an insight to the performance of each electrode. In addition, results of EIS measurements obtained during the ageing study are presented.

Using the data of the ageing study as presented in the previous section, the applicability and accuracy of the methods are compared. To achieve this, the ageing data are used to identify the different sources of capacity fade within the cell. In a final step, half-cells, built with harvested samples from the degraded cells, are used to verify the conclusions by comparing their electrochemical performance to half-cells built from new cells. The detailed assembly process is described in Sec. 3.6.1. The data sets for the cells B 4_{cyc} and B 4_{cal}, which were characterised by DVA and the cells B 1_{cyc} and B 1_{cal}, which were characterized by ATM are analysed in detail, while the peculiarities of cell A and cell C with a blended and a two-phase cathode material respectively, are addressed separately.

Tbl. 6.1 states the discharge capacities under different discharge conditions. For half-cell measurements using coin cells, the 0.2C discharge capacity determination is only applicable with restrictions due to high overpotential during the measurement. Especially in the case of aged anode half-cells, the cell voltage reaches quickly the discharge cut-off limit and the graphite material is not fully lithiated if the applied current is too high.

The capacity fade of the analysed cycled cells is 22.3 % and 24 %. The calendar aged cells lost 15.3 % and 16.3 %. The capacity fade determined during the DVA measurements is smaller as for the 0.2C characterisation due to the lower discharge current and the lower overpotential. The capacity fade during the thermodynamic characterisation is larger than the 0.2C characterization for the calendar aged cell. Possible reasons for this phenomenon are assumed to be the stepwise-discharge procedure and the self-discharge of the cell during the longer characterisation procedure.

Table 6.1 – Various discharge capacities of different cells from type B, used for further analysis

	Cell B 4_{cyc}	Cell B 4_{cal}	Cell B 1_{cyc}	Cell B 1_{cal}
0.2C BoL / mAh	2235.9	2235.4	2197.0	2203.2
0.2C EoL / mAh	1738.2	1893.0	1670.8	1844.2
Loss %	22.3	15.3	24.0	16.3
DVA BoL / mAh	2241.7	2242.4		
DVA EoL / mAh	1793.4	1946.2		
Loss %	20.0	13.2		
ATM BoL / mAh			2225.1	2231.5
ATM EoL / mAh			1698.8	1845.0
Loss %			23.7	17.3

6.2.1 EIS of degraded lithium-ion cells

The EIS measurements during the ageing study were performed using a Soltaron 1470E multi-channel potentiostat. The cells were fully charged at 25 °C using a CC-CV protocol (0.1C CC, 4.2 V CV, I $<$ 0.01C CV) and subsequently stepwise discharged by applying a current of 0.1C. Every 5 % SoC, an EIS measurement with a current of 0.02C and a frequency range from 100 kHz to 10 mHz was performed. To compromise between the duration of the testing and the influence of relaxation effects on the spectra, a rest period of 30 min was included [107].

Fig. 6.7 depicts the resulting spectra for cell A every four weeks of storage at elevated temperature (60 °C, 100 % SoC), measured at 100 % a, 75 % SoC b and 15 % SoC c. To allow for a clearer distinction of the degradation effects on the spectra, Fig. 6.7d - f were aligned along the Z'-axis.

The shift towards a higher internal resistance ($Z'' = 0$) is observed for all SoCs. It is caused by an increasing SEI layer, the continuous consumption of electrolyte and its changes in properties due to a variation in salt concentration and the dissolution of further side reaction products. Consequently, the cell's capability to deliver high currents is reduced. Furthermore, the increasing overpotential causes the cell to reach the respective charge and discharge cut-off voltage faster, limiting the deliverable capacity of the cell under the applied current. Aligning the Nyquist plots allows to analyse the effect of the degradation of the cell. In the spectra recorded at 100 % SoC, a second semi-circle occurs, representing a second dynamic process with a different time constant. The characteristic of the local minimum is reduced and shifted towards higher Z' and Z''[1]. As stated in Sec. 6.2, the loss of inventory lithium leads to a misalignment of the electrodes. The impedance spectra are sensitive to the degree of lithiation of the respective electrode, leading to a variation in the observable time constants. With increasing cell degradation, the two semi-circles start to merge again, resulting in a more highlighted local minimum. The slope of the branch, attributed to the lithium-ion diffusion in the

[1]Please note that Z'' is plotted inversely, consequently the terms *decrease, increase* and *minimum* describe rather the graphical change of Z'' than the actual numerous values

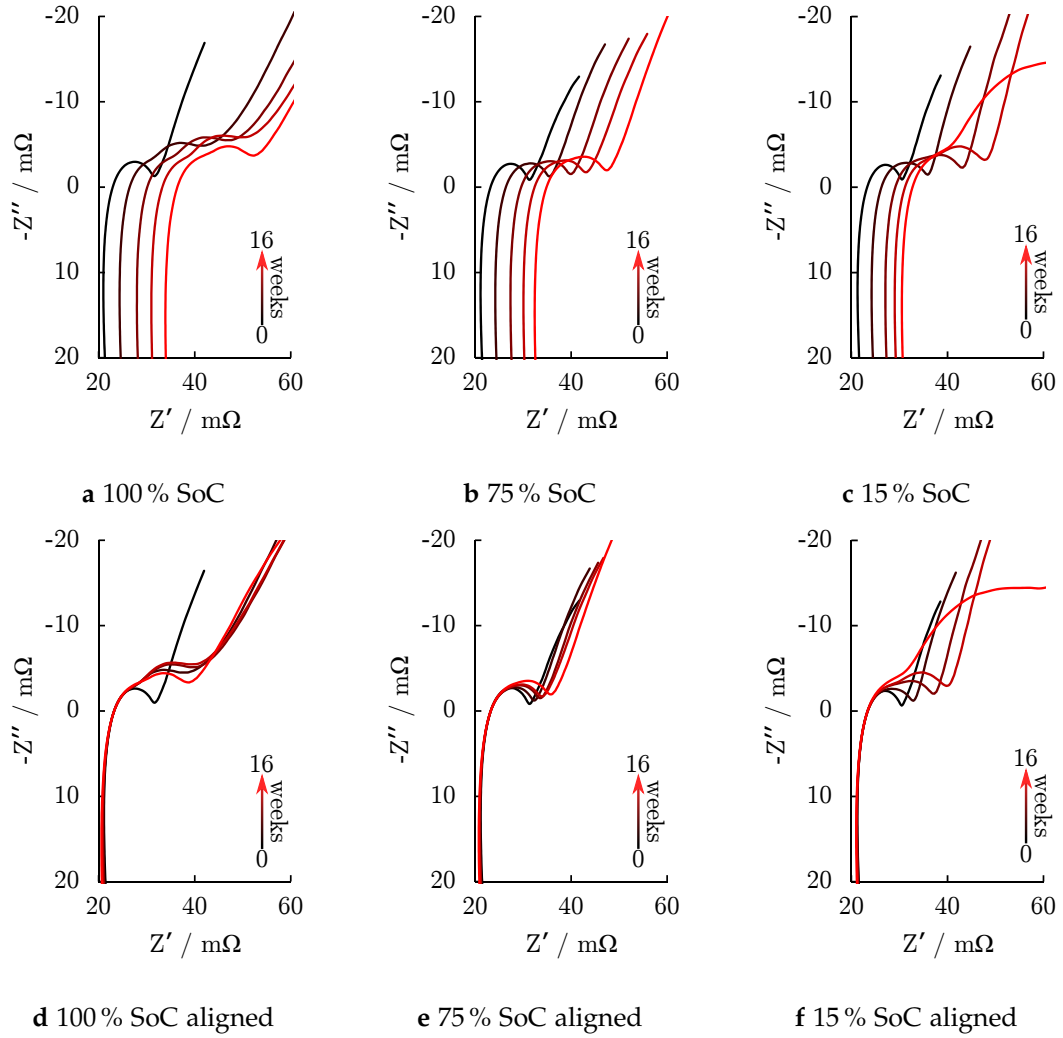

a 100 % SoC **b** 75 % SoC **c** 15 % SoC

d 100 % SoC aligned **e** 75 % SoC aligned **f** 15 % SoC aligned

Figure 6.7 – Nyquist plots of cell A 25 °C for various storage durations at 60 °C and 100 % SoC

active material, remains constant, indicating no changes in the cell's kinetic properties. For the spectra measured at 75 % SoC, no second semi-circle appears but the semi-circle radii increase and the minimum is shifted linearly towards higher Z' and Z'' values. For the nearly discharged cell at 15 % SoC a similar effect is observed in the beginning and the semi-circle radii increase. With continuous degradation, a second semi-circle occurs and for the last measurement set, the radius increases significantly, superimposing the linear slope at the low frequency range of the spectra.

The resistance of the cell ($Z'' = 0$) varies with the SoC of the cell. While the variation is rather small at the BoL of the cell, considerable differences are observed after storing the cells for 16 weeks at elevated temperatures. Fig. 6.8 illustrates the increase in resistance during the ageing study, exemplified using the three different SoCs, namely 100 %, 75 % and 15 %. The resistances increase for all SoCs, but with a different slope and resistance increase of the fully charged cell is approximately 30 % higher as for the almost fully discharged cell. This leads to the assumption that the power capability of

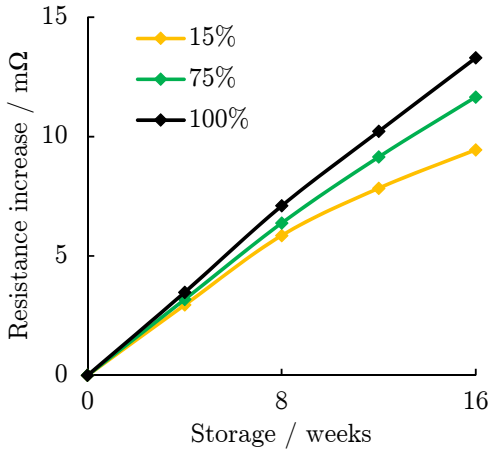

Figure 6.8 – Increase in $\Delta Z'$ at $Z'' = 0$ for different SoCs during the ageing study of cell A

the cell needs to be expressed as a function of SoC, whereas lower values towards the end of the discharge, as observed for cell A, are favourable.

By identifying and attributing the different time domains, a calculation of the cell balancing and the shifting due to electrode degradation might be possible in the same manner as demonstrated using DC measurement techniques such as DVA and ATM. But the resulting calculation might be superimposed due the technique's high sensitivity to the cell's geometry and the evoked AC current density distribution during the excitation as presented in Sec. 4. Unfortunately, the investigations presented in Sec. 4 are not possible for the commercial 18650 cells used in this work due to the cell's design, compromising just one tab pair. To give a valid statement regarding the applicability of EIS measurements as a reliable degradation tracking tool, detailed insights into local variations would be necessary to allow for a clear distinction, if the change in the EIS spectra can be attributed to a certain degradation mechanism or if the measurement is superimposed by local inhomogeneities affecting the local current distribution of the cell.

This leads to the conclusion that EIS is mainly useful to investigate electrochemical properties of various active materials on a lab-scale, e.g. in half-cells. But due to the significant remaining uncertainties, as the geometrical influence of the electrode windings and possible local variations in the degradation cannot be excluded, the applicability of impedance measurements as degradation tracking tool in real-life applications seems to be limited.

6.2.2 Differential voltage analysis

The DVA is calculated based on a C/20 discharge cycle at 25 °C, which was performed as a check-up during the ageing study as schematically shown in Fig 6.1. Distinct features are denoted as C_{I} and C_{II} for the cathode and A_{I} and A_{II} for the anode as illustrated in Fig. 6.9. The remaining capacity of the full-cell is determined during the discharge, which is, according to Fig. 6.9, the difference between the values A_{limit} and C_{limit}.

The prominent features of the anode are correlated to the phase transitions from

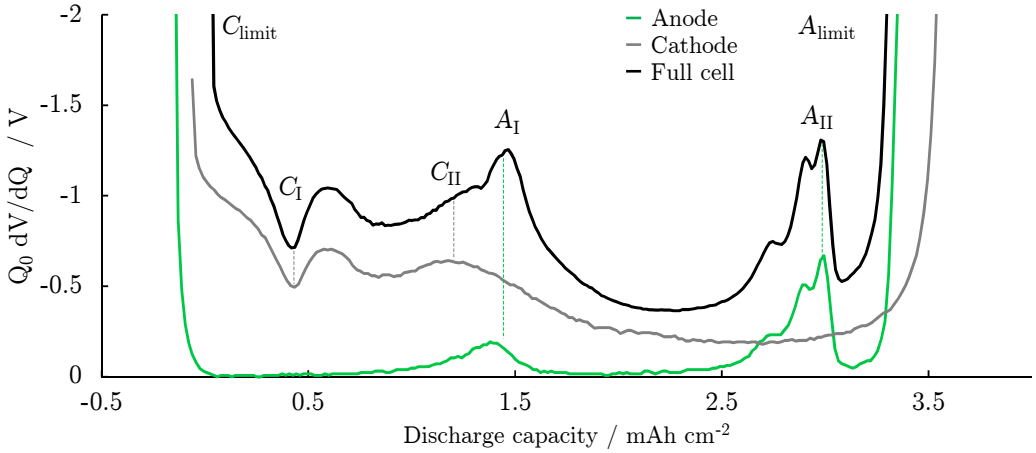

Figure 6.9 – Anode, cathode and full-cell DVA of a new cell B

stage 1 to stage 2 (A_I) and from stage 3 to stage 4 (A_{II}) [28, 53]. A decreasing distance between these two features is directly correlated to a loss of active material, lowering the specific capacity of the anode. The specific capacity fade for the cathode can be calculated accordingly, using the difference between C_{II} and C_I. Unfortunately, C_{II} occurs close to A_I and is superimposed in the full-cell DVA by the anode feature. A clear distinction of the maximum's position becomes difficult, if the relative positions of the peaks change. As an alternative, the difference C_I - C_{limit} is used. The cathode's potential increases during charge, while the anode's potential remains at the stage 1 - stage 2 plateau. Using a CV phase to fully charge the cell results in a constant degree of lithiation of the cathode during the ageing study. As the structural change indicated by C_I also occurs at a constant degree of lithiation throughout the ageing study, a decreasing distance between the two values can be used to evaluate the active material loss on the cathode. The correlation between the full-cell and half-cell DVAs, expressed in Eq. 3.7 is extended to

$$Q_{cell}(t)\frac{dV(x,y)}{dQ_{cell}} = Q_{cathode}(t)\frac{dV(x)}{dQ_{cathode}} + Q_{anode}(t)\frac{dV(y)}{dQ_{anode}} \tag{6.1}$$

whereas x is the degree of lithiation in the cathode and y the corresponding degree of lithiation in the anode. In literature, y is commonly expressed by $1 - x$, but in regard to ongoing degradation and changing amounts of accessible active material, this correlation is only valid for a cell's BoL. In addition, the change in capacity with time is expressed by $Q(t)$. During discharge, x increases and y decreases.

Fig. 6.10 presents the ageing study data of cell B. To allow for a clearer distinction, the DVA curves in all sub-figures were separated by 0.25 V. In a, the DVA after every 300 cycles up to 1800 cycles is shown. In b the data sets after every four weeks of the cells stored at 60 °C are shown for up to 24 weeks. In both scenarios, a capacity fade of the cell is observed. Only minor changes in the position of the two anode features A_I and A_{II} are observed, while C_I significantly shifted towards A_I.

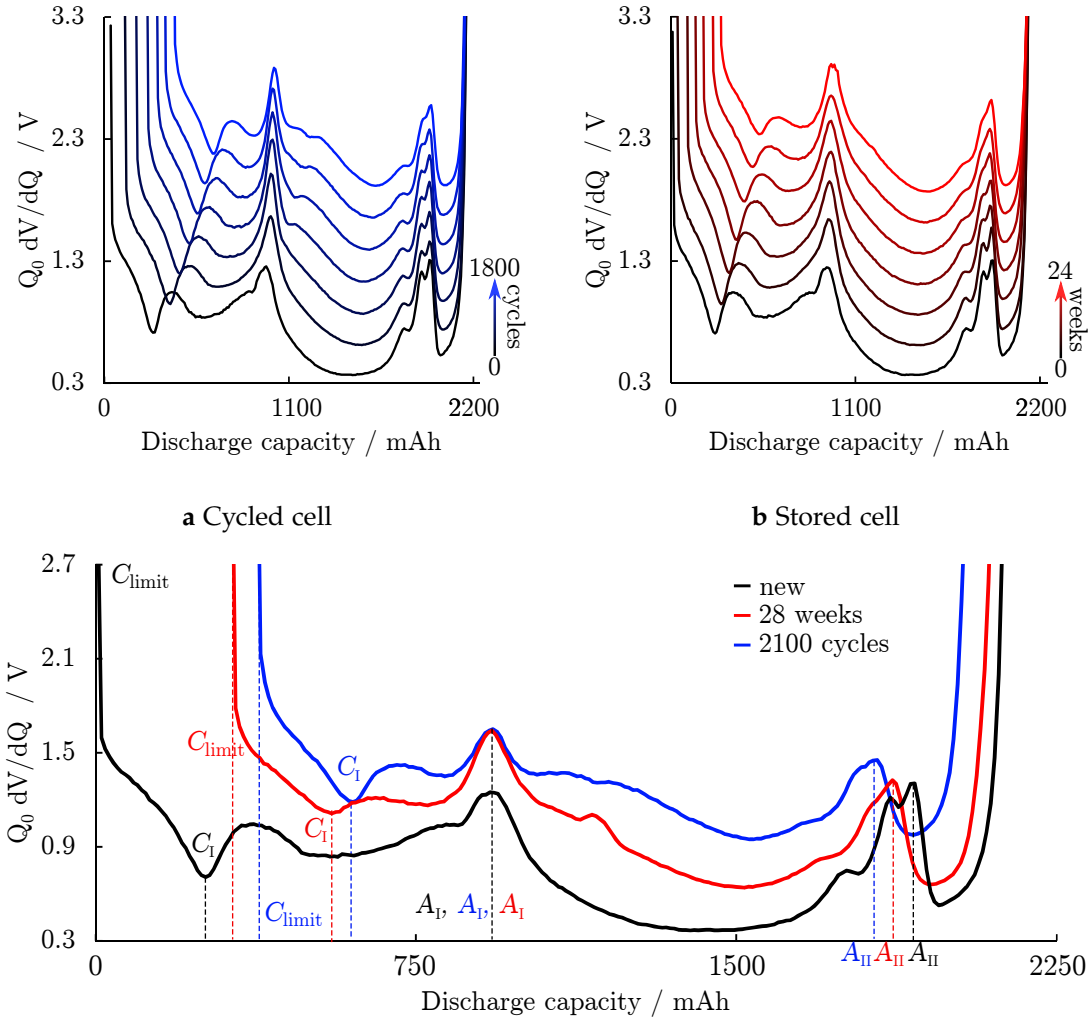

Figure 6.10 – DVA of cell B every 300 cycles a, every 4 weeks of storage b and final comparison between BoL and EoL c. Please note that the curves in all sub-figures were separated by 0.25 V for purposes of illustration

Fig. 6.10c compares the DVA at BoL and EoL for both cells to analyse the changes in detail. Due to the high similarity and reproducibility of the DVA from new cells, only one data set is shown. The specific characteristics of anode and cathode, identified in Fig. 6.9, are highlighted as C_{I}, C_{limit}, A_{I} and A_{II}. To emphasise the differences between the curves, the data sets were aligned in A_{I}. ΔC, the difference between $C_{\mathrm{limit}} - C_{\mathrm{I}}$ is used to calculate the LAM in the cathode during the study. The LAM in the anode is calculated by $\Delta A = A_{\mathrm{II}} - A_{\mathrm{I}}$ accordingly.

The ratio of intercalated lithium in cathode and anode at a certain SoC at BoL changes when lithium is consumed in side reactions. Therefore, the loss of lithium inventory will lead to a misalignment of the two electrodes and the operating range of the electrodes, as indicated in Fig. 6.9 will change. As the structural changes in the respective electrodes occur always at a defined degree of lithiation, the misalignment can be used to calculate the resulting capacity fade. LLI results in a shrinking width of the stage 1 – stage 2 phase in the graphite, as the amount of intercalated lithium becomes smaller when the cell is fully charged, leading to a faster transition into the stage 2 – stage 3 phase during discharge. This is observed by the decreasing distance between the anode and cathode characteristics and the misalignment is calculated from the shift between A_{I} and C_{I}.

The uneven degradation rate of both electrodes will also lead to a decreasing distance between A_{I} and C_{I}. Consequently, to calculate the LLI in the cell, the misalignment in the cell balancing needs to be compensated by the LAM of the electrodes. The specific capacities of the cells at BoL and EoL are given in the upper part of Tbl. 6.2. Half-cell measurements from new cells are compared to measurements performed during the post-mortem study and the capacity of each electrode was determined to evaluate the respective capacity fade.

As stated, the loss of capacity is 8.8 % for the anode and 13.2 % for the cathode for the cycled cell and 3.4 % and 9.7 % for the stored cell respectively. The positions of the distinct features and the calculated values for ΔC, ΔA and the misalignment are stated in the lower part of Tbl. 6.2. Based on these features, the capacity fade of each electrode and the misalignment due to LLI is calculated. The resulting changes in the operating range are schematically drawn in Fig. 6.11. The structural changes in anode and cathode are highlighted and the operating range of the new cell with $3.32\,\mathrm{mAh\,cm^{-2}}$ is defined as 100 %. For the cycled cell, a capacity fade of 9.5 % for the anode and 11.4 % for the cathode are calculated. The additional misalignment leads to a calculated over-all capacity fade of 22.8 %, which agrees well with the measured data of 22.3 %. For the stored cell, the capacity fade of anode and cathode is calculated to be 5.7 % and 7.5 % respectively.

Fig. 6.12 depicts the DVA half-cell data of the cathode and anode at BoL and EoL. The data are plotted versus the respective half-cell voltage and analysed, if changes in the structural transitions are observable without a distortion by the capacity fade.

In a, for low degrees of lithiation (above 4.2 V) in the cathode, deviations between the new and the degraded states are observed, whereas the slope for the cycled cells increased and for the stored cells decreased. The amplitude of the local extrema of the stored cell at 4.1 V became smaller and new one occurred at 3.6 V. While the origin for the second one remains unclear, the decreasing amplitude can be attributed to cation

Table 6.2 – Capacities and capacity fade evaluated by half-cell measurements and calculated by DVA at BoL and EoL for cells B 4_{cyc} and B 4_{cal}

	new	B 4_{cyc}	B 4_{cal}
Capacity Cell / mAh cm^{-2}	3.32	2.57	2.80
Capacity loss / %		22.3	15.3
Capacity anode / mAh cm^{-2}	4.11	3.75	3.97
Loss anode / %		8.8	3.4
Capacity cathode / mAh cm^{-2}	4.00	3.48	3.61
Loss cathode / %		13.2	9.7
	DVA	DVA	DVA
Position A_I / mAh	936	936	936
Position A_{II} / mAh	1921	1827	1865
Position C_{limit} / mAh	8	383	327
Position C_I / mAh	262	608	562
Distance A_{II} - A_I / mAh	985	891	929
Distance C_I - C_{limit} / mAh	254	225	235
Distance A_I - C_I / mAh	678	328	374
Loss anode calculated / %		9.5	5.7
Loss cathode calculated / %		11.4	7.5
Misalignment / mAh		327.3	286.0
Misalignment / %		14.6	12.8

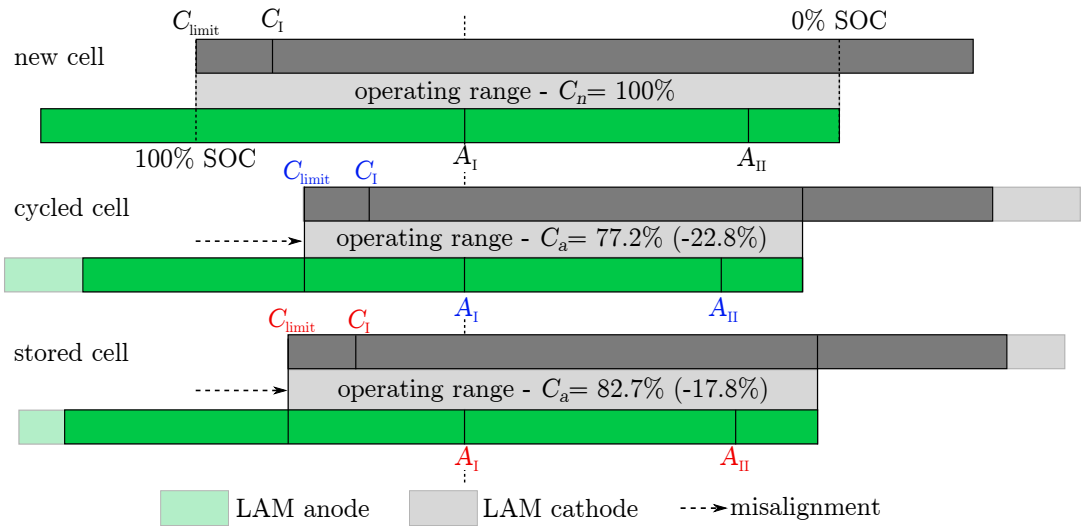

Figure 6.11 – Capacity fade determination of cell B by means of DVA

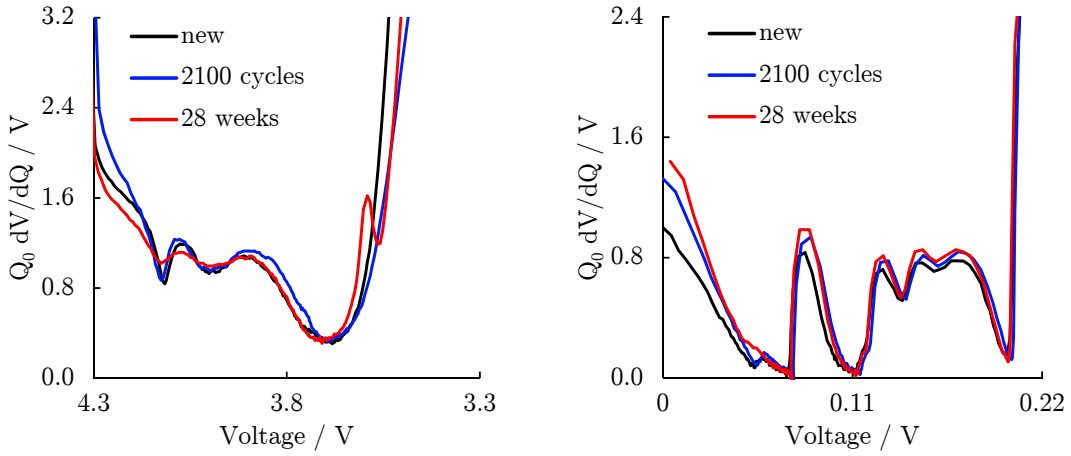

a DVA Cathode **b** DVA Anode

Figure 6.12 – Half-cell DVA of cell B at BoL and EoL

mixing during the storage at elevated temperatures, blocking the diffusion path in the NMC and lowering the cell performance [32, 200]. For the anode b, the DVA matches well for the three different states. No significant changes are observed, except a small increase in the slope for the aged cells towards full lithiation at 0 V, evoked by the thicker SEI and the accompanying higher overpotential.

6.2.3 Advanced thermodynamic measurements

Advanced thermodynamic measurements (ATM) are used to characterise the cell during the ageing study and were performed with a larger number of SoCs to analyse the degradation mechanisms at BoL and EoL. In analogy to the DVA in the previous section, the full-cell properties are expressed as the sum of their respective electrodes and Eq. 3.11 is extended by the variables x and y to include the variation in active material and degree of lithiation during the ageing study. The full-cell entropy is expressed by

$$\Delta_r S_{cell}(x,y) = \Delta_r S_{cathode}(x) + \Delta_r S_{anode}(y) \tag{6.2}$$

The change in entropy $\Delta_r S$ is driven by the configurational entropy S_{conf}, defined by distribution possibilities of the lithium-ions within the active material and the calculated values are given per mole. As a result, a loss of active material does not change the magnitude of the calculated value nor is a normalization required to compare full- and half-cells. Furthermore, structural changes can be observed, presumed that they are electrochemically reversible. The obtained data from a full-cell as well as from anode and cathode half-cells are illustrated in Fig. 6.13 and the specific characteristics of anode and cathode contributing to the full-cell profile are identified.

For the anode, the structural changes are assigned as A_{I} and A_{II} and the fully delithiated state, limiting the discharge process, is denoted as A_{limit}. For the cathode, two local maxima at the beginning of discharge are identified and highlighted with C_{I} and C_{II}. In contrast to the DVA, C_{II} and A_{I} are clearly distinguishable in the full-cell

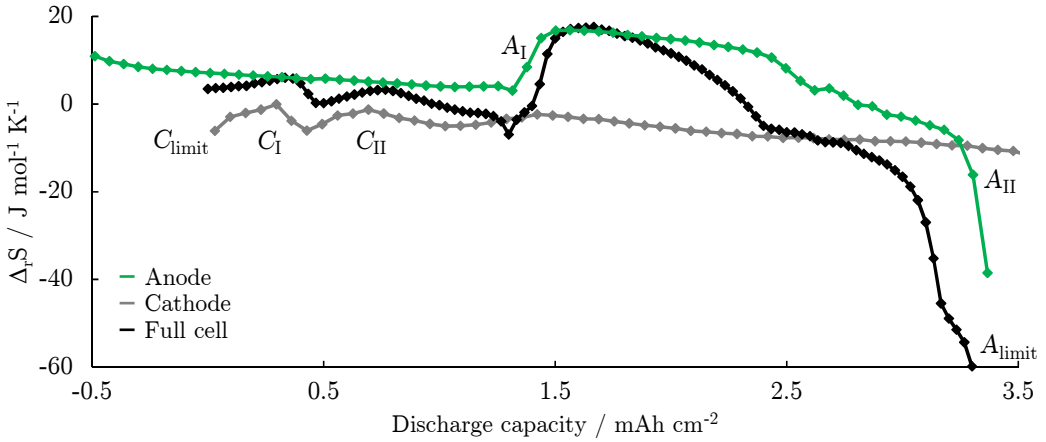

Figure 6.13 – Anode, cathode and full-cell ATM of a new cell B

profile. In addition, the delithiated cathode, limiting the charge process, is indicated by C_{limit}. Due to the lower number of data points the data were interpolated to identify the position of each feature.

The capacity fade is determined to be 24 % for the cycled cell and 16.3 % for the stored cell. The progress of the degradation and its effect on the thermodynamic properties of the cell is presented in Fig. 6.14. The data after every 600 cycles a and after every 8 weeks of storing at 60 °C b are shown. The data sets in a and b are separated by 1 J mol^{-1} K^{-1} for purposes of illustration. The capacity fade is accompanied by a shift of A_I towards a higher SoC, indicating a lower utilization of the stage 1 – stage 2 plateau. In addition, the distance between the two cathode features is observed to become smaller.

In Fig. 6.14c, the comparison between BoL and EoL are shown. The highlighted features are used in the same manner as for the DVA to calculate the capacity fade for each electrode as well as the respective misalignment of the electrodes. The data are aligned in A_I. In addition to the full-cell capacities, the results of half-cell measurements of both anodes and cathodes are given to analyse the LAM of the electrodes. The obtained results are listed in Tbl. 6.3 together with the positions of the various anode and cathode features. As an advantage compared to DVAs, the ATM curve exhibits two distinct cathode features C_I and C_{II}, which are used to calculate the active material loss. Using C_{limit} as done before is acceptable as long as the capacity fade does not exceed the capacity of the anode's stage 1 - stage 2 plateau. If the cathode's capacity fade exceeds this value, the anode will not be lithiated above 50 % and the phase transition will not occur. An increase of the cathode's charge cut-off voltage by approximately 40 mV, the difference between the two anode plateaus will be the result. This will lead to a higher delithiation of the cathode and to a falsification of the result as C_{limit} will be shifted. For an accurate calculation, a high number of data points is necessary to minimise the inaccuracy of the measurement. The initial characterisation at BoL requires a higher number of data points in the expected SoC range to allow for a detailed profile used for reference. During reoccurring check-ups, the number of data points can be reduced as long as a meaningful interpretation of the data is possible as a certain inaccuracy is

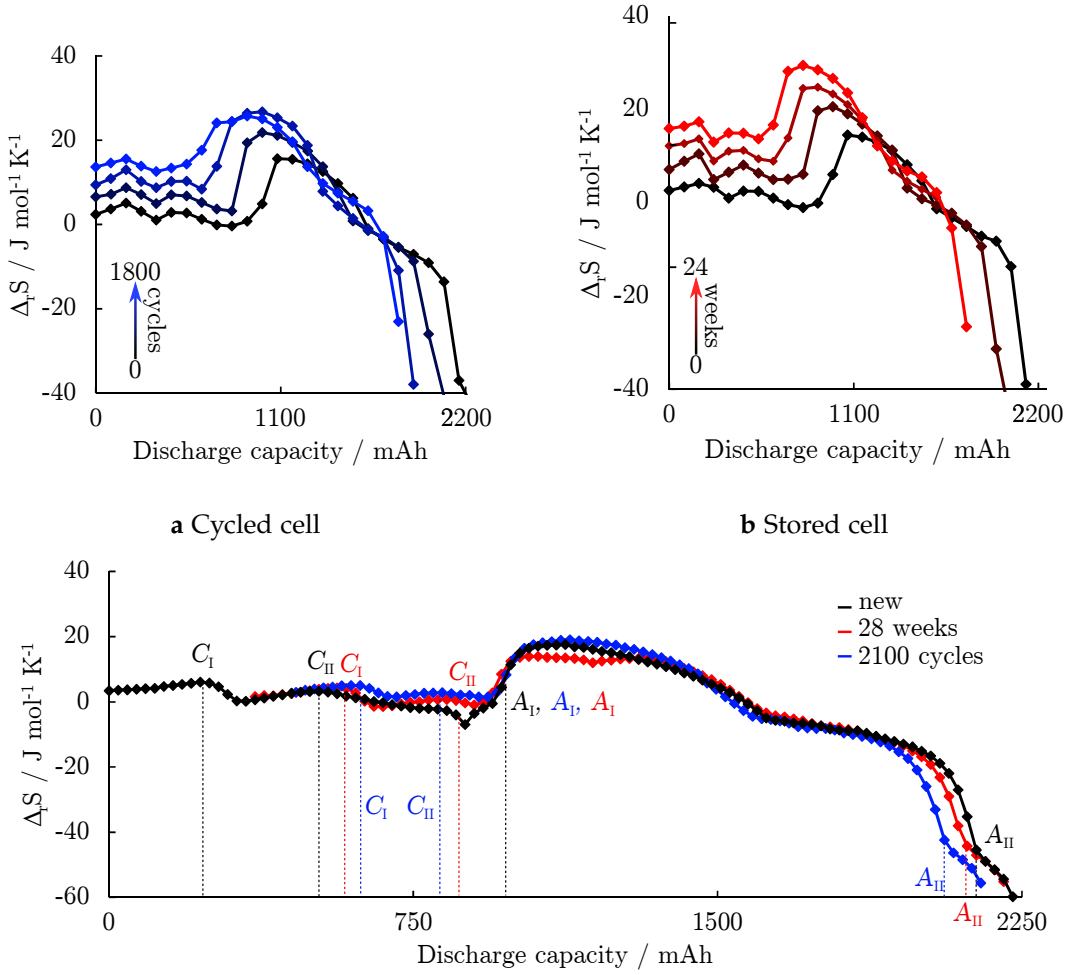

a Cycled cell

b Stored cell

c Comparison between new and degraded state

Figure 6.14 – Thermodynamic characterisation of cell B every 600 cycles a, every 8 weeks of storage b and final comparison between BoL and EoL c Please note that the curves in a and b were separated by 1 J mol^{-1} K^{-1} for purposes of illustration

acceptable. For the final characterisation at EoL, again, a higher number of data points is desirable, e.g. to allow for an accurate SoH determination to estimate the resale value of the cell.

The calculated capacity fade for the cathodes is 16.7 % for the cycled and 10.4 % for the stored cell. While the value for the stored cell is in well agreement with half-cell measurements, the difference for the cycled cell is 2.2 %. This difference is assumed to origin from an inhomogeneous degradation of the material, leading to uncertainties in the measurement and will be discussed shortly in the next section. The differences between the measured and the calculated values of the anode's capacity fade (8.9 % and 3.5 %) are comparably small.

The loss of lithium inventory and the loss of active material in both electrodes is higher for the cycled cell, which is expected as the cycled and stored cell's had

Table 6.3 – Capacities and capacity fade evaluated by half-cell measurements and calculated by ATM at Bol and EoL for cells B 1_{cyc} and B 1_{cal}

	new	B 1_{cyc}	B 1_{cal}
Capacity Cell / mAh cm^{-2}	3.30	2.48	2.73
Capacity loss / %		24.0	16.3
Capacity anode / mAh cm^{-2}	4.11	3.7	3.94
Loss anode / %		9.9	4.1
Capacity cathode / mAh cm^{-2}	4.00	3.42	3.55
Loss cathode / %		14.5	11.3
	ATM	ATM	ATM
Position A_I / mAh	975	975	975
Position A_{II} / mAh	2160	2055	2118
Position C_I / mAh	247	599	569
Position C_{II} / mAh	517	824	811
Distance ΔA / mAh	1185	1080	1143
Distance ΔC / mAh	270	225	242
Distance A_I - C_I / mAh	728	376	406
Loss anode calculated / %		8.9	3.5
Loss cathode calculated / %		16.7	10.4
Misalignment / mAh		320.7	301.0
Misalignment / %		14.4	13.6

different degradation rates, resulting in different remaining capacities at EoL of the cells. Nevertheless, comparing both ageing techniques, it is concluded that LLI and LAM contribute equally to the capacity fade of the cycled cell, whereas the cathode degradation was significantly higher as the anode degradation. For the stored cell, the side reaction rate was accelerated by storing the cell at 60 °C at 100 % SoC. As a result, an increasing share of LLI on the overall capacity fade compared to the cycled cell is observed. The degradation rate of the anode is smaller as for the cathode. It is assumed that the absence of mechanical stress in the anode, which occurs in the cycled cell, helps to maintain the protecting passivation layer. On the other hand, the high capacity fade on the cathode indicates a high rate of metal dissolution, which, as discussed in Sec. 2.3.3 results in an increase in SEI thickness due to the catalysing effect of the metal, once it is deposited on the anode. The degradation of each electrode and the capacity fade due to the misalignment of the cell is depicted in Fig 6.15. The calculated values for the capacity fade of the cycled (25.2 %) and stored cell (17.1 %) are slightly higher than the measured values (24.0 %, 16.3 %) but within the expected range of uncertainty.

The reliability of ATMs highly depends on the identification of various structural changes within the material during cycling. To investigate if these structural changes at BoL are the same as for the EoL or if other unexpected phase transitions occur, are the cathode a and anode b half-cell measurements at BoL and EoL for both ageing procedures depicted in Fig. 6.16. The data are presented versus the OCV to compensate for the capacity fade of the active material. A small difference in the profile of the stored

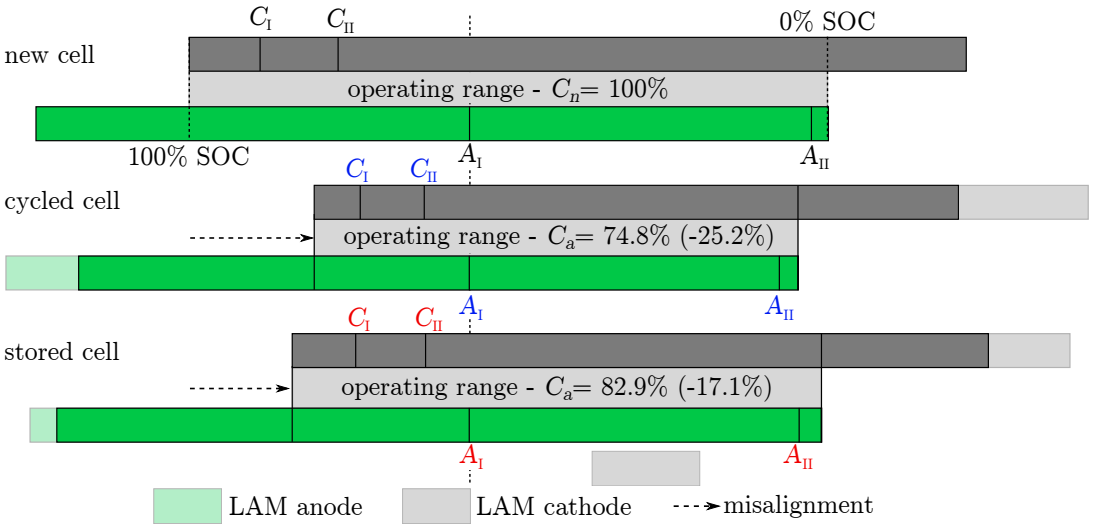

Figure 6.15 – Capacity fade determination of cell B by means of ATM

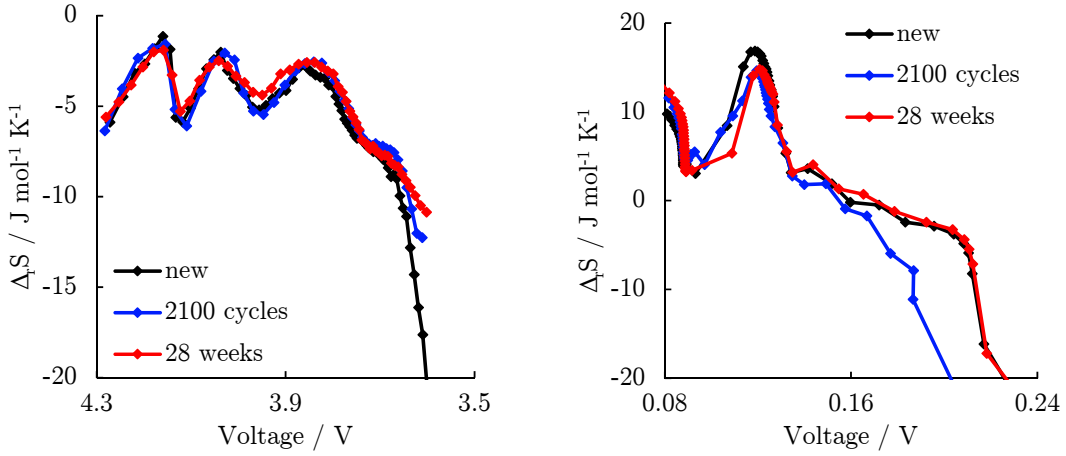

a Cathode ATM **b** Anode ATM

Figure 6.16 – ATM half-cell measurements of cell B at BoL and EoL

cathode is observed between 4 V to 3.9 V where the values are not as low as for the new and cycled cell. Below 3.6 V, the new cell reaches $-20\,\mathrm{J\,mol^{-1}\,K^{-1}}$ whereas both degraded cells reach only $-11\,\mathrm{J\,mol^{-1}\,K^{-1}}$ and $-13\,\mathrm{J\,mol^{-1}\,K^{-1}}$. Based on the results presented in Fig 6.6, this degree of lithiation is not reached during the full-cell measurement. Therefore, changes in the cathode in this range will not affect the full-cell profile. It is also not expected to affect the full-cell profile during the ageing, as the LLI is nearly as large as the capacity fade of the cathode, preventing the cathode to reach the mentioned degree of lithiation.

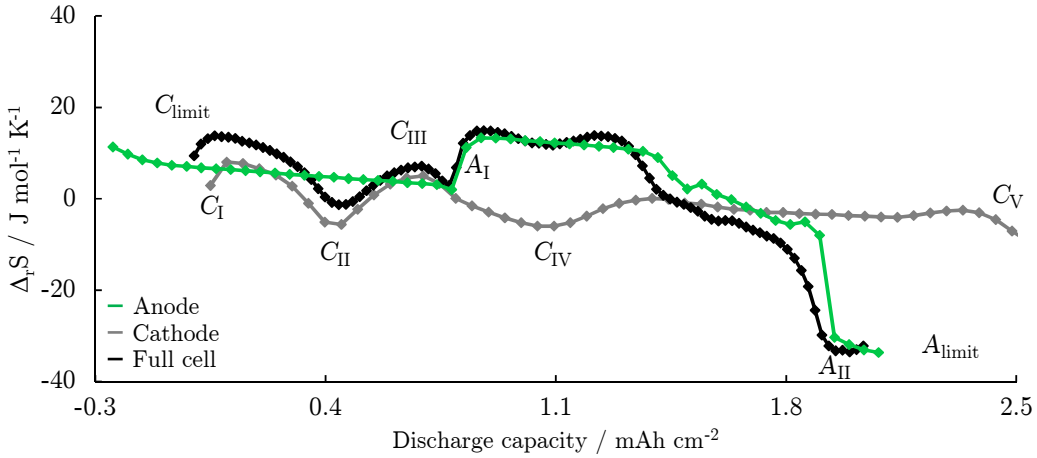

Figure 6.17 – Anode, cathode and full-cell ATM of a new cell A

6.3 Application on blended cathode materials

The electrode of cell A was determined by XRD, XPS and ICP measurements to consist of a NCA-LMO with a 3:1 ratio. Fig. 6.17 illustrates the entropy profile of cell A.

Beside the previously described anode features A_I and A_{II} and the limits of the operating range A_{limit} and C_{limit}, various cathode features C_I - C_V are highlighted. First principle calculations by van der Ven and co-workers [211] and experimental data presented by Bach et al. [15] and by Kashiwagi et al. [102] of the thermodynamic properties of LMO lead to the conclusion that the cathode features C_I - C_{III} can be attributed to the spinel materials. Despite the diverse statements in literature regarding the structural changes [4, 123, 175], C_{IV} and C_V are believed to belong to NCA, as it agrees well with the expected major intercalation potential of the material. As no thermodynamic data of pure NCA is known to be published, it remains unclear if the feature C_{III}, assigned to LMO is superimposed by NCA.

Fig. 6.18 depicts the changing characteristics of cell A during cycling with 1C at 25 °C a and storage at 100 % SoC at 60 °C b. For a clearer distinction, the curves were separated by 1 J mol^{-1} K^{-1} for purposes of illustration.

In Fig. 6.18c, the data are shown for the BoL and for the EoL for both ageing procedures after 2700 cycles and 32 weeks of storage. The data were aligned using the point with the steepest gradient in A_I. In the profile of the new cell, the cathode feature denoted as C_V in Fig. 6.17 does not occur, as the cathode does not reach the required degree of lithiation in the full-cell arrangement. For the cycled and the stored cell, feature C_{III} nearly disappears and is superimposed by the anode feature A_I due to the misalignment of the electrodes. The cycled cell depicts a similar behaviour as the new cell between C_I and C_{II}. The steep increase between 500 mAh to 700 mAh up to 22 J mol^{-1} K^{-1} is followed by a nearly linear decrease before the value drops to –34 J mol^{-1} K^{-1} at A_{II}.

Tbl. 6.4 lists the positions of the various anode and cathode features of the new and aged cells after the data were aligned in A_I as shown in Fig. 6.18c. The LAM calculated based on the decreasing distance $\Delta A = A_{II} - A_{II}$ for the anode as well as

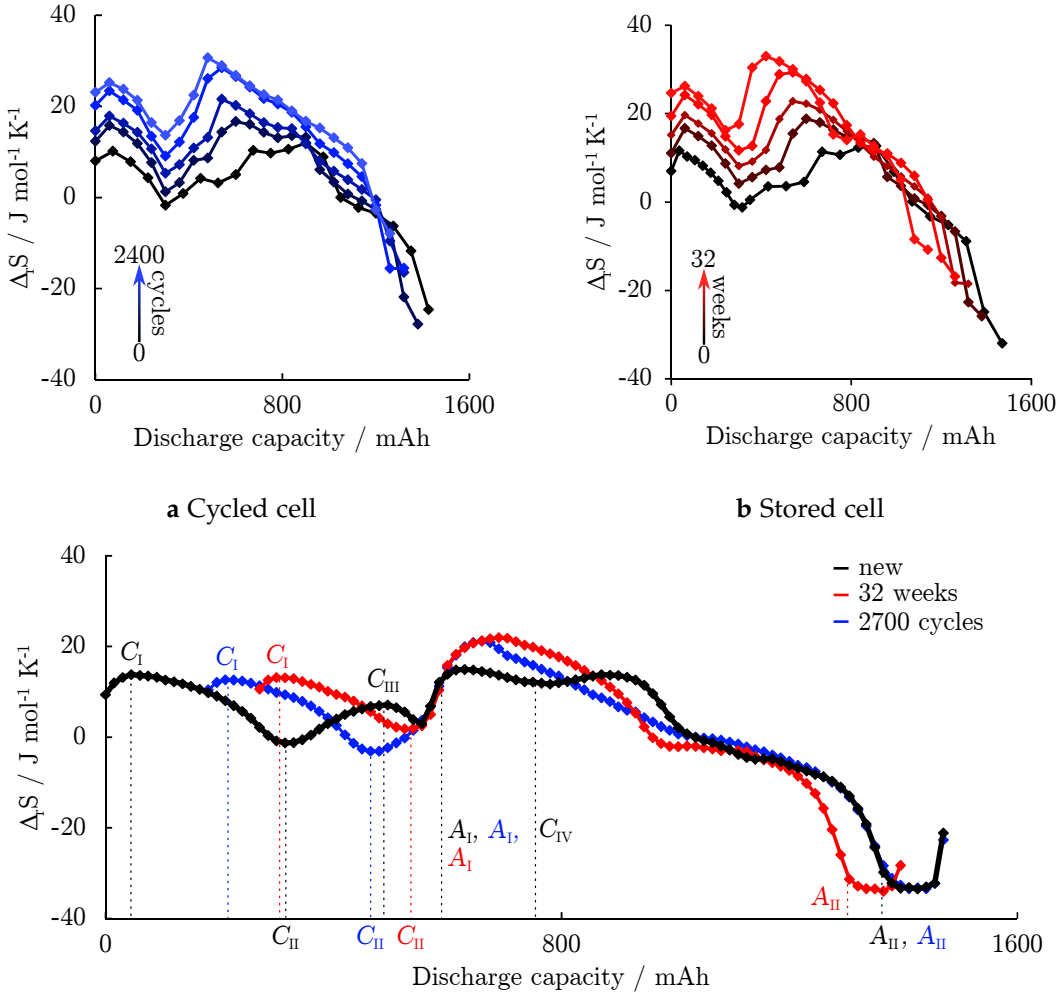

Figure 6.18 – Thermodynamic characterisation of cell A every 600 cycles a, every 8 weeks of storage b and final comparison between BoL and EoL c. Please note that the curves in a and b were separated by $1\,\mathrm{J\,mol^{-1}\,K^{-1}}$ for purposes of illustration

$C_{\mathrm{II,I}} = C_{\mathrm{II}} - C_{\mathrm{I}}$ for the cathode is given together with the misalignment due to LLI. Half-cell measurements of new and aged electrode samples are used to validate the calculations.

The measured capacity fade is 14.7 % for the cycled and 21.3 % for the stored cell. Based on the half-cell measurements, the loss of active material on the anode is rather low with 2.4 % for the cycled and 4.5 % for the stored cell. In contrast to the cell B, the capacity loss for the stored electrode is higher as for the cycled one. For the stored cell, the calculated capacity fade of 5.0 % agrees well. No LAM was observed in the ATM of the cycled cell as the distance ΔA remained constant. It is assumed that this rather unexpected discrepancy may result from a combination of two uncertainties. On the one hand from the half-cell measurements, where a loss in active material due to delamination during the building process can lead to a capacity fade. On the other hand

Table 6.4 – Capacities and capacity fade evaluated by half-cell measurements and calculated by ATM at begin and end of life of cell A

Cell A	new	cycled	stored
Position A_{I} / mAh	570	570	570
Position A_{II} / mAh	1380	1380	1341
Position C_{I} / mAh	45	235	307
Position C_{II} / mAh	315	468	538
Position C_{IV} / mAh	770	705	725
Distance ΔA / mAh	810	810	771
Distance $C_{\mathrm{II,I}}$ / mAh	270	233	231
Distance A_I - C_I / mAh	525	335	263
Distance $C_{\mathrm{IV,I}}$ / mAh	725	470	418
Capacity / mAh	1479	1262	1164.7
Capacity loss / %		14.7	21.3
Capacity anode half-cell / mAh	2.47	2.41	2.36
Loss anode half-cell / %		2.4	4.5
Loss anode ATM / %		0.0	5.0
Capacity cathode half-cell / mAh	2.35	2.00	2.04
Loss cathode half-cell / %		15.0	13.2
Loss cathode ATM / %		13.7	14.4
Misalignment A_I - C_I / mAh		161.9	214.9
Misalignment A_I - C_I / %		10.9	14.5

due to the uncertainty of the ATM itself.

The degradation of the cathode was observed to be significantly higher, whereas the cycled cathode lost 15.0 % of the active material and the stored cathode 13.2 %. The calculated values of 13.7 % and 14.4 % are very similar, whereas the capacity fade was slightly underestimated for the cycled cell and overestimated for the stored cell. A possible explanation might a difference in the degradation rate of both materials, discussed in more detail in Sec. 6.5.2.

Fig. 6.19 illustrates the ATM data of the cathodes from cell A, plotted versus the OCV of the half-cell a and versus the specific discharge capacity 6.19b for the new state as well as for both ageing studies after the material was harvested at the EoL. The features C_{I}, C_{II} and C_{IV} are shown, whereas the first two were assigned to LMO and the third to NCA.

Between 4.3 V and 3.9 V, the entropic coefficients range from 7.5 $\mathrm{J\,mol^{-1}\,K^{-1}}$ for the new and 15 $\mathrm{J\,mol^{-1}\,K^{-1}}$ for the stored cell down to −7.5 $\mathrm{J\,mol^{-1}\,K^{-1}}$, and the sign of the entropic values changes multiple times, indicating a transition from an endothermic to exothermic reaction, driven by the configurational entropy in LMO. The local extrema still occur at the same intercalation potentials without a significant shift.

For the stored cell, the local minimum at C_{II} increases and the maximum at 4.05 V (C_{III}) decreases. A possible explanation is assumed to be the accelerated degradation rate of LMO at elevated temperatures. If C_{III} is a superposition of structural changes in LMO and NCA, a change in the ratio of the materials due to an accelerated ageing would increase the effect of the NCA with a lower number of possible lithium-ions

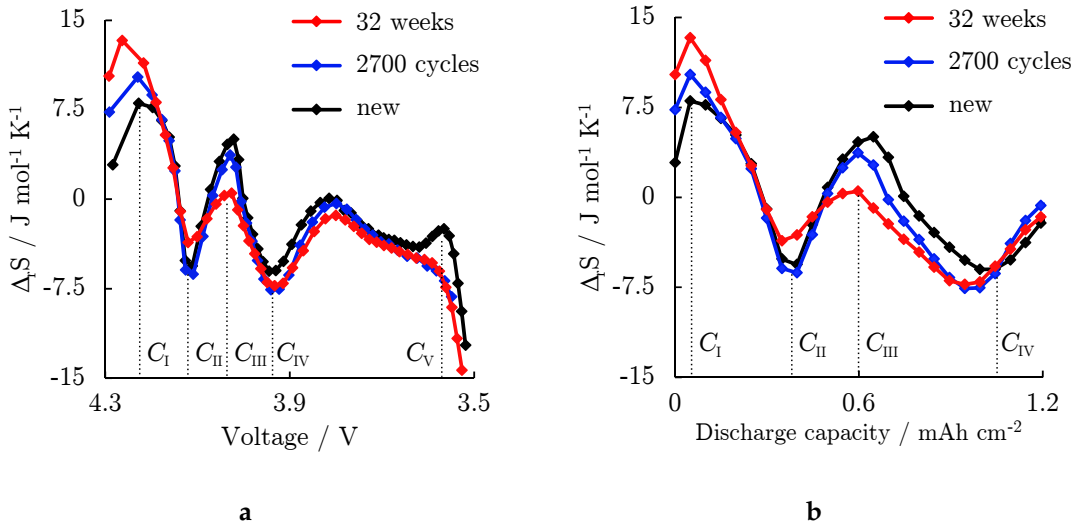

Figure 6.19 – Comparison of ATM of cell A's cathode plotted versus the OCV a and discharge capacity b at BoL and EoL

configurations within the host structure. Below 3.8 V, the values continuously decrease and the local maximum, previously denoted as C_V at 3.55 V vanishes for both of the aged cells.

In Fig. 6.19b the focus is set on the first 1.2 mAh cm^{-2} during the discharge of the half-cells. The previously made assumption is supported by the decreasing distance $\Delta C_{II,I}$ for the stored cell, whereas its remains constant for the cycled cell. The measurement indicates that the cycled cell suffered a lower LMO material loss compared to the stored cell. In contrast, the lower values for $\Delta C_{IV,I}$ might indicate a higher degradation of the NCA for the cycled cell.

6.4 Application on two-phase cathode materials

Fig. 6.20 displays the results of the ATM of anode, cathode and full-cell of cell C with a LFP cathode and graphite anode. The cells are compared using the specific capacity of the cell in mAh cm^{-2} and the half-cell profiles are shifted to match the full-cell profile.

Similar to the other investigated cells, the cathode limits the charge process and the anode limits the discharge process, indicated as C_{limit} and A_{limit}, respectively. The thermodynamic properties of the anode dominate the full-cell behaviour and the phase transition in the graphite, observed as a step in the profile, indicated by A_{I}, is well observable in the full-cell profile. The decrease from 10 J mol^{-1} K^{-1} to –20 J mol^{-1} K^{-1} towards lower degrees of lithiation in the anode is also mainly driven by the thermodynamic properties of the anode.

The fully delithiated cathode material ($FePO_4$) shows a strong increase from –20 J mol^{-1} K^{-1} to 6 J mol^{-1} K^{-1} for a small change in lithiation, caused by an anomaly in the configurational entropy in the disordered phase [231]. For further lithiation, $\Delta_r S$ decreases with a constant slope, becomes negative for $Li_{0.15}FePO_4$ and reaches –12 J mol^{-1} K^{-1} for the

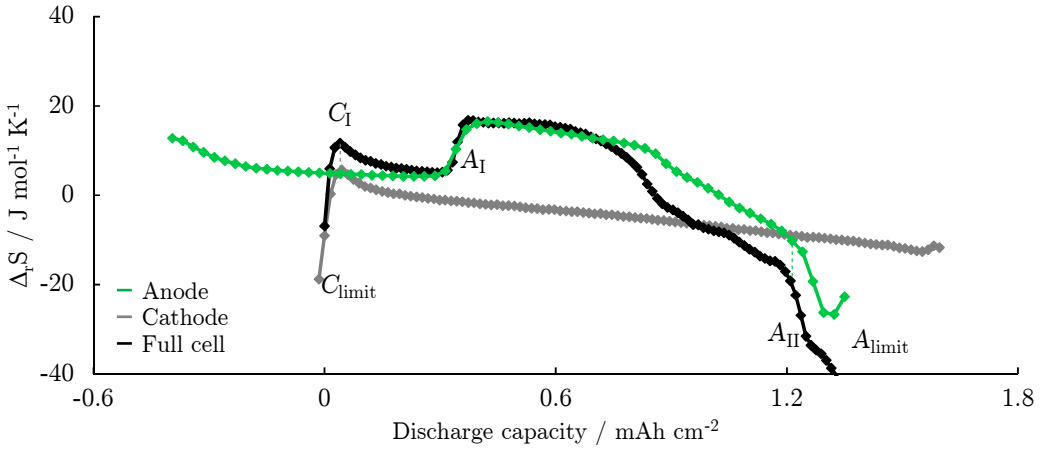

Figure 6.20 – Anode, cathode and full-cell ATM of a new cell C

fully lithiated state. The small increase at the end is assigned to originating from the disordered phase, when the material is fully lithiated.

A slope is characteristic for one-phase materials whereas two-phase materials are expected to exhibit a constant value of $\Delta_r S$. Possible explanations, presented by Dodd [57] include surface contributions originating from the changing surface-to-bulk ratio of nano particles during intercalation, quasi-equilibrium conditions, also responsible for the voltage hysteresis of LFP or unequal expansion of the particles during lithiation leading to thermal strains. Independent of the origins of the slope, due to the strong superposition of the anode characteristics, an extraction of the cathode profile from the full-cell profile remains difficult with the exception of the feature indicated by C_I.

The results of the ageing study are presented in Fig. 6.21 and the impact of the two different ageing approaches on the thermodynamic properties is compared. In a the data for the cycled cells are shown and in b the calendar aged cells. During the ageing study, calendar ageing lead to a fast capacity fade whereas the good cycle stability of the cells allowed more than 3000 cycles without significant capacity fade. The data obtained at BoL and EoL shown in Fig. c is used to identify the origins of the capacity fade. The characteristics C_I, A_I and A_II are indicated. To allow for a clearer observation of the differences, all three sets were adjusted to match A_I, equivalent to a 50 % lithiated anode.

A_I and A_II are used to calculate the capacity fade of the anode and A_I and C_I are used to calculate the misalignment caused by LLI. The respective values are listed in Tbl. 6.5. The capacity fade of the full-cells is compared with half-cells and the calculated values based on the ATM measurements. The electrochemically determined degradation of the anode using half-cells is in well agreement with the calculated values using the full-cell ATM profiles.

For the calendar aged cells, the capacity fade of anode and cathode is 2.6 % and 2.3 %, respectively. The calculated misalignment is responsible for capacity loss of 18.4 % whereas the capacity fade of the full-cell is measured to be 19.1 %. It can be concluded that the loss of active material contributes only to a negligible share to the overall capacity fade and that LLI, consumed in side reactions with the electrolyte is mainly responsible

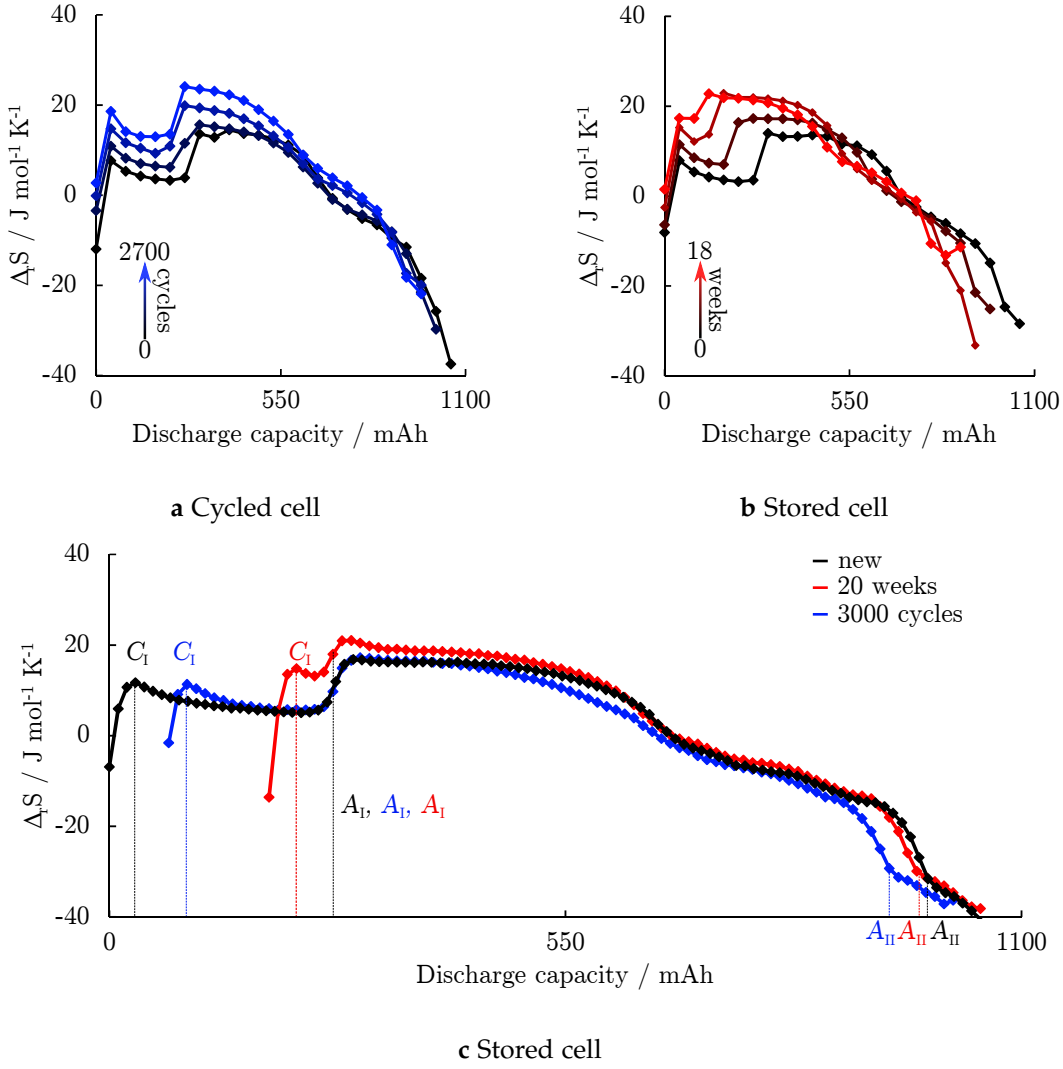

Figure 6.21 – Thermodynamic characterisation of cell C every 900 cycles a, every 6 weeks of storage b and final comparison between BoL and EoL c. Please note that the curves in a and b were separated by 1 J mol^{-1} K^{-1} for purposes of illustration

for the loss in capacity. This results meets the expectations as discussed in Sec. 2.3.1, where storage conditions of 100 % SoC and at 60 °C trigger the rate of side-reactions significantly. The discussed impact of iron dissolution on the cathode degradation might be still present, but is small as shown by the half-cell capacity measurements.

The capacity fade of the cathode harvested from the cycled cell is 2.8 % and nearly as large as for the stored cells. The capacity fade of the anode is determined to be 6.2 % and 2.5 times higher as for the stored cell. The misalignment calculated based on the shift of A_I and C_I results in a capacity fade of 5.5 %. In contrast to the stored cell, where LAM was only a minor contributor the overall capacity loss, the degradation of the anode cannot be neglected. The overbalancing enables the anode to compensate the loss without lowering the overall cell capacity, but will result in a shift of feature A_I towards lower SoC. Thus, it will partially compensate the decreasing distance between A_I and

Table 6.5 – Capacities and capacity fade evaluated by half-cell measurements and calculated by ATM at begin and end of life of cell C

Cell C	new	cycled	stored
Position A_I / mAh	273	273	273
Position A_{II} / mAh	987	943	970
Position C_I / mAh	31.5	93.5	231
Distance A_{II} - A_I / mAh	714	670	697
Distance A_I - C_I / mAh	241.5	179.5	42
Capacity / mAh	1061	946	858
Capacity loss / %		10.8	19.1
Capacity anode half-cell / mAh	1.91	1.77	1.86
Loss anode half-cell / %		7.3	2.6
Loss anode ATM / %		6.2	2.4
Capacity cathode half-cell / mAh	1.87	1.82	1.83
Loss cathode half-cell / %		2.8	2.3
Loss cathode ATM / %		/	/
Misalignment / mAh		58	194
Misalignment / %		5.5	18.4

C_I. This indicates that the calculated misalignment needs to be corrected by this shift. In combination with the anode degradation, both values match the overall cell capacity fade of 10.8 %.

As determined electrochemically by the half-cell measurements, the capacity fade of the cathode is less than 3 %. Even though thermodynamic data exhibit more information as DVA data, more distinct characteristics in the profile are necessary to make a precise statement, especially in case of such a small loss of capacity.

6.5 Limitations in accuracy

Both techniques, DVA and ATM, use structural transitions and the corresponding changes in the voltage behaviour of the cell and the respective electrodes to determine the current state of the electrode. As discussed, thermally stable and electrochemically equilibrated systems are needed to allow for a precise measurement. When applying these methods on degraded cells, certain aspects, which may reduce the accuracy of the measurement need to be considered.

6.5.1 Inhomogeneous degradation

In the post mortem investigation after the presented ageing study, numerous samples from anode and cathode were harvested from the different cells. As discussed in Sec. 3.3 and 3.5, a crucial requirement for accurate measurements is a homogeneous lithium-ion distribution in the host structure and thermally equilibrated conditions and eventually a well defined reference point to start the measurement. During the ageing of the cell, an inhomogeneous degradation will lead to uncertainties, as the characteristic features in the anode and cathode profiles will become a mixture of various states. For calendar

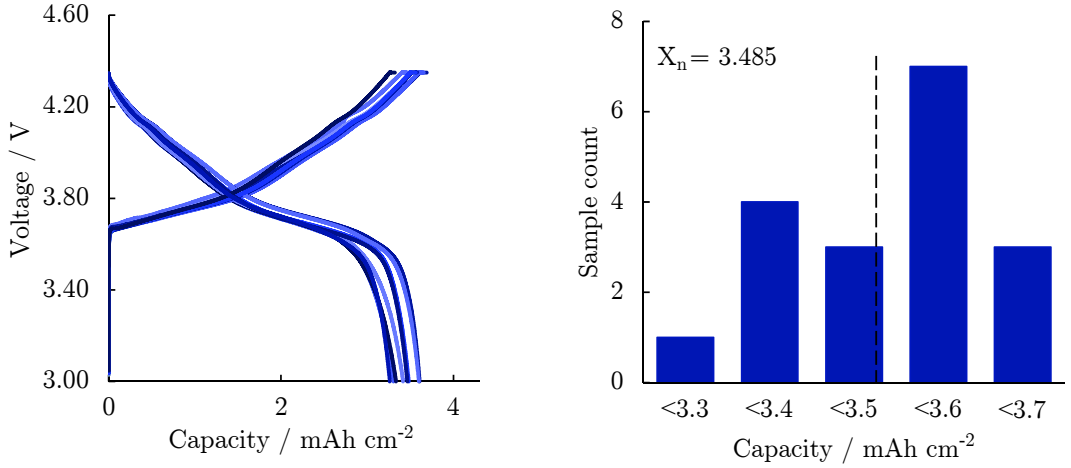

a Voltage of cathodes from cycled cell B

b Distribution of half-cell capacity

Figure 6.22 – 0.05C charge and discharge characteristic of cycled cathodes from cell B a at 25 °C and the resulting distribution of half-cell capacities b

aged cells stored at elevated temperatures, a homogeneous degradation is expected, as the enhanced side reaction rate is constant throughout the cell. Variations are more likely to occur during operation, as gradients in temperature and current density distribution can lead to an uneven utilisation of the material [68, 151, 157].

For the cycled cells, all anodes as well as the cathodes from cell A and cell C showed only small variations in the discharge capacity within a range of ± 1.5 %, similar to the deviations in measurements of new cells. These discrepancies are more likely to occur due to mechanical delamination during the assembly process than due to an inhomogeneous coating or degradation.

In Fig. 6.22, the charge and discharge voltages of numerous half-cells harvested from cell B 1_{cyc} are depicted in a and the resulting distribution of discharge capacities is shown in b. The capacities were determined during 0.1C cycles at 25 °C and the used electrode samples were extracted at random positions of the electrode. The average capacity is determined to be 3.485 mAh cm^{-2} with variations of more than ± 6 %.

As shown for the cycled cell B, variations during the ageing process can partially lead to local inhomogeneities in the electrode. Based on the measurement, careful statements regarding the accuracy of the applied method are required, as the measurements might be affected by inhomogeneous degradation due to the cell design and the operating conditions of the cell during its lifetime.

6.5.2 Blended cathodes

Blended cathodes, consisting of a mixture of two or more different active materials as NCA-LMO or NMC-LMO are used in numerous commercial cells to combine the advantages of the different materials [62, 192, 206]. As a result, the characterisation of the cell becomes difficult as features from anode and cathode are still distinguishable but the characteristics of the different cathode components may not. The different equilibrium

potentials of the cathode components can cause an asymmetric charge and discharge behaviour and the ratio in lithium concentration change can vary for the materials, if the lithium diffusion coefficient varies with changing SoC [128]. For ATM, the entropic coefficient of the respective cathode materials needs to be considered and included based on their respective ratio. Eq. 3.11

$$\Delta_r S_{cell} = \Delta_r S_{cathode} + \Delta_r S_{anode} \tag{3.11}$$

is extended for i components of active cathode materials

$$\Delta_r S_{cell}(x) = \Delta_r S_{anode}(x) + \sum_{1}^{i} \frac{n_i}{n} \Delta_r S_{cathode,i}(x) \tag{6.3}$$

whereas n_i/n defines the ratio of each component on the overall mass of active material. In addition to the mass ratio, the temperature coefficient of each material in dependence of its degree of lithiation x needs to be known to analyse the contribution to the overall cell voltage. For commercial cells, this information is not accessible and the specific stoichiometry varies for every manufacturer. Based on available literature, estimations can be made to identify and assign the various characteristics, but uncertainties remain, as variation in the synthesising process [226], stoichiometry [49, 111, 142] as well as particles size [99] can affect the structural properties of the electrode material and will result in a significant change of the thermodynamic properties. The temperature dependence of the equilibrium potential for the components a and b is expressed by

$$\begin{aligned} E_{eq,a}(x, T_2) &= E_{eq,a}(x, T_1) + \left(\frac{\partial E_{eq}(x)}{\partial T} \right)_a \Delta T \\ E_{eq,b}(x, T_2) &= E_{eq,b}(x, T_1) + \left(\frac{\partial E_{eq}(x)}{\partial T} \right)_b \Delta T \end{aligned} \tag{6.4}$$

whereas x refers to the extent of reaction of the full-cell. From Eq. 6.4 it becomes obvious that different entropic coefficients will lead to a potential difference between the two materials when the temperature is changed and the requirement for equilibrium

$$E_{cell} = E_a = E_b \tag{6.5}$$

is violated. Consequently, an equalisation current within the cathode will occur between the two active materials. The equilibrated cell voltage, measured at T_2, will correspond to a different degree of lithiation within both materials than the cell voltage measured at T_1. Considering these effects occurring in blended cathode materials, the interpretation of DVAs and ATMs results needs to be done carefully and a limitation of the temperature range is recommended.

6.6 Conclusion

An ageing study was performed on three different cells, using various cathode materials and graphite as anode material. The study is designed to simulate the accelerated degradation under operation and storage conditions. A set of lithium-ion cells was fully charged and discharged at 25 °C with 1C, and another set was stored at 60 °C and 100 % SoC. At pre-defined intervals, various check-ups as capacity check, DVA, ATM, CV and EIS were performed to track the continuous degradation of the cells. Due to the significant reduction in the measurement time, thermodynamic measurements became available as a characterisation technique to be used during the study. The loss of active material of both electrodes as well as the misalignment of the cell due to loss of lithium inventory is calculated, when the ageing study was finished. The obtained results were compared to the well-established differential voltage analysis and the accuracy of the measurements of both techniques was subsequently confirmed by post mortem analysis of the degraded cells. After proving ATM as a meaningful alternative to DVA, the results of the two other sets of lithium-ion cells were analysed and were confirmed, with some restriction for two-phase cathode materials, to be accurate.

Chapter 7

Conclusion

In the public discussion, an extended driving distance and a long cycle-life of the lithium-ion cells in the vehicle's battery pack are discussed as the crucial requirements for the acceptance of electric vehicles (EVs) as economically reasonable alternative to internal combustion engine vehicles (ICEs). However, a safe operation of the battery in the EV is taken for granted, even though a high demand for research in this field exists. To fulfil the growing demand of large lithium-ion cells as electrochemical power sources, the necessary increase in energy density is accomplished by improving the manufacturing process and by developing and introducing new active materials. With new materials, proper methods to investigate and track the ongoing degradation of a cell need to be developed to allow for a safe operation at any time, either during operation or when the cell is at rest. While various parameters as cell voltage, current, and surface temperature are observed in-operando, the accurate estimation of internal parameters becomes crucial with increasing size and complexity of the electrochemical system.

This thesis critically addressed various electrochemical characterisation techniques such as electrochemical impedance spectroscopy (EIS), differential voltage analysis (DVA), cyclic voltammetry (CV), and thermodynamic measurements (TM) regarding their applicability as degradation tracking technique. For this, a modification procedure was developed, which enabled the observation of additional cell parameters as internal cell temperature and local potentials along the electrodes of cylindrical cells. The method was proven to have a minor effect on the EIS spectra and negligible effects on the cell's discharge performance within the first 200 cycles.

The approach allowed the investigation of variations in the EIS spectra, caused by cell design, temperature, and excitation frequency. A direct correlation between the number of windings within the current path and the impedance of the cell at 10 kHz was found. In addition, the electrode area utilised during the measurement was shown to be frequency and temperature dependent. Consequently, an increase in cell temperature resulted in a significant variation of the signal intensity along the electrode, experiencing a larger decay. As a result, the observed changes in the EIS spectra do not only reflect the changing properties of the active material and electrolyte but also the changes caused by the differences in the evoked current path and consequently by the change in cell design. Transferring this statement to the variations in current density distribution caused by

inhomogeneous cell degradation, the applicability of EIS measurements for meaningful statements regarding the cell's degradation is questioned.

Consequently, the focus was set on DC measurements techniques, where the well established DVA was compared to thermodynamic measurements. As they require significantly more time than DVA measurements, the concept of advanced thermodynamic measurements (ATM) was presented as a possible candidate to gain further information of the current status of the respective electrode and the misalignment of the electrode balancing.

To minimise gradients in the lithium-ion concentration within the active material and along the electrode, an optimised discharge procedure was applied during the stepwise discharge. By means of local potential measurements, an estimation regarding the possible equalisation time was given. In addition, the influence of the cell temperature on the SoC inhomogeneities and the equalisation was investigated. A compromise between fast equalisation due to enhanced transport and kinetic properties, accelerated ageing due to an increased side reaction rate, and larger local inhomogeneities due to the enhanced material properties and increasing current collector resistance was found. To precisely determine the time for the cell to reach thermal equilibrium after an externally triggered change of temperature, cell's were equipped with thermocouples and the difference between surface and core temperature was measured.

Those findings were used as an input to optimise the experimental set-up and test procedure. In a final step, a mathematical approach was presented to process the gained measurement data. The occurring voltage relaxation of a cell after a discharge was fitted, which allowed for a faster change of the cell's temperature, even though the cell did not reach an electrochemical equilibrium within the given time. Compared to available literature discussing thermodynamic measurements, the measurement time was reduced by a factor of ten. The combination of faster measurements and the focus on SoC ranges of interest allowed a complete ATM measurements to be performed within 24 h, which is in the same range as DVA.

To quantify the accuracy of the method, a cell ageing study using commercially available cells with graphite anodes and NMC, NCA-LMO, and LFP cathodes was conducted. With graphite being the anode material of choice, the influence of the various cathode materials on the ATM measurements were of special interest, as the configurational entropy, caused by the different arrangements of the lithium-ions in the host structure dominate the thermodynamic properties. For the compared cells, DVA and ATM displayed very similar results. Using half-cell measurement during the subsequent post-mortem study, the accuracy and applicability of ATM as possible degradation tracking technique was confirmed. The method allowed for a precise determination of the degradation in the cell with the blended cathode. For two-phase materials, for example LFP, limitations apply, as the degradation of the cathode was very small and the number of distinct features did not allow for a precise statement.

To include the concept of ATM in EVs, a precise voltage measurements is required. As the absolute values are not of particular interest and only the voltage changes during a temperature change need to be determined, a differential amplifier can be used. The required temperature change would need to be conducted by the attached charging

station, whereas patents allowing for the thermal conditioning of the battery pack have already been filed [129].

Gaining various data points within defined SoC ranges - e.g. at cathode and anode features - during each charging process of the vehicle would a allow for a continuous observation of the degradation state of the single electrodes and the overall misalignment of the cell. This would lead to an improvement of the system's safety and would allow for an economically advanced usage of the cell.

List of Abbreviations

AC alternating current

ATM advanced thermodynamic measurements

BoL begin of life

CC constant current

CIF crystallographic information file

CMC carboxymethyl cellulose

CV cyclic voltammetry

CV constant voltage

DC direct current

DEC diethyl carbonate

DMC dimethyl carbonate

DoS density of states

DVA differential voltage analysis

EC ethylene carbonate

EIS electrochemical impedance spectroscopy

EoL end of life

EV electric vehicle

HEV hybrid electric vehicle

ICA incremental capacity analysis

ICE internal combustion engine vehicle

ICP inductive coupled plasma

LAM loss of active material

LCO Li_xCoO_2

LFP Li_xFePO_4

$LiClO_4$ lithium perchlorate

$LiPF_6$ lithium hexafluorophosphate

LLI loss of lithium inventory

LMO $Li_xMn_2O_4$

LNCO $Li_xNi_yCo_{1-y}$

LNO Li_xNiO_2

LTO $Li_4Ti_5O_{12}$

NCA $Li_xNi_{0.8}Co_{0.15}Al_{0.05}O_2$

NMC $Li_xNi_{1/3}Mn_{1/3}Co_{1/3}O_2$

NMP N-Methyl-2-Pyrrolidone

OCV open circuit voltage

OEM original equipment manufacturer

PC polycarbonate

PE polyethylene

PMMA poly(methyl methacrylate)

PP polypropylene

PVdF polyvinylidene fluoride

SEI solid electrolyte interphase

SEM scanning electrode microscope

SoC state of charge

SoH state of health

TM thermodynamic measurements

VC vinylene carbonate

XPS X-ray photoelectron spectroscopy

XRD X-ray diffraction

Nomenclature

$\hat{n}$ Number of available sites

μ Chemical potential [$\mathrm{J\,mol^{-1}}$]

η Over-potential [V]

ϵ Energy state [J]

ϕ Phase shift [°]

ν Sweep rate [$\mathrm{V\,min^{-1}}$]

ϑ Observational error [ ]

τ Time constant [$\mathrm{s^{-1}}$]

μ^* Electrochemical potential [$\mathrm{J\,mol^{-1}}$]

θ_D Debye-Temperature [K]

$\Delta_r S$ change in reaction entropy [$\mathrm{J\,K^{-1}}$]

A Area [$\mathrm{m^2}$]

C_{el} Electron heat capacity [$\mathrm{J\,K^{-1}}$]

C_n Nominal capacity [Ah]

C_{n,cm^2} Capacity [$\mathrm{mAh\,cm^{-2}}$]

D_0 Diffusion coefficient [$\mathrm{m^2\,s^{-1}}$]

E_{eq} Equilibrium potential [V]

F Faraday constant = $96\,485.3\,\mathrm{As\,mol^{-1}}$

G Gibbs' Free Energy [J]

H Enthalpy [J]

I Current [A]

N_A Avogadro constant = $6.022 \cdot 10^{23}\,\mathrm{mol^{-1}}$

R Ideal gas constant = 8.314 46 J mol^{-1} K^{-1}

S Entropy [J K^{-1}]

S^{e}_{conf} Configurational electronic entropy [J K^{-1}]

S^{e}_{mot} Electron motion entropy [J K^{-1}]

S_{conf} Configurational ionic entropy [J K^{-1}]

S_{vib} Vibrational entropy [J K^{-1}]

T Temperature [K]

U Internal energy [J]

U_{OCV} Open circuit voltage [V]

U_{cco} Charge cut-off voltage [V]

U_{cell} Cell voltage [V]

U_{dco} Discharge cut-off voltage [V]

U_{el} Electronic thermal energy [J]

U_{n} Nominal cell voltage [V]

V Volume [m^{3}]

W Number of micro states [ ]

$Z''(\omega)$ Impedance imaginary part [Ω]

$Z'(\omega)$ Impedance real part [Ω]

$Z(\omega)$ Impedance [Ω]

a Activity [ ]

c Concentration [molL^{-1}]

f Frequency [Hz]

f_{i} Activity coefficient [Lmol^{-1}]

n Number of moles [ ]

$n(\epsilon)$ Phonon occupancy factor [ ]

n_{e} Number of electrons [ ]

p Pressure [kg m^{-1} s^{-2}]

x Filling factor [ ]

x_e Electron filling factor [ ]

x_i Mole fraction [ ]

List of Publications

The manuscripts and presentations published during my time as Research Associate at TUM CREATE Ltd. from July 2011 until March 2016 are supported by the Singapore National Research Foundation (NRF) through its Campus for Research Excellence and Technological Enterprise (CREATE) program. The work published afterwards are partially based on the achieved results during this time. The additional support by the Bavarian Ministry of Economic Affairs and Media, Energy and Technology under the auspices of the EEBatt project is greatly acknowledged.

Journal article - Author

Osswald, P. J., Erhard S. V., Rheinfeld A., Rieger B., Hoster H.E., Jossen A., „Temperature Dependency of State of Charge Inhomogeneities and their Equalization in Cylindrical Lithium-Ion Cells", *Journal of Power Sources*, 329, 546-552, 2016.

Osswald, P. J., Erhard S. V., Noel A., Keil P., Kindermann F., Hoster H.E., Jossen A., „Current Density Distribution in Cylindrical Li-Ion Cells during Impedance Measurements", *Journal of Power Sources*, 314, 93-101, 2016.

Osswald, P. J., Erhard S. V., Wilhelm J., Hoster H.E., Jossen A., „Simulation and Measurement of Local Potentials of Modified Commercial Cylindrical Lithium-Ion Cells - Part I: Cell Preparation and Measurements", *Journal of The Electrochemical Society*, 162(10), A2099–A2105, 2015.

Osswald, P. J., Del Rosario, M., Garche, J., Jossen, A., Hoster, H. E., „Fast and Accurate Measurement of Entropy Profiles of Commercial Lithium-Ion Cells", *Electrochimica Acta*, 177, A270-276, 2015.

Journal article - Co-author

Kindermann F., Osswald, P. J., Ehlert G., Schuster J., Rheinfeld A., Jossen A., "Reducing Inhomogeneous Current Density Distribution in Graphite Electrodes by Design Variation", *Journal of The Electrochemical Society*, 164(11), E3105-3113, 2017.

Rieger B., Schuster S. F., Erhard S. V., Osswald P. J., Rheinfeld A., Willmann C., Jossen A., „Multi-directional laser scanning as innovative method to detect local cell damage during fast charging of lithium-ion cells" *Journal of Energy Storage*, 8, 1-5, 2016.

Erhard S.V., Osswald P.J., Keil P., Höffer E., Haug M., Noel A., Wilhelm J., Rieger B., Schmidt K., Kloust H., Thoennessen T., Kosch S., Kindermann F., Rheinfeld A., Jossen A., „Simulation and Measurement of Current Density Distribution within Lithium-Ion Batteries by a Multi-Tab Cell Approach", *Journal of The Electrochemical Society*, 164(1), A6324-A6333, 2017.

Kindermann F., Osswald, P. J., Klink S., Ehlert G., Schuster J., Noel A., Erhard S. V., Schuhmann W., Jossen A., "Measurements of lithium-ion concentration equilibration processes inside graphite electrodes", *Journal of Power Sources*, 342, 638-643, 2017.

von Lüders C., Zinth V., Erhard S. V., Osswald P.J., Hofmann M., Gilles R., Jossen A., "Lithium plating in lithium-ion batteries investigated by voltage relaxation and in situ neutron diffraction", *Journal of Power Sources*, 342, 17-23, 2017.

Rheinfeld A., Kosch S., Erhard S., Rieger B., Osswald P.J., Jossen A., Thermal-electric modelling of large format lithium-ion pouch cells based on a cell temperature corrected polarization expression", *Journal of The Electrochemical Society*, 163(14), A3046-A3062, 2016.

Erhard S. V., Osswald P. J., Wilhelm J., Rheinfeld A., Kosch S., Jossen A., „Simulation and Measurement of Local Potentials within Modified Commercial Cylindrical Cells - Part II: Multi-Dimensional Modeling and Validation", *Journal of The Electrochemical Society*, 162(14), A2707–A2719, 2015.

Book chapter

Ciechanowicz D., Knoll A., Osswald P.J., Pelzer D., „Plug In Electric Vehicles in Smart Grids - Towards a Business Case for Vehicle-to-Grid - Maximizing Profits in Ancillary Service Markets", Springer, 2015.

Bibliography

[1] A123 Systems. Specification of product - APR18650M1. Technical report, 2008. 43

[2] H. Abe, K. Zaghib, K. Tatsumi, and S. Higuchi. Performance of lithium-ion rechargeable batteries: graphite whisker/electrolyte/$LiCoO_2$ rocking-chair system. *Journal of Power Sources*, 54(2):236–239, Apr 1995. 29

[3] D. P. Abraham, S. D. Poppen, A. N. Jansen, J. Liu, and D. W. Dees. Application of a lithium–tin reference electrode to determine electrode contributions to impedance rise in high-power lithium-ion cells. *Electrochimica Acta*, 49(26):4763–4775, Oct 2004. 58

[4] S. Albrecht, J. Kümpers, M. Kruft, S. Malcus, C. Vogler, M. Wahl, and M. Wohlfahrt-Mehrens. Electrochemical and thermal behavior of aluminum- and magnesium-doped spherical lithium nickel cobalt mixed oxides $Li_{1-x}(Ni_{1-y-z}Co_yM_z)O_2$ (M = Al, Mg). *Journal of Power Sources*, 119-121:178–183, Jun 2003. 30, 116

[5] G. Amatucci, A. Du Pasquier, A. Blyr, T. Zheng, and J.-M. Tarascon. The elevated temperature performance of the $LiMn_2O_4$/C system: failure and solutions. *Electrochimica Acta*, 45(1-2):255–271, Sep 1999. 36

[6] G. Amatucci, C. Schmutz, A. Blyr, C. Sigala, A. Gozdz, D. Larcher, and J. Tarascon. Materials' effects on the elevated and room temperature performance of C/$LiMn_2O_4$ Li-ion batteries. *Journal of Power Sources*, 69(1-2):11–25, Nov 1997. 36

[7] R. Amin and Y.-M. Chiang. Characterization of Electronic and Ionic Transport in $Li_{1-x}Ni_{0.33}Mn_{0.33}Co_{0.33}O_2$ and $Li_{1-x}Ni_{0.5}Mn_{0.2}Co_{0.3}O_2$ as a Function of Li Content. *Journal of The Electrochemical Society*, 163(8):A1512–A1517, May 2016. 32

[8] R. Amin, D. B. Ravnsbaek, and Y.-M. Chiang. Characterization of Electronic and Ionic Transport in $Li_{1-x}Ni_{0.8}Co_{0.15}Al_{0.05}O_2$. *Journal of the Electrochemical Society*, 162(7):A1163–A1169, Mar 2015. 30

[9] K. Amine, C. Chen, J. Liu, M. Hammond, A. Jansen, D. Dees, I. Bloom, D. Vissers, and G. Henriksen. Factors responsible for impedance rise in high power lithium ion batteries. *Journal of Power Sources*, 97-98:684–687, Jul 2001. 29, 58

[10] K. Amine, J. Liu, and I. Belharouak. High-temperature storage and cycling of C-$LiFePO_4$ /graphite Li-ion cells. *Electrochemistry Communications*, 7(7):669–673, Jul 2005. 34

[11] P. W. Atkins and J. De Paula. *Atkins' Physical chemistry*. New York: W.H. Freeman, 2006. 17, 25

[12] AUDI AG. The battery technology. retrived 16.10.2016, from `https://www.audi-mediacenter.com/en/audi-future-performance-days-2015-5097/the-battery-technology-5100`. 41

[13] D. Aurbach. Common Electroanalytical Behavior of Li Intercalation Processes into Graphite and Transition Metal Oxides. *Journal of The Electrochemical Society*, 145(9):3024, Sep 1998. 46

[14] D. Aurbach. Electrode-solution interactions in Li-ion batteries: A short summary and new insights. *Journal of Power Sources*, 119-121:497–503, Jun 2003. 38, 98

[15] S. Bach, J. Pereira-Ramos, N. Baffier, and R. Messina. Thermodynamic data of electrochemical lithium intercalation in $Li_xMn_2O_4$. *Electrochimica Acta*, 37(7):1301–1305, Jun 1992. 53, 116

[16] A. Badia. Encyclopedia of Electrochemistry. Volume 1. Thermodynamics and Electrified Interfaces. *Journal of the American Chemical Society*, 125(22):6839–6840, Jun 2003. 17

[17] A. Barai, Y. Guo, A. Mcgordon, and P. Jennings. A Study of the Effects of External Pressure on the Electrical Performance of a Lithium-ion Pouch Cell. In *2013 International Conference on Connected Vehicles and Expo (ICCVE)*, pages 2–6, Dec 2013. 72

[18] S. J. Bazinski and X. Wang. The Influence of Cell Temperature on the Entropic Coefficient of a Lithium Iron Phosphate (LFP) Pouch Cell. *Journal of the Electrochemical Society*, 161(1):A168–A175, Dec 2013. 52

[19] J. R. Belt, D. M. Bernardi, and V. Utgikar. Development and Use of a Lithium-Metal Reference Electrode in Aging Studies of Lithium-Ion Batteries. *Journal of the Electrochemical Society*, 161(6):A1116–A1126, May 2014. 59

[20] H. Berg and J. O. Thomas. Neutron diffraction study of electrochemically delithiated $LiMn_2O_4$ spinel. *Solid State Ionics*, 126:227–234, Nov 1999. 35

[21] D. M. Bernardi, R. Chandrasekaran, and J. Y. Go. Solid-State Transport of Lithium in Lithium-Ion-Battery Positive Electrodes. *Journal of the Electrochemical Society*, 160(9):A1430–A1441, Jul 2013. 90

[22] D. M. Bernardi and J.-Y. Go. Analysis of pulse and relaxation behavior in lithium-ion batteries. *Journal of Power Sources*, 196(1):412–427, Jan 2011. 24, 77, 90

[23] W. Bernhart. The Lithium-Ion Battery Value Chain—Status, Trends and Implications. In *Lithium-Ion Batteries*, pages 553–565. Elsevier, 2014. 13

[24] C. Birkenmaier, B. Bitzer, M. Harzheim, A. Hintennach, and T. Schleid. Lithium Plating on Graphite Negative Electrodes: Innovative Qualitative and Quantitative Investigation Methods. *Journal of The Electrochemical Society*, 162(14):A2646–A2650, Oct 2015. 39

[25] G. E. Blomgren. Electrolytes for advanced batteries. *Journal of Power Sources*, 81-82:112–118, Sep 1999. 38

[26] I. Bloom, J. Christophersen, and K. Gering. Differential voltage analyses of high-power lithium-ion cells. *Journal of Power Sources*, 139(1-2):304–313, Jan 2005. 49

[27] I. Bloom, J. P. Christophersen, D. P. Abraham, and K. L. Gering. Differential voltage analyses of high-power lithium-ion cells. *Journal of Power Sources*, 157(1):537–542, Jun 2006. 49

[28] I. Bloom, A. N. Jansen, D. P. Abraham, J. Knuth, S. A. Jones, V. S. Battaglia, and G. L. Henriksen. Differential voltage analyses of high-power, lithium-ion cells. *Journal of Power Sources*, 139(1-2):295–303, Jan 2005. 48, 49, 107

[29] I. Bloom, L. K. Walker, J. K. Basco, D. P. Abraham, J. P. Christophersen, and C. D. Ho. Differential voltage analyses of high-power lithium-ion cells. 4. Cells containing NMC. *Journal of Power Sources*, 195(3):877–882, Feb 2010. 49

[30] A. Blyr, C. Sigala, G. Amatucci, D. Guyomard, Y. Chabre, and J.-M. Tarascon. Self-Discharge of $LiMn_2O_4$ / C Li-Ion Cells in Their Discharged State, Jan 1998. 58

[31] J. W. Braithwaite. Corrosion of Lithium-Ion Battery Current Collectors. *Journal of The Electrochemical Society*, 146(2):448, Oct 1999. 40, 69

[32] I. Buchberger, S. Seidlmayer, A. Pokharel, M. Piana, J. Hattendorff, P. Kudejova, R. Gilles, and H. A. Gasteiger. Aging Analysis of Graphite / $LiNi_{1/3}Mn_{1/3}Co_{1/3}O_2$ Cells Using XRD, PGAA, and AC Impedance. *Journal of The Electrochemical Society*, 162(14):A2737–A2746, Oct 2015. 33, 111

[33] L. Cai, K. An, Z. Feng, C. Liang, and S. J. Harris. In-situ observation of inhomogeneous degradation in large format Li-ion cells by neutron diffraction. *Journal of Power Sources*, 236:163–168, Aug 2013. 69

[34] J. Cannarella and C. B. Arnold. Ion transport restriction in mechanically strained separator membranes. *Journal of Power Sources*, 226:149–155, Mar 2013. 72

[35] F. Cao, I. V. Barsukov, H. J. Bang, P. Zaleski, and J. Prakash. Evaluation of Graphite Materials as Anodes for Lithium-Ion Batteries. *Journal of The Electrochemical Society*, 147(10):3579, Jun 2000. 57

[36] G. Ceder, Y.-M. Chiang, D. R. Sadoway, M. K. Aydinol, Y.-I. Jang, and B. Huang. Identification of cathode materials for lithium batteries guided by first-principles calculations. *Nature*, 392(6677):694–696, Apr 1998. 31

[37] G. Ceder and A. Van der Ven. Phase diagrams of lithium transition metal oxides: investigations from first principles. *Electrochimica Acta*, 45(1-2):131–150, Sep 1999. 27

[38] G. Ceder, a. V. D. Ven, C. Marianetti, and D. Morgan. First-principles alloy theory in oxides. *Modelling and Simulation in Materials Science and Engineering*, 8(3):311–321, May 2000. 27

[39] K. Chang, B. Hallstedt, and D. Music. Thermodynamic and Electrochemical Properties of the LiCoO and LiNiO Systems. *Chemistry of Materials*, 24(1):97–105, Jan 2012. 29

[40] C. Chen, J. Liu, M. Stoll, G. Henriksen, D. Vissers, and K. Amine. Aluminum-doped lithium nickel cobalt oxide electrodes for high-power lithium-ion batteries. *Journal of Power Sources*, 128(2):278–285, Apr 2004. 30

[41] W. Chen, M. Niepel, and P. Sorger. Classic and contemporary approaches to modeling biochemical reactions. *Genes & development*, pages 1861–1875, Sep 2010. 91

[42] Z. Chen, Z. Lu, and J. R. Dahn. Staging Phase Transitions in Li_xCoO_2. *Journal of The Electrochemical Society*, 149(12):A1604, Oct 2002. 29, 32

[43] J. Cho, Y. J. Kim, T.-J. Kim, and B. Park. Zero-Strain Intercalation Cathode for Rechargeable Li-Ion Cell. *Angewandte Chemie International Edition*, 40(18):3367–3369, sep 2001. 29

[44] Y. Cho and J. Cho. Significant Improvement of $LiNi_{0.8}Co_{0.15}Al_{0.05}O_2$ Cathodes at 60 °C by SiO_2 Dry Coating for Li-Ion Batteries. *Journal of The Electrochemical Society*, 157(6):A625, Apr 2010. 31

[45] R. Clausius. Ueber die bewegende Kraft der Wärme und die Gesetze, welche sich daraus für die Wärmelehre selbst ableiten lassen. *Annalen der Physik*, 155(4):500–524, 1850. 18

[46] R. Clausius. Ueber eine veränderte Form des zweiten Hauptsatzes der mechanischen Wärmetheorie. *Annalen der Physik*, 169(12):481–506, 1854. 18

[47] R. Clausius. *The London, Edinburgh and Dublin Philosophical Magazine and Journal of Science.*, volume XII. London: Taylor and Francis, Aug 1856. 19

[48] R. Clausius. Ueber verschiedene für die Anwendung bequeme Formen der Hauptgleichungen der mechanischen Wärmetheorie. *Annalen der Physik und Chemie*, 201(7):353–400, 1865. 19

[49] L. Croguennec, J. Bains, J. Breger, C. Tessier, P. Biensan, S. Levasseur, and C. Delmas. Effect of Aluminum Substitution on the Structure, Electrochemical Performance and Thermal Stability of $Li_{1+x}(Ni_{0.40}Mn_{0.40}Co_{0.2-z}Al_z)_{1-x}O_2$. *Journal of The Electrochemical Society*, 158(6):A664, Apr 2011. 30, 124

[50] T. R. Crompton. *Battery reference book*. Newnes, 2000. 39

[51] M. Dahbi, F. Ghamouss, F. Tran-Van, D. Lemordant, and M. Anouti. Comparative study of EC/DMC, LiTFSI and $LiPF_6$ electrolytes for electrochemical storage. *Journal of Power Sources*, 196(22):9743–9750, Nov 2011. 37

[52] J. Dahn, E. Fuller, M. Obrovac, and U. Vonsacken. Thermal stability of Li_xCoO_2, Li_xNiO_2 and λ-MnO_2 and consequences for the safety of Li-ion cells. *Solid State Ionics*, 69(3-4):265–270, Aug 1994. 29

[53] J. R. Dahn. Phase diagram of Li_xC_6. *Physical Review B*, 44(17):9170–9177, Nov 1991. 37, 38, 56, 107

[54] D. W. Dees, A. N. Jansen, and D. P. Abraham. Theoretical examination of reference electrodes for lithium-ion cells. *Journal of Power Sources*, 174(2):1001–1006, Dec 2007. 61

[55] C. Delacourt, P. Poizot, J.-M. Tarascon, and C. Masquelier. The Existence of a Temperature-Driven Solid Solution in Li_xFePO_4 for $0 \leq x \leq 1$. *Nature Materials*, 4(3):254–260, Mar 2005. 33, 34

[56] D. E. Demirocak and B. Bhushan. Probing the aging effects on nanomechanical properties of a $LiFePO_4$ cathode in a large format prismatic cell. *Journal of Power Sources*, 280:256–262, Apr 2015. 40

[57] J. L. Dodd. *Phase Composition and Dynamical Studies of Lithium Iron Phosphate*. Phd thesis, California Institute of Technology, 2007. 120

[58] J. L. Dodd, R. Yazami, and B. Fultz. Phase Diagram of Li_xFePO_4. *Electrochemical and Solid-State Letters*, 9(3):A151, Jan 2006. 33, 34

[59] M. Dollé, F. Orsini, A. S. Gozdz, J.-M. Tarascon, and P. J. Verne. Development of Reliable Three-Electrode Impedance Measurements in Plastic Li-Ion Batteries. *Journal of The Electrochemical Society*, 148(8):A851, Jul 2001. 58

[60] O. Dolotko, A. Senyshyn, M. Mühlbauer, K. Nikolowski, and H. Ehrenberg. Understanding structural changes in NMC Li-ion cells by in situ neutron diffraction. *Journal of Power Sources*, 255:197–203, Jun 2014. 29

[61] M. Dubarry, C. Truchot, M. Cugnet, B. Y. Liaw, K. Gering, S. Sazhin, D. Jamison, and C. Michelbacher. Evaluation of commercial lithium-ion cells based on composite positive electrode for plug-in hybrid electric vehicle applications. Part I: Initial characterizations. *Journal of Power Sources*, 196(23):10328–10335, Dec 2011. 49

[62] M. Dubarry, C. Truchot, A. Devie, B. Y. Liaw, K. Gering, S. Sazhin, D. Jamison, and C. Michelbacher. Evaluation of Commercial Lithium-Ion Cells Based on Composite Positive Electrode for Plug-In Hybrid Electric Vehicle (PHEV) Applications: IV. Over-Discharge Phenomena. *Journal of the Electrochemical Society*, 162(9):A1787–A1792, Jun 2015. 36, 123

[63] M. Dubarry, C. Truchot, and B. Y. Liaw. Cell degradation in commercial $LiFePO_4$ cells with high-power and high-energy designs. *Journal of Power Sources*, 258:408–419, Jul 2014. 34

[64] M. Dubarry, C. Truchot, B. Y. Liaw, K. Gering, S. Sazhin, D. Jamison, and C. Michelbacher. Evaluation of commercial lithium-ion cells based on composite positive electrode for plug-in hybrid electric vehicle applications. Part II. Degradation mechanism under 2C cycle aging. *Journal of Power Sources*, 196(23):10336–10343, Dec 2011. 49

[65] S. V. Erhard, P. J. Osswald, P. Keil, E. Höffer, M. Haug, A. Noel, J. Wilhelm, B. Rieger, K. Schmidt, S. Kosch, F. M. Kindermann, F. Spingler, H. Kloust, T. Thoennessen, A. Rheinfeld, and A. Jossen. Simulation and Measurement of the Current Density Distribution in Lithium-Ion Batteries by a Multi-Tab Cell Approach. *Journal of The Electrochemical Society*, 164(1):A6324–A6333, Jan 2017. 69

[66] S. V. Erhard, P. J. Osswald, J. Wilhelm, A. Rheinfeld, S. Kosch, and A. Jossen. Simulation and Measurement of Local Potentials of Modified Commercial Cylindrical Cells. *Journal of The Electrochemical Society*, 162(14):A2707–A2719, Oct 2015. 54, 69

[67] EU. Regulation No 333/2014 of the European Parliament and of the Council of 11 March 2014 amending Regulation (EC) No 443/2009 to define the modalities for reaching the 2020 target to reduce CO_2 emissions from new passenger cars. retrived 02.12.2016, from `http://eur-lex.europa.eu/legal-content/EN/TXT/?uri=uriserv:OJ.L_.2014.103.01.0015.01.ENG`. 13

[68] M. Fleckenstein, O. Bohlen, M. A. Roscher, and B. Bäker. Current density and state of charge inhomogeneities in Li-ion battery cells with $LiFePO_4$ as cathode material due to temperature gradients. *Journal of Power Sources*, 196(10):4769–4778, May 2011. 123

[69] B. Fultz. Vibrational thermodynamics of materials. *Progress in Materials Science*, 55(4):247–352, May 2010. 25, 27

[70] B. Fultz. *Phase Transitions in Materials*. Cambridge University Press, Cambridge, 2014. 28

[71] B. Fultz, P. D. Bogdanoff. Vibrational entropies of alloying and compound formation: experimental trends. *Philosophical Magazine B*, 79(5):753–765, May 1999. 25

[72] H. Gabrisch, Y. Ozawa, and R. Yazami. Crystal structure studies of thermally aged $LiCoO_2$ and $LiMn_2O_4$ cathodes. *Electrochimica Acta*, 52(4):1499–1506, Dec 2006. 35, 36

[73] L. L. Gaines and R. Cuenca. Costs of Lithium-Ion Batteries for Vehicles. Technical report, Center for Transportation Research Argonne National Laboratory, Argonne, 2000. 42

[74] J. S. Gnanaraj, Y. S. Cohen, M. D. Levi, and D. Aurbach. The effect of pressure on the electroanalytical response of graphite anodes and $LiCoO_2$ cathodes for Li-ion batteries. *Journal of Electroanalytical Chemistry*, 516(1-2):89–102, Dec 2001. 72

[75] J. L. Gómez-Cámer and P. Novák. Electrochemical impedance spectroscopy: Understanding the role of the reference electrode. *Electrochemistry Communications*, 34:208–210, Sep 2013. 58

[76] G. Grégoire. Simple Linear Regression. *EAS Publications Series*, 66:19–39, Jan 2014. 87, 89

[77] J. Groot, M. Swierczynski, A. I. Stan, and S. K. Kær. On the complex ageing characteristics of high-power $LiFePO_4$/graphite battery cells cycled with high charge and discharge currents. *Journal of Power Sources*, 286:475–487, Jul 2015. 47, 69

[78] A. Guerfi, M. Dontigny, P. Charest, M. Petitclerc, M. Lagacé, A. Vijh, and K. Zaghib. Improved electrolytes for Li-ion batteries: Mixtures of ionic liquid and organic electrolyte with enhanced safety and electrochemical performance. *Journal of Power Sources*, 195(3):845–852, Feb 2010. 37

[79] M. Guilmard. Structural and electrochemical properties of $LiNi_{0.70}Co_{0.15}Al_{0.15}O_2$. *Solid State Ionics*, 160(1-2):39–50, May 2003. 30, 31

[80] M. Guo and R. E. White. Mathematical model for a spirally-wound lithium-ion cell. *Journal of Power Sources*, 250:220–235, Mar 2014. 74

[81] D. Guyomard and J. M. Tarascon. High voltage stable liquid electrolytes for $Li_{1+x}Mn_2O_4$ /carbon rocking-chair lithium batteries. *Journal of Power Sources*, 54(1):92–98, Mar 1995. 36

[82] H. He, C. Huang, C.-W. Luo, J.-J. Liu, and Z.-S. Chao. Dynamic study of Li intercalation into graphite by in situ high energy synchrotron XRD. *Electrochimica Acta*, 92:148–152, Mar 2013. 56

[83] J. Heinze. Cyclovoltammetrie - die Spektroskopie des Elektrochemikers. *Angewandte Chemie*, 96(11):823–916, Nov 1984. 50

[84] A. Hentunen, T. Lehmuspelto, and J. Suomela. Time-Domain Parameter Extraction Method for Thevenin-Equivalent Circuit Battery Models. *IEEE Transactions on Energy Conversion*, 29(3):558–566, Sep 2014. 90

[85] K. Hoang and M. Johannes. Defect Physics and Chemistry in Layered Mixed Transition Metal Oxide Cathode Materials: (Ni,Co,Mn) vs (Ni,Co,Al). *Chemistry of Materials*, 28(5):1325–1334, 2016. 30

[86] J. Huang, Z. Li, B. Y. Liaw, Z. Wang, S. Song, N. Wu, and J. Zhang. Entropy Coefficient of a Blended Electrode in a Lithium-Ion Cell. *Journal of The Electrochemical Society*, 162(12):A2367–A2371, Sep 2015. 89

[87] N. S. Hudak, L. E. Davis, and G. Nagasubramanian. Cycling-Induced Changes in the Entropy Profiles of Lithium Cobalt Oxide Electrodes. *Journal of the Electrochemical Society*, 162(3):A315–A321, Dec 2014. 53

[88] B. J. Hwang, Y. W. Tsai, D. Carlier, and G. Ceder. A Combined Computational/Experimental Study on $LiNi_{1/3}Co_{1/3}Mn_{1/3}O_2$. *Chemistry of Materials*, 15(19):3676–3682, Sep 2003. 31

[89] J. Illig, M. Ender, T. Chrobak, J. P. Schmidt, D. Klotz, and E. Ivers-Tiffee. Separation of Charge Transfer and Contact Resistance in $LiFePO_4$-Cathodes by Impedance Modeling. *Journal of the Electrochemical Society*, 159(7):A952–A960, Jan 2012. 46

[90] J. Illig, J. P. Schmidt, M. Weiss, A. Weber, and E. Ivers-Tiffée. Understanding the impedance spectrum of 18650 $LiFePO_4$-cells. *Journal of Power Sources*, 239:670–679, Oct 2013. 46, 78

[91] R. Jackey, M. Saginaw, P. Sanghvi, J. Gazzarri, T. Huria, and M. Ceraolo. Battery Model Parameter Estimation Using a Layered Technique: An Example Using a Lithium Iron Phosphate Cell. *MathWorks*, pages 1–14, Jan 2013. 90

[92] K. Jalkanen, T. Aho, and K. Vuorilehto. Entropy change effects on the thermal behavior of a $LiFePO_4$/graphite lithium-ion cell at different states of charge. *Journal of Power Sources*, 243:354–360, Dec 2013. 53

[93] K. Jalkanen, J. Karppinen, L. Skogström, T. Laurila, M. Nisula, and K. Vuorilehto. Cycle aging of commercial NMC/graphite pouch cells at different temperatures. *Applied Energy*, 154:160–172, Sep 2015. 69

[94] K. Jalkanen and K. Vuorilehto. Entropy change charcteristics of $LiMn_{0.67}Fe_{0.33}PO_4$ and $Li_4Ti_5O_{12}$ electrode materials. *Journal of Power Sources*, 273:351–359, Jan 2015. 53

[95] A. N. Jansen, D. W. Dees, D. P. Abraham, K. Amine, and G. L. Henriksen. Low-temperature study of lithium-ion cells using a Li_ySn micro-reference electrode. *Journal of Power Sources*, 174(2):373–379, Dec 2007. 58, 77

[96] A. Jossen. Fundamentals of battery dynamics. *Journal of Power Sources*, 154(2):530–538, Mar 2006. 46, 77

[97] C. Julien and M. Massot. Lattice vibrations of materials for lithium rechargeable batteries III. Lithium manganese oxides. *Materials Science and Engineering: B*, 100(1):69–78, Jun 2003. 35

[98] C. Julien, A. Mauger, A. Vijh, and K. Zaghib. *Lithium Batteries*. Springer International Publishing, Cham, 2016. 29

[99] K. Kai, Y. Kobayashi, H. Miyashiro, G. Oyama, S. I. Nishimura, M. Okubo, and A. Yamada. Particle-size effects on the entropy behavior of a $LixFePO_4$ electrode. *ChemPhysChem*, 15(10):2156–2161, Apr 2014. 124

[100] S.-H. Kang, D. P. Abraham, W.-S. Yoon, K.-W. Nam, and X.-Q. Yang. First-cycle irreversibility of layered Li–Ni–Co–Mn oxide cathode in Li-ion batteries. *Electrochimica Acta*, 54(2):684–689, Dec 2008. 33

[101] U. Kasavajjula, C. Wang, and A. J. Appleby. Nano- and bulk-silicon-based insertion anodes for lithium-ion secondary cells. *Journal of Power Sources*, 163(2):1003–1039, Jan 2007. 39

[102] T. Kashiwagi, M. Nakayama, K. Watanabe, M. Wakihara, Y. Kobayashi, and H. Miyashiro. Relationship between the electrochemical behavior and Li arrangement in $Li_xM_yMn_{2-y}O_4$ (M = Co, Cr) with spinel structure. *Journal of Physical Chemistry B*, 110(10):4998–5004, 2006. 116

[103] M. Kassem, J. Bernard, R. Revel, S. Pélissier, F. Duclaud, and C. Delacourt. Calendar aging of a graphite/$LiFePO_4$ cell. *Journal of Power Sources*, 208:296–305, Jun 2012. 49

[104] M. Kassem and C. Delacourt. Postmortem analysis of calendar-aged graphite/$LiFePO_4$ cells. *Journal of Power Sources*, 235:159–171, Aug 2013. 54

[105] H. Kawai, M. Nagata, H. Kageyama, H. Tukamoto, and A. R. West. 5 V lithium cathodes based on spinel solid solutions. *Electrochimica Acta*, 45(1-2):315–327, Sep 1999. 35

[106] H. Kawai, M. Nagata, H. Tukamoto, and A. R. West. High-voltage lithium cathode materials. *Journal of Power Sources*, 81-82:67–72, Sep 1999. 35

[107] F. M. Kindermann, A. Noel, S. V. Erhard, and A. Jossen. Long-term equalization effects in Li-ion batteries due to local state of charge inhomogeneities and their impact on impedance measurements. *Electrochimica Acta*, 185:107–116, Dec 2015. 24, 46, 104

[108] F. M. Kindermann, P. J. Osswald, S. Klink, G. Ehlert, J. Schuster, A. Noel, S. V. Erhard, W. Schuhmann, and A. Jossen. Measurements of lithium-ion concentration equilibration processes inside graphite electrodes. *Journal of Power Sources*, 342:638–643, Feb 2017. 92

[109] C. Kittel and P. McEuen. *Introduction to solid state physics.* Hoboken, NJ: J. Wiley, 2005. 28

[110] M. Klett, R. Eriksson, J. Groot, P. Svens, K. Ciosek Högström, R. W. Lindström, H. Berg, T. Gustafson, G. Lindbergh, and K. Edström. Non-uniform aging of cycled commercial $LiFePO_4$ /graphite cylindrical cells revealed by post-mortem analysis. *Journal of Power Sources*, 257:126–137, Jul 2014. 69

[111] Y. Kobayashi, Y. Mita, S. Seki, Y. Ohno, H. Miyashiro, M. Nakayama, and M. Wakihara. Configurational Entropy of Lithium Manganese Oxide and Related Materials, $LiCr_yMn_{2-y}O_4$. *Journal of The Electrochemical Society*, 155(1):A14, Jan 2008. 124

[112] Y. Kojima, S. Muto, K. Tatsumi, H. Kondo, H. Oka, K. Horibuchi, and Y. Ukyo. Degradation analysis of a Ni-based layered positive-electrode active material cycled at elevated temperatures studied by scanning transmission electron microscopy and electron energy-loss spectroscopy. *Journal of Power Sources*, 196(18):7721–7727, Sep 2011. 30

[113] M. Koltypin, D. Aurbach, L. Nazar, and B. Ellis. On the Stability of $LiFePO_4$ Olivine Cathodes under Various Conditions (Electrolyte Solutions, Temperatures). *Electrochemical and Solid-State Letters*, 10(2):A40, Nov 2007. 34

[114] Y. Koyama, I. Tanaka, H. Adachi, Y. Makimura, and T. Ohzuku. Crystal and electronic structures of superstructural $Li_{1-x}Co_{1/3}Ni_{1/3}Mn_{1/3}O_2$ $(0 \leq x \leq 1)$. *Journal of Power Sources*, 119-121:644–648, Jun 2003. 32

[115] F. La Mantia, C. D. Wessells, H. D. Deshazer, and Y. Cui. Reliable reference electrodes for lithium-ion batteries. *Electrochemistry Communications*, 31:141–144, Jun 2013. 58

[116] F. C. Laman, M. W. Matsen, and J. A. R. Stiles. Inductive Impedance of a Spirally Wound Li/MoS_2 Cell. *Journal of the Electrochemical Society*, 133(12):2441–2446, Dec 1986. 76

[117] H.-H. Lee, Y.-Y. Wang, C.-C. Wan, M.-H. Yang, H.-C. Wu, and D.-T. Shieh. The function of vinylene carbonate as a thermal additive to electrolyte in lithium batteries. *Journal of Applied Electrochemistry*, 35(6):615–623, Jun 2005. 37

[118] M. D. Levi. Solid State Electrochemical Kinetics of Li-Ion Intercalation into $Li_{1-x}CoO_2$: Simultaneous Application of Electroanalytical Techniques SSCV, PITT, and EIS. *Journal of The Electrochemical Society*, 146(4):1279, Nov 1999.

[119] M. D. Levi and D. Aurbach. Diffusion coefficients of lithium ions during intercalation into graphite derived from the simultaneous measurements and modeling of electrochemical impedance and potentiostatic intermittent titration characteristics of thin graphite electrodes. *Journal of Physical Chemistry B*, 101(23):4641–4647, Jun 1997. 62

[120] M. D. Levi, K. Gamolsky, D. Aurbach, U. Heider, and R. Oesten. On electrochemical impedance measurements of $Li_xCo_{0.2}Ni_{0.8}O_2$ and Li_xNiO_2 intercalation electrodes. *Electrochimica Acta*, 45:1781–1789, Feb 2000. 77

[121] J. Li, E. Murphy, J. Winnick, and P. A. Kohl. The effects of pulse charging on cycling characteristics of commercial lithium-ion batteries. *Journal of Power Sources*, 102(1-2):302–309, Dec 2001. 38

[122] W. Li, J. N. Reimers, and J. R. Dahn. Lattice-gas-model approach to understanding the structures of lithium transition-metal oxides $LiMO_2$. *Physical Review B*, 49(2):826–831, Jan 1994. 29

[123] S. Madhavi, G. Subba Rao, B. Chowdari, and S. Li. Effect of aluminium doping on cathodic behaviour of $LiNi_{0.7}Co_{0.3}O_2$. *Journal of Power Sources*, 93(1-2):156–162, Feb 2001. 30, 116

[124] K. Maher and R. Yazami. Effect of overcharge on entropy and enthalpy of lithium-ion batteries. *Electrochimica Acta*, 101:71–78, Jul 2013. 53

[125] K. Maher and R. Yazami. A study of lithium ion batteries cycle aging by thermodynamics techniques. *Journal of Power Sources*, 247:527–533, Feb 2014. 53

[126] K. Maher and R. Yazami. A thermodynamic and crystal structure study of thermally aged lithium ion cells. *Journal of Power Sources*, 261:389–400, Sep 2014. 53

[127] J. Maier and R. Amin. Defect Chemistry of $LiFePO_4$. *Journal of The Electrochemical Society*, 155(4):A339, Apr 2008. 33

[128] Z. Mao, M. Farkhondeh, M. Pritzker, M. Fowler, and Z. Chen. Charge/Discharge Asymmetry in Blended Lithium-Ion Electrodes. *Journal of The Electrochemical Society*, 164(2):A39–A47, Dec 2017. 124

[129] J. Mardall and C. Van Dyke. Charging station providing thermal conditioning of electric vehicle during charging session, Oct. 29 2015. US Patent App. 14/264,364. 129

[130] C. Marianetti, D. Morgan, and G. Ceder. First-principles investigation of the cooperative Jahn-Teller effect for octahedrally coordinated transition-metal ions. *Physical Review B*, 63(22):1–15, May 2001. 31, 32

[131] E. Markevich, M. D. Levi, and D. Aurbach. New Insight into Studies of the Cycling Performance of Li-Graphite Electrodes. *Journal of The Electrochemical Society*, 152(4):A778, Mar 2005. 51

[132] E. Markevich, G. Salitra, M. D. Levi, and D. Aurbach. Capacity fading of lithiated graphite electrodes studied by a combination of electroanalytical methods, Raman spectroscopy and SEM. *Journal of Power Sources*, 146(1-2):146–150, Aug 2005. 98

[133] A. Marongiu, M. Roscher, and D. U. Sauer. Influence of the vehicle-to-grid strategy on the aging behavior of lithium battery electric vehicles. *Applied Energy*, 137:899–912, Jan 2015. 69

[134] H. Matsui, T. Nakamura, Y. Kobayashi, M. Tabuchi, and Y. Yamada. Open-circuit voltage study on $LiFePO_4$ olivine cathode. *Journal of Power Sources*, 195(19):6879–6883, Oct 2010. 33

[135] Y. Matsuo, R. Kostecki, and F. McLarnon. Surface Layer Formation on Thin-Film $LiMn_2O_4$ Electrodes at Elevated Temperatures. *Journal of The Electrochemical Society*, 148(7):A687, May 2001. 36

[136] E. McTurk, C. R. Birkl, M. R. Roberts, D. A. Howey, and P. G. Bruce. Minimally Invasive Insertion of Reference Electrodes into Commercial Lithium-Ion Pouch Cells. *ECS Electrochemistry Letters*, 4(12):A145–A147, Nov 2015. 59

[137] N. Meethong, H. Y. S. Huang, S. A. Speakman, W. C. Carter, and Y. M. Chiang. Strain accommodation during phase transformations in olivine-based cathodes as a materials selection criterion for high-power rechargeable batteries. *Advanced Functional Materials*, 17(7):1115–1123, Nov 2007. 33

[138] R. Mingant, J. Bernard, V. Sauvant Moynot, A. Delaille, S. Mailley, J.-L. Hognon, and F. Huet. EIS Measurements for Determining the SoC and SoH of Li-Ion Batteries. *ECS Transactions*, 33(39):41–53, 2011. 47, 69

[139] K. Mizushima, P. Jones, P. Wiseman, and J. Goodenough. Li_xCoO_2 (0 Li_xCoO_2 (0 : A new cathode material for batteries of high energy density. *Materials Research Bulletin*, 15(6):783 – 789, Jun 1980. 29

[140] K. Momma and F. Izumi. *VESTA3* for three-dimensional visualization of crystal, volumetric and morphology data. *Journal of Applied Crystallography*, 44(6):1272 – 1276, Dec 2011. 30

[141] D. Morgan, A. Van der Ven, and G. Ceder. Li Conductivity in Li_xMPO_4 (M = Mn, Fe, Co, Ni) Olivine Materials. *Electrochemical and Solid-State Letters*, 7(2):A30, Dec 2004. 33

[142] S.-T. Myung, S. Komaba, N. Hirosaki, N. Kumagai, K. Arai, R. Kodama, and I. Nakai. Structural Investigation of Layered $Li_{1-\delta}Mn_xCr_{1-x}O_2$ by XANES and In Situ XRD Measurements. *Journal of The Electrochemical Society*, 150(12):A1560, Nov 2003. 124

[143] S.-T. Myung, S. Komaba, N. Hirosaki, H. Yashiro, and N. Kumagai. Emulsion drying synthesis of olivine $LiFePO_4$ / C composite and its electrochemical properties as lithium intercalation material. *Electrochimica Acta*, 49(24):4213–4222, Sep 2004. 33

[144] S. P. Nadimpalli, V. A. Sethuraman, D. P. Abraham, A. F. Bower, and P. R. Guduru. Stress Evolution in Lithium-Ion Composite Electrodes during Electrochemical Cycling and Resulting Internal Pressures on the Cell Casing. *Journal of The Electrochemical Society*, 162(14):A2656–A2663, Oct 2015. 72

[145] G. Nagasubramanian. Two- and three-electrode impedance studies on 18650 Li-ion cells. *Journal of Power Sources*, 87(1-2):226–229, Apr 2000. 59

[146] G. Nagasubramanian and D. Doughty. 18650 Li-ion cells with reference electrode and in situ characterization of electrodes. *Journal of Power Sources*, 150:182–186, Oct 2005. 59

[147] P. Nelson, K. Gallagher, I. Bloom, and D. Dees. Modeling the Performance and Cost of Lithium-Ion Batteries for Electric-Drive Vehicles, Second Edition. Technical

report, Chemical Sciences and Engineering Division, Research Argonne National Laboratory, 2012. 42

[148] B. Nykvist and M. Nilsson. Rapidly falling costs of battery packs for electric vehicles. *Nature Climate Change*, 5(4):329–332, Mar 2015. 13

[149] T. Ohzuku. Electrochemistry of Manganese Dioxide in Lithium Nonaqueous Cell. *Journal of The Electrochemical Society*, 136(11):3169, Mar 1989. 35

[150] T. Ohzuku and Y. Makimura. Layered Lithium Insertion Material of $LiCo_{1/3}Ni_{1/3}Mn_{1/3}O_2$ for Lithium-Ion Batteries. *Chemistry Letters*, 30(7):642–643, Feb 2001. 31

[151] P. Osswald, S. Erhard, A. Noel, P. Keil, F. Kindermann, H. Hoster, and A. Jossen. Current density distribution in cylindrical Li-Ion cells during impedance measurements. *Journal of Power Sources*, 314:93–101, May 2016. 40, 69, 70, 75, 123

[152] P. Osswald, S. Erhard, A. Rheinfeld, B. Rieger, H. Hoster, and A. Jossen. Temperature dependency of state of charge inhomogeneities and their equalization in cylindrical lithium-ion cells. *Journal of Power Sources*, 329:546–552, Oct 2016. 82

[153] P. J. Osswald, S. V. Erhard, J. Wilhelm, H. E. Hoster, and A. Jossen. Simulation and Measurement of Local Potentials of Modified Commercial Cylindrical Cells. *Journal of The Electrochemical Society*, 162(10):A2099–A2105, Aug 2015. 54, 63, 69, 81

[154] P. J. Osswald, M. D. Rosario, J. Garche, A. Jossen, and H. E. Hoster. Fast and Accurate Measurement of Entropy Profiles of Commercial Lithium-Ion Cells. *Electrochimica Acta*, 177:270–276, Sep 2015. 89

[155] A. K. Padhi, K. S. Nanjundaswamy, and J. B. Goodenough. Phospho-olivines as Positive-Electrode Materials for Rechargeable Lithium Batteries. *Journal of The Electrochemical Society*, 144(4):1188, Apr 1997. 33

[156] M. Park, X. Zhang, M. Chung, G. B. Less, and A. M. Sastry. A review of conduction phenomena in Li-ion batteries. *Journal of Power Sources*, 195(24):7904–7929, Dec 2010. 61, 84

[157] S. Paul, C. Diegelmann, H. Kabza, and W. Tillmetz. Analysis of ageing inhomogeneities in lithium-ion battery systems. *Journal of Power Sources*, 239:642–650, Oct 2013. 69, 123

[158] L. Pei, T. Wang, R. Lu, and C. Zhu. Development of a voltage relaxation model for rapid open-circuit voltage prediction in lithium-ion batteries. *Journal of Power Sources*, 253:412–418, May 2014. 90

[159] C. Pillot. Battery Market Development for Consumer Electronics , Automotive , and Industrial : Materials Requirements and Trends. In *5th Israeli Power Sources Conference*, volume 33, pages 1–39, Herzelia, 2015. 41

[160] H. A. Radi and J. O. Rasmussen. *Principles of Physics*. Undergraduate Lecture Notes in Physics. Springer Berlin Heidelberg, Berlin, Heidelberg, 2013. 40

[161] J. N. Reimers. Predicting current flow in spiral wound cell geometries. *Journal of Power Sources*, 158(1):663–672, Jul 2006. 74, 76

[162] J. N. Reimers. Accurate and Efficient Treatment of Foil Currents in a Spiral Wound Li-Ion Cell. *Journal of the Electrochemical Society*, 161(1):A118–A127, Nov 2013. 74, 76

[163] J. N. Reimers and J. R. Dahn. Electrochemical and in situ X-ray diffraction studies of lithium intercalation in Li_xCoO_2. *Journal of The Electrochemical Society*, 139(8):2091–2096, Aug 1992. 29

[164] Y. Reynier, J. Graetz, T. Swan-Wood, P. Rez, R. Yazami, and B. Fultz. Entropy of Li intercalation in Li_xCoO_2. *Physical Review B*, 70(17):174304, Nov 2004. 25, 28, 53

[165] Y. Reynier, R. Yazami, and B. Fultz. Thermodynamics and kinetics of self-discharge in graphite-lithium electrodes. In *Seventeenth Annual Battery Conference on Applications and Advances. Proceedings of Conference (Cat. No.02TH8576)*, pages 145–150. IEEE, Jan 2002. 57

[166] Y. Reynier, R. Yazami, and B. Fultz. The entropy and enthalpy of lithium intercalation into graphite. *Journal of Power Sources*, 119-121:850–855, Jun 2003. 25, 27, 53

[167] Y. F. Reynier, R. Yazami, and B. Fultz. Thermodynamics of Lithium Intercalation into Graphites and Disordered Carbons. *Journal of The Electrochemical Society*, 151(3):A422, Feb 2004. 25, 66

[168] D. E. Richardson and P. Sharpe. Vibrational and electronic contributions to entropy changes for oxidation-reduction reactions of metal complexes. *Inorganic Chemistry*, 32(9):1809–1812, Apr 1993. 25

[169] R. R. Richardson, P. T. Ireland, and D. A. Howey. Battery internal temperature estimation by combined impedance and surface temperature measurement. *Journal of Power Sources*, 265:254–261, Nov 2014. 46

[170] M. Ried. *Lösungsraumanalyse für Plug-In-Hybridfahrzeuge hinsichtlich Wirtschaftlichkeit und Bauraumkonzept*. Dissertation, Universität Duisburg-Essen, 2016. 41

[171] B. Rieger, S. V. Erhard, K. Rumpf, and A. Jossen. A New Method to Model the Thickness Change of a Commercial Pouch Cell during Discharge. *Journal of The Electrochemical Society*, 163(8):A1566–A1575, May 2016. 40

[172] B. Rieger, S. Schlueter, S. Erhard, J. Schmalz, G. Reinhart, and A. Jossen. Multi-scale investigation of thickness changes in a commercial pouch type lithium-ion battery. *Journal of Energy Storage*, 6:213–221, May 2016. 38

[173] B. Rieger, S. Schlueter, S. V. Erhard, and A. Jossen. Strain Propagation in Lithium-Ion Batteries from the Crystal Structure to the Electrode Level. *Journal of The Electrochemical Society*, 163(8):A1595–A1606, May 2016. 40

[174] B. Rieger, S. Schuster, S. Erhard, P. Osswald, A. Rheinfeld, C. Willmann, and A. Jossen. Multi-directional laser scanning as innovative method to detect local cell damage during fast charging of lithium-ion cells. *Journal of Energy Storage*, 8:1–5, Nov 2016. 40

[175] R. Robert, C. Bünzli, E. J. Berg, and P. Novák. Activation Mechanism of $LiNi_{0.80}Co_{0.15}Al_{0.05}O_2$: Surface and Bulk Operando Electrochemical, Differential Electrochemical Mass Spectrometry, and X-ray Diffraction Analyses. *Chemistry of Materials*, 27(2):526–536, Jan 2015. 116

[176] M. Roberts, J. J. Biendicho, S. Hull, P. Beran, T. Gustafsson, G. Svensson, and K. Edström. Design of a new lithium ion battery test cell for in-situ neutron diffraction measurements. *Journal of Power Sources*, 226:249–255, Mar 2013. 33, 34

[177] J. B. Robinson, J. A. Darr, D. S. Eastwood, G. Hinds, P. D. Lee, P. R. Shearing, O. O. Taiwo, and D. J. Brett. Non-uniform temperature distribution in Li-ion batteries during discharge – A combined thermal imaging, X-ray micro-tomography and electrochemical impedance approach. *Journal of Power Sources*, 252:51–57, Apr 2014. 46

[178] M. Safari and C. Delacourt. Aging of a Commercial Graphite/LiFePO4 Cell. *Journal of The Electrochemical Society*, 158(10):A1123, Aug 2011. 49, 62

[179] M. Safari and C. Delacourt. Mathematical Modeling of Lithium Iron Phosphate Electrode: Galvanostatic Charge/Discharge and Path Dependence. *Journal of The Electrochemical Society*, 158(2):A63, Dec 2011. 62

[180] Y. Saito, M. Shikano, and H. Kobayashi. State of charge (SOC) dependence of lithium carbonate on $LiNi_{0.8}Co_{0.15}Al_{0.05}O_2$ electrode for lithium-ion batteries. *Journal of Power Sources*, 196(16):6889–6892, Aug 2011. 30, 31

[181] Samsung. Specification of product INR18650-15Q. Technical Report 0, 2011. 43

[182] T. Sasaki, T. Nonaka, H. Oka, C. Okuda, Y. Itou, Y. Kondo, Y. Takeuchi, Y. Ukyo, K. Tatsumi, and S. Muto. Capacity-Fading Mechanisms of $LiNiO_2$-Based Lithium-Ion Batteries. *Journal of The Electrochemical Society*, 156(4):A289, Feb 2009. 51

[183] N. Sato. Entropy control and surface analysis of energy storage systems for advanced vehicles. *Surface and Coatings Technology*, 169-170:758–763, Jun 2003. 53

[184] W. V. Schalkwijk and B. Scrosati. *Advances in Lithium-Ion Batteries*. Springer US, Boston, MA, 2002. 37

[185] J. P. Schmidt, T. Chrobak, M. Ender, J. Illig, D. Klotz, and E. Ivers-Tiffée. Studies on $LiFePO_4$ as cathode material using impedance spectroscopy. *Journal of Power Sources*, 196(12):5349–5355, Jun 2011. 46, 77

[186] R. Scipioni, P. S. Jørgensen, D. T. Ngo, S. B. Simonsen, Z. Liu, K. J. Yakal-Kremski, H. Wang, J. Hjelm, P. Norby, S. A. Barnett, and S. H. Jensen. Electron microscopy investigations of changes in morphology and conductivity of $LiFePO_4$/C electrodes. *Journal of Power Sources*, 307:259–269, Mar 2016. 34

[187] B. Scrosati and J. Garche. Lithium batteries: Status, prospects and future. *Journal of Power Sources*, 195(9):2419–2430, May 2010. 37, 40

[188] R. N. Seefurth and R. A. Sharma. Dependence of Lithium-Silicon Electrode Potential and Lithium Utilization on Reference Electrode Location. *Journal of The Electrochemical Society*, 127(5):1101–1104, May 1980. 58

[189] Y. Shao-Horn, S. Levasseur, F. Weill, and C. Delmas. Probing Lithium and Vacancy Ordering in O3 Layered Li_xCoO_2. *Journal of The Electrochemical Society*, 150(3):A366, Feb 2003. 29

[190] M. Shikano, H. Kobayashi, S. Koike, H. Sakaebe, Y. Saito, H. Hori, H. Kageyama, and K. Tatsumi. X-ray absorption near-edge structure study on positive electrodes of degraded lithium-ion battery. *Journal of Power Sources*, 196(16):6881–6883, Aug 2011. 33

[191] J. Shirafuji and J. E. Field. CoO_2, The End Member of the $LiCoO_2$ Solid Solution. *Electrochemical Society*, 143(3):1114–1123, Mar 1996. 29

[192] A. J. Smith, S. R. Smith, T. Byrne, J. C. Burns, and J. R. Dahn. Synergies in Blended $LiMn_2O_4$ and $LiNi_{1/3}Mn_{1/3}Co_{1/3}O_2$ Positive Electrodes. *Journal of the Electrochemical Society*, 159(10):A1696–A1701, Aug 2012. 123

[193] D. H. Snydacker, M. Aykol, S. Kirklin, and C. Wolverton. Lithium-Ion Cathode/-Coating Pairs for Transition Metal Containment. *Journal of The Electrochemical Society*, 163(9):A2054–A2064, Jul 2016. 36

[194] S. Solchenbach, D. Pritzl, E. J. Y. Kong, J. Landesfeind, and H. A. Gasteiger. A Gold Micro-Reference Electrode for Impedance and Potential Measurements in Lithium Ion Batteries. *Journal of The Electrochemical Society*, 163(10):A2265–A2272, Aug 2016. 58

[195] Sony. Specification of Product - US186503V. Technical report, 2011. 43

[196] B. Stiaszny, J. C. Ziegler, E. E. Krauß, J. P. Schmidt, and E. Ivers-Tiffée. Electrochemical characterization and post-mortem analysis of aged $LiMn_2O_4$–NMC/graphite lithium ion batteries. Part I: Cycle aging. *Journal of Power Sources*, 251:439–450, Apr 2014. 51, 54, 69

[197] B. Stiaszny, J. C. Ziegler, E. E. Krauß, M. Zhang, J. P. Schmidt, and E. Ivers-Tiffée. Electrochemical characterization and post-mortem analysis of aged $LiMn_2O_4$–NMC/graphite lithium ion batteries. Part II: Calendar aging. *Journal of Power Sources*, 258:61–75, Jul 2014. 51, 69, 100

[198] P. Svens, R. Eriksson, J. Hansson, M. Behm, T. Gustafsson, and G. Lindbergh. Analysis of aging of commercial composite metal oxide - $Li_4Ti_5O_{12}$ battery cells. *Journal of Power Sources*, 270:131–141, Dec 2014. 69

[199] K. Takano, Y. Saito, K. Kanari, K. Nozaki, K. Kato, A. Negishi, and T. Kato. Entropy change in lithium ion cells on charge and discharge. *Journal of Applied Electrochemistry*, 32(3):251–258, Jan 2002. 52, 53

[200] T. Q. Tan, M. S. Idris, R. A. M. Osman, M. Reddy, and B. Chowdari. Structure and electrochemical behaviour of $LiNi_{0.4}Mn_{0.4}Co_{0.2}O_2$ as cathode material for lithium ion batteries. *Solid State Ionics*, 278:43–48, Oct 2015. 111

[201] H. Tanida, H. Yamashige, Y. Orikasa, Y. Gogyo, H. Arai, Y. Uchimoto, and Z. Ogumi. Elucidating the Driving Force of Relaxation of Reaction Distribution in $LiCoO_2$ and $LiFePO_4$ Electrodes Using X-ray Absorption Spectroscopy. *The Journal of Physical Chemistry C*, 120(9):4739–4743, Mar 2016. 92

[202] Tesla. Model S Performace options. retrieved 04.12.2016, from `https://www.tesla.com/models/design`, Dez 2016. 14

[203] K. E. Thomas, C. Bogatu, and J. Newman. Measurement of the Entropy of Reaction as a Function of State of Charge in Doped and Undoped Lithium Manganese Oxide. *Journal of The Electrochemical Society*, 148(6):A570, Feb 2001. 35, 53

[204] A. Thompson. Thermodynamics of Li intercalation batteries: Entropy measurements on $LixTiS_2$. *Physica B+C*, 105(1-3):461–465, May 1981. 53

[205] C. Thurston, J. Owen, and N. Hargreaves. Diffusional limitations at the lithium polymer electrolyte interface. *Journal of Power Sources*, 39(2):215–224, Jan 1992. 58

[206] H. Y. Tran, C. Täubert, M. Fleischhammer, P. Axmann, L. Küppers, and M. Wohlfahrt-Mehrens. $LiMn_2O_4$ Spinel / $LiNi_{0.8}Co_{0.15}Al_{0.05}O_2$ Blends as Cathode Materials for Lithium-Ion Batteries. *Journal of The Electrochemical Society*, 158(5):A556, Mar 2011. 36, 123

[207] N. M. Trease, I. D. Seymour, M. D. Radin, H. Liu, H. Liu, S. Hy, N. Chernova, P. Parikh, A. Devaraj, K. M. Wiaderek, P. J. Chupas, K. W. Chapman, M. S. Whittingham, Y. S. Meng, A. Van der Van, and C. P. Grey. Identifying the Distribution of Al^{3+} in $LiNi_{0.8}Co_{0.15}Al_{0.05}O_2$. *Chemistry of Materials*, 28(22):8170–8180, Nov 2016. 30

[208] Y. Troxler, B. Wu, M. Marinescu, V. Yufit, Y. Patel, A. J. Marquis, N. P. Brandon, and G. J. Offer. The effect of thermal gradients on the performance of lithium-ion batteries. *Journal of Power Sources*, 247:1018–1025, Feb 2014. 46

[209] C. A. Truesdell. *The Tragicomical History of Thermodynamics, 1822–1854*, chapter Act IV. Internal Energy: the First Paper of Clausius. Entropy: the First Paper of Rankine, pages 187–218. Springer New York, New York, NY, 1980. 18

[210] L. O. Valøen and J. N. Reimers. Transport Properties of $LiPF_6$-Based Li-Ion Battery Electrolytes. *Journal of The Electrochemical Society*, 152(5):A882, Mar 2005. 37, 61, 84

[211] A. Van der Ven. Phase transformations and volume changes in spinel $Li_xMn_2O_4$. *Solid State Ionics*, 135(1-4):21–32, Nov 2000. 35, 116

[212] G. Venugopal, J. Moore, J. Howard, and S. Pendalwar. Characterization of microporous separators for lithium-ion batteries. *Journal of Power Sources*, 77(1):34–41, Jan 1999. 39, 72

[213] J. Vetter, P. Novák, M. Wagner, C. Veit, K.-C. Möller, J. Besenhard, M. Winter, M. Wohlfahrt-Mehrens, C. Vogler, and A. Hammouche. Ageing mechanisms in lithium-ion batteries. *Journal of Power Sources*, 147(1-2):269–281, Sep 2005. 54, 77

[214] C. von Lüders, V. Zinth, S. V. Erhard, P. J. Osswald, M. Hofmann, R. Gilles, and A. Jossen. Lithium plating in lithium-ion batteries investigated by voltage relaxation and in situ neutron diffraction. *Journal of Power Sources*, 342:17–23, Feb 2017. 69

[215] W. Waag, S. Käbitz, and D. U. Sauer. Experimental investigation of the lithium-ion battery impedance characteristic at various conditions and aging states and its influence on the application. *Applied Energy*, 102:885–897, Feb 2013. 46

[216] M. Wagemaker, F. M. Mulder, and A. Van Der Ven. The role of surface and interface energy on phase stability of nanosized insertion compounds. *Advanced Materials*, 21(25-26):2703–2709, Jul 2009. 33

[217] T. Waldmann, G. Geramifard, and M. Wohlfahrt-Mehrens. Influence of current collecting tab design on thermal and electrochemical performance of cylindrical Lithium-ion cells during high current discharge. *Journal of Energy Storage*, 5:163–168, Feb 2016. 63

[218] T. Waldmann, N. Ghanbari, M. Kasper, and M. Wohlfahrt-Mehrens. Correlations between Electrochemical Data and Results from Post-Mortem Analysis of Aged Lithium-Ion Batteries. *Journal of the Electrochemical Society*, 162(8):A1500–A1505, May 2015. 100

[219] T. Waldmann, S. Gorse, T. Samtleben, G. Schneider, V. Knoblauch, and M. Wohlfahrt-Mehrens. A Mechanical Aging Mechanism in Lithium-Ion Batteries. *Journal of the Electrochemical Society*, 161(10):A1742–A1747, Jul 2014. 72

[220] G. X. Wang, S. Bewlay, J. Yao, J. H. Ahn, S. X. Dou, and H. K. Liu. Characterization of LiM_xFePO_4 Cathode Materials Prepared by the Sol-Gel Method. *Electrochemical and Solid-State Letters*, 7(12):A503, Nov 2004. 33

[221] S. Watanabe, M. Kinoshita, T. Hosokawa, K. Morigaki, and K. Nakura. Capacity fade of $LiAl_yNi_{1-x-y}Co_xO_2$ cathode for lithium-ion batteries during accelerated calendar and cycle life tests (surface analysis of $LiAl_yNi_{1-x-y}Co_xO_2$ cathode after cycle tests in restricted depth of discharge ranges). *Journal of Power Sources*, 258:210–217, Jul 2014. 31

[222] S. Watanabe, M. Kinoshita, T. Hosokawa, K. Morigaki, and K. Nakura. Capacity fading of $LiAl_yNi_{1-x-y}Co_xO_2$ cathode for lithium-ion batteries during accelerated calendar and cycle life tests (effect of depth of discharge in charge-discharge cycling on the suppression of the micro-crack generation of $LiAl_yNi_{1-x-y}Co_xO_2$ particles. *Journal of Power Sources*, 260:50–56, Aug 2014. 31

[223] E. W. Weisstein. "Archimedes' Spiral." From MathWorld–A Wolfram Web Resource. retrieved 15.02.2016, from `http://mathworld.wolfram.com/ArchimedesSpiral.html`, Sep 2015. 74

[224] M. Winter, J. O. Besenhard, M. E. Spahr, and P. Novák. Insertion Electrode Materials for Rechargeable Lithium Batteries. *Advanced Materials*, 10(10):725–763, Jul 1998. 38

[225] Q. Wu, W. Lu, and J. Prakash. Characterization of a commercial size cylindrical Li-ion cell with a reference electrode. *Journal of Power Sources*, 88(2):237–242, Jun 2000. 59

[226] Y.-F. Xia, M. Nie, Z.-B. Wang, F.-D. Yu, Y. Zhang, L.-L. Zheng, J. Wu, and K. Ke. Structural, morphological and electrochemical investigation of $LiNi_{0.6}Co_{0.2}Mn_{0.2}O_2$ cathode material synthesized in different sintering conditions. *Ceramics International*, 41:11815–11823, Nov 2015. 124

[227] L. Xiao, X. Chen, R. Cao, J. Qian, H. Xiang, J. Zheng, J.-g. Zhang, and W. Xu. Enhanced performance of $Li/LiFePO_4$ cells using $CsPF_6$ as an electrolyte additive. *Journal of Power Sources*, 293:1062–1067, Oct 2015. 37

[228] K. Xu, S. P. Ding, and T. Richard Jow. Toward Reliable Values of Electrochemical Stability Limits for Electrolytes. *Journal of The Electrochemical Society*, 146(11):4172, Jul 1999. 37

[229] Y. Xu, Y. Chen, J. Wu, D. Li, H. Ju, and J. Zheng. The determination of the kinetic parameters of electrochemical reaction in chemical power sources: A critical review. *International Journal of Hydrogen Energy*, 35(12):6366–6380, Jun 2010. 50

[230] N. Yabuuchi and T. Ohzuku. Novel lithium insertion material of $LiCo_{1/3}Ni_{1/3}Mn_{1/3}O_2$ for advanced lithium-ion batteries. *Journal of Power Sources*, 119-121:171–174, Jun 2003. 32

[231] A. Yamada, H. Koizumi, S.-I. Nishimura, N. Sonoyama, R. Kanno, M. Yonemura, T. Nakamura, and Y. Kobayashi. Room-temperature miscibility gap in Li_xFePO_4. *Nature Materials*, 5(5):357–360, May 2006. 119

[232] A. Yamada, H. Koizumi, N. Sonoyama, and R. Kanno. Phase change in Li_xFePO_4. *Electrochemical and Solid State Letters*, 8(8):A409–A413, Jun 2005. 33

[233] X. Yan and X. G. Su. *Linear Regression Analysis*. World Scientific, Jun 2009. 89

[234] R. Yazami and Y. Reynier. Mechanism of self-discharge in graphite–lithium anode. *Electrochimica Acta*, 47(8):1217–1223, Feb 2002. 47

[235] S.-C. Yin, Y.-H. Rho, I. Swainson, and L. F. Nazar. X-ray/Neutron Diffraction and Electrochemical Studies of Lithium De/Re-Intercalation in $Li_{1-x}Co_{1/3}Ni_{1/3}Mn_{1/3}O_2$ $(0 < x < 1)$. *Chemistry of Materials*, 18(2):1901–1910, Apr 2006. 32

[236] W. S. Yoon, K. Y. Chung, J. McBreen, and X. Q. Yang. A comparative study on structural changes of $LiNi_{1/3}Mn_{1/3}Co_{1/3}O_2$ and $LiNi_{0.8}Co_{0.2}Al_{0.05}O_2$ during first charge using in situ XRD. *Electrochemistry Communications*, 8(8):1257–1262, Aug 2006. 30, 31

[237] M. Yoshio, R. J. Brodd, and A. Kozawa, editors. *Lithium-Ion Batteries*, volume 53. Springer New York, New York, NY, 2009. 29

[238] D. Y. W. Yu, C. Fietzek, W. Weydanz, K. Donoue, T. Inoue, H. Kurokawa, and S. Fujitani. Study of $LiFePO_4$ by Cyclic Voltammetry. *Journal of The Electrochemical Society*, 154(4):A253, Feb 2007. 51, 77

[239] K. Zaghib, N. Ravet, M. Gauthier, F. Gendron, A. Mauger, J. B. Goodenough, and C. M. Julien. Optimized electrochemical performance of $LiFePO_4$ at 60 °C with purity controlled by SQUID magnetometry. *Journal of Power Sources*, 163(1 SPEC. ISS.):560–566, Dec 2006. 34

[240] G. Zhang, C. E. Shaffer, C.-Y. Wang, and C. D. Rahn. Effects of Non-Uniform Current Distribution on Energy Density of Li-Ion Cells. *Journal of the Electrochemical Society*, 160(11):A2299–A2305, Oct 2013. 63

[241] G. Zhang, C. E. Shaffer, C.-Y. Wang, and C. D. Rahn. In-Situ Measurement of Current Distribution in a Li-Ion Cell. *Journal of the Electrochemical Society*, 160(4):A610–A615, Feb 2013. 63

[242] S. Zhang and T. Jow. Aluminum corrosion in electrolyte of Li-ion battery. *Journal of Power Sources*, 109(2):458–464, Jul 2002. 40

[243] S. S. Zhang. A review on electrolyte additives for lithium-ion batteries. *Journal of Power Sources*, 162(2 SPEC. ISS.):1379–1394, Nov 2006. 37

[244] S. S. Zhang. A review on the separators of liquid electrolyte Li-ion batteries. *Journal of Power Sources*, 164(1):351–364, Jan 2007. 39

[245] W. J. Zhang. Lithium insertion/extraction mechanism in alloy anodes for lithium-ion batteries. *Journal of Power Sources*, 196(3):877–885, Feb 2011. 39

[246] W. J. Zhang. Structure and performance of $LiFePO_4$ cathode materials: A review. *Journal of Power Sources*, 196(6):2962–2970, Mar 2011. 33

[247] Z. Zhang, D. Fouchard, and J. Rea. Differential scanning calorimetry material studies: implications for the safety of lithium-ion cells. *Journal of Power Sources*, 70(1):16–20, Jan 1998. 54

[248] Z. Zhang and S. S. Zhang, editors. *Rechargeable Batteries*. Green Energy and Technology. Springer International Publishing, Cham, 2015. 29

[249] H. Zheng, Q. Sun, G. Liu, X. Song, and V. S. Battaglia. Correlation between dissolution behavior and electrochemical cycling performance for $LiCo_{1/3}Ni_{1/3}Mn_{1/3}O_2$ based cells. *Journal of Power Sources*, 207:134–140, Jun 2012. 33

[250] S. Zheng, R. Huang, Y. Makimura, Y. Ukyo, C. A. J. Fisher, T. Hirayama, and Y. Ikuhara. Microstructural Changes in $LiNi_{0.8}Co_{0.15}Al_{0.05}O_2$ Positive Electrode Material during the First Cycle. *Journal of The Electrochemical Society*, 158(4):A357, Feb 2011. 30

[251] F. Zhou, T. Maxisch, and G. Ceder. Configurational electronic entropy and the phase diagram of mixed-valence oxides: The case of $LixFePO_4$. *Physical Review Letters*, 97(15):1–4, Oct 2006. 28

[252] Y.-R. Zhu, Y. Xie, R.-S. Zhu, J. Shu, L.-J. Jiang, H.-B. Qiao, and T.-F. Yi. Kinetic study on $LiFePO_4$-positive electrode material of lithium-ion battery. *Ionics*, 17(5):437–441, Feb 2011. 77

[253] V. Zinth, C. von Lüders, M. Hofmann, J. Hattendorff, I. Buchberger, S. Erhard, J. Rebelo-Kornmeier, A. Jossen, and R. Gilles. Lithium plating in lithium-ion batteries at sub-ambient temperatures investigated by in situ neutron diffraction. *Journal of Power Sources*, 271:152–159, Dec 2014. 69